

This work is protected by copyright and other intellectual property rights and duplication or sale of all or part is not permitted, except that material may be duplicated by you for research, private study, criticism/review or educational purposes. Electronic or print copies are for your own personal, non-commercial use and shall not be passed to any other individual. No quotation may be published without proper acknowledgement. For any other use, or to quote extensively from the work, permission must be obtained from the copyright holder/s.

An integrated analysis of facies control on deformation bands
in mixed aeolian-fluvial sandstone reservoirs



A thesis submitted in accordance with the requirements of Keele University for the degree
of Doctor of Philosophy

Karl Clark

December 2021

Abstract

Deformation bands are the primary structural element of fault damage zones within porous granular rocks. They are sub-seismic structures that act to modify the petrophysical properties of the host lithology, and as such are an area of focused research to understand their impact on fluid flow in subsurface reservoirs. Deformation bands have been shown to negatively impact fluid flow in reservoirs, with reduced porosity and permeability, and therefore pose a problem for many subsurface energy resources including hydrocarbon exploration and production, groundwater aquifer management, geothermal energies, and carbon sequestration.

Deformation bands require a diverse methodological approach in order to fully understand the mechanisms of their formation and their impacts on rock properties. Current understanding of deformation bands has been drawn primarily from field outcrops, subsurface sampling, as well as insights provided by experimental rock mechanics. It is suggested that the formation of these structures and their properties is strongly related to host lithological properties, such as porosity, grain size, sorting and mineralogy, as well as the stress conditions at which they form. Their prevalence within high porosity, coarse-grained lithologies of aeolian origin has shown that grain size and porosity are the primary controls on their formation. However, the prevalence of this facies in the literature presents sampling bias and therefore bias in interpretation of the controls on their formation, with other lithological variables such as grain sorting and bed thickness, relatively understudied.

This thesis presents results of an integrated approach to understand the controls on deformation band formation, and the controls on their petrophysical properties. Mixed aeolian-fluvial reservoirs of the United Kingdom, the Triassic Sherwood Sandstone Group and

the Devonian Old Red Sandstone Group are host to pervasive deformation band networks associated with faulting, and also offer the unique opportunity to examine the role of extreme lithological variability on their formation. Field sampling of fault damage zones and deformation bands is combined with petrographic and microstructural analysis and complemented with experimental rock mechanics to investigate the link between sedimentary facies and deformation band formation and petrophysical impact.

Results of petrographic and microstructural analysis show that the type of deformation band structure formed is function of the porosity and grain size of the host lithology. Grain size distribution analysis reveals fractal grain size relationships which reflect the deformation mechanisms of band formation that is strongly influenced by grain sorting. Deformation bands within aeolian lithofacies display higher porosity and cataclasis than those within fluvial lithofacies, resulting in greater reduction in permeability. This field observation is also supported by triaxial deformation experiments on unconsolidated quartz aggregates in which the porosity, grain size, and mineralogy remain fixed, and sorting is varied. Sorting is found to influence the micromechanics of deformation, and thus the grain textures produced by cataclasis, resulting in greater permeability reduction within well-sorted materials. Measurements of deformation band intensity using two-dimensional window sampling also reveal a strong influence of grain sorting on both the intensity of fault damage zones, and the width of deformation bands. Intensity is highest within well-sorted lithologies, where permeability reduction is also highest, however, the average width and width variability of deformation bands is greatest within fluvial facies. It may be proposed that the increased intensity of bands within aeolian facies, may be balanced by the increased width within fluvial facies, and therefore these structures may act to maintain any inherent fluid flow

heterogeneity. These observations provide crucial insight into the effects of facies and ultimately lithological properties on deformation bands in mixed aeolian-fluvial reservoirs.

Table of Contents

Abstract	ii
List of figures and tables	viii
Funding Information	xxv
1. Introduction	1
1.1 <i>Project motivation</i>	1
1.2 <i>Research Aims</i>	4
1.3 <i>Thesis Structure</i>	5
2. Background	7
2.1 <i>Fault damage zones in sandstones</i>	7
2.2 <i>Classification</i>	11
2.2.1 <i>Kinematics</i>	11
2.2.2 <i>Mechanism</i>	14
2.3 <i>Controls on deformation bands</i>	21
2.3.1 <i>Porosity and Grain Size</i>	21
2.3.2 <i>Stress</i>	26
2.3.3 <i>Mineralogy</i>	30
2.3.4 <i>Grain Size Distribution</i>	32
2.3.5 <i>Cementation</i>	34
3. Methodology	35
3.1 <i>Logging and Sampling</i>	35
3.2 <i>Petrographic Analysis</i>	35
3.3 <i>Porosity measurement</i>	39
3.4 <i>Permeability measurement</i>	42
3.5 <i>Fault damage zone measurements</i>	45
3.6 <i>Experimental rock mechanics</i>	50
4. Study locations and lithofacies descriptions	53
4.1 <i>Case study 1 – Cheshire Basin, UK.</i>	53
4.1.1 <i>Stratigraphy of the Sherwood Sandstone Group</i>	55
4.1.2 <i>Deformation bands in the Cheshire Basin</i>	59
4.1.3 <i>Localities</i>	60
4.2 <i>Facies Associations</i>	75
4.2.1 <i>Aeolian Dune</i>	77
4.2.2 <i>Aeolian Sand sheet</i>	77

4.2.3. Aeolian Interdune/Overbank	80
4.2.4. Fluvial Sheet Flood.....	80
4.2.5. Fluvial Channel facies	80
4.2.6. Fluvial Barforms	80
4.3. Porosity – permeability relationship	83
4.4. Case Study 2 - Devonian Old Red Sandstone, Pease Bay, Scotland	85
4.4.1 Stratigraphy of Pease Bay	85
4.4.2. Localities.....	88
4.4.3. Undeformed Lithofacies and Facies Associations.....	94
4.5. Conclusions	97
4.6. Supplementary material	98
5. Microstructure and petrophysical properties of deformation bands.	99
5.1. Deformation band properties	99
5.2. Porosity – permeability relationships	107
5.3. Grain size distribution analysis	110
5.4. Discussion	117
5.5. Conclusions	122
6. Deformation Band Fault Damage zones	123
6.1. Introduction	123
6.2. Fault Damage Zone Intensity.....	126
6.2.1. Cheshire Basin	126
6.2.2. Pease Bay	131
6.3. Deformation Band Width.....	134
6.3.1. Pease Bay	134
6.3.2. Cheshire Basin	136
6.4. Discussion	138
6.4.1. Deformation band geometry.....	138
6.4.2. Displacement versus damage zone width scaling	141
6.4.3. Lithological Control on Deformation Band Attributes	143
6.4.4. Role of Bed Thickness	148
6.4.5. Implications for Fluid Flow	149
6.5. Conclusions	154
7. Insights from experimental rock mechanics	156
7.1. Introduction	156

7.1.1. Deformation of unconsolidated sands.....	158
7.2. Methods.....	160
7.2.1. Sample material and preparation	160
7.2.2. Experimental Procedure	169
7.2.3. Microstructural analysis	172
7.2.4. Grain size distribution analysis.....	172
7.3. Results.....	173
7.3.1. Hydrostatic loading experiments.....	173
7.3.2. Triaxial loading experiments	179
7.3.3. Microstructural and grain size analysis.....	182
7.4. Discussion	190
7.4.1. Inelastic deformation during hydrostatic compaction of unconsolidated sands.	190
7.4.2. The role of grain sorting on micromechanics and post-yield deformation	192
7.4.3. Implications for Sedimentary Basins	195
7.5 Conclusions	199
8. Summary and Conclusions	201
References	206
<i>Appendix</i>	223

List of figures and tables

Figure 2.1. Schematic diagram of a normal fault zone within porous sandstone. The fault core is an amalgamation of deformation bands in which a fault plane is formed.

Deformation bands are the major feature of the fault damage zone, with a conjugate arrangement, at low angles to the main fault plane in both plan and section view. Band density increases with proximity to the fault.

Figure 2.2. Log-log plot of damage zone width versus fault displacement for deformation band fault damage zones shows a power-law trend with an exponent n of 0.68. Data compiled by Choi et al. (2016) and references therein.

Figure 2.3. Kinematic classification of deformation bands. Bands are classified based on the amount and type of volumetric change and sense of any shear. Adapted from (Fossen et al., 2007)

Figure 2.4. Deformation band classification by deformation mechanism and associated physical properties. Four major types are identified, although it is not uncommon to find a combination of mechanisms within a single band. Adapted from (Fossen et al., 2007)

Figure 2.5. A comparison of the Gullfaks and Gullfaks Sor sands using SEM and BSE images. (A, C) Gullfaks is characterised by minor phyllosilicates and lower temperature conditions, inhibiting syntaxial quartz cementation, resulting in a high porosity and a productive reservoir. (B, D) Gullfaks Sor is characterised by cataclasis of quartz grains and higher temperatures, promoting the growth of syntaxial quartz cements, significantly reducing porosity and the productivity of the reservoir. Modified from Hesthammer et al. (2002).

Figure 2.6. (a) Stress-strain curve for the hydrostatic compaction of porous rock. The inflection, P^* , marks the transition from quasi-linear elastic compaction to non-linear

inelastic compaction and the onset of grain fracturing, also known as the critical pressure.

(b) Critical pressure at which grain crushing occurs as a function of porosity and grain radius.

Data shows that rock strength decreases with increasing porosity and grain size. Initial experiments by Zhang et al. (1990) determined a linear relationship with slope of $-3/2$ (solid line). Later experiments and compilation of various data sets yield a linear relationship of $0.603-1.089$ (dashed line). (Wong et al., 1997; Rutter and Glover, 2012).

Figure 2.7. Q-P- Φ R diagram showing the effects of porosity and grain size on the yield cap of porous sandstones. Larger grain sizes and high porosity are inherently weaker than finer, less porous sandstones, and therefore have smaller yield caps. The critical state line marks the division of dilation (dark grey) and compaction (light grey). Modified from (Cuss et al., 2003).

Figure 2.8. Force chain network of fracturing in both poorly sorted and well sorted sands. Grain contacts are more distributed in poorly sorted sands, where the smaller grains bare the stresses between the larger grains, limiting fracturing amongst the finer fraction, whose connectivity may be limited. Grain contacts are less dense in well sorted sands and therefore, stresses at contacts are higher, enabling the propagation of fractures from grain to grain.

Figure 3.1. Petrog software and optical microscope stage used for point counting textural analysis. Thin sections are scanned systematically to obtain textural and compositional data through point counting. An example data output sheet from Petrog is shown, and included grain size statistics, grains size distribution histogram, and a rose diagram of grain orientation.

Figure 3.2. ImageJ jPORv1.1 porosity calculation method. (i) Tiff image of a thin section of blue resin impregnated sandstone sample. (ii) an 8-bit palette filter is applied to the photomicrograph and saved as a bitmap. (iii) jPORv1.1 plug-in for imageJ is used to manually threshold the blue pore filling resin (red). (iv) ImageJ calculates the area of red threshold pore space as a percentage of total image area to give a porosity value. A binary black and white image of the photomicrograph is produced representing grains and pore space respectively.

Figure 3.3. The relationship between porosity obtained using optical images against porosity obtained using back scattered electron images shows a strong power-law relationship that may be used for correction of values obtained by the former, particularly those at lower porosity levels.

Figure 3.4. NER TinyPerm II permeameter used for measurements on both outcrop and core.

Figure 3.5. The Pxy system for fracture measurements based on dimensions of feature and sampling method. One dimensional intensity P10 and two-dimensional intensity P21 measurements show greater uncertainty for P10 due to censoring and user bias.

Figure 3.6. Deterministic model of fault zone development with increased displacement (Schueller et al., 2013). Different zones of varying deformation band intensity can be identified by the gradient of cumulative band intensity, to define damage zone width (Choi et al., 2016). Damage zone intensity is shown to independent of displacement, and may be controlled by other factors such as lithology.

Figure 3.7. (a) Schematic drawing of the triaxial deformation apparatus used for both hydrostatic and triaxial experiments. (b) Schematic drawing of the sample preparation prior to testing.

Figure 4.1. Stratigraphy and geological map of the Cheshire Basin. The Helsby Formation is the main formation of interest, expressing the most facies variation within the Sherwood Sandstone Group. Field localities are indicated on the map.

Figure 4.2. Stratigraphy of the Cheshire Basin, with lateral equivalents and petroleum reservoir sands of the East Irish Sea Basin, Shetland Basin, Northern, central and southern North Sea. (Adapted from (Aydin and Johnson, 1978; Ruffell, 2003; McKie and Williams, 2009)

Figure 4.3. (a) Geological map of Helsby including the study areas and major faults of interest. (b) Helsby Hill Fault with extensive deformation band damage zone. (c) Deformation bands within aeolian beds of Helsby Quarry.

Figure 4.4. (a) Geological map of Grinshill including major faults of interest. (b) Two structural trends in deformation bands corresponding to two major faults. (c) A dense deformation band zone containing a deformation band cluster.

Figure 4.5. (a) Geological map of Thurstaston including study area and major faults of interest. (b) Two Faults observed in the road cutting on Telegraph road displace beds of quartz arenite and sub-arkosic sandstones.

Figure 4.6. (a) Geological map of Alderley Edge including study area and major faults of interest. (b) The Engine Vein fault exposed along a mine working.

Figure 4.7. Geological map of the Nesscliffe locality including the highlighted study area in Nesscliffe Country Park. Between two approximately E-W striking faults.

Figure 4.8. (a) Fluvial Helsby Formation eroding into aeolian units of the Wilmslow Formation at Bickerton. (b) Fluvial sequences of the Delamere Member observed at Helsby Hill show pebbly channel sandstones, and cross bedded and rippled fluvial bars. (c) Faulted fluvial channel units at the top of Grinshill. (d) Interbedded fluvial muds and fine sands at Helsby Quarry show the transition to a fluvial dominated environment. (e) Synthetic faults cut through a massive aeolian sequence at Grinshill. (f) Massive aeolian sequences transition to fluvial at Nesscliffe. (g) Deformation bands in heterolithic fluvial sheet flood beds of the Wilmslow formation in the Holcroft Lane borehole. (h) Deformation bands in aeolian sandstones of the Frodsham Member of the Helsby Sandstone Formation in the Saughall Massie borehole.

Figure 4.9. Equal area stereonet plots showing structural data for the localities across the Cheshire Basin study: (a) Grinshill. (b) Helsby. (c) Nesscliffe. (d) Alderley Edge. (e) Saughall Massie. (f) Thurstaston. Plots show poles to deformation bands with mean planes in red in relation to the principal fault planes in yellow.

Figure 4.10. Sedimentary logs of outcrop and core localities, coloured by facies association. Permeability logs are shown adjacent to core logs

Figure 4.11. Optical photomicrographs of examples of 6 facies association. Refer to logs (Fig 4.10) for sample locations. (a) Aeolian dune facies from the Saughall Massie borehole. Well-sorted, sub-rounded clasts of quartz and minor amounts of feldspar. (b) Fluvial channel facies from Helsby. Poorly-sorted, angular clasts of quartz, feldspar and minor clays. (c) Aeolian sand sheet from the Abbey Arms Wood borehole. Bi-modal grain-size distribution of

very well-rounded coarse clasts and sub-rounded fine clasts. (d) Interdune/overbank facies from the Holcroft Lane borehole. Fine-grained, moderately-sorted grains in a muddy-silty matrix. (e) Fluvial sheet facies from the Holcroft Lane borehole. Bi-modal grain-size distribution with laminations of large, sub-angular grains, and fine-grained muddy clasts. (f) Fluvial bar form facies from Helsby. Moderately well-sorted, sub-angular, medium-grained quartz arenite.

Figure 4.12. (a) Box and whisker plot of permeability by facies association. (b) Ternary diagram showing the abundance of quartz, feldspar and lithic grains for the lithofacies sampled, coloured by facies association.

Figure 4.13. Figure 4.13. Porosity versus permeability for undeformed samples of the upper Sherwood Sandstone. Both measured permeability shown in green, and calculated permeability in red, show a power law relationship. Data from the Abbey Arms Wood borehole, obtained using mini permeameter are shown for comparison (Bloomfield et al., 2006).

Figure 4.14. Location and geological map of the study area including mapped localities and stratigraphy of the local area.

Figure 4.15. (a) Outcrops in the hillside of Pease Bay showing localities and major faults and fault damage zones. (b) Locality 3 displays a highly deformed and complex zone of deformation bands associated with an inferred fault to the north toward locality 2. (c) A fault displaces a small succession of fluvial sandstones of varying grain sizes as well as a minor mudstone horizon. Deformation band density and thickness are recorded for each of the beds. (d) Locality 5 displays a 25m damage zone of deformation bands within aeolian beds. (e) Fault zone at locality 6 in which a sequence of mudstones and small channel

sandstones are displaced by a fault with approximately 1.5m throw, and a pair of antithetic faults with displacements of 7 and 18cm. Damage zone density is measured in the three beds indicated. (f) Locality 6, Red Rocks, displays faulted beds of aeolian and fluvial facies mudstones and sandstones dipping shallowly to the north-east.

Figure 4.16. Equal area stereonet plots of deformation bands and faults for (a) Locality 3, (b) Locality 4, (c) Locality 5, and (d) Locality 6. The same structural trend is observed across the bay, with east-west trending faults and conjugate sets of deformation bands at low angle to the faults with an intersection of 45-50°.

Figure 4.17. Sedimentary logs across Pease Bay recording lithofacies and facies association variation across three localities. Logs show the overall facies change within the Upper Devonian Greenheugh Formation. Recording a predominantly arid wind-blown environment to a humid fluvial environment.

Figure 5.1. Examples of deformation bands. (a) Bands are cataclastic in the Saughall Massie borehole. (b) Disaggregation shear bands displace laminations and show evidence for fluid flow within fluvial sheet flood facies in the Holcroft Lane borehole. (c) Cataclastic bands within aeolian dune facies in Helsby Quarry. (d) Disaggregation shear bands displace laminations of fluvial sheet flood deposits in the Holcroft Lane borehole. (e) Disaggregation bands weather more than adjacent undeformed rock and show evidence for fluid flow pathways in fine-grained aeolian facies at Pease Bay. (f) Cataclastic shear deformation bands displace laminations within aeolian facies at Pease Bay.

Figure 5.2. Photomicrographs of host lithologies and their deformation bands, including their respective porosity values, grain sphericity (i) and grain fabric (ii). (a) A coarse-grained fluvial channel unit from Helsby. (b) A medium-grained aeolian dune sample from the

Saughall Massie borehole. (c) A fine-grained fluvial bar unit from Grinshill. (d) A fine grained, fluvial sheet flood sample from the Holcroft Lane borehole.

Figure 5.3. Back scattered electron (BSE) photomicrographs of the internal microstructure of deformation bands. (a) Deformation band with micro-breccia-protocataclastic texture in a fine-grained aeolian dune, Pease Bay, Scotland. (b) High magnification of image a showing grain size reduction within a deformation band. (c) Protocataclastic texture within a deformation band in a coarse-grained fluvial channel, Helsby Hill, Cheshire, UK. (d) High magnification of protocataclastic texture within a deformation band. (e) Deformation band with micro-breccia texture within a fine-grained aeolian dune, Nesscliffe, Shropshire, UK. (f) High magnification image showing grain size reduction of quartz and feldspar grains. (g) Fault core sample from the Helsby Hill fault. Cataclastic-ultracataclastic texture has a low porosity of 4.7%, with large grains supported in a very fine-grained matrix. (h) High magnification of fault core ultracataclasite, very fine-grained matrix fills pore spaces.

Figure 5.4. Log-log plot of host rock versus deformation band porosity. Our data shown in red against published deformation band porosity data for sandstones from (Rowe and Burley, 1997; Ogilvie and Glover, 2001; Shipton and Cowie, 2001; Shipton et al., 2002; Torabi and Fossen, 2009; Farrell et al., 2014; Ballas et al., 2015; de Lima Rodrigues et al., 2015; Wilkins et al., 2019)

Figure 5.5. Porosity permeability relationships for undeformed lithofacies and deformation bands measured with both permeameter (green) and calculated using Bergs method for permeability estimation (red). Shown for comparison is a data set also obtained from image analysis from Torabi et al. (2013).

Figure 5.6. Graph showing the grain size distribution of undeformed host rock and deformation bands. Data shows the results of cataclasis in which grains fracture and grain size is reduced. Both host rock and deformation bands show a high degree of variability.

Figure 5.7. Grain size distribution represented on a log-log plot of grain size against number of grains. A power-law relationship is indicative of a fractal distribution where the exponent D is the fractal dimension. It is proposed that D will develop with increasing cataclasis as well as increasing fractal range. Figure adapted from Blenkinsop (1991) & Zhong et al. (2018).

Figure 5.8. Log-log plots of grain size distribution for deformation bands, used to record the fractal dimension and fractal range.

Figure 5.9. Log-log plot of deformation band permeability versus host rock permeability for our deformation bands. Solid symbols represent measured host permeability. Open symbols represent calculated host permeability. Included is a large published data set of different cataclastic structures; individual bands, slipped bands, band clusters and fault core, from Ballas et al. (2015) and references therein.

Figure 5.10. Cross plots of lithological properties and deformation band properties.

Figure 6.1. Linear and cumulative plots of deformation band intensity for series of fault damage zones within different lithologies. Lithological properties are included in each plot. (a) Footwall of the Helsby Hill fault within a medium-grained fluvial sandstone. (b) Hanging wall of the Helsby Hill fault within a medium-grained fluvial sandstone. (c) Hanging wall of the Grinshill Hill fault within a fine-grained fluvial sandstone, and Corbet Wood fault within a fine-grained aeolian dune sandstone at Grinshill.

Figure 6.2. Deformation band density for fault damage zones at Telegraph road, Thurstaston. Data from Griffiths et al. (2016). Both damage zones occur in coarse-grained quartz arenites, aeolian in origin, adjacent to faults with displacements of approx. 19 and 64 cm.

Figure 6.3. Frequency and cumulative frequency plots of deformation bands within different lithofacies in three fault zones, FDZ3, FDZ4 and FDZ5. Bands decay logarithmically with distance in FDZ4 up until a series of minor faults induce spikes in frequency. The cumulative data plot shows damage zone intensity of 6 bands per metre up until 17m where a decrease to 2 bands per metre occurs. FDZ5 and FDZ3 show band density within three distinct lithologies, with minor faults corresponding to peaks in band frequency. Cumulative frequency plots show variation in average band density (trend lines) between lithofacies.

Figure 6.4. Histograms of deformation band width for fault zones at Pease Bay.

Figure 6.5. Histograms of deformation band width for a variety of lithologies within fault damage zones of the Cheshire Basin case study.

Figure 6.6. Summary diagram showing faulting and deformation band geometry across the localities of the study.

Figure 6.7. Log-log plots of deformation band damage zone width versus displacement. Previous data compiled by Choi et al. (2016) and references therein.

Figure 6.8. Cross-plots of deformation band attributes with lithological properties. (a) Inner and outer damage zone intensity against grain size. (b) Deformation band and lens width against grain size. (c) Inner and outer damage zone intensity against bed thickness. (d) Deformation band and lens width against bed thickness. (e) Inner and outer damage zone intensity against sorting. (f) Deformation band and lens width against sorting.

Figure 6.9. Deformation band width data by facies association.

Figure 7.1. Photomicrographs of sand material used in experiments. (a) Fine grains (150-200 μ m) from the Chelford sand formation. (b) Coarse grains (500-600 μ m) of the Chelford sand formation. (c) Fine grains (150-200 μ m) of the Congleton sand. (d) Coarse grains (400-500 μ m) of the Congleton sand.

Figure 7.2. Example sample statistics output from Gradistat analysis of grain size data obtained using LPSA.

Figure 7.3. Grain size distribution profiles of four samples used in hydrostatic loading experiments.

Figure 7.4. Grain size distribution profiles for samples prepared for hydrostatic and triaxial testing. (a) Grain size distribution by number of grains. (b) Grain size distribution by volume of grains.

Figure 7.5. Sample configuration for triaxial experiments.

Figure 7.6. (a) The hydrostatic loading method used for all experiments. Confining pressure is increased in small increments of 3-5 MPa once pore volume has equalised with each increment. (b) A q-p diagram showing the triaxial experimental strategy. P^* defines the point of failure during hydrostatic compaction experiments. Further triaxial tests are performed at effective stress conditions as a percentage of this value, in order to explore deformation at different points around the yield envelope, and make fair comparisons between samples with slight variations in strength.

Figure 7.7. (a) Results of hydrostatic loading experiments on samples of different grain size. Samples show an initial non-linear loading, followed by a quasi-linear elastic phase of

deformation. In two of the four samples (700 and 390 micron) an inflection marks the onset of permanent deformation, P^* , followed by a region of non-linear compaction. All samples show considerable unrecoverable deformation upon unloading. (b) P^* values from hydrostatic tests are plotted on a log P^* vs log (porosity x grain radius), as well as a compilation of results from the literature of both sandstone and unconsolidated materials, references shown in key.

Figure 7.8. SEM photomicrographs of 200 micron (a), 390 micron (b), and 700 micron (c) samples deformed hydrostatically showing grain crushing and surpassing of the critical pressure P^* .

Figure 7.9. (a) Results of hydrostatic compaction tests on 350mm sand with four levels of grain sorting. (b) Results of hydrostatic stress cycling experiments on a sample of VWS sand. Unloading curves of each cycle show accumulation of inelastic strain. Inelastic strain is plotted against the maximum stress of each cycle, and accounts for approx. 65% of total strain.

Figure 7.10. Photomicrographs of a 344 micron moderately well-sorted sand. Deformed hydrostatically and removed at 19 (a), 37 (b) and 75 MPa (c) to confirm the onset of grain crushing (P^*). Samples taken to 19 and 37 MPa display no grain deformation. Sample taken to 75 MPa confirms the occurrence of P^* , marked by pervasive grain fracturing.

Figure 7.11. Results of triaxial experiments for very well-sorted sand. Yield (C'/C^*) is determined from two methods; deviation of porosity change from the hydrostat with mean effective stress (a), indicated by solid symbols, and differential stress vs axial strain curves where the data becomes non-linear(b), indicated by open symbols. The conditions at which samples were axially loaded are indicated next to data curves. (c) Yield points are plotted in

differential stress (Q) versus mean effective stress (P) space, and form a broadly elliptical yield envelope.

Figure 7.12. Results of triaxial experiments for moderately well-sorted sand. Yield (C'/C^*) is determined from two methods; deviation of porosity change from the hydrostat with mean effective stress (a), indicated by solid symbols, and differential stress vs axial strain curves where data becomes non-linear (b), indicated by open symbols. (c) Yield points are plotted in differential stress (Q) versus mean effective stress (P) space, and form a broadly elliptical yield envelope.

Figure 7.13. Back Scattered Electron (BSE) photomicrographs of triaxially deformed very well-sorted sands (a, c, e, g), and moderately well-sorted sands (b, d, f, h) deformed at approx. 10, 32, 50 and 80% of P^* respectively. Samples are shown side by side for comparison, with the confining conditions at which each sample was deformed indicated. Samples show a transition in deformation mechanism from grain chipping (a, b), to chipping accompanied by Hertzian grain fracturing between grains of similar size at intermediate pressures (c, d). At higher pressures, Hertzian grain fracturing becomes the primary deformation mechanism, resulting in pervasive hertzian fracture networks and cataclasis in VWS sample (e, g), to more isolated pockets of cataclasis within MWS samples, which display lots of undeformed coarse outliers (f, h).

Figure 7.14. (a) Particle size distribution for a naturally deformed cataclastic deformation band and undeformed host. (b) Fault rocks can be described as fractal when a power-law relation when plotted in a log-log plot of grain size (GS) versus number of particles greater than size GS, where the exponent D is the fractal dimension. The fractal dimension, and the fractal range increases with increasing grain comminution to a fractal dimension of up to

2.58 (Sammis et al., 1987). Grain size distribution (GSD) plots for triaxially deformed samples of both very well sorted (c) and moderately well-sorted (d) quartz sands. GSD is observed for a linear trend deviating from the undeformed GSD curve, indicating a fractal, or power law distribution. The gradient of the linear trend corresponds to a fractal dimension D . GSD curves show a progressive shift and steepening to the left with increasing effective pressure. Data colours correspond to different effective confining pressures as in figures 7.11 & 7.12.

Figure 7.15. Experimental results plotted in Q-P space normalized to P^* . Results plot an elliptical yield envelope. Micromechanics of deformation show a broad continuum with dominant mechanism increasing with stress. (I) Grain sliding and rearrangement. (II) Grain chipping. (III) Intragranular grain fracturing.

Figure 7.16. Relative permeability reduction as a function of effective mean stress.

Figure 7.17. Experimental results of yield plotted in Q-P space form elliptical envelopes. Solid symbols represent values obtained from deviation from the hydrostat. Open symbols represent values obtained from differential stress-strain curves. Permeability reduction of samples calculated from textural properties can be plotted in the post yield region up to the peak stress values attained during triaxial loading (red symbols).

Table 1. Folk and Ward (1957) sorting classification

Table 2. Facies associations, lithofacies descriptions and approximate bed thickness in the Cheshire Basin

Table 3. Samples of undeformed host facies and their properties

Table 4. Facies associations, descriptions and bed thicknesses at Pease Bay.

Table 5. Deformation band samples and their properties.

Table 6. Results of fault damage zone measurements and lithological properties.

Table 7. Textural properties of four sand samples for testing.

Table 8. Summary table of results. Mechanical, textural and petrophysical data for triaxially deformed samples. ' Yield determined from deviation of porosity from the hydrostat with mean effective stress. * Yield determined from differential stress vs axial strain curves.

Acknowledgements

I am incredibly humbled and grateful to a large number of people who have provided support in so many ways. Firstly, my supervisor, Dr Ian Stimpson, for supporting and advising my research and allowing me the freedom to explore. The incredible group at the Basin Dynamics Research Group at Keele University, led by Dr Stuart Clarke, who in the final year of my studies, and quite possibly the most difficult year of my life, fought to secure my continuation. I have the utmost respect for all you do for BDRG and its research students. The rest of the group, Oli, Graham, Stuart E, Stuart B, Bernard, Gilbert, Guido, Steve, Tom, for providing support, feedback, and laughs during our meetings and preparations for conferences. My fellow researchers, Charlotte, Ross, Louis, James, Andy, Dave, Amy, Tom, Layth, Mark. You are all an inspirational group of scientists, and I have enjoyed every second of your company in the lab, field, and of course travelling to conferences. My only regret is not spending more downtime with you down at the KPA or whatever sweaty metal gig we can find. The night in Salt Lake City seeing Sum41 is to this day the best gig I've ever been to, not to mention the afterparty, Dave coming out, and James meeting his soul mate.

I am grateful for the opportunity to conduct half of this PhD at the Rock Deformation Laboratory at the University of Liverpool. The team, including my undergraduate lecturers who didn't mind me sticking around, Dan, Gary, John B, Mike, John W, Betty, Elliot, Izzy, Louisa, Steve, Joe. You all made me feel part of the team and inspired me with your own research.

The NERC CDT in Oil & Gas was a unique and incredible thing to be a part of. I have had the opportunity to visit so many unique places, get training, network and most important to me,

meet some incredible friends whose achievements and drive kept me inspired. I thank Lorna, Anna, and John for making this happen and all the work they do behind the scenes.

To all my friends who have shown support, and ridicule, it's been in equal measure. I was always known as rock boy, or the rock licker, after I licked a piece of halite in my first ever geology class in 2004. To my fellow Liverpool graduates, I am thankful that we all remain so close even though we're now so far apart. Thanks for the encouragement and laughs while I've taken this on. I've long questioned some of your characters for a while now, but I am still confident that together we will make *Penaeus* a reality someday.

To the kings; Jamie, Ad, Sam, Paddy, Phil, Tom. You are all a huge influence in my life, you kept me going when I was most down, keep me laughing when I am up, and I am eternally grateful for your friendship. Your own personal and professional successes are an inspiration to me. You make me push my emotional, intellectual, and physical boundaries, and I strive to do the same for all of you.

To my parents, who have been supportive of me since day one, despite not having a clue what it is I do, and I know are proud of what I have achieved. You instil in me my work ethic, strength and determination.

And lastly, but no means least, my wife, Leanna. You have been my best friend for nearly 14 years, you have been instrumental in my personal growth, in my ambitions, and I am so grateful that I have had you to support me during these last four years. We have both come a long way together, and I am incredibly proud to call you my wife, even though half of our friends and family don't know yet. The last year has been the most difficult for us both, but you have continued to support me emotionally and financially, and I promise we will have the wedding you deserve in the not-too-distant future.

Funding Information

The work contained in this thesis was conducted during a PhD study undertaken as part of the Natural Environment Research Council (NERC) Centre for Doctoral Training (CDT) in Oil & Gas [grant number Const20NEM00578X/1]. It is sponsored by Keele University whose support is gratefully acknowledged.

1. Introduction

1.1 Project motivation

Faults are a major structure of the Earth's lithosphere that influence the mechanical and petrophysical properties of rock. They have been a major focus of research in a range of geoscience disciplines, from earthquake seismology, engineering, hydrogeology and petroleum and economic geology. Understanding of the hydrological properties of faults in the upper crust is of particular interest and of economic importance since many fluid bearing reservoirs are charged, sealed or have their fluid flow properties affected by the presence of faults. First identified in the early 1970s (Dunn et al., 1973; Engelder, 1974; Aydin, 1978), deformation bands are the main structural element of faulting within porous granular rocks such as sandstones (Aydin, 1978; Hippler, 1993; Antonellini et al., 1994; Fossen and Hesthammer, 1998; Ogilvie and Glover, 2001; Schultz and Siddharthan, 2005; Fossen and Bale, 2007), and less commonly in porous carbonate grainstones (Mikkelsen and Floodpage, 1997; Meadows, 2006; Cilona et al., 2012) and volcanic tuffs (Evans et al., 1993; Wilson et al., 2003), and have been shown to both impede and enhance fluid flow. Deformation bands are sub-seismic, planar features of localised deformation with length scales of tens to hundreds of metres, and widths on the scale of millimetres to centimetres, and are often associated with faults with displacements below the seismic resolution. Therefore, to understand their fluid flow behaviour in the subsurface requires knowledge of the controls on their formation to predict their occurrence. Current understanding of deformation bands has been drawn from a combination of outcrop study (Schultz and Siddharthan, 2005; Rotevatn et al., 2008; Ballas et al., 2013; Ballas et al., 2014; Ballas et al., 2015; Griffiths et al., 2016) subsurface sampling (Fossen and Hesthammer, 2000; Hesthammer et al., 2002; Wilkins et al., 2019), and

experimental formation of bands in the laboratory (Zhang et al., 1990; Wong et al., 1997; Mair et al., 2002; Tembe et al., 2008; Charalampidou et al., 2011). Through this research it is found that the formation of deformation bands is strongly controlled by lithological properties of the host sandstone, such as grain size, porosity, sorting and mineralogy. These properties are inherently controlled and related to the depositional facies of the sandstones, through different sediment provenance and different sediment transport mechanisms. Deformation bands have been identified and studied in different depositional facies in outcrop, including most predominantly in aeolian facies, with excellent exposures of deformation band fault zones in the western United States in formations such as the Aztec, Entrada and Navajo Sandstones (Antonellini et al., 1994; Fossen and Bale, 2007; Eichhubl et al., 2010; Fossen et al., 2011b; Deng and Aydin, 2012), fluvial facies (Du Bernard et al., 2002a; Rotevatn et al., 2008; Torabi et al., 2013) and a little work in marine facies (Saillet and Wibberley, 2010; Ballas et al., 2014). Results have shown that porosity and grain size are the primary controlling factors on the type and intensity of deformation bands formed, and a secondary control from factors such as sorting (Cheung et al., 2012) and mineralogy (Rawling and Goodwin, 2003; Exner and Tschegg, 2012). However, many of these findings are from comparing different localities of studies of deformation bands in relatively monolithic successions with little facies variation, nor have deformation band properties been comprehensively or quantitatively studied in great detail with respect to facies directly. This presents the question of how deformation bands develop in more lithologically heterogeneous successions, and how their properties vary with more extreme variation in lithological parameters such as grain size, porosity, sorting, grain shape and mineralogy. This research will integrate a variety of methods to investigate the links between facies and deformation band properties directly and quantitatively, using outcrop and core examples of Triassic and Devonian mixed aeolian-

fluvial sandstones of the UK as principal case studies. Mixed aeolian-fluvial sandstones present a high degree of lithofacies variation across a wide range of bed thickness scales (Meadows and Beach, 1993; Mountney and Thompson, 2002; Wakefield et al., 2015; Priddy and Clarke, 2020) and therefore offer a unique opportunity to examine the role of facies variation on deformation band properties. Mixed aeolian-fluvial sandstones of the UK continental shelf (UKCS) are also of economic importance, as hydrocarbon bearing reservoirs which are also host to deformation bands (Cowan, 1993; Leveille et al., 1997; Fisher and Knipe, 2001; Meadows, 2006), as well as major ground water aquifers to the North West of England (Sternlof et al., 2006; Medici et al., 2019). More recently, in light of tackling climate change and the search for alternative energy resources and managing carbon emissions, the Triassic of the Cheshire Basin has been the focus of both geothermal potential, where formations with favourable fluid flow properties are subject to high geothermal gradients (Hirst et al., 2015; Brown et al., 2019b, a), and carbon capture and storage (CCS) (Armitage et al., 2013). Improving knowledge of deformation bands and the fluid modification of faults is therefore crucial in assessing the viability and maximising efficiency of these emerging technologies.

1.2. Research Aims

The aim of this thesis is to increase the understanding of deformation bands. In particular, the controls on their formation with respect to facies directly. We employ broadly two complimentary methods: Two outcrop case studies of mixed aeolian-fluvial sandstones in the Triassic and Devonian of the UK are examined, utilising outcrop and core sampling, and petrographic and microstructural analysis. This field-based work is then complimented with experimental rock mechanics to test controls on rock failure, with the following aims:

1. What are the controls on the formation of deformation bands in mixed aeolian-fluvial successions?
2. What are the controls on the petrophysical properties of deformation bands in mixed aeolian-fluvial successions?

1.3. Thesis Structure

Chapter 1 – Introduces the research topic, and the motivation and aims of the thesis.

Chapter 2 – Provides a review of the literature, introducing the kinematic and mechanistic classification of deformation bands, and current knowledge of the controls on their formation.

Chapter 3 – Introduces and discusses the methodologies used for analysis in chapters 4, 5, 6 and 7.

Chapter 4 – Introduces the geological background, stratigraphy and occurrence of deformation bands for the localities of two case studies. Presents results of petrographic and petrophysical analysis of undeformed host lithologies.

Chapter 5 – Presents results of petrographic, petrophysical and microstructural analysis of deformation bands. Discusses the control of lithofacies on microstructure and permeability.

Chapter 6 – Presents results of macroscale analysis of fault damage zones. Discusses the control of lithofacies on the intensity and thickness of deformation bands.

Chapter 7 – Presents results of rock deformation experiments on unconsolidated sands investigating the role of grain sorting on mechanisms of cataclasis and permeability reduction.

Chapter 8 – Integrates and provides a summary of the conclusions found in previous chapters, addressing the research aims presented in the introduction.

2. Background

2.1. Fault damage zones in sandstones

Although faults are often represented on a basic conceptual level as finite planes along which stratigraphy is displaced, it is widely recognised that in nature faults are complex three dimensional features comprising many individual structural elements to form a *fault zone* (Braathen et al., 2009). Fault zones typically have a well-defined, high-strain central *fault core*, comprised of heavily deformed material such as gouge or cataclasite, often with displacement accommodated on multiple slip surfaces, with structures that may split, anastomose and vary in width in both dip and strike directions. Surrounding the fault core is a larger volume of deformed rock known as the *fault damage zone* (Caine et al., 1996; Faulkner et al., 2010; Faulkner et al., 2011). Damage zones occur as a precursor to fault genesis as strain is accommodated until a fault plane is formed, and may continue to form in response to displacement on these fault planes, leading to flexure of the surrounding rock mass and/or fault rupture in stick-slip seismic events (Johri et al., 2014). Damage zones may also form in response to fluid flow associated with the faults behaving as fluid conduits, which may cause hydraulic fracturing, brecciation and/or diagenetic alteration (Hausegger et al., 2010). Deformation bands are the main structural element within fault damage zones in porous sandstones (Fig. 2.1), whilst also being associated with folding (Brandenburg et al., 2012; Zuluaga et al., 2014), salt diapirism (Wilkins et al., 2019) and uplift. They are the precursor to the formation of a fault plane, where deformation bands coalesce to form a dense cluster of bands that strain harden before a localised slip surface is then formed (Shipton and Cowie, 2001; Shipton and Cowie, 2003; De Jossineau and Aydin, 2007). They may also then continue

to form in the damage zone as strain is accommodated with increasing fault displacement (Fossen et al., 2007; Fossen et al., 2018).

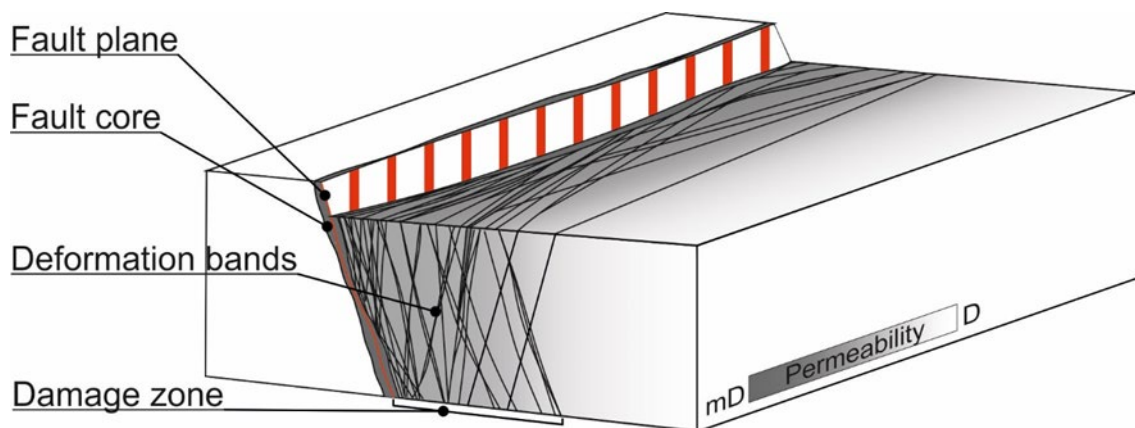


Figure 2.1. Schematic diagram of a normal fault zone within porous sandstone. The fault core is an amalgamation of deformation bands in which a fault plane is formed. Deformation bands are the major feature of the fault damage zone, with a conjugate arrangement, at low angles to the main fault plane in both plan and section view. Band density increases with proximity to the fault.

Outcrop studies have been the main method for establishing an understanding of the spatial and temporal evolution of deformation bands surrounding faults, with observations made at a number of scales, from individual bands with grain scale damage zones to basin-scale fault systems with damage zones hundreds of metres wide (Aydin and Johnson, 1978; Chadwick, 1997; Fossen and Bale, 2007; Mitchell and Faulkner, 2009, 2012; Ballas et al., 2013). Analysis of fault damage zone width and displacement data for porous rocks from the available literature suggests a strong power-law relationship for faults with displacements of between 1-1000m (Fig. 2.2) (Knott, 1994; Shipton and Cowie, 2003; Shipton et al., 2006; Schueller et al., 2013; Choi et al., 2016), although a great deal of scatter in damage zone width-displacement data is observed, obscured by log-log plots, with variability of two orders of magnitude. A change in this scaling component has also been identified for displacements in excess of ~150m where the damage zone growth decreases, which has been attributed to the nucleation of new fault strands, as well as limited sampling at these scales (Savage and Brodsky, 2011; Torabi et al., 2019), as well as some findings of a linear rather than power-law relationship for displacements of less than 25m (Shipton and Cowie, 2001). Variations in this relationship may be affected by the temporal evolution of the fault damage zone if it is assumed that the damage zone develops prior to fault initiation, as well as along strike variations of fault damage zones (Kim et al., 2004; Laubach et al., 2014), complex fault interactions (Childs et al., 1995; Childs et al., 2009), different tectonic settings (Solum et al., 2010; Soliva et al., 2013), damage zone asymmetry across the fault (Schueller et al., 2013) and inconsistencies in the way in which fault rocks and damage zones are defined (Choi et al., 2016; Torabi et al., 2019). This makes the application of a single power-law relationship to predict fault growth and damage zone width for faults somewhat unreliable. The influence of

lithology is a commonly discussed influence on the aforementioned variables, and remains an important factor in understanding various aspects of deformation bands.

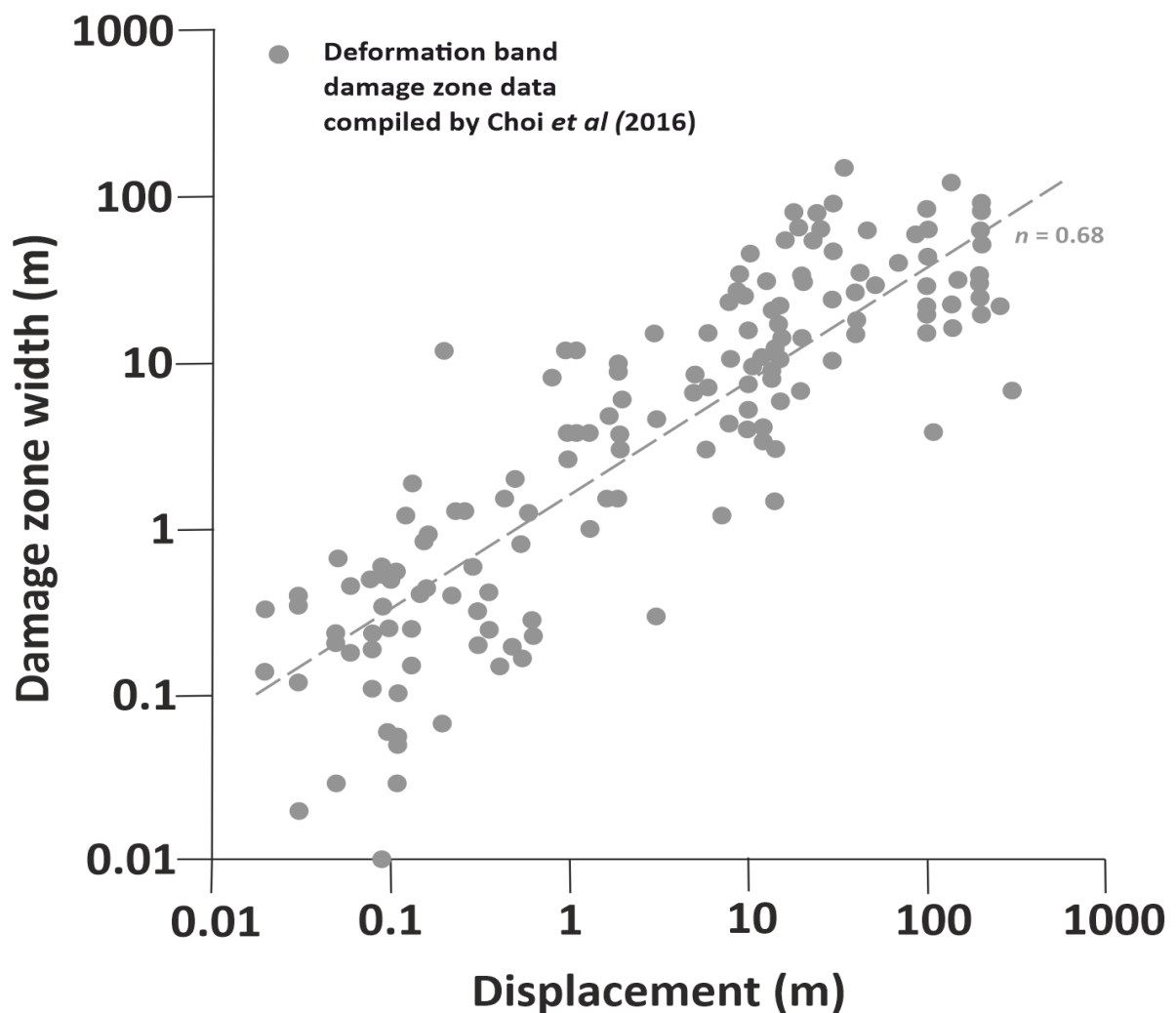


Figure 2.2. Log-log plot of damage zone width versus fault displacement for deformation band fault damage zones shows a power-law trend with an exponent n of 0.68. Data compiled by Choi et al. (2016) and references therein.

2.2. Classification

Throughout the literature there have been many different names to describe deformation bands including many broad terms such as micro-faults, cataclastic faults and fractures (Jamison and Stearns, 1982; Fisher and Knipe, 2001) and granulation seams (Pittman, 1981; Beach et al., 1999), however, these terms failed to describe the wide variation in kinematics, internal structure and deformation mechanisms, which control their petrophysical properties and impact on a reservoir. Deformation bands have since been universally classified and described in detail in terms of their kinematics, describing volumetric changes and displacement (Aydin et al., 2006), and deformation mechanism, describing grain scale processes including cataclasis, disaggregation, cementation, and clay smearing (Antonellini et al., 1994; Fossen et al., 2007). The details of the classification of deformation bands, their occurrence and properties are described below.

2.2.1. Kinematics

The petrophysical properties of deformation bands may be strongly linked to the kinematics of their formation. Deformation bands were first classified based on kinematics by Aydin et al. (2006) where they were divided in to two main categories, volumetric deformation bands and shear deformation bands (Fig. 2.3). Volumetric deformation bands involve either a volume increase or decrease and are termed pure dilation bands and pure compaction bands respectively (Fig. 2.3d, 2.3e). Whilst the former may kinematically be similar to a mode I fracture, differences in microstructure and mechanics have been identified, where dilation bands form via pore size growth, whereas mode I fractures form discrete surfaces (Du Bernard et al., 2002a). Pure compaction bands are considered to be porosity and permeability reducing, and dilation bands porosity and permeability enhancing.

Like the faults of which they form and evolve from, deformation bands most commonly display an offset of host rock structures such as laminations, often only millimetres to a few centimetres, and are termed shear bands. Pure shear bands display only lateral shearing of grains with no volume change (Fig. 2.3b), and may therefore maintain porosity, although this is largely dependent on the deformation mechanism. Most commonly found in both outcrop and core are hybrid bands which display both shear displacement and positive or negative volume change, and are termed shear enhanced dilation/compaction bands respectively (Fig. 2.3a, 2.3c). Shear bands accompanied by dilation are considered to increase porosity and permeability relative to the surrounding host rock, and those with compaction are considered to decrease porosity and permeability (Wong and Baud, 2012).

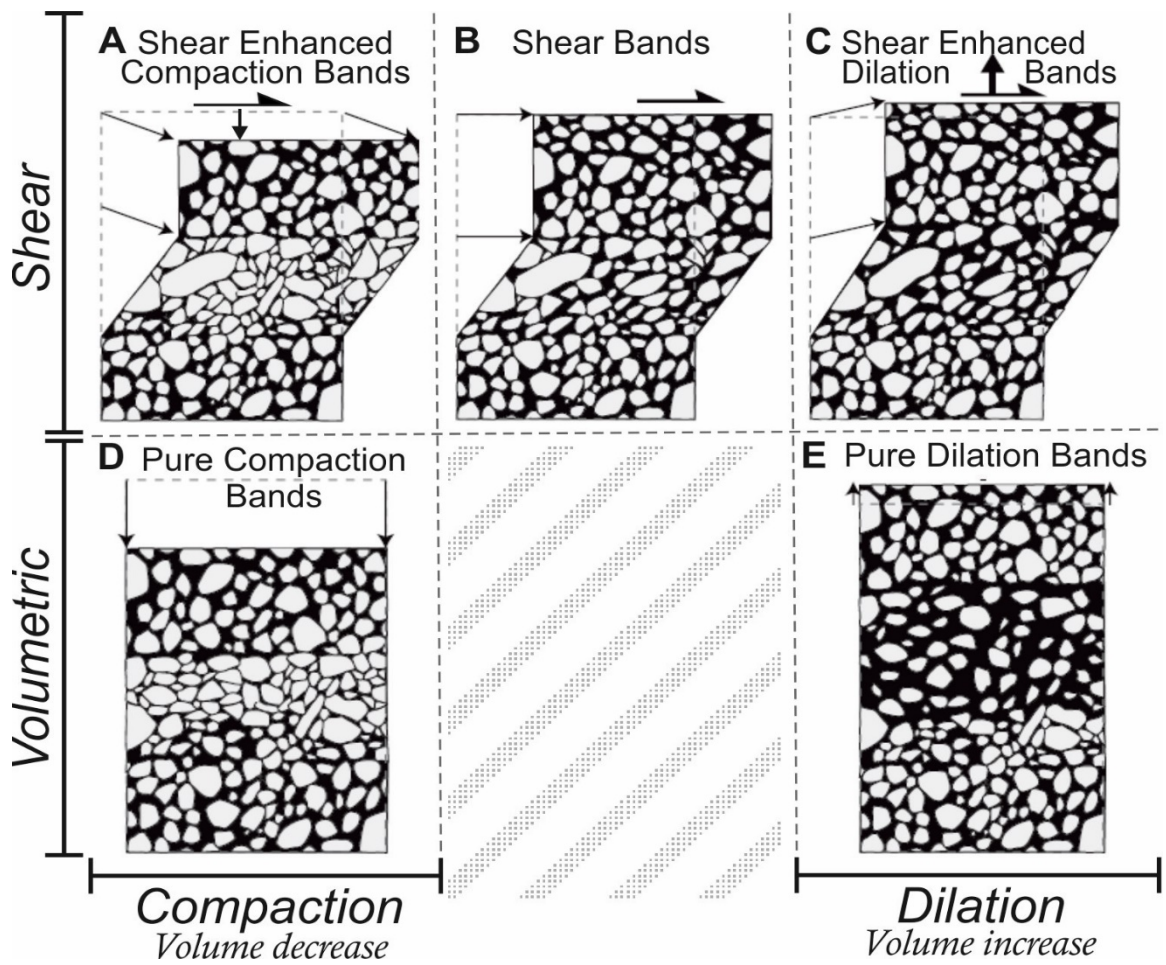


Figure 2.3. Kinematic classification of deformation bands. Bands are classified based on the amount and type of volumetric change and sense of any shear. (Adapted from Fossen et al. (2007))

2.2.2. Mechanism

Whilst a kinematic classification may be somewhat useful to infer the petrophysical properties of deformation bands, there may be other controls on the petrophysical properties of deformation bands that may not be described by kinematics alone. A variety of micromechanical processes have been identified within deformation bands that further influence both their mechanical and petrophysical properties. Hence a mechanical classification was developed. Aydin (1978) first identified deformation mechanisms following experimental work where deformation bands were formed as a result of brittle fracture tests (Dunn et al., 1973; Friedman and Logan, 1973). Aydin noted there were two zones within a deformation band; an outer zone characterised by deformation by compaction where the matrix and pores deform, and an inner zone characterized by grain fracture and crushing. These mechanisms were identified from the study of shear compaction bands from the monomineralic Entrada and Navajo Sandstones, and as such only represented mechanisms of a single band type. Antonellini et al. (1994) made further observations during a study of microstructure within deformation bands in various sandstones from Utah in which he identified three dominant deformation mechanisms: (1) Bands with no cataclasis; (2) Bands with cataclasis; (3) Bands with clay smearing. In light of further observations of deformation bands, a mechanical classification of deformation bands was finally summarised in a review by Fossen et al. (2007), in which four distinct classifications were made based solely on mechanical processes: (1) disaggregation/granular flow; (2) cataclasis; (3) clay smearing/phyllosilicate banding; (4) dissolution and cementation (Fig. 2.4), the details and petrophysical impacts of which are summarised below.

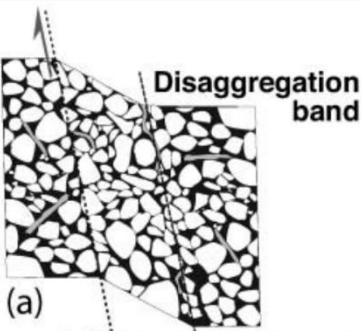
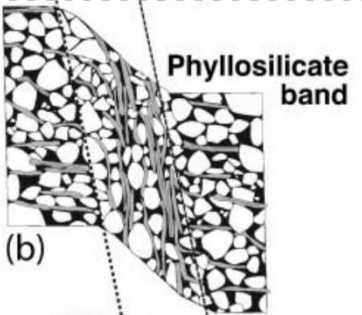
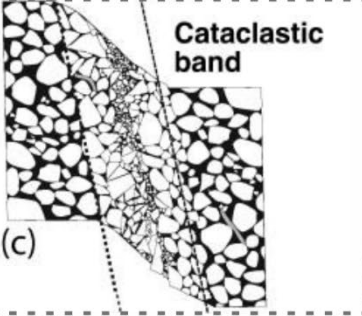
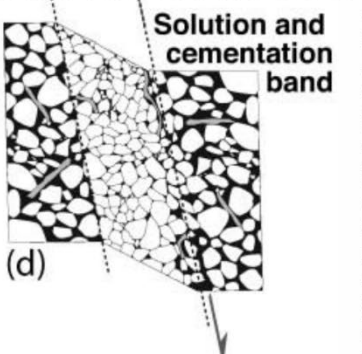
	Mechanism	Properties
 <p>(a) Disaggregation band</p>	Breaking of intergranular cement Grain rolling Grain sliding	Porosity and permeability modification depends on dilation or compaction
 <p>(b) Phyllosilicate band</p>	Ductile deformation of clay Smearing (>40%) Inhibits grain fracturing	Permeability decrease Strain softening (wt% dependant) frictional strength changes (mineral dependant)
 <p>(c) Cataclastic band</p>	Pore collapse Increased grain contact Grain fracturing Grain size decrease Increased grain angularity Increased grain size distribution	Porosity decrease Permeability decrease Strain hardening behaviour
 <p>(d) Solution and cementation band</p>	<p>Dissolution</p> Reduced grain size Pore volume increase	Porosity increase Permeability increase Decrease in cohesion
	<p>Cementation</p> Overgrowth on grains Pore volume decrease	Porosity decrease Permeability decrease Increase in cohesion

Figure 2.4. Deformation band classification by deformation mechanism and associated physical properties. 4 major types are identified, although it is not uncommon to find a combination of mechanisms within a single band. Adapted from Fossen et al. (2007)

2.2.2.1. Disaggregation

Often referred to as granular flow (Twiss and Moores, 1992), this process is most common in unlithified sediments and poorly consolidated sandstones typical of those at shallow burial depths. It is a typical process of bands with simple shear kinematics with little or no apparent volumetric change (Fossen et al., 2018), although care must be taken in this interpretation, as increased burial and compaction may continue after band formation. Deformation is accommodated through the breaking of existing intergranular cements, and subsequent rotation and sliding of grains. In the absence of compaction, porosity and permeability remain unaltered. However, with an element of compaction before the onset of grain crushing, porosity and permeability may be reduced through grain reorganisation and improved packing arrangement, particularly in unconsolidated or poorly consolidated sands that haven't been subject to burial related compaction. Similarly, in sandstones that are heavily cemented, porosity and permeability may be enhanced through intergranular fracturing of cements. Disaggregation bands may often be difficult to identify, and only apparent where a significant offset of laminae or other structure occurs.

2.2.2.2. Cataclasis

Cataclasis can be described as a mechanism of deformation involving fracturing of grains resulting in a decrease in grain size and sorting with increasing effective stress and displacement (Engelder, 1974). The most common band type, and typical of bands with shear and compaction kinematics, cataclastic deformation bands were first described by Aydin and Johnson (1983) in a petrographic study of faulted sandstones. Following initial disaggregation and compaction, there is a significant increase in grain contact as grains are reorganised, this increase in grain contacts also leads to a strain hardening behaviour (Wong et al., 1997).

Further strain may only then be accommodated via intragranular grain fracturing, where fractures develop between point contacts, creating a fracture network described by Hertzian fracture model (Frank and Lawn, 1967; Wong and Baud, 1999). The result of these processes is a band which consists of an inner core of crushed grains with a reduced mean grain size and wider grain size distribution than the undeformed host, and an outer zone of overall compaction due to disaggregation (Aydin, 1978). It is suggested that the amount of cataclasis is the most important factor influencing the permeability of deformation bands (Fossen *et al.*, 2018). It was once thought that this process and the formation of these bands was restricted to porous sandstones having undergone faulting at depths greater than 1km (Fisher and Knipe, 2001), however, cases of cataclastic bands in poorly consolidated rocks that have undergone much shallower burial at depths as shallow as 50m (Cashman and Cashman (2000); Ujiie *et al.* (2004); Wibberley *et al.* (1999), suggest that burial depth, or effective stress, is not the only controlling factor.

2.2.2.3. Phyllosilicate bands

First identified by Antonellini *et al.* (1994) as deformation bands with clay mixing, phyllosilicate bands occur in sandstones with a clay content exceeding approximately 10-15%, although some have been identified with clay content as low as 5% (Fossen *et al.*, 2007). Disaggregation or cataclasis is often an accompanying deformation mechanism, with clay mixing occurring sporadically along the deformation band where clay grains are apparent. With enough clay content, however, cataclasis may be suppressed in favour of clay smearing and frictional sliding. Fisher and Knipe (2001) recorded that clay content of 15-40% results in sufficient clay smearing to produce sealing deformation bands with permeability reduced to as low as 0.0001mD. Phyllosilicate bands can typically accommodate greater offsets than

other types of bands due to ductile clay grains which significantly delay, or inhibit strain hardening behaviour that is normally typical of grain interlocking, such as with cataclasis or disaggregation.

2.2.2.4. Dissolution and cementation

Dissolution and cementation bands form from solution of minerals within the host rock, typically but not exclusively limited to quartz. This process can occur during, or more commonly after localisation of a deformation band has taken place via one or more of the previous mechanisms (Fossen et al., 2007), however, it is a major mechanism controlling the petrophysical properties of deformation bands. Dissolution of a mineral phase such as quartz, can lead to cementation of deformation bands and can drastically reduce reservoir quality through the closing of pore space. The effect of cement on deformation bands, although there are few studies, is illustrated with examples from the Gullfaks oil fields of Norway. Hesthammer et al. (2002) documented the effects of cementation of deformation bands and the sealing capacity in a reservoir. The Gullfaks field is a faulted sandstone with numerous shear bands within damage zones less than a few tens of metres wide. The shear bands within the Gullfaks field, whilst having some fluid flow impact, were understood and production from this field was largely unaffected. When the drilling of two wells into the neighbouring Gullfaks Sor was complete, production from this field was approximately 15% less, the cause of which was quartz cementation of the deformation bands. Quartz cementation is the most common diagenetic mineral and the principal cause of porosity loss in reservoir sandstones (Walderhaug, 1994). Homogenization temperatures of fluid inclusions in quartz cements from North Sea reservoirs show that the temperatures of their formation range from 75° – 165°, with between 70 – 90°C considered to be the temperature at which quartz cementation

starts, correlating to a depth of approximately 3 km (geothermal gradient of 30°C/km) (Labaume and Moretti, 2001). The occurrence and extent of quartz cement may also be related to the burial history, particularly the time spent at quartz favourable depths/temperatures. In the case of the Gullfaks field, Gullfaks Sor was displaced approximately 1km deeper with respect to Gullfaks. This meant that Gullfaks Sor had a much higher temperature, currently in excess of 120°C, compared to less than 80°C, and so quartz cementation was favourable, leading to syntaxial quartz overgrowths which reduced porosity (Fig. 2.5). Gullfaks Sor also hosts shear enhanced compaction bands exhibiting greater cataclasis under increased effective pressure associated with burial depth. Syntaxial quartz overgrowths are enhanced by cataclasis of grains, creating fresh quartz faces for cements to nucleate and grow. Cementation can also occur at shallower depths and lower temperatures involving other minerals derived from authigenic grains and/or hydrothermal fluids. Deformation bands observed in the Vienna Basin of Austria, at a burial depth of 1651m, within medium grained litharenites with a composition of only 60% quartz, 30-40% dolomite, and very small amounts of feldspar, are heavily cemented by dolomite sourced from the high percentage dolomite in the host rock mobilised by hydrothermal fluids, recording host rock porosity of between 18 and 31%, and deformation bands reduced to between 1% and 9% (Exner et al., 2013).

In light of these four mechanisms that describe the types of deformation bands, reservoir sandstones typically have long and complex burial histories, during which conditions are ever changing, therefore it is important to note that the kinematics and deformation mechanism may change with respect to time, and that a single band may exhibit features of many different band types.

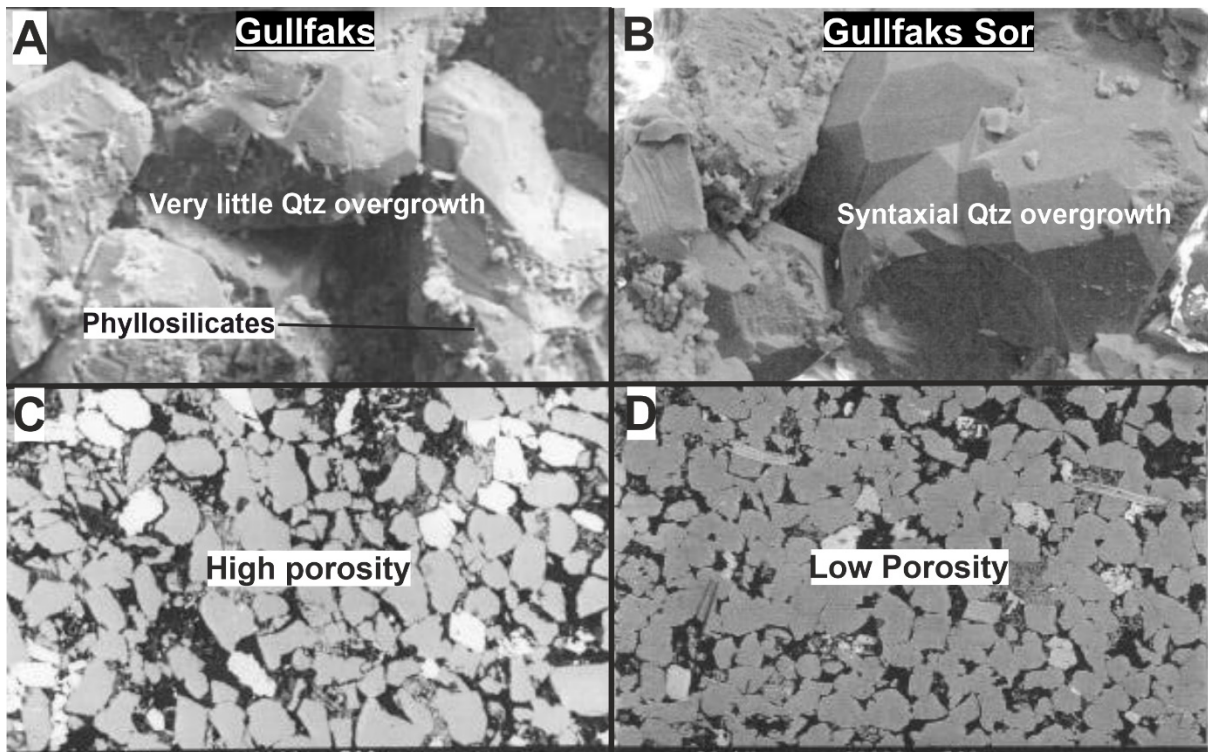


Figure 2.5. A comparison of the Gullfaks and Gullfaks Sor sands using SEM and BSE images. (A, C) Gullfaks is characterised by minor phyllosilicates and lower temperature conditions, inhibiting syntaxial quartz cementation, resulting in a high porosity and a productive reservoir. (B, D) Gullfaks Sor is characterised by cataclasis of quartz grains and higher temperatures, promoting the growth of syntaxial quartz cements, significantly reducing porosity and the productivity of the reservoir. Modified from Hesthammer et al. (2002).

2.3. Controls on deformation bands

The identification of different deformation mechanisms of deformation bands introduces a number of different factors that may control how they deform. For instance, clay smearing is identified in sandstones with significant presence of lithic or clay grains, thus highlighting the important control that sandstone mineralogy has on the deformation band type. Sandstones are inherently varied in terms of their textural and petrophysical properties, as a function of their provenance and depositional environment. Current understanding of the mechanical behaviour of sandstones with respect to their properties has been drawn largely from both field-based studies, and experimental rock mechanics. Field studies enable observations and interpretations of naturally occurring deformation bands with respect to the different lithologies in which they are found. However, complex burial and diagenetic histories make comparisons between different localities difficult. Experimental rock mechanics allows testing of mechanical theories, and controlled testing under pre-determined conditions and where properties may be varied (Hirth and Tullis, 1989; Wong, 1990; Mair et al., 2002; Charalampidou et al., 2011). Through these methods there is insight into the controls on band formation, which are discussed below.

2.3.1. Porosity and Grain Size

It is widely recognised that deformation band formation is more favourable in higher porosity, coarser-grained sandstones (Fossen et al., 2007). This is primarily due to their relatively low grain crushing strength which is a function of both porosity (ϕ) and grain radius (r) (Wong, 1990). Higher porosity, coarse-grained sandstones are therefore more susceptible to localised deformation and subsequent band formation (Schultz et al., 2010). Conversely, low-porosity, fine-grained sandstones have a much higher grain crushing threshold, and are therefore less

susceptible to band formation. Thus, in an aeolian setting where textural maturity is high, and successions are relatively homogenous in terms of rock properties, band formation is often pervasive throughout the entire succession, this is most famously observed in the Navajo and Entrada sandstones of the Western United States (Aydin and Johnson, 1978; Shipton and Cowie, 2001). In cases with high grain size and porosity variability, such as those with variations in dune type and size, band formation may be restricted to, or more pervasive in the higher porosity, coarser-grained units, such as those dominated by grain-flow (Schultz et al., 2010; Fossen et al., 2011b). In less favourable units, bands may thin or terminate at bed boundaries across which porosity and/or grain size decreases significantly (Fossen and Bale, 2007).

The effect of porosity and grain size on the behaviour and physical properties of rocks is the most extensively covered by both outcrop studies and experimental work. Hydrostatic deformation tests in which samples of sandstones are subject to increasing isotropic stresses offer insight into the effects of porosity and grain size on mechanical behaviour. The strength of rocks can be defined by the point at which the stress-strain behaviour transitions from quasi-linear elastic compaction to accelerated non-linear inelastic compaction, referred to as the critical pressure, denoted by P^* , and marks the onset of brittle grain fracturing or crushing (Fig. 2.6a). Earliest experimental studies on the strength and behaviour of rocks concluded that porosity had a profound effect on the strength of the rock (Dunn et al., 1973). In samples with porosity ranging from 2% to 24%, at high porosity with significant pore space and looser packing of grains, there is a lower energy required for grain cracking to occur and propagate through grain contacts and free pore space, referred to as the Hertzian fracture model (Frank and Lawn, 1967). At lower porosity, with greater grain packing, a greater critical pressure is

required to cause grain fracturing. Thus, lower porosity sandstones are typically stronger than high porosity sandstones, provided other controls remain equal. The hertzian fracture theory also predicts grain fracturing from grain contacts at a critical stress level to propagate any pre-existing cracks in the grain. It is for this reason that larger grains, with more pre-existing flaws, are inherently weaker (Zhang et al., 1990).

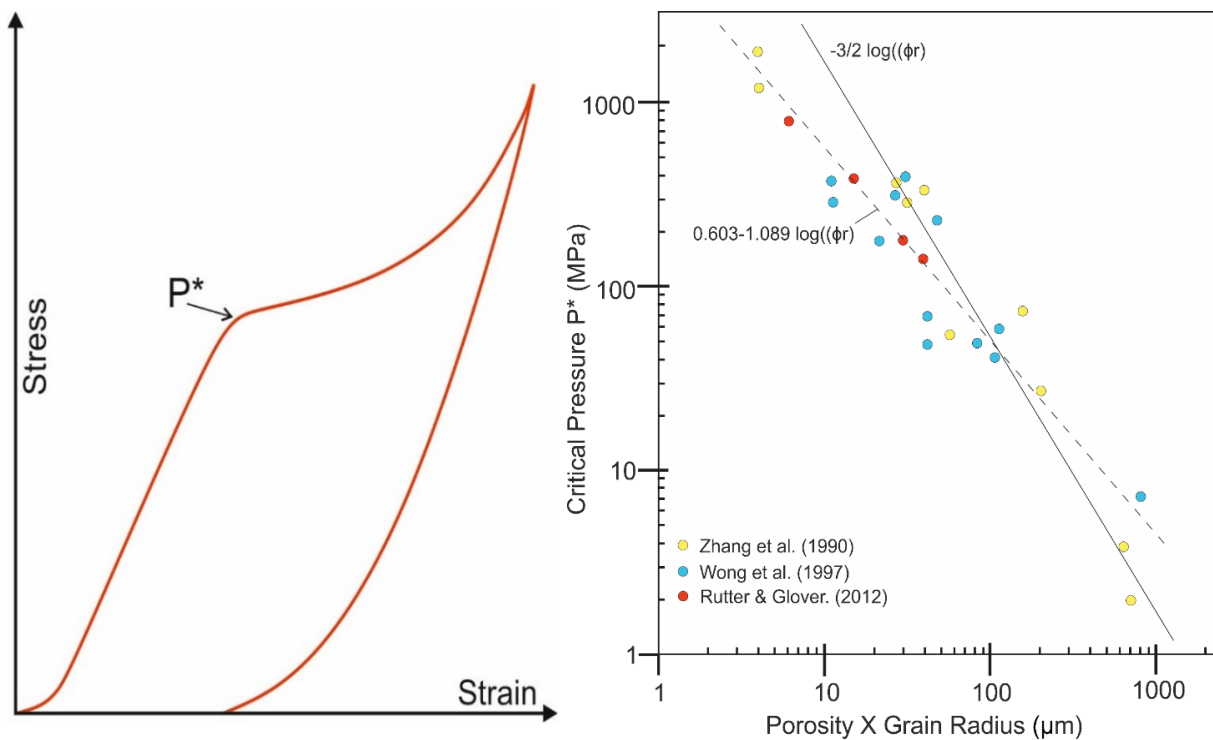


Figure 2.6. (a) Stress-strain curve for the hydrostatic compaction of porous rock. The inflection, P^* , marks the transition from quasi-linear elastic compaction to non-linear inelastic compaction and the onset of grain fracturing, also known as the critical pressure. (b) Critical pressure at which grain crushing occurs as a function of porosity and grain radius. Data shows that rock strength decreases with increasing porosity and grain size. Initial experiments by Zhang et al. (1990) determined a linear relationship with slope of $-3/2$ (solid line). Later experiments and compilation of various data sets yield a linear relationship of $0.603-1.089$ (dashed line). (Wong et al., 1997; Rutter and Glover, 2012).

This theory was investigated further by Zhang et al. (1990) who tested a much broader range of porosity, as well as introducing the variance of grain size using data from other studies (Lee and Farhoomand, 1967; Zoback, 1975; Hirth and Tullis, 1989). With porosity values ranging from 7.4% – 52%, and grain size ranging from 0.05mm – 1.4mm, the results showed that the pressure at which grain crushing occurs (P^*) is a function of both porosity (ϕ) and grain radius (r) with the linear relationship given by equation (1), which is in accordance with the hertzian model.

$$\text{Log } P^* = -1.5 \log (\phi r) \quad (1)$$

Further experiments were compiled by Wong et al. (1997) of various sandstones in which the same -1.5 trend lines were used as best fit lines. However, further analysis of this compiled data by Rutter and Glover (2012) including some new experimental data, conclude that the data is better described by the empirical relationship (2). The data is shown in figure 2.6b.

$$\text{Log } P^* \text{ (MPa)} = 0.603 - 1.09 \log (\phi r) \quad (2)$$

The results of these experimental tests support field observations in which deformation bands favour higher porosity, coarser grained sandstones. The Entrada Sandstone of Utah, USA, displays pervasive deformation bands within aeolian sandstones with an increase in density and thickness within coarser higher porosity sandstones, and a decrease at the bed boundary to lower porosity siltstones of interdune facies (Fossen and Bale, 2007).

Additionally, porosity and grain size would also influence the type of deformation bands formed. With an aim to examine the control on deformation band type, studies of the Navajo Sandstone, Utah, USA, and sandstones from the Provence area of France are compared (Schultz et al., 2010; Fossen et al., 2011a; Ballas et al., 2013). In the Navajo Sandstone, it is

found that pure compaction bands (PCB) formed in beds with the largest porosities of 28-29%, and permeabilities >10 Darcy. Shear enhanced compaction bands (SECB) continued to form in layers with porosities as low as 17% but phased out in layers with a grain size of 0.16mm. When compared with data from Provence, France (Ballas et al., 2013), the pure compaction bands dominate the lower porosities for this area which are very similar values to those of Navajo Sandstone, and do not occur in sandstones with higher porosity values of 33% – 38%. This may suggest there is an upper porosity limit to pure compaction band formation, where deformation may be accommodated by bulk compaction of the rock rather than localized compaction in the form of deformation bands. The SECB of Provence also do not agree with the findings in Utah, as a layer with a porosity as high as 33% contains no DBs, and the highest porosity (38.8%) contains very few SECB. These inconsistencies suggest that porosity and grain size is not the major control in these cases. Therefore, care and consideration should be made when drawing conclusions from different localities, exhibiting other variables other than porosity and grain size, such as burial depth, stress state, sorting and mineralogy.

With the strong control of porosity on the formation of deformation bands, it can be inferred that permeability may show a similarly strong correlation. However, this is not a primary control, but a secondary correlation, as permeability is a function of both porosity and grain size (Beard and Weyl, 1973). The Navajo Sandstone, Utah, USA shows a strong correlation with permeability, in which the development of clusters of deformation bands (thick accumulations of single deformation bands) favour high porosity, and therefore high permeability sandstones (Fossen et al., 2011a). The results of this are a much greater permeability reduction within higher porosity units, with an average reduction two orders higher than that of single deformation bands.

2.3.2. Stress

The derivation of P^* is obtained from experiments under hydrostatic conditions in which the stresses are isotropic ($\sigma_1=\sigma_2=\sigma_3$). Whilst this is a useful approximation for sandstones under lithostatic loading, in which all principal stresses are equal. This does not describe the failure for sandstones under differential stresses ($Q = \sigma_1 - \sigma_3$) in which the principal stresses are anisotropic. Sandstones deformed under a variety of conditions ranging from tension to pure compaction, may be visually represented by an elliptical curve or yield envelope, as plotted in Q-P space, where P = effective mean stress, equation 3.

$$(P = (\sigma_1 + \sigma_2 + \sigma_3)/3 - Pf) \quad (3)$$

and Q is the differential stress, equation 4.

$$(\sigma_1 - \sigma_3). \quad (4)$$

When used in conjunction with porosity x grain size dependence, the strength, stress state and type of failure may be visually represented in 3D by the cam-cap model of Cuss et al. (2003) (Fig. 2.7), and can be used to describe the formation and evolution of deformation bands (Schultz and Siddharthan, 2005). Figure 2.7 shows that the radius of the yield cap or yield surface, changes with porosity and grain size. A decrease in porosity during progressive deformation also causes the yield cap to grow and so the stresses needed for further deformation also increase. The kinematic classification for deformation bands discussed earlier, demonstrates the variability in deformation band types due to different stress states which may also be indicative of the tectonic regime (Solum et al., 2010; Soliva et al., 2013; Ballas et al., 2014). Contractional and extensional tectonic regimes have distinctly different stresses, producing different structural styles and geometries of faults and fault zones. Three studies compare the types and distribution of deformation bands in different tectonic regimes

(Solum et al., 2010; Soliva et al., 2013; Ballas et al., 2014) that lead to the same conclusion that a contractional tectonic environment yields an aerially extensive and even distribution of compaction bands and shear enhanced compaction bands, due to a high rate of increase in mean stress leading to failure in the middle to lower right part of the yield cap (Fig. 2.7). An extensional tectonic environment yields highly localised shear and shear compaction bands in the damage zones of normal faults due to greater differential stress and a reduction in mean stress causing failure in the peak of the yield envelope, across the critical state line. Considerable differences in the burial depth between these studies of between 0.8-2.3km, equating to a pressure of 20-57.5MPa, suggest that tectonic setting and differential stress is a more controlling factor than burial depth and effective mean stress.

In early experiments studying the effects of mean effective stress, Sammis and Ashby (1986) observed that at moderate pressures samples failed by shearing, and at large confining pressures resulted in homogeneous micro-cracking. Antonellini et al. (1994) first hypothesised that the style of deformation within deformation bands, particularly dilation or compaction, was in part controlled by burial depth and mean effective stress. Under low confining pressures faulting develops as dilation and disaggregation, and higher confining pressures are characterized by compaction and cataclasis along with strain hardening behaviour (Wong and Baud, 2012). This behaviour can be graphically represented by the cam-clay model previously mentioned. Developed from soil mechanics (Wood, 1990), this model describes the stress states and mechanical behaviour of the rock at the point of yielding, either dilation or compaction, with or without an element of shear.

Cases of cataclastic bands formed in poorly consolidated sediments with very shallow burials as shallow as 50m depth (Lucas and Moore, 1986; Cashman and Cashman, 2000; Ujiie et al.,

2004), prompt the need for further experiments as the only way of studying the effects of stress. Experiments by Mair et al. (2002) and Bésuelle et al. (2000) performed on fine grained sandstones both with 20% porosity, gave very similar results. In tests performed at between 10-41MPa corresponding to depths of up to 1.6km, dilation occurs as well as an increase in differential stress until inelastic deformation. And in tests from 50-64MPa corresponding to depths between 2-2.56km, compaction dominates as well as a decrease in differential stress. In both of these experimental studies, an increase in the band angle with respect to the maximum principal stress σ_1 , and an increase in deformation band density is observed. The orientation of shear compaction bands may be used to infer the orientation of maximum principal stress. In these experiments shear bands are produced leaving pure compaction bands open to interpretation. Pure compaction bands are inferred to form perpendicular to the maximum principal stress with maximum principal compressive stress of around 20MPa, and requiring a high initial porosity, large pore size and coarse grain size, whereas the shear bands are thought to form under less compressive stress (Eichhubl et al., 2010). Recent experimental work by Heap et al. (2015b) looking at the time dependency of compaction band formation, confirmed the hypothesis of compaction band formation occurring at higher pressures, and saw that at an effective pressure of 80MPa (Pore fluid pressure = 10MPa) the deformation is entirely compactive, forming bands perpendicular to the applied stress. The sandstone in this case had similar grain size and porosity to the studies by Mair et al. (2002) and Bésuelle et al. (2000) but very different composition, with only 66% quartz and 28% K-feldspar compared to what were mature pure quartz sandstones. The high abundance of feldspar may have an effect on the onset of grain crushing and so the values attained for pure compaction band formation may be lower than for a comparably pure quartz sandstone.

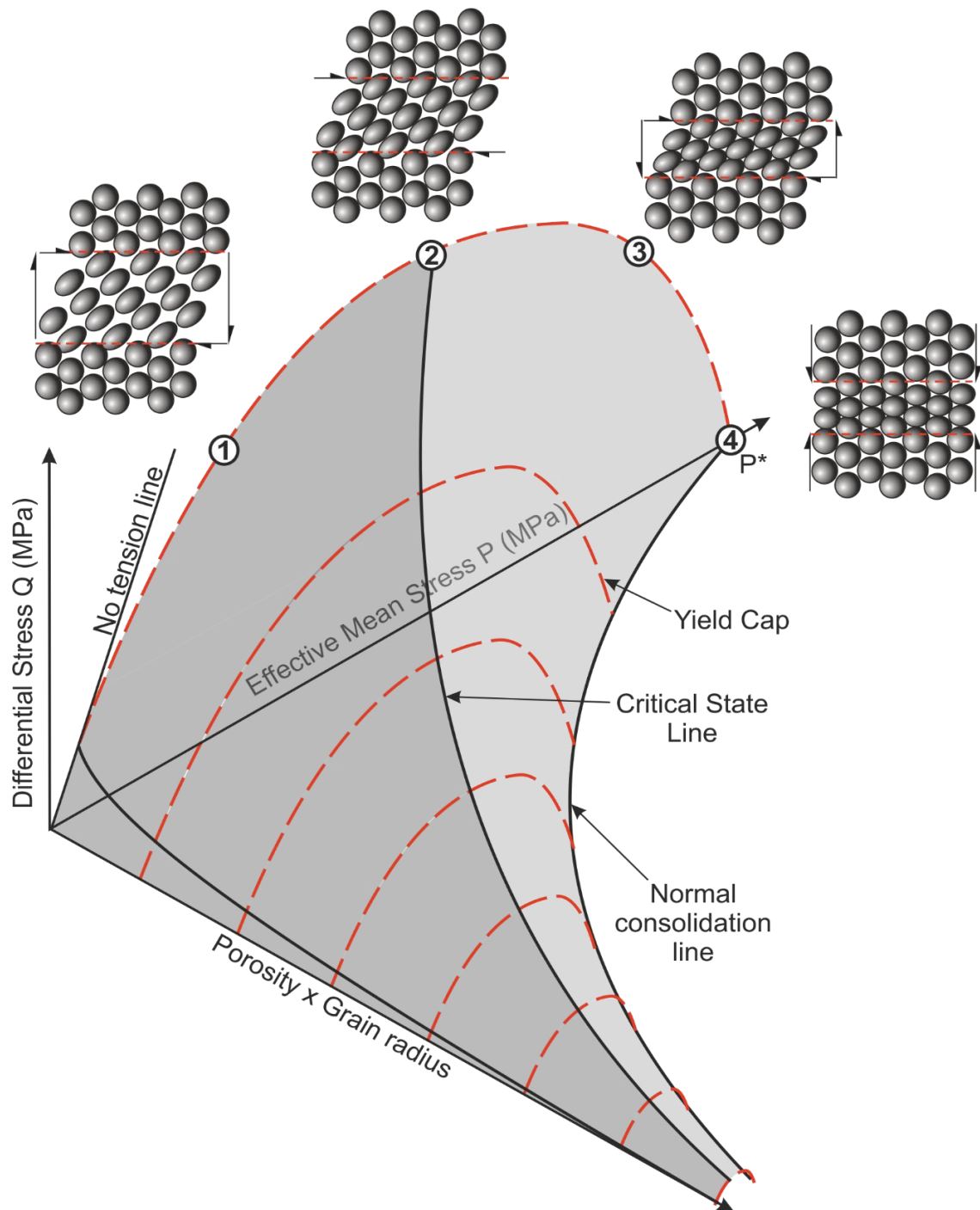


Figure 2.7. Q-P- Φ R diagram showing the effects of porosity and grain size on the yield cap of porous sandstones. Larger grain sizes and high porosity are inherently weaker than finer, less porous sandstones, and therefore have smaller yield caps. The critical state line marks the division of dilation (dark grey) and compaction (light grey). Modified from (Cuss et al., 2003).

From the experiments presented, it is clear that there is a relationship between burial depth and the type of compaction band formed. However, the results come from very limited samples in terms of porosity, permeability and mineralogy. There is also the issue of compaction bands, described here as forming at higher pressures, having been found in shallow and poorly consolidated sands. More experimental work is needed to test a range of properties reflective of those found in the field, as well as better constrained burial histories of outcrop examples, so that more accurate comparisons can be made from field to laboratory.

2.3.3. Mineralogy

Mineralogy is an important controlling factor on the strength of a rock. Quartz is the most abundant mineral in reservoir sandstones host to deformation bands, and so is the controlling mineral on its mechanical behaviour. However, with phyllosilicate bands, clay content as low as 5% can have an effect on the deformation mechanism as well as the petrophysical properties of the deformation bands. Clay content significantly weakens quartz rich rocks. Crawford et al. (2008) recorded a reduction in frictional strength (μ) from 0.7 to 0.45 with progressive addition of kaolinite clay up to 40 wt%. Field examples from Provence, France (Ballas et al., 2013) display compaction bands and shear enhanced compaction bands in a succession of texturally and mineralogically variable sandstones of deltaic origin. A comparison between two units which have very similar porosity and grain size values of ~35 % and 0.23 mm, shows that both types of bands terminate at the boundary between the two units. The unit that hosts both compaction and shear bands contains less clay than the lower unit, it is inferred that mineralogy controls the formation of bands. As previously covered in the band classification discussion, clays will inhibit quartz grain-to-grain contact, and

therefore cataclasis, in favour of ductile deformation of the clay fraction, and in sandstones with >15% clay, will produce phyllosilicate bands. An important aspect of phyllosilicate bands yet to be considered, is the type of phyllosilicate minerals present, detrital or authigenic, as the clay type, and in the case of authigenic clays, the timing of formation, may impact the reservoir quality in different ways. Different phyllosilicate minerals, such as illite, kaolinite, chlorite and biotite, have different frictional strengths, with coefficients ranging from 0.2 to 0.8 in dry samples (Moore and Lockner, 2004). This may be a significant control on the type of band formed, the extent of porosity and permeability reduction, and the intensity of deformation band formation since it is hypothesised that strain hardening of bands leads to the formation of new bands in order to accommodate strain.

Feldspar grains, with a lower frictional strength of between 0.5-0.7 (Scruggs and Tullis, 1998), are inherently weaker than quartz grains and so they fracture first during deformation (Aydin, 1978). Preferential fracturing of these grains results in grain size reduction of the feldspar fraction, and if feldspar content is particularly high, grain size distribution will increase, acting to potentially inhibit band formation. Wong et al. (1997) conducted experiments on a variety of sandstones of varying porosity, grain size, and composition, in order to investigate the transition from brittle to cataclastic flow. He compared grain crushing pressure (P^*) to a number of other studies. The data show little relation between feldspar content and P^* and the formation of DBs. Despite the lack of data supporting a relationship between feldspar content and onset of cataclasis, a study by Exner and Tschegg (2012) examined arkosic sandstones with a feldspar content of between 26-48%, and found that the preferential crushing of feldspar grains in cataclastic bands leads to an increase in phyllosilicate enrichment (sericite) due to seritization by hydrothermal alteration. This leads to a change in

deformation mechanism from cataclasis to clay smearing and the formation of phyllosilicate bands, which can cause a massive porosity reduction of up to 20%.

2.3.4. Grain Size Distribution

Although mean grain size is identified as a primary control on band formation, it has been found that the grain size distribution, or grain sorting, may also play an important secondary role on the mechanical behaviour, and formation of deformation bands in porous sandstones. It has been discussed that poorer grain sorting, a wide grain size distribution, favours deformation via distributed cataclastic flow as opposed to localised deformation band formation (Morgan and Boettcher, 1999; Cheung et al., 2012; Fossen et al., 2018), and that localisation is favoured within sandstones with a high degree of textural maturity, with good grain sorting, or a narrow grain-size distribution. The mechanism by which a wide grain size distribution inhibits strain localization and the formation of deformation bands, is through the distribution of stress at grain contact points. In a sandstone with a broad grain size distribution, grains have more contact points due to more finer grains within the sample, which then act as cushions for the larger particles to distribute stress (Sammis et al., 1987). Hertzian fracturing (Frank and Lawn, 1967) is then inhibited, or at least restricted to those smaller grain sizes bearing greater stress, whilst the larger particles remain largely undeformed (Fig. 2.8). The result is an even wider grain size distribution and strain hardening of the sandstone (Kaproth et al., 2010) which further inhibits band formation. Such conclusions about the effects of grain size distribution on strain localization, explain the prevalence and sampling bias of deformation bands within largely well-sorted sandstones typically of aeolian and marine origin. Although there are studies of bands within moderate- to poorly-sorted sandstones of fluvial origin (Rotevatn et al., 2008), the question remains of

how common band formation is in sandstones of this type, and how their geometry and petrophysical properties might vary. The effects of grain size distribution on the mechanical behaviour of sandstones and the formation of deformation bands is relatively under studied.

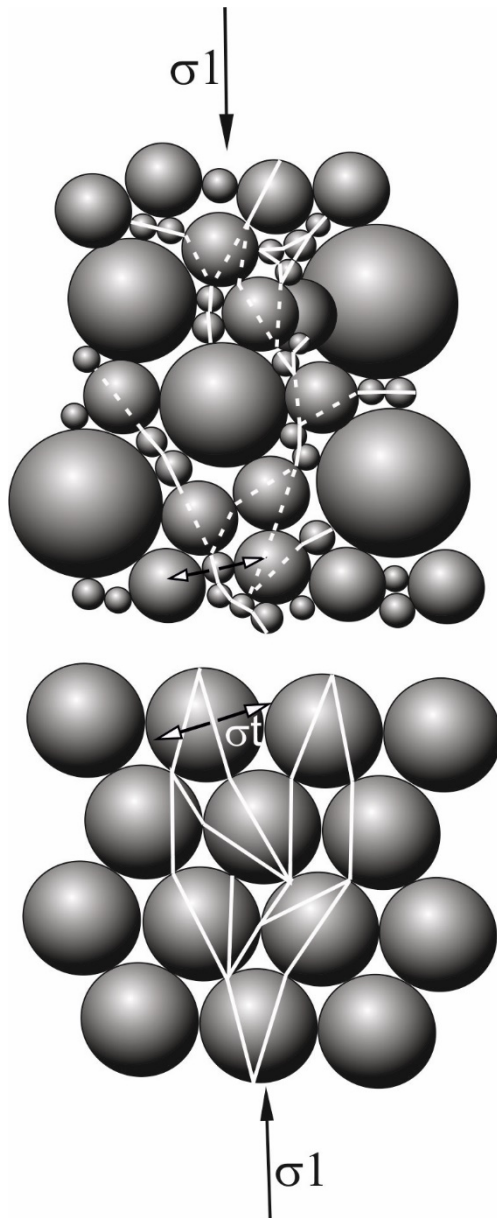


Figure 2.8. Force chain network of fracturing in both poorly sorted and well sorted sands. Grain contacts are more distributed in poorly sorted sands, where the smaller grains bare the stresses between the larger grains, limiting fracturing amongst the finer fraction, whose connectivity may be limited. Grain contacts are less dense in well sorted sands and therefore, stresses at contacts are higher, enabling the propagation of fractures from grain to grain.

2.3.5. Cementation

There are many inconsistencies regarding the effects of burial depth on the type of deformation band formed. These inconsistencies may be related to the effects of cementation, which is highly, although not exclusively, depth and temperature dependant (Worden and Burley, 2003). Cements have been shown to alter the mechanical properties of sandstones, increasing their strength and increased cohesion (Yale et al., 1995). Cements alter many of the aforementioned controls on deformation band formation; increasing grain size through syntaxial overgrowth, increasing grain angularity, which in turn invades pore spaces and reduces porosity, and most importantly increasing the area of grain contacts, and thus reducing stress concentrations and fracturing. The effects of heterogenous cementation on a reservoir has shown to directly influence the presence and type of deformation bands formed, with cataclastic band formation inhibited in well-cemented intervals in favour of discrete fracturing (Beke et al., 2019).

3. Methodology

In this thesis an integrated approach is employed to investigate the role of lithofacies on deformation bands. This includes a field-based approach, incorporating various methods of outcrop and core sampling, and analysis at macroscale. A petrographic approach, examining the petrophysical and microstructural properties on a microscale. And an experimental approach in order to supplement and test hypotheses under controlled conditions. These methods are detailed below.

3.1. Logging and Sampling

Outcrop and core were logged to record lithofacies variation at localities where faults and deformation bands are observed. Samples of undeformed lithofacies were taken to characterise the petrographic variation across the localities. Samples of deformation bands were also taken in lithofacies adjacent to faults where deformation band intensity is also recorded.

3.2. Petrographic Analysis

For petrographic analysis, samples were cut perpendicular to band orientation to display the deformation band and surrounding host rock, and thin sections 30 μm thick impregnated with blue resin were produced for optical microscope, back scattered electron (BSE) microscope, and image analysis.

Textural analysis was performed using PetrogTM point counting software and an automated microscope stage (Fig. 3.1). The method uses optical microscopy and an automated microscope stage that allows a systematic scan of the sample to point count grains. By measuring both the long and short axis of individual grains we are able to obtain grain size distribution statistics such as mean, median, percentiles, sorting and skewness. In addition,

measurements of the long and short grain axis provide a measure of grain sphericity, and also grain orientation for indication of any primary grain fabric from sedimentary structure, and secondary grain fabric created by deformation (Fig. 3.1).

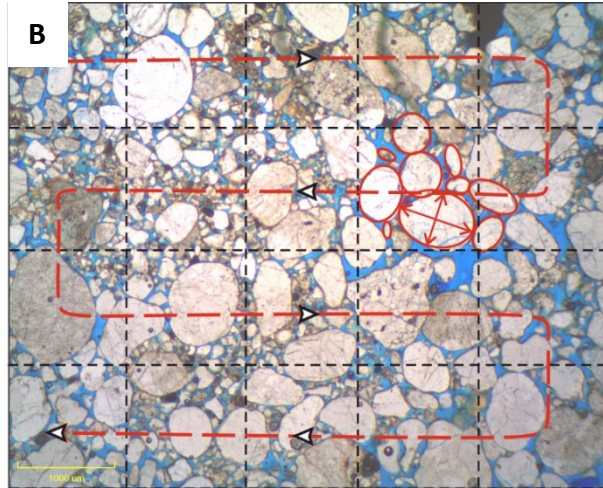
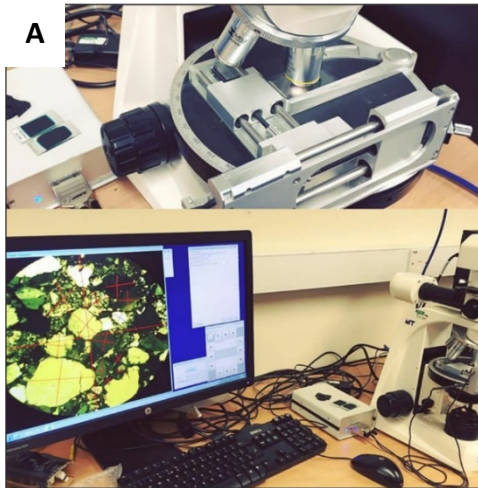
Grain size distribution is calculated from the same grain size measurements, and using the Folk and Ward (1957) classification (Table 1), sorting is given in Phi units (ϕ) in order to transform the Wentworth grain size scale (mm) into a dimensionless scale using the following:

$$\phi = -\log_2 d \quad (5)$$

Where d is the grain diameter in millimetres. Sorting is then calculated using the following equation:

$$\phi = \frac{\phi_{84} - \phi_{16}}{4} + \frac{\phi_{95} - \phi_5}{6.6} \quad (6)$$

Where ϕ_{84} , ϕ_{16} , ϕ_{95} and ϕ_5 are the phi grain size values at their respective percentiles. This is considered the best representation of sorting, accounting for 90% of the distribution.



C

No. grains measured	264
Mean major length	0.095 mm
Mean (phi)	3.536
Median major length	0.083 mm
Mode (Wentworth)	Very fine sand
Mode (phi scale)	[3.0, 4.0]
Std. dev.	0.047 mm
Std. dev. (phi)	0.631
Skewness	1.686 mm
Skewness (phi)	-0.295
Kurtosis	6.5
Sorting (Trask)	1.443
Sorting (Trask, after Tucker)	1.71
Sorting (Trask, (sqrt(phi)))	1.115
Sorting (Trask) Description	moderately sorted
Skewness (Trask)	1.017
Skewness (Trask) Description	strongly fine skewed
Mean (Inman)	0.021
Sorting (Inman)	0.214
Skewness (Inman)	1.063
Sorting (Folk & Ward) Value	0.639 (phi)
Sorting (Folk & Ward) Description	moderately well sorted
Skewness (Folk & Ward) Value	-0.086 (phi)
Skewness (Folk & Ward) Description	Near symmetrical
Kurtosis (Folk & Ward) Value	0.735 (phi)
Kurtosis (Folk & Ward) Description	Platykurtic
Minimum	0.029 mm
5th percentile	0.041 mm
10th percentile	0.052 mm
15th percentile	0.056 mm
20th percentile	0.061 mm
1st quartile	0.064 mm
30th percentile	0.067 mm
35th percentile	0.073 mm
40th percentile	0.077 mm
45th percentile	0.080 mm
Median	0.083 mm
55th percentile	0.088 mm
60th percentile	0.093 mm
65th percentile	0.098 mm
70th percentile	0.106 mm
3rd quartile	0.110 mm
80th percentile	0.118 mm
85th percentile	0.132 mm
90th percentile	0.159 mm
95th percentile	0.190 mm
Maximum	0.310 mm

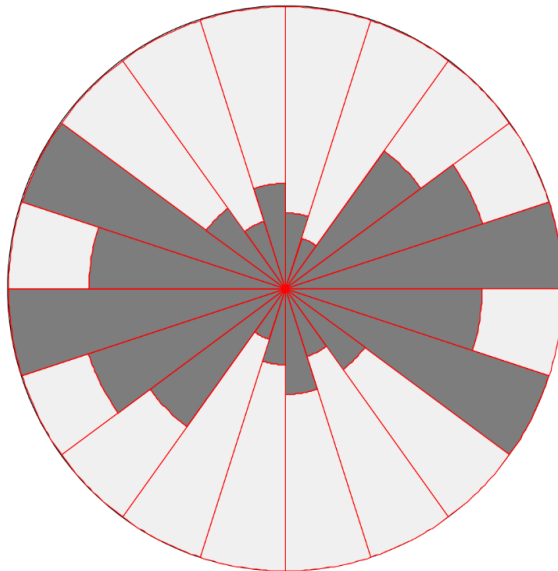
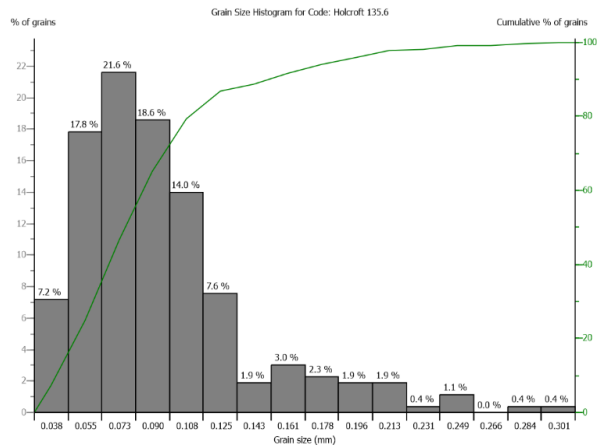


Figure 3.1. (a) Petrog software and optical microscope stage used for point counting textural analysis. (b) Thin sections are scanned systematically to obtain textural and compositional data through point counting. (c) An example data output sheet from Petrog is shown, and included grain size statistics, grains size distribution histogram, and a rose diagram of grain orientation.

Phi value from	To	Classification
0.00	0.35	Very well sorted
0.35	0.5	Well sorted
0.5	0.71	Moderately well sorted
0.71	1	Moderately sorted
1	2	Poorly sorted
2	3	Very poorly sorted
4	∞	Extremely poorly sorted

Table 1. Folk and Ward (1957) sorting classification

It has been demonstrated that a minimum of 200 grain measurements are required before no observed change in mean grain size with increased sampling (Duller *et al.* 2014). Therefore, a total of 250 grains were measured in both deformed and undeformed samples to ensure accurate representation of the samples.

Compositional analysis is performed using optical microscopy to estimate the mineral abundance of quartz, feldspar and lithic grains, to classify sandstone composition.

Microstructural observations are made using back scattered electron (BSE) images obtained using a Hitachi TM3000 scanning electron microscope (SEM).

3.3. Porosity measurement

The porosity of both undeformed and faulted sandstones was obtained from both optical and back-scattered electron images of samples in order to quantify petrophysical changes with deformation band formation. Using ImageJ analysis, an optical photomicrograph is first processed with an 8-bit colour palette filter. An ImageJ plug-in, jPORv1.1, is then used to threshold the colours of the image, and quantify by area the blue pore filling resin, calculating porosity as a percentage of the total image area (Fig. 3.2). This method of porosity calculation is comparable to conventional methods such as point counting, with a reported operator error standard deviation of 1.2%, due to dependence on photomicrograph quality and subjective judgements in thresholding and identification of grain-pore boundaries (Grove and Jerram, 2011). As this method relies on quantifying blue pore-filling resin, it is sensitive to the quality of impregnation. In very fine-grained and low porosity samples, such as deformation bands, it may not be possible to get full impregnation of resin, and therefore be unable to obtain accurate porosity values using optical photomicrographs. To combat this, the same method was applied to back-scattered electron images to calculate porosity. We find that BSE images result in higher and more accurate porosity values particularly at lower levels of porosity and grain size and higher levels of magnification, due to the clarity of defined grain-pore boundaries. A strong power-law relationship was identified between porosity from BSE and optical photomicrographs, which may be used to correct values of porosity in fine-grained low porosity rocks obtained using optical photomicrographs (Fig. 3.3).

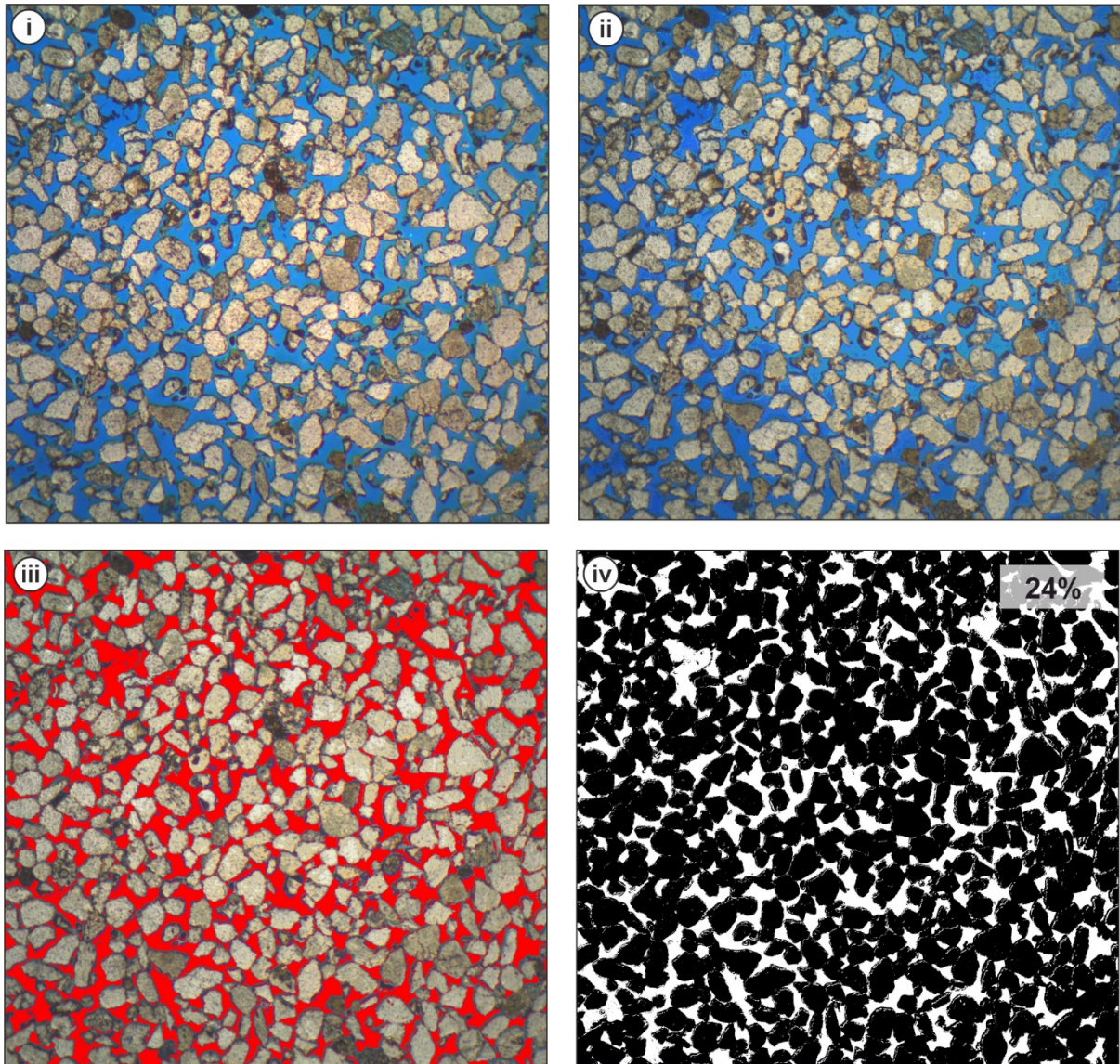


Figure 3.2. ImageJ jPORv1.1 porosity calculation method. (i) Tiff image of a thin section of blue resin impregnated sandstone sample. (ii) an 8-bit palette filter is applied to the photomicrograph and saved as a bitmap. (iii) jPORv1.1 plug-in for imageJ is used to manually threshold the blue pore filling resin (red). (iv) ImageJ calculates the area of red threshold pore space as a percentage of total image area to give a porosity value. A binary black and white image of the photomicrograph is produced representing grains and pore space respectively.

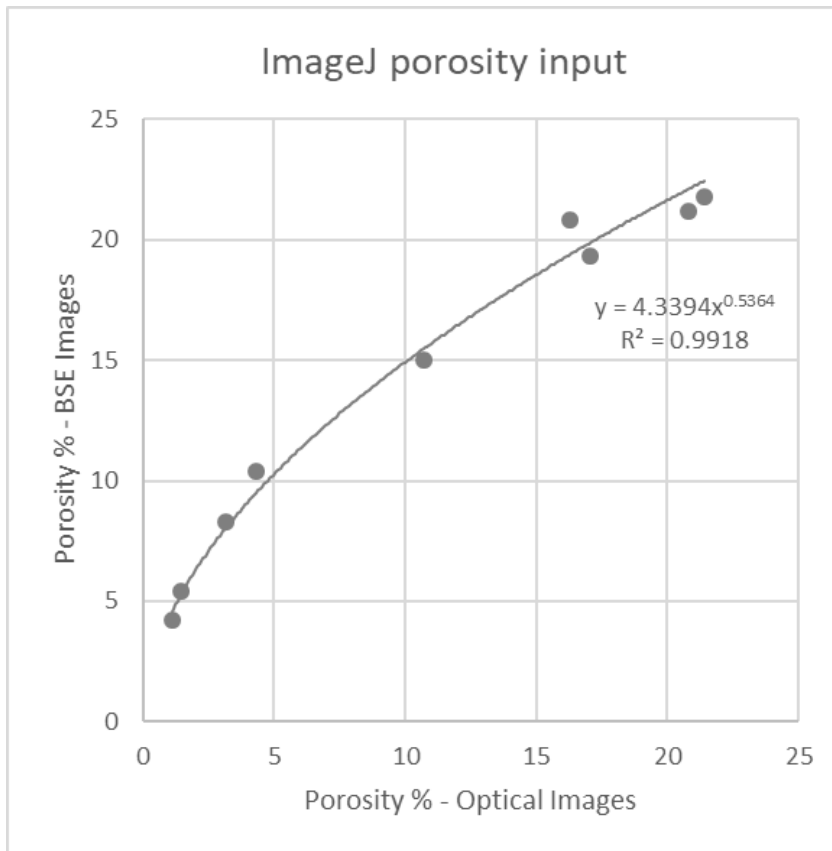


Figure 3.3. The relationship between porosity obtained using optical images against porosity obtained using back scattered electron images shows a strong power-law relationship that may be used for correction of values obtained by the former, particularly those at lower porosity levels.

3.4. Permeability measurement

The permeability of undeformed host rock was measured using an NER TinyPermIII™ handheld probe permeameter (Fig. 3.4), which provides a non-destructive method of permeability measurement on both outcrop and core. This method uses a probe which is applied to the rock surface, the user then applies a vacuum within the probe and the rate of its decay is measured and converted to millidarcys using the following formula:

$$T = -0.8206 \log_{10}(k) + 12.8737 \quad (7)$$

where T is time, and k is the permeability in millidarcys (md). This method of permeability measurement is reported to result in values up to 1.8 times higher than conventional lab based permeameter using core plugs on high porosity sandstones, which may be attributed to the effects of surface weathering, and measurement of a 2D surface rather than a 3D volume (Filomena et al., 2014). Therefore, outcrop measurements will be taken from sampled horizons to minimise the effect of weathering, taking the mean of ten readings, and core measurements will be taken every 0.5 m, again with an average of 10 measurements.

Due to the probe aperture, with an internal diameter of 9mm, often being much larger than the thickness of the deformation bands, a permeability measurement representative of the deformation band is difficult to obtain without simultaneously measuring the higher permeability, undeformed host rock adjacent to the bands. Therefore, it is necessary to determine band permeability using other methods.

Various methods for predicting permeability from other measurable rock properties exist, including from porosity, pore dimensions, grain size parameters, and mineralogy (Nelson, 1994). Given the rigor in obtaining grain size distribution data for the samples using Petrog,

which includes various grain size and sorting statistics, three grain-size based methods for calculating permeability were chosen.

The first method by Krumbein and Monk (1943), was derived from measuring permeability of sand packs of different sizes and approximately 40% porosity, with sorting controlled to be log-normal, and uses grain size as the main parameter:

$$k = 760d_g^2 \exp(-1.31\sigma_D),$$

where k is permeability in darcys, d_g is geometric mean grain diameter in millimetres, and σ_D is standard deviation of grain diameter in phi units, where $\phi = -\log_2(d)$.

Calculations of permeability from Berg (1970) considers the effect of grain sorting on permeability and assumes that permeability will be controlled by the smaller grains in a packing of mixed sized spheres, and also relates permeability to porosity with the following:

$$k = 80.8\phi^{5.1}d^2e^{-1.385p}$$

Where k is permeability in millidarcys, ϕ is porosity, d is mean grain size, and p is a sorting term which = $P_{90} - P_{10}$ the percentile of grain diameter in phi units.

A third method, derived from mercury injection data to relate permeability and porosity, and incorporating grain size and sorting, Baaren (1978) gives the following permeability calculation:

$$k = 10d_d^2\phi^{3.64+m}C^{-3.64},$$

Where k is permeability in millidarcys, ϕ is porosity, d_d is mean grain size, m is a cementation exponent, and C is a sorting index which relates to the spread of grain size $d_{max} - d_{min}$.

The above methods will be used to calculate permeability for our deformation band samples. They will also be used to calculate permeability for host rock samples so they can be directly compared to permeability values obtained by probe permeameter, to establish which method correlates best with those obtained with the permeameter, and thus will be used for analysis of poro-perm relationships of deformation bands and host lithology.

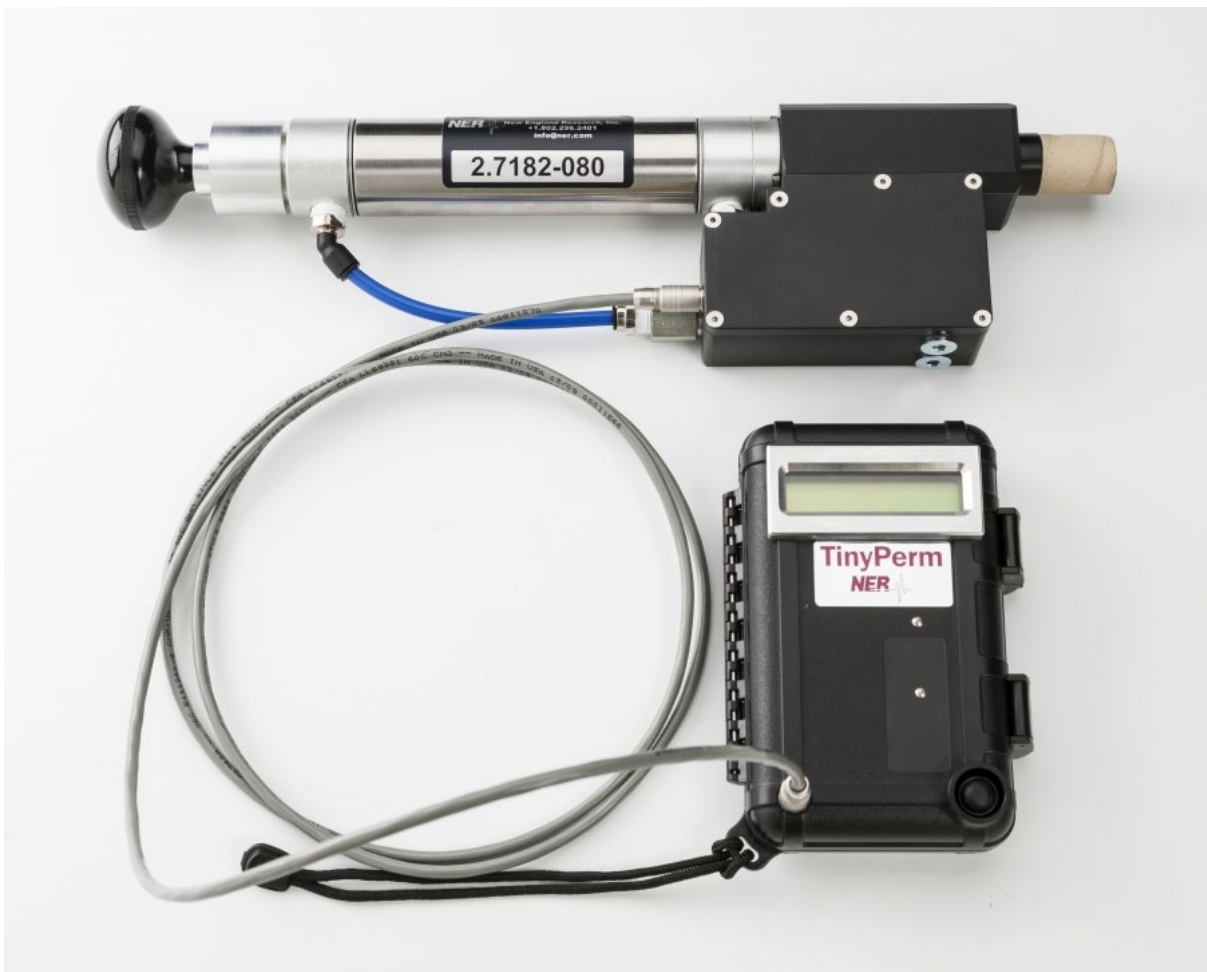


Figure 3.4. NER TinyPerm II permeameter used for measurements on both outcrop and core.

3.5. Fault damage zone measurements

The spatial distribution, density and intensity of fault damage zones can be characterised using the P_{XY} dimension based system which incorporates different dimensions of both the sampling method (x); in 1-dimension using scanlines, in 2-dimensions using areal measurements of sampling windows, or in 3-dimensions by measuring rock volumes, and the feature dimension (y); number of fractures (no dimension), trace length (1D), fracture area (2D) and fracture volume (3D) (Dershowitz and Herda, 1992)(Fig. 3.5). Fractures and joints have been well characterized in all 3 dimensions (Mauldon, 1998; Mauldon et al., 2001; Sanderson and Nixon, 2015), however measurements of deformation bands have typically only been measured in 1-dimension, measuring the number of bands along scan lines perpendicular to the fault plane or fault core, and expressed as number of bands per unit length, to provide a measure of frequency (P10) (Knott et al., 1996; Hesthammer et al., 2000; Du Bernard et al., 2002b; Johansen et al., 2005; Shipton et al., 2005; Johansen and Fossen, 2008; Griffiths et al., 2016). Whilst this method may capture the overall spatial decay of the number with distance from the fault, there are many drawbacks to scanline sampling. The sample area is small, there is often bias in scanline location selection, resulting in a high degree of censoring, and the potential for over- or under-sampling (Zeeb et al., 2013; Watkins et al., 2015). A worked example of this is shown in figure 3.5, with band intensity measured using both line transects and window sampling. Here line transect data is converted to length/area with assumptions of the bands length, geometry and orientation. Assuming that the bands sampled in a linear interval of defined length, in this example 15cm, are straight, and vertically inclined within the window area, we can estimate that 8 bands of length 15cm, have a 2-D intensity of 1.2m of bands per unit area. Results show that estimations of band frequency from scanline measurements have a high degree of uncertainty and are subject to

user bias when compared to window sampling. Additionally, line transects also do not capture geometric variations of the bands such as length, width or orientation and so estimations of 2-D intensity from 1-D density are inaccurate and unrepresentative of the outcrop (Mauldon et al., 2001). To minimise these sampling issues, we employ the 2-D areal window sampling method using square quadrats, recording the 2-D trace length of the bands to record deformation band intensity (P21) expressed as m/m^2 . Intensity is recorded in fault zones of different facies using square quadrats of one of three sizes; 15x15cm, 25x25cm and 50x50cm, depending on bed thickness and the sample area required to most accurately represent the fault damage zone for that bed. Trace length of deformation bands is measured, either in the field by hand or digitally from photographs, as well as thickness measurements of the bands within each window, providing a more accurate measure of intensity, reducing censoring, and allowing for the subtle changes between different facies within a fault damage zone to be captured.

		Feature Dimension			
		0 Number	1 Length	2 Area	3 Volume
Sampling Dimension	1 Line	P₁₀ Number of fractures per unit length <i>Frequency</i>	P₁₁ length of fractures per unit length <i>Dimensionless Intensity</i>		
	2 Area	P₂₀ Number of fractures per unit area <i>Frequency</i>	P₂₁ length of fracture traces per unit area <i>Intensity</i>	P₂₂ Area of fractures per unit area <i>Dimensionless Intensity</i>	
	3 Volume	P₃₀ Number of fractures per unit volume <i>Frequency</i>	P₃₁	P₃₂ area of fractures per unit volume <i>Intensity</i>	P₃₃ volume of fractures per unit volume <i>Dimensionless Intensity</i>

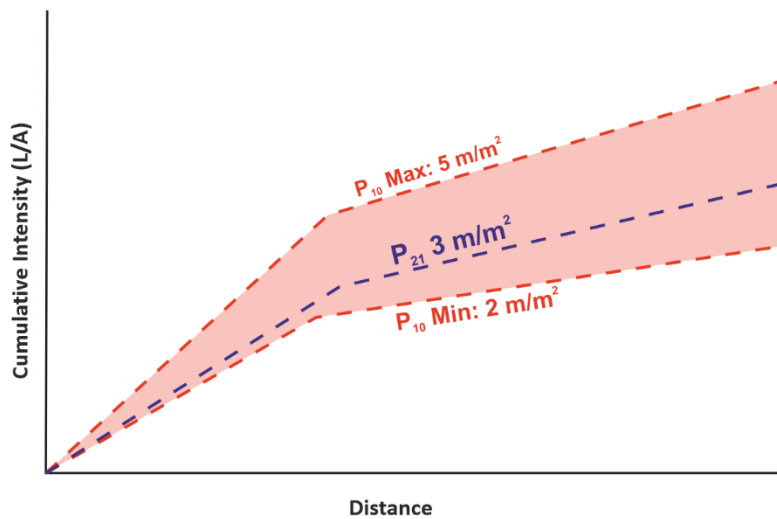
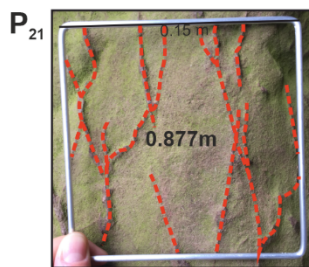
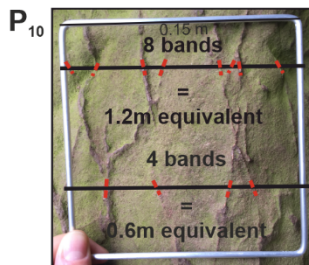


Figure 3.5. The P_{xy} system for fracture measurements based on dimensions of feature and sampling method. One dimensional intensity P_{10} and two-dimensional intensity P_{21} measurements show greater uncertainty for P_{10} due to censoring and user bias.

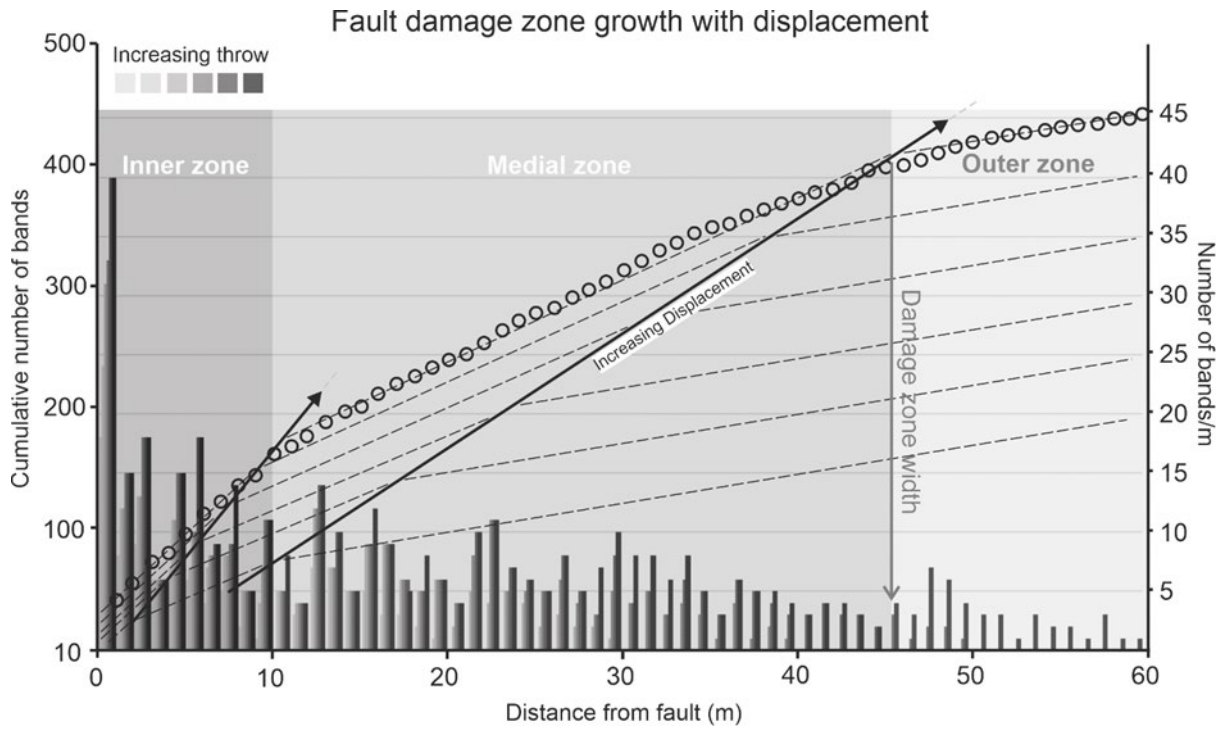


Figure 3.6. Deterministic model of fault zone development with increased displacement (Schueller et al., 2013). Different zones of varying deformation band intensity can be identified by the gradient of cumulative band intensity, to define damage zone width (Choi et al., 2016). Damage zone intensity is shown to be independent of displacement and may be controlled by other factors such as lithology.

The deformation band density transects are plotted both as a function of deformation band frequency, as well as the cumulative number of deformation bands. Plotting the cumulative number of bands for fault zones shows the distribution of structures in the damage zone that can otherwise be difficult to interpret with conventional linear band frequency plots and provides a less subjective means of determining damage zone width (Choi et al., 2016). The average band density can be defined by fitting a trend line to the cumulative number of deformation bands and is represented by the gradient of the trend line (Figure 3.6). A plot of the cumulative number of deformation bands with distance for a series of deterministically modelled faults shows that the fault damage zone may be subdivided into a series of zones based on deformation band density defined by the line gradient; an inner zone of intense deformation, a medial zone of moderate deformation, and beyond that an outer zone, which may represent 'background' damage (Schueller et al., 2013). Therefore, the intersection of trend lines of the medial and outer zones can be used to quantitatively define the damage zone width. The average density of deformation bands within this defined damage zone width is shown to remain reasonably constant with increasing fault displacement and damage zone growth, and may instead be controlled by other factors, including lithology and the petrophysical properties of the sandstones. Cumulative band density is plotted for a number of different units adjacent to faults and their damage zones, in order to compare and determine the influence of lithology on damage zone intensity.

Band width is recorded using digital Vernier callipers along each damage zone transect, allowing the measurement of cumulative width through a sequence. This may then also be used to calculate total fault rock volume for the purposes of estimating the effect on bulk permeability, as well as for the defining of fault facies based on fault rock volume (Braathen et al., 2009).

3.6. Experimental rock mechanics

Deformation experiments were performed in the triaxial apparatus at the University of Liverpool Rock Deformation Laboratory. The triaxial apparatus (Fig. 3.7a) is capable of applying 250MPa of hydrostatic confining pressure, using silicone oil as a confining medium, and 200MPa of pore fluid pressure using either argon gas or de-ionized water. The samples are placed between the upper and lower parts of the sample assembly, encased in silicone and/or copper jackets, and sealed via O-rings (Fig. 7.5b & c). The sample assembly is then placed into the pressure vessel of the triaxial apparatus submerged in confining oil and secured via the top nut. Pore fluid is introduced to the sample via two small diameter inlets at either end of the sample. Both confining and pore pressure systems are servo controlled, with volume monitored to a resolution of 0.1mm³. Hydrostatic experiments in which all stresses are equal:

$$\sigma_1 = \sigma_2 = \sigma_3$$

are performed on samples by increasing the pressure of confining silicone oil in the triaxial vessel via an air-driven hydraulic pump. Pressure is measured via a transducer with a resolution of 0.007MPa. The triaxial experiments are performed under axisymmetric compression, with the principal stress (σ_1) increased via a servo controlled, gear driven piston that can load samples axially up to 300kN, at displacement rates of between 0.1 and 23 μ m/s, whilst σ_2 and σ_3 are applied by the confining pressure and held constant during axial loading:

$$\sigma_1 \geq \sigma_2 = \sigma_3$$

enabling loading of the samples to failure to desired states of stress in order to explore different kinematics and mechanisms of failure (Fig. 2.7).

A comprehensive overview of the sample preparation and configuration, and experimental procedures will be covered in chapter 7.

Triaxial Apparatus

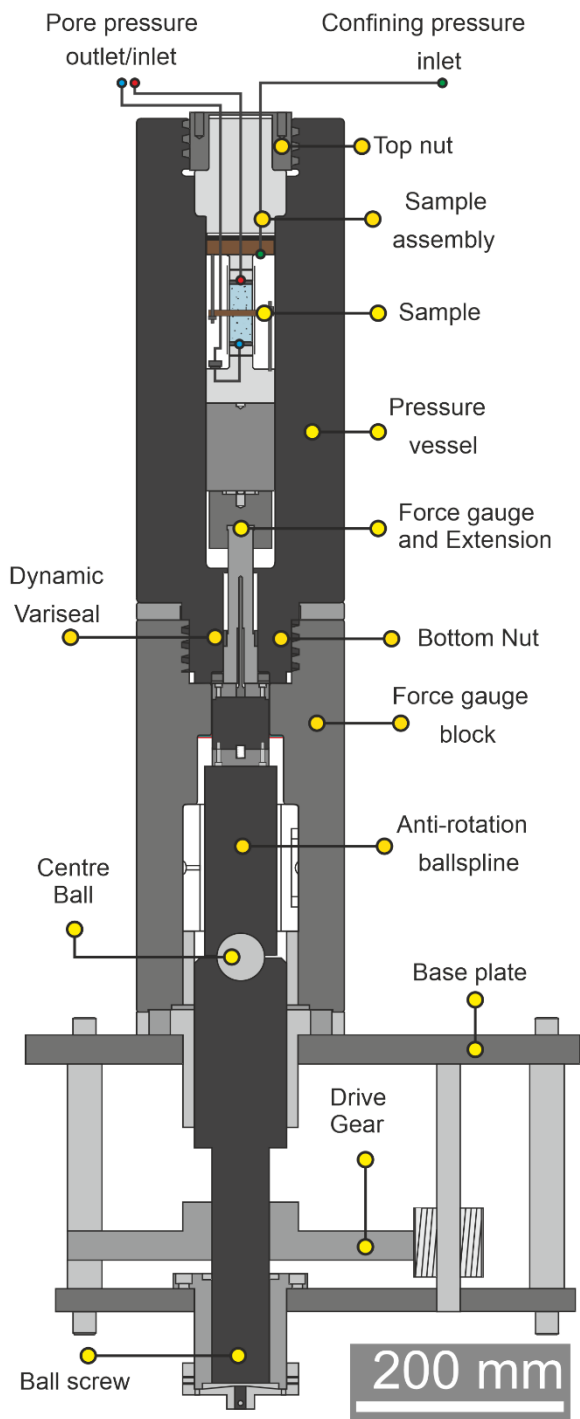


Figure 3.7. (a) Schematic drawing of the triaxial deformation apparatus used for both hydrostatic and triaxial experiments. (b) Schematic drawing of the sample configuration prior to testing.

4. Study locations and lithofacies descriptions

Field based studies of deformation bands have been the primary source of understanding of their occurrence and physical properties, as they act as direct analogues for sandstones in the subsurface (Aydin, 1978; Antonellini et al., 1994; Schultz and Siddharthan, 2005; Shipton et al., 2005; Solum et al., 2010; Schueller et al., 2013; Griffiths et al., 2016). Two mixed aeolian-fluvial sandstone case studies are chosen for this study on the merit of hosting deformation bands within fault zones, having sufficient outcrop availability, and also providing useful analogues to many subsurface reservoirs of the UK Continental Shelf (UKCS) as hydrocarbon (Meadows and Beach, 1993; Williams and Eaton, 1993; Fisher and Knipe, 2001; Mark et al., 2008), groundwater (Sternlof et al., 2006; Medici et al., 2019), geothermal (Hirst et al., 2015), and carbon capture and storage (CCS) reservoirs (Armitage et al., 2013). These two case studies, their stratigraphy, localities, lithofacies and deformation band occurrence are detailed below.

4.1. Case study 1 – Cheshire Basin, UK.

The Cheshire Basin provides a large, basin scale study, with the thickest accumulation of Permo – Triassic, mixed aeolian-fluvial stratigraphy in the UK of up to 4km.

The basin has a complex tectonic history with many periods of compression and extension and is formed off the north-west edge of the Caledonian/Acadian basement structure of the Midlands Micro-craton. The basin is controlled by, and follows the NE-SW trend of the Wem – Red Rock Fault System (WRRF) located in the south of the basin, a transpressional thrust fault of the Acadian orogenic belt.

Early Carboniferous back-arc extension led to normal movement on these faults, providing accommodation space for Carboniferous carbonates. By the late Carboniferous, extension

had ceased and thermal subsidence became the main driver for basin evolution (Waters and Davies, 2006). Basin inversion during the Variscan Orogeny is marked by an angular unconformity at the base Permo-Triassic sequence. Several local unconformities are also observed that may be explained by localized uplift on the crest of footwall blocks (Evans et al., 1993).

Regional extension associated with the opening of the Atlantic created accommodation space for the Permo-Triassic stratigraphy. E-W extension was accommodated by N-S trending normal faults with dip-slip displacement that extend through the Cheshire and neighbouring East Irish Sea Basin (Knott, 1994), while the major basin controlling faults, the NE-SW Wem-Red Rock Fault (WRRF) had oblique slip displacement.

By early Cretaceous, extension had slowed and considerable erosion led to development of the Late Cimmerian Unconformity which marks the syn-rift to post-rift transition, offering a distinct horizon in the North Sea (Kyrkjebø et al., 2004). By mid-Cretaceous extension had concluded and structural control on basin development was insignificant, and regional subsidence became the main control on basin development

4.1.1. Stratigraphy of the Sherwood Sandstone Group

The Sherwood Sandstone Group (SSG), formerly known as the Bunter and Keuper Sandstones, is a Triassic succession of continental sediments that outcrop across the UK from the Dorset coast to the north east coast of Teesside. Thick accumulations occur within fault-controlled basins such as the East Midlands Shelf, North Sea Basin, East Irish Sea Basin, Stafford Basin, and the Cheshire Basin. Lateral equivalents of the SSG in the East Irish Sea and North Sea provide economical oil and gas plays (figure 4.2), and the Cheshire Basin itself has potential economic importance as a shale gas (Andrews, 2013) and geothermal resource (Hirst et al., 2015). Therefore, onshore outcrops of the SSG provide the ideal analogous study for these reservoirs, with three dimensional outcrops, and spatial and temporal variations in facies observed across the UK.

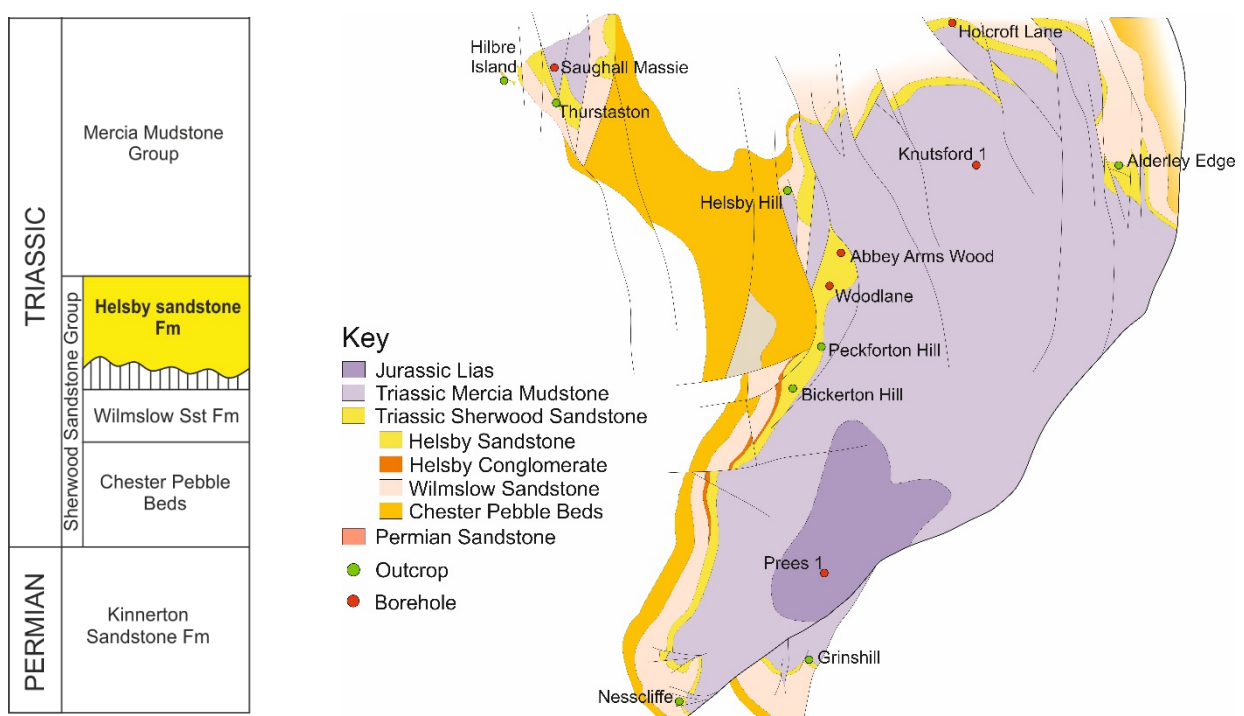


Figure 4.1. Stratigraphy and geological map of the Cheshire Basin. The Helsby Formation is the main formation of interest, expressing the most facies variation within the Sherwood Sandstone Group. Field localities are indicated on the map.

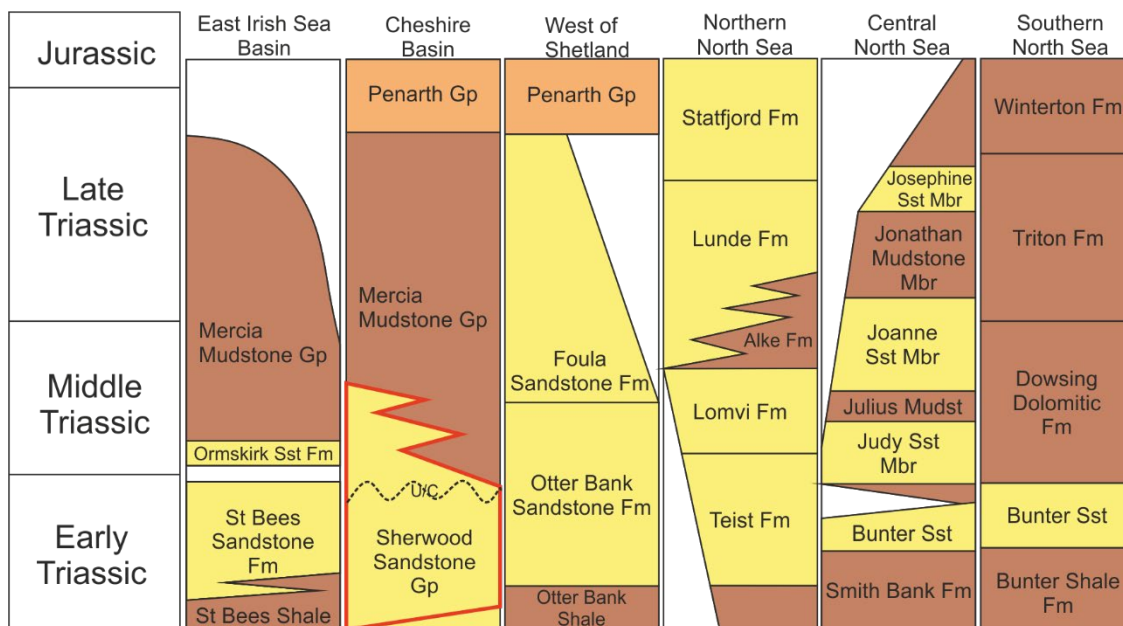


Figure 4.2. Stratigraphy of the Cheshire Basin, with lateral equivalents and petroleum reservoir sands of the East Irish Sea Basin, Shetland Basin, Northern, central and southern North Sea. (Adapted from (Aydin and Johnson, 1978; Ruffell, 2003; McKie and Williams, 2009)

The SSG had previously been given a Germanic nomenclature and classification scheme (Hull, 1869) in which UK Triassic units were broadly correlated with European formations of similar stratigraphic age. The names Bunter, a lower Triassic division, and Keuper, an upper Triassic division were used. Problems occurred in correlating these units as the middle Triassic Germanic unit Muschelkalk does not occur in Britain. This broad division of the Triassic also did not reflect the lithological and facies variation observed both at outcrop in the UK and in early boreholes. Acquisition of borehole data from the North Sea in the 60s and 70s led to further subdivision of strata based on lithological and biostratigraphical considerations from palynological studies. Palynological studies also revealed that the base and top of the SSG are diachronous, with base ages ranging from late Permian to early Triassic, and the top of the

succession becoming younger from the Irish and North Seas towards the Midlands of England (Ruffell, 2003).

The SSG comprises predominantly sandstones with small pebble conglomerates and occasional siltstones that are ascribed to terrestrial mixed fluvial and aeolian environments, with wet interdune deposits (Mountney and Thompson, 2002; Wakefield et al., 2015). There is regional variability in the dominant facies, with the East Midland Shelf dominated by braided fluvial facies and an absence of aeolian facies, whilst the western Cheshire Basin hosts a mixture of aeolian, interdune and fluvial facies. Its thickness varies throughout the UK but is estimated to be up to 1100m thick in the Cheshire Basin, based on observations in the Knutsford borehole (Griffiths et al., 2003). Present day division of the SSG comprises three formations; Chester Formation, Wilmslow Sandstone Formation, and the Helsby Sandstone Formation (Ambrose et al., 2014).

4.1.1.1 Chester Formation

Approximately 300m thick in north west England, this formation rests conformably, unconformably and disconformably on underlying units (Ambrose et al., 2014) and it is considered the base of the Triassic in many stratigraphical correlations (Audley-Charles, 1970). It outcrops across the UK including the Devon coast where it is known as the Budleigh Salterton Pebble Beds. Here it is a coarse-grained conglomerate comprised of pebbles, cobbles and boulders, and interpreted as being close to sediment source, in this case the Variscan/American Massif in the north of France. Contrary to what its name suggests, in the Cheshire Basin it comprises mostly of medium- to coarse-grained sandstones with only occasional pebbly units that become rarer in the north of the basin. In the eastern margin of the Cheshire Basin an unconformity at the base of the Chester Formation occurs and may coincide with uplift and erosion on the footwall blocks of major basin controlling faults (Evans

et al., 1993). The formation shows an overall fining upwards trend with the interbedding of siltstones and mudstones toward the top. The upper boundary may be defined by a change in dominant facies from fluvial deposition to that of aeolian deposition in the overlying Wilmslow Sandstone Formation, as well as decrease in the level of cementation, strongly cemented by carbonate cements, in contrast to the overlying Wilmslow Sandstone Formation which is poorly cemented.

4.1.1.2 Wilmslow Sandstone Formation

The thickest unit of the SSG succession is observed at 900m depth in the Knutsford borehole in the north east of the basin, where it is approximately 950m thick (Fig. 4.1). This unit also occurs in the depocentre of the basin in the Prees borehole, but is observed to be significantly thinner at up to 550m thick (Evans et al., 1993). In the Cheshire Basin the formation predominantly comprises fine- to medium-grained cross bedded sandstones of aeolian origin, with well-rounded and frosted grains, with minor thin siltstone beds. The formation is generally poorly cemented and friable, much softer than the underlying Chester Formation, from which it can be distinguished. Its poorly cemented and friable texture makes this formation particularly susceptible to faulting and the formation of deformation bands.

4.1.1.3. Helsby Sandstone Formation

The Helsby Sandstone Formation lies disconformably on the Wilmslow Sandstone Formation and is approximately 250m thick (Ambrose et al., 2014). A both temporally and spatially variable sandstone, a northward facies change is observed from fluvial to increasingly aeolian. It was originally subdivided into three main units according to the dominant facies (Thompson (1970); The lowermost Thurstaston Sandstone Member comprises a hard bed of aeolian cross-bedded sandstones and other less cemented cross-bedded sands and interdune fines.

The middle fluvial floodplain Delamere Sandstone Member comprises three units, a middle unit of laterally extensive soft yellow aeolian sandstones, which is under- and overlain by cross-bedded and pebbly, fluvial sandstones. Lastly, the uppermost Frodsham Sandstone Member is dominated by large-scale aeolian cross-bedded facies (Mountney and Thompson, 2002). More recent mapping of the Cheshire Basin places the lower boundary of the Helsby Sandstone at the unconformable base of the Delamere Member, with the Thurstaston Member included within the Wilmslow Sandstone Formation (Meadows, 2006; Ambrose et al., 2014).

Due to the facies heterogeneity across relatively small scales, the Helsby Formation and parts of the upper-most Wilmslow Formation are chosen as the primary subjects of this study.

4.1.2. Deformation bands in the Cheshire Basin

Deformation bands are a prevalent feature of fault zones within the Cheshire Basin, and can be observed at outcrop along the basin's periphery, where outcrops of Wilmslow and Helsby Sandstones, with their favourable properties, are plentiful. However, the study of deformation bands in this region is lacking when compared to other regions such as those in Utah, U.S.A. and Provence, France. Bands were first identified here during the early 1990s out of necessity of understanding fault zones within the neighbouring East Irish Sea Basin, where oil and gas is produced from the Ormskirk Sandstone, for which the Helsby Sandstone is analogous. Whilst the deformation bands themselves were not studied in any great detail, they are the main structural element of fault damage zones and were grouped as faults in the classical sense. Knott (1994) established fault displacement versus damage zone thickness relationships using a number of localities; Thurstaston, Heathfield, Bidston and Helsby, in order to establish the fault sealing potential. A similar regional study of fault zones was

conducted by Beach et al. (1997) in order to calculate fault transmissibility with displacement-width scaling relationships.

More detailed work on deformation bands in the Cheshire Basin was conducted by Rowe and Burley (1997). A major fault was studied through a variety of lithologies, with an aim to understanding the paragenesis of the SSG with application to the East Irish Sea Basin oil and gas prospects. Deformation bands were identified as the major structural feature of the fault zone and a major modification to the porosity in addition to mineralization. They were found to baffle formation brines and lead to cement precipitation in the footwalls of the shear bands. The lithological variation in the sandstones at this locality and sporadic occurrence of deformation bands suggests a lithofacies control on deformation band development, and thus a control on poro-perm modification.

In a recent study by Griffiths et al. (2016) on the Thurstaston Sandstone Member of the Helsby Sandstone Formation at its type locality, the occurrence and properties of deformation bands in relation to host rock properties was investigated. It found that fault zones were less pervasive in fine-grained sub-arkosic interdune facies, and more pervasive in coarse-grained arenitic aeolian facies. Grain size was identified as the major control on deformation band formation, secondary to mineralogy. In both cases, porosity was reduced by 60%.

4.1.3. Localities

The localities on which this study is based are situated along the periphery of the basin (Fig. 4.1), where the upper-most Sherwood Sandstone Group, which represent the most heterogeneity in terms of lithofacies, can be observed in outcrop and/or in shallow observatory boreholes for which core recovery is generally good. Localities are logged (Fig.

4.10) and sampled, with a description of the facies variability present at each locality, as well as a general description of fault and deformation band occurrence, described below.



Figure 4.3. (a) Geological map of Helsby including the study areas and major faults of interest. (b) Helsby Hill Fault with extensive deformation band damage zone. (c) Deformation bands within aeolian beds of Helsby Quarry.

4.1.3.1. Helsby Hill (Grid ref: 349500 375500)

At Helsby, the type locality for the Helsby Sandstone Formation, outcrops display a dominance of fluvial facies. At the base of the succession in Helsby Quarry, aeolian dune, interdune and fluvial facies compete, with bed scales on the order of 0.2m – 2m, creating lithological heterogeneity in terms of grain size, sorting and porosity, with clean and texturally mature aeolian beds and relatively poorly sorted and texturally immature fluvial beds interbedded with mudstones (Fig. 4.8d). Further up the succession on Helsby Hill, fluvial facies become the dominant facies displaying lithological variability in varied levels of grain size, sorting and occurrence of mud and pebble clasts in the form of fluvial lag in fluvial channels, bars, and overbank facies with bed and facies scales on the order of 1m–8m thickness (Fig. 4.8b). Two major faults cut through the Helsby area, the Dungeon Banks Fault strikes N-S just west of Helsby Quarry, while a smaller fault strikes NE-SW through Helsby Hill with approximately 7m of normal displacement (Fig 4.3). At Helsby Quarry, deformation bands strike parallel to the Dungeon Banks Fault at 174° with a conjugate geometry, dipping 64.7° and 76.6° east and west respectively, with an intersection angle of 38.8° (Fig. 4.9b i). Further east deformation bands rotate slightly to strike $134\text{--}155^{\circ}$ parallel to the Helsby Hill Fault (132° 59° SW) dipping 59.5° and 65.1° with an angle of intersection of 58° (Fig. 4.9b ii).

4.1.3.2. Grinshill (Grid ref: 351927 323701)

At Grinshill a gradual facies change is observed from a predominantly aeolian environment in the Wilmslow Sandstone Formation, to a fluvial environment of the Helsby Sandstone Formation. The former is dominated by large scale, high porosity texturally mature aeolian dune beds displaying high angle cross bedding and grain-flow and grain-fall laminations. Individual bed scales are on the order of 2m – 6m, with successions of these beds up to 20m in thickness (Fig. 4.8e). The transition into a fluvial environment is not directly observed

due to a break in outcrop. The upper most beds are characterised by poor level of sorting, mud intraclasts and channel geometries. Beds are of the order of 2m–6m thick (Fig. 4.8c). Both aeolian and fluvial beds are affected by deformation bands relating to two pairs of faults. At Grinshill, two pairs of fault structures and therefore two sets of conjugate deformation bands are evident. The first are a series of NNE-SSW trending fault zones exposed in the hillsides with minor <0.5m displacements, synthetic and antithetic to the Brockhurst Fault situated to the east, a splay fault of the basin-controlling Wem Fault structure. The second are a series of normal faults perpendicular to these striking NW-SE (Fig. 4.4), with fault planes exposed in Corbet Wood with a series of synthetic slip surfaces displacing aeolian lithologies with <0.5m displacement. Deformation bands are the primary structural element of damage zones to both of these fault pairs. In the east of the locality deformation bands strike approximately 115° , parallel to the major fault plane ($126^{\circ} 73^{\circ}$ NE), with a conjugate geometry dipping $\sim 73^{\circ}$ with an intersection angle of 35° (Fig. 4.9a i). Moving west the damage zone of the NNE-SSW faults become apparent with another set of conjugate deformation bands striking 015° , parallel to the major fault plane ($026^{\circ} 72^{\circ}$ NW), dipping 62° and 80° with an intersection angle of 40° (Fig. 4.9a ii). Further west the NNE-SSW deformation bands dominate as the primary damage zone structures (Fig. 4.9a, iii, iv).

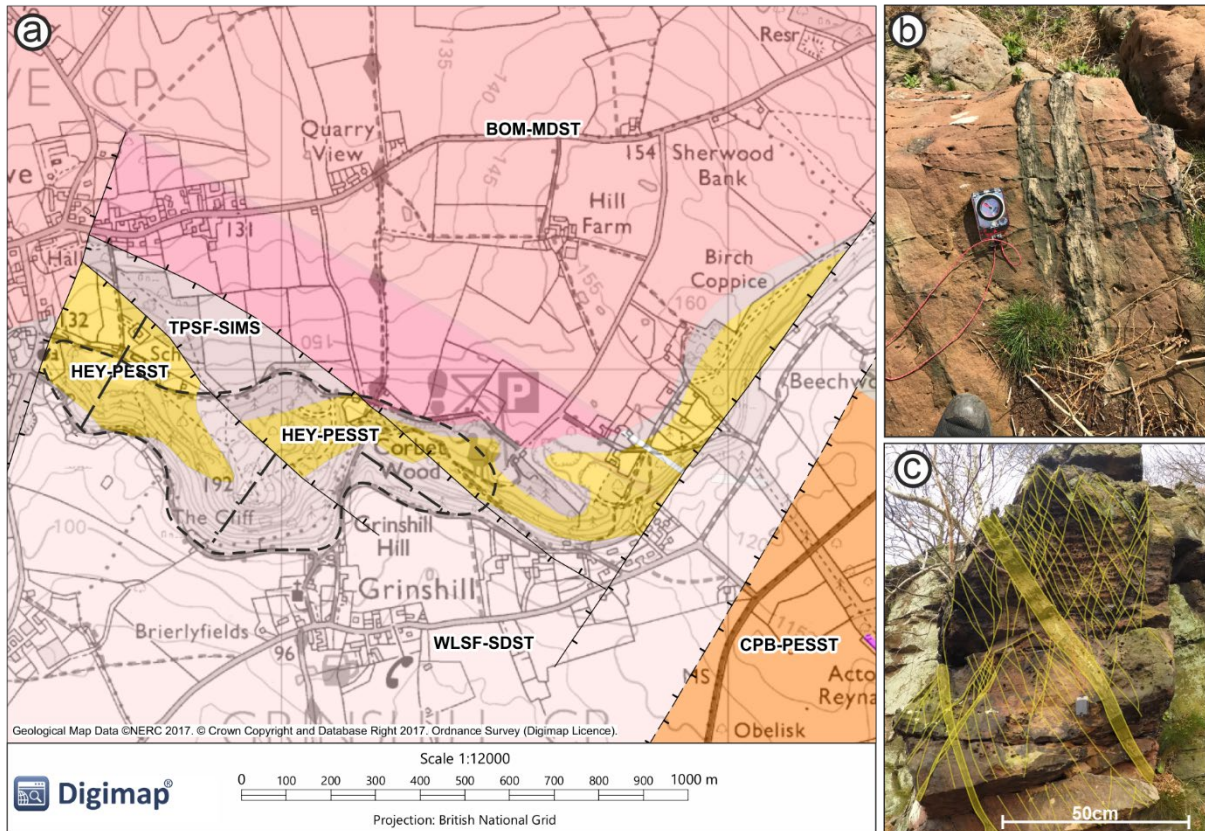


Figure 4.4. (a) Geological map of Grinshill including major faults of interest. (b) Two structural trends in deformation bands corresponding to two major faults. (c) A dense deformation band zone containing a deformation band cluster.

4.1.3.3. Thurstaston (Grid ref: 324376 384673)

Thurstaston, the type locality for the Thurstaston Sandstone Member of the upper Wilmslow Formation, displays a ~6m thick succession of aeolian dune facies sandstones in cross-section along Telegraph Road (Fig. 4.5b). Individual beds are of the order of 0.5m-1m thick, and lithologies are fine- coarse-grained, extremely well-sorted and well-rounded, asymptotic cross-bedded sandstones, and for the most part poorly cemented, with the exception of the Thurstaston Hard Bed, a bed of extremely well cemented aeolian sandstone. A series of three, approximately E-W trending normal faults are observed in a ~ 3m section of coarse-grained lithofacies which display damage zones of deformation bands. Displacements on these faults are estimated at 7, 19.5 and 64 cm.

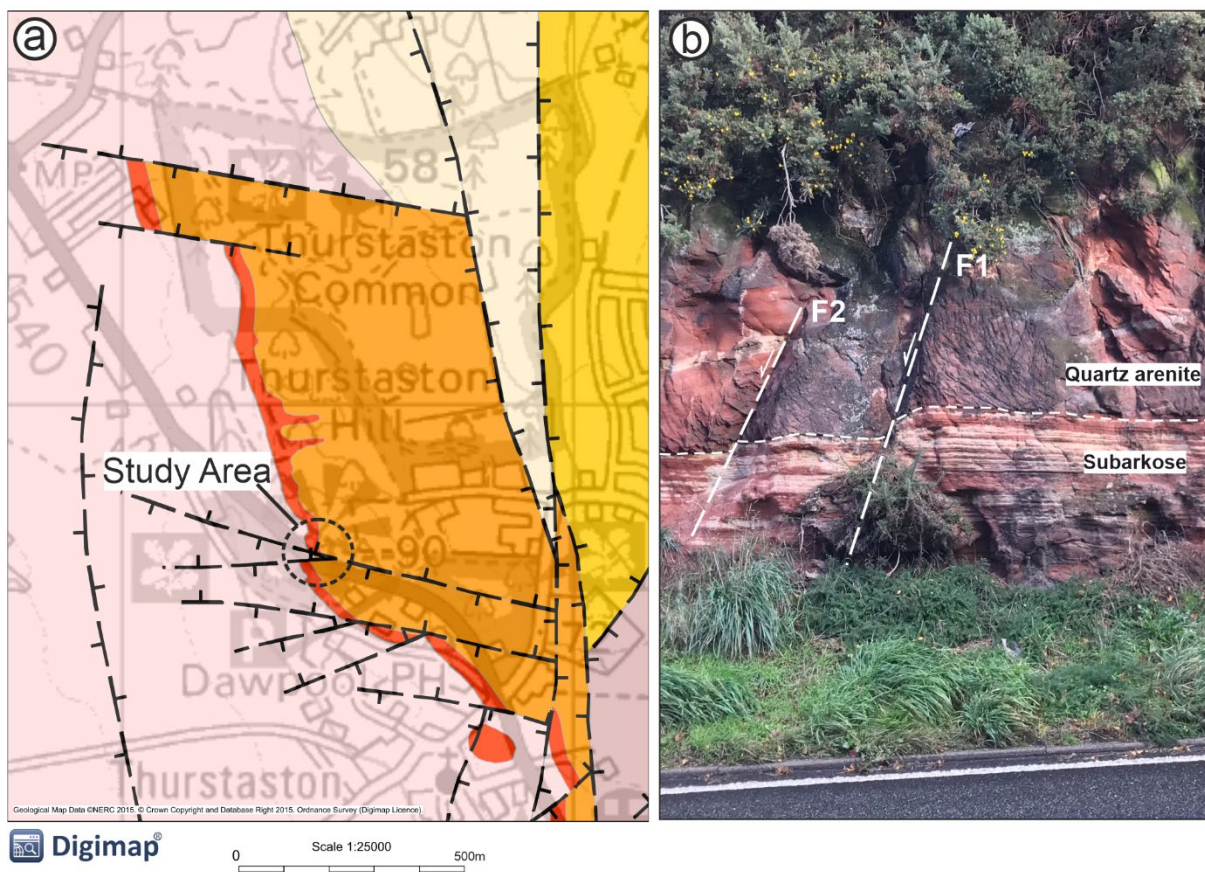


Figure 4.5. (a) Geological map of Thurstaston including study area and major faults of interest. (b) Two faults observed in the road cutting on Telegraph Road displace beds of quartz arenite and sub-arkosic sandstones.

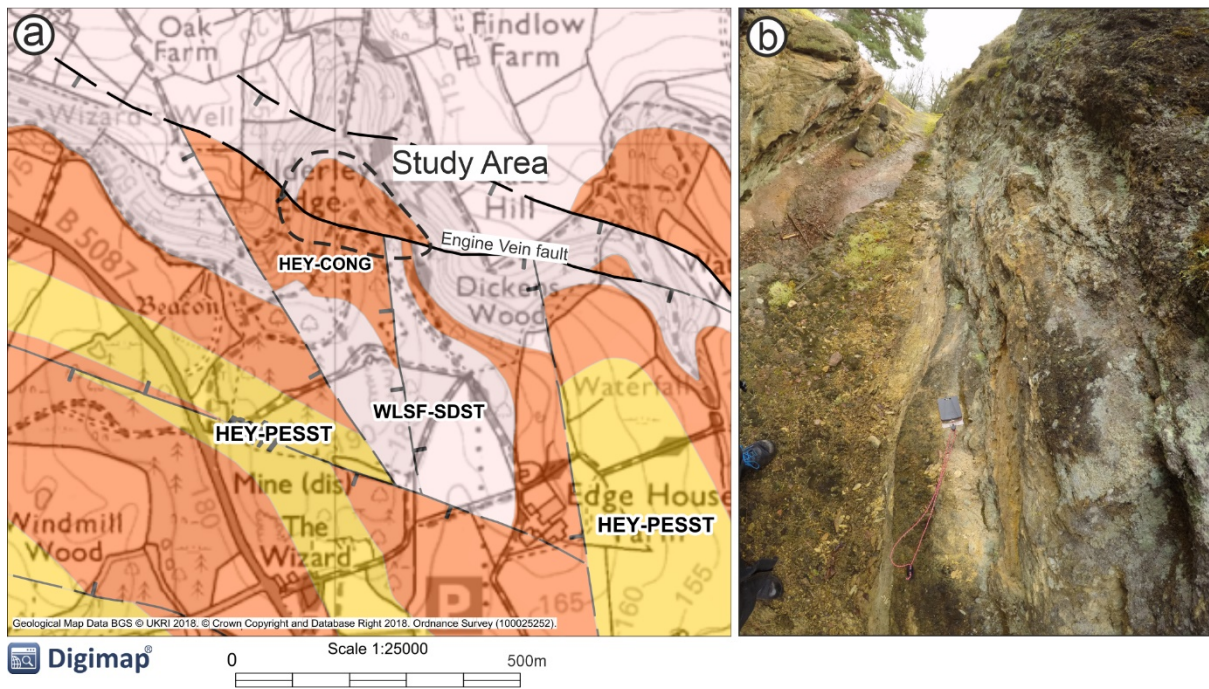


Figure 4.6. (a) Geological map of Alderley Edge including study area and major faults of interest. (b) The Engine Vein fault exposed along a mine working.

4.1.3.4. Alderley Edge (Grid ref: 386085 377842)

In the east of the basin at Alderley Edge there are localised pebble conglomerates that represent alluvial fans that originated from the fault scarps of the basin-bounding WRRF (Ambrose et al., 2014). Alderley Edge is a tilted horst block between two major N-S trending faults on the eastern edge of the Cheshire Basin, within which are a series of WNW-ESE oriented normal faults are host to mineralisation and mine workings. These faults strike approximately $100\text{-}110^\circ$ dipping $\sim 70^\circ$ NNW. Deformation bands in the damage zone of these faults strike approximately 120° in conjugate sets dipping 68.7° and 80.1° to the NNW and SSE respectively with an angle of intersection of 31.3° (Fig. 4.9d).

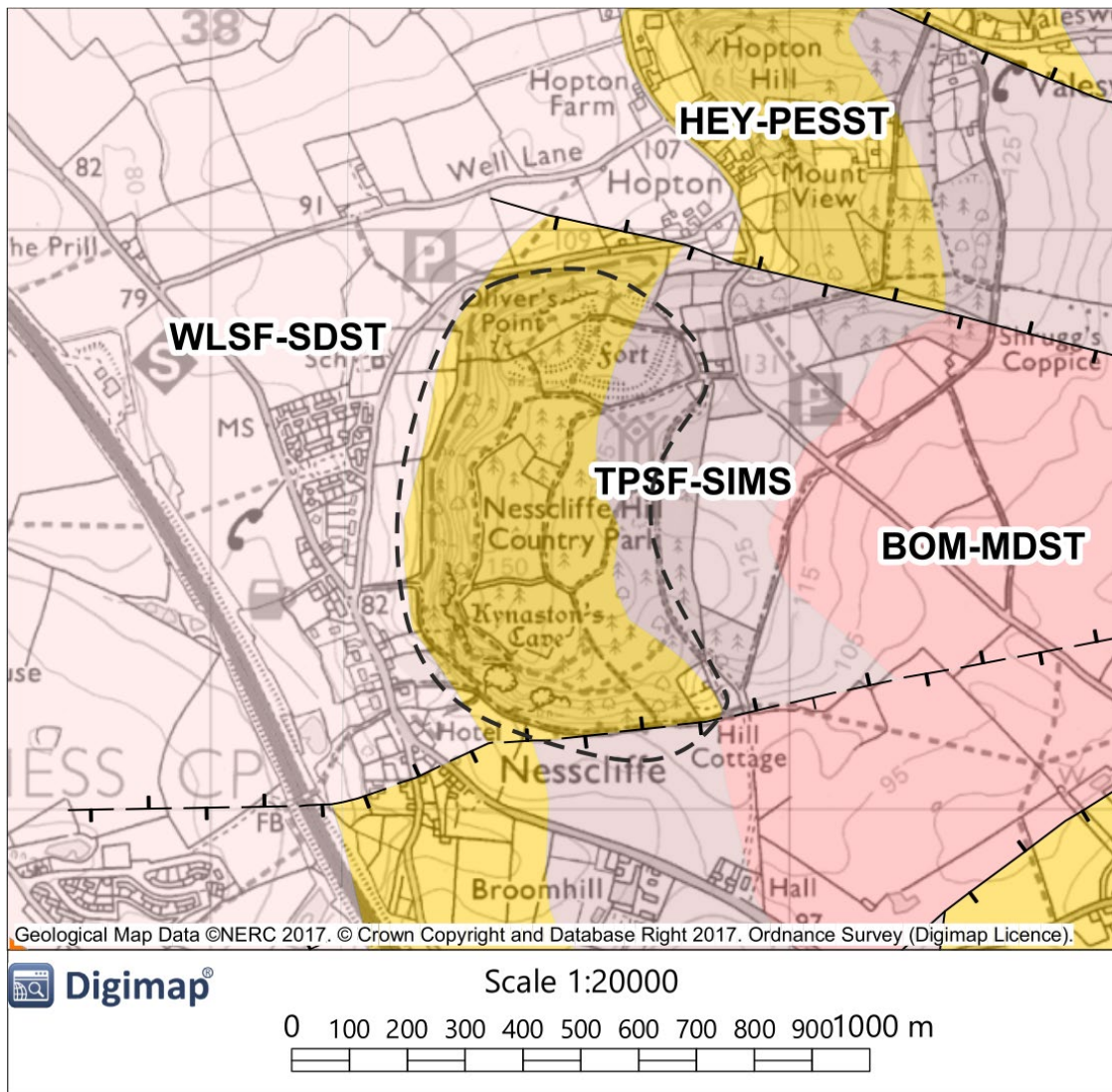


Figure 4.7. Geological map of the Nesscliffe locality including the highlighted study area in Nesscliffe Country Park. Between two approximately E-W striking faults.

4.1.3.5. Nesscliffe (Grid ref: 338432 , 319360)

The Nesscliffe locality provides a thick ~30 m succession of high-porosity, well-sorted, fine-grained aeolian sandstones of the lowermost Thurstaston Member of the Helsby Sandstone Formation (Fig. 4.8f). It is very well-cemented, distinguishing it from the underlying aeolian Wilmslow Sandstone Formation. No fault planes are directly observed at Nesscliffe, although deformation bands occur throughout the outcrops relating to damage zones of major W-E structures to the north and south of the field locality as part of the major basin-controlling Wem Fault system (Fig. 4.1 & 4.7). Deformation bands dip at high angles to the north and south at 81° and 84° respectively, with an intersection angle of 18.6° (Fig. 4.9c).

4.1.3.6. Saughall Massie (Grid ref: 324313 388446)

The Saughall Massie borehole records up to 150m strata, with ~30m of the upper-most Helsby Sandstone Formation. Fluvial channel facies are recorded at the base in the Delamere Member, represented by a ~6m thick succession of medium- coarse-grained, cross-bedded sandstones containing sporadic mud intraclasts. This is succeeded by an aeolian sequence of fine- medium-grained, cross-bedded and massive aeolian sandstones of the Frodsham Member, and a subordinate interdune mudstone bed. Aeolian beds are heavily deformed by cataclastic deformation bands (Fig. 4.8h). Deformation band orientation from core is recorded relative to the orientation of the slabbed face of the core as opposed to north, in order to observe their relative geometry. Deformation bands also display conjugate geometries with two opposing dipping sets. Assuming a vertical borehole, deformation bands dip at 63° and 68° , with an intersection angle of 47.9° (Fig. 4.9e).



Figure 4.8. (a) Fluvial Helsby Formation eroding into aeolian units of the Wilmslow Formation at Bickerton. (b) Fluvial sequences of the Delamere Member observed at Helsby Hill show pebbly channel sandstones, and cross bedded and rippled fluvial bars. (c) Faulted fluvial channel units at the top of Grinshill. (d) Interbedded fluvial muds and fine sands at Helsby Quarry show the transition to a fluvial dominated environment. (e) Synthetic faults cut through a massive aeolian sequence at Grinshill. (f) Massive aeolian sequences transition to fluvial at Nesscliffe. (g) Deformation bands in heterolithic fluvial sheet flood beds of the Wilmslow Formation in the Holcroft Lane borehole. (h) Deformation bands in aeolian sandstones of the Frodsham Member of the Helsby Sandstone Formation in the Saughall Massie borehole.

[4.1.3.7. Abbey Arms Wood \(Grid ref: 356418 368133\)](#)

The Abbey Arms Wood borehole shows approximately 100m succession of the upper-most Wilmslow Sandstone Formation and the lowermost Helsby Sandstone Formation, recording a transition from an arid aeolian environment to a wet fluvial environment. The Wilmslow Sandstone Formation comprises a thick ~40m succession of fine-grained silty sandstones of aeolian sand sheet/sabkha origin, evident by irregular and wavy laminations of fine sand and silt deposited on a damp substrate. A change of environment is observed with an increase in grain size and poorer level of sorting, as well as the presence of cross-laminations, representing fluvial sheet flood deposits providing more heterogeneity in terms of lithologies, and bed thickness variations on the order of 1m – 2 m. The Helsby Sandstone is marked by an erosive base of medium- coarse-grained, poorly-sorted sandstones of fluvial channel facies interbedded with interdune mudstones. This succession displays a high degree of lithological heterogeneity with bed thicknesses of 1m – 2m.

4.1.3.8. Holcroft Lane (Grid ref: 367808 394482)

The Holcroft Lane borehole records approximately 35m of stratigraphy through older strata of the Chester Formation and the lower boundary of the Wilmslow Sandstone Formation. This records a transition from fluvial facies, with poorly-sorted, fine-grained sandstones with mud intraclasts, to fluvial sheet flood deposits characterised by poorly-sorted, laminated and heterolithic sandstones, into aeolian sabkha facies, similar to those observed in the Abbey Arms Wood borehole. Bed thicknesses are on the order of decimeters. Coarser grained lithofacies of the fluvial sheet flood association are affected by a minor fault characterised by cataclastic fault gouge, slickensides and slickenlines, with adjacent cataclastic deformation bands.

4.1.3.9. Woodlane (Grid ref: 354440 364860)

The Woodlane borehole records a short and incomplete 10m succession of the upper-most Frodsham Member of the Helsby Sandstone Formation. The member is characterised by a heterolithic succession of fine- coarse-grained, poorly sorted, silty sandstones of fluvial sheet flood origin, with beds on the scale of <1m.

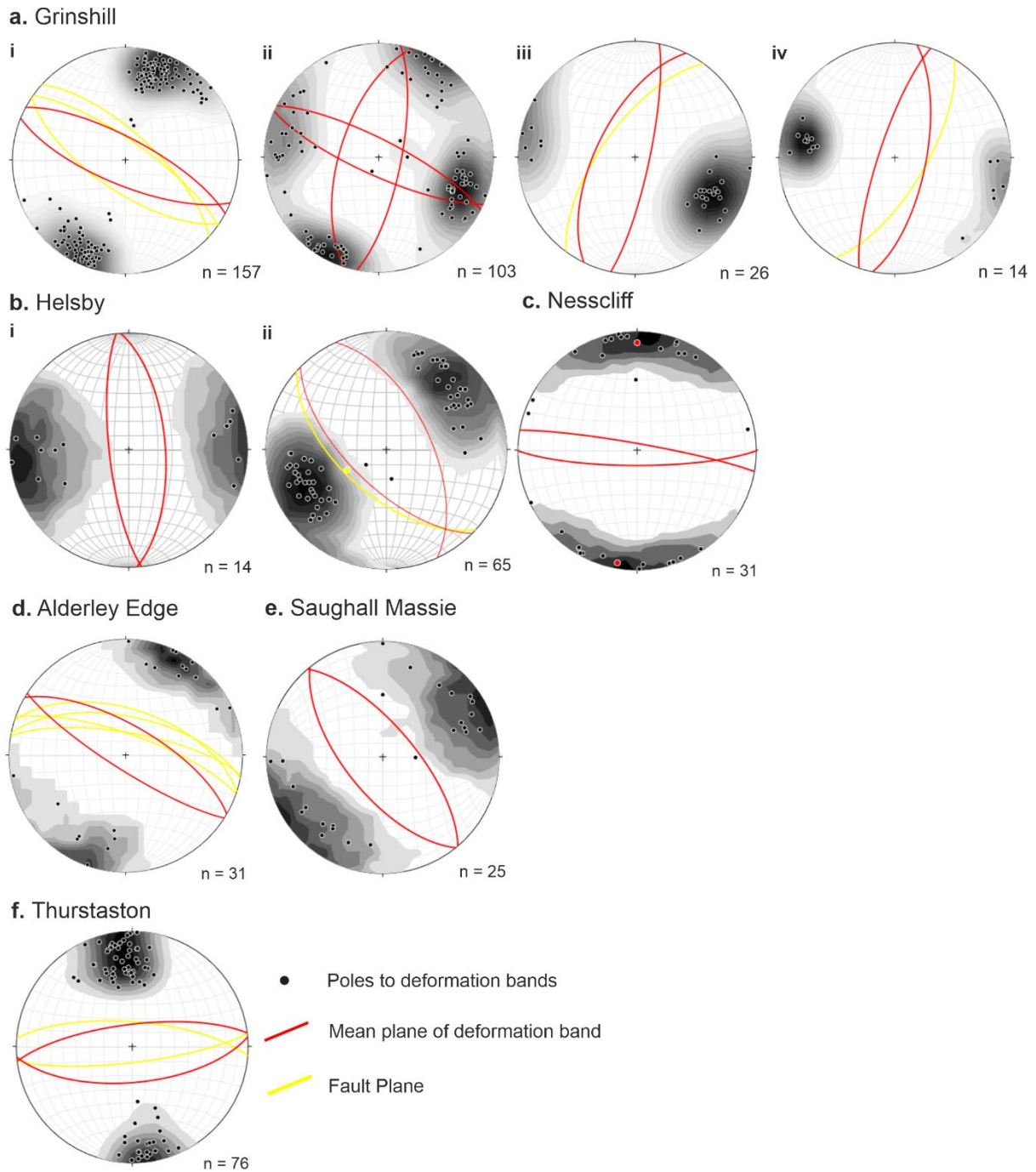
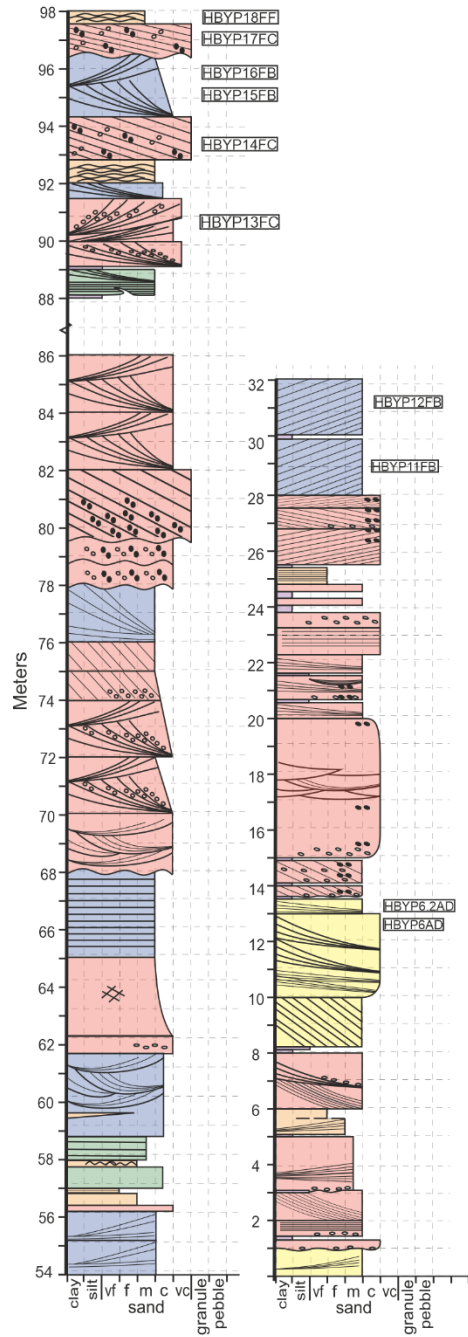
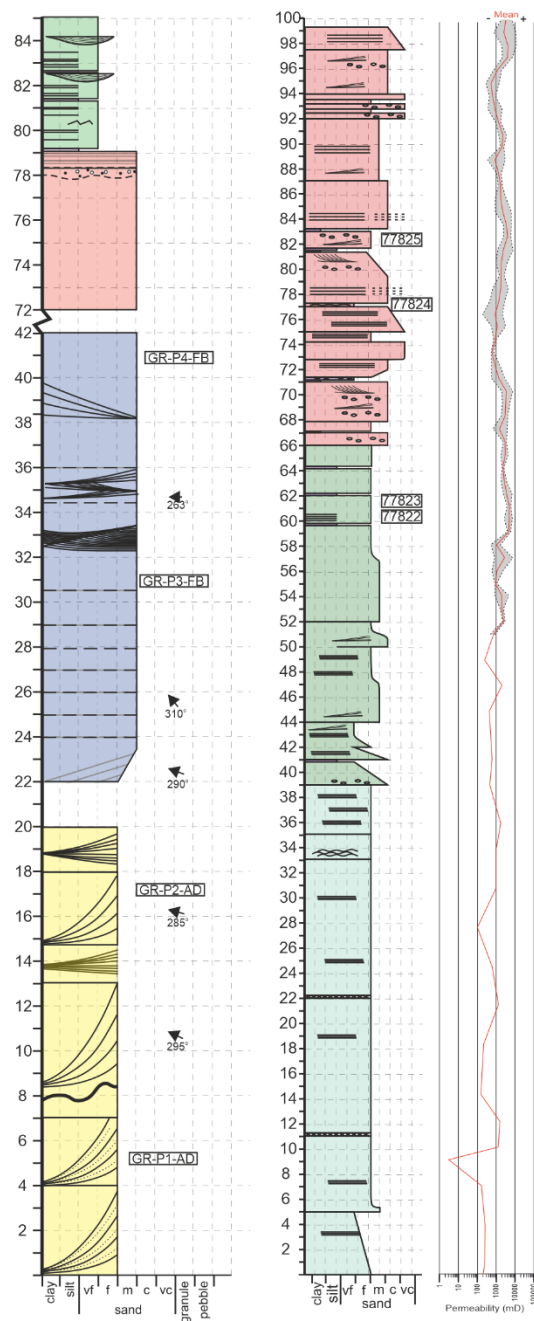


Figure 4.9. Equal area stereonet plots showing structural data for the localities across the Cheshire Basin study: (a) Grinshill. (b) Helsby. (c) Nesscliffe. (d) Alderley Edge. (e) Saughall Massie. (f) Thurstaston. Plots show poles to deformation bands with mean planes in red in relation to the principal fault planes in yellow.

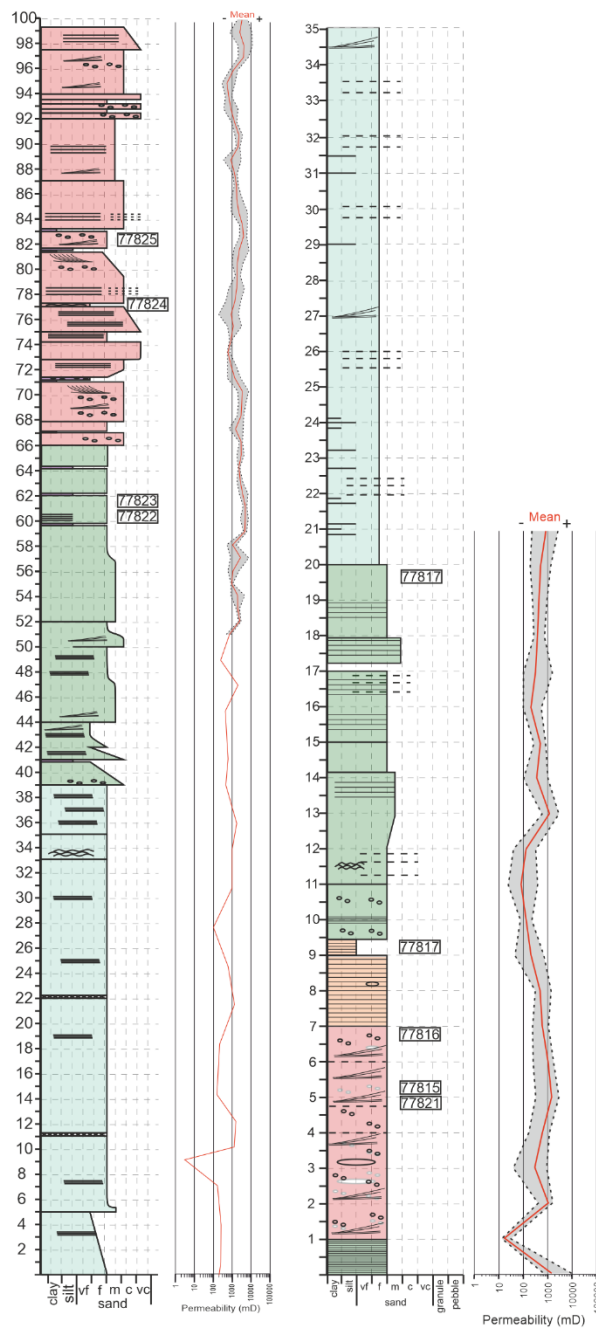
Helsby



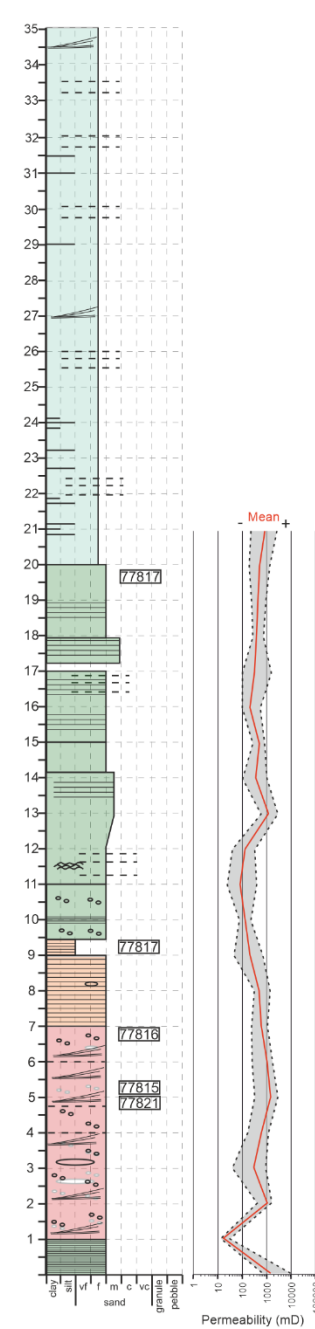
Grinshill



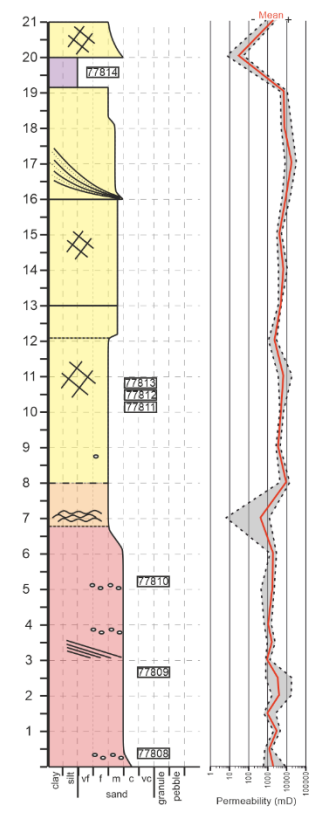
Abbey Arms Wood



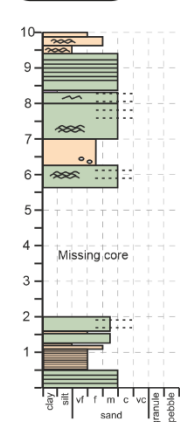
Holcroft Lane



Saughall Massie



Woodlane



Facies Association

- Aeolian dune
- Aeolian interdune
- Aeolian sand sheet/sabkha
- Fluvial bar
- Sheet flood
- Fluvial Overbank
- Fluvial Channel

- Trough cross bedding
- Massive Bedding
- Low angle planar laminations
- Wavy laminations
- Channel
- Pebbles
- clay rip up clasts
- Low angle cross bedding
- Asymptotic high cross bedding - Grain fall/flow

Figure 4.10. Sedimentary logs of outcrop and core localities coloured by facies association. Permeability logs are shown adjacent to core logs.

4.2. Facies Associations

A high degree of facies variability is observed across the Cheshire Basin localities, with many different scales and degrees of heterogeneity, recording both regional and local trends in depositional environment. A total of seven facies associations are identified; aeolian dune, aeolian interdune, aeolian sabkha, fluvial sheet flood, fluvial channel, fluvial bar forms and fluvial overbank. 38 samples of these facies were taken for petrographic analysis which are summarised in table 2 with lithology descriptions and bed thickness scales for each facies. The seven facies associations identified each present characteristic textural, compositional, and petrophysical characteristics. Representative examples of each of the facies associations are shown by optical photomicrographs in figure 4.11. Identification of facies associations is made difficult in core, less so in outcrop, due to the interbedded nature of both competing aeolian and fluvial systems, and therefore reworking of aeolian sediments within fluvial systems. Beds of both aeolian and fluvial facies are typically red in colour by grain coating iron-oxide cements formed during or soon after deposition under oxidising redox conditions.

ID	Facies	Porosity (%)	Grain size (µm)	Sorting (Phi)				Permeability (mD) (measured)	Permeability (mD) (Berg)	Permeability (mD) (Krumbein)	Permeability (mD) (Van Baaren)
					Quartz	k-feldspar	Lithics				
HBY-P14-FC	Chl	21.2	636	0.918	90	10	trace	4487	29000	50615	1234
HBY-P15-FB	CHb	14.3	400	0.475	87	9.9	3	9351	3339	2246	77
HBY-P16-FC	CHb	15.5	266	0.53	94	5	1	6720	2370	556	46
HBY-P17-FC	CHI	19.3	375	0.686	89	8	3	24525	27738	5200	303
HBY-P18-FF	FF	21.7	274	0.443	92.9	6.1	1	4148	11765	517	348
TH-AI	AI	10	170	0.5	83	11	7	-	3197	-	-
TH-AD	AD	26	537	0.4	96	4	trace	-	24194	-	-
GR-P1-AD	AD	19.2	189	0.391	97	3	0	1069	2358	102	85
GR-P2-AD	AD	23	206	0.408	97	3	0	6949	7611	144	270
GR-P3-FF	FF	10.9	188	0.465	85	10	5	906	188	145	4
GR-P3-FB2	CHb	17.8	174	0.43	90	7	3	906	1772	86	48
GR-P4-FB	CHb	18.3	210	0.559	85	15	trace	891	4201	297	71
HBY-P6.2-AD	AD	22.9	422	0.463	98	1	1	35039	42803	2740	1184
HBY-P6-AD	AD	21.1	348	0.534	96	3	1	35039	21514	1647	424
HBY-P11-FB	CHb	20.08	291	0.487	95	5	0	22837	11224	708	257
HBY-P12-FB	CHb	19.7	218	0.701	96	3	1	7309	11340	431	115
HBY-P13-FC	CHI	18.65	350	0.609	92	5	3	2169	17022	2086	219
77819.Hol.109m	FS	13.49	130	0.541	80	10	10	433	318	63	5
77816.Hol.144.1m	CHb	22	202	0.481	88	5	7	1452	7435	157	204
77813.Sau 127.3m	AD	24.6	258	0.326	96	3	<1	5775	12474	203	838
SM G1519	AD	23.44	230	0.474	95	3	2	30990	14512	271	373
SM G1519.2	AD	24.4	230	0.474	97	2	1	13842	17809	271	464
Nesscliffe 001	AD	23.8	238	-	97	3	0	-	-	-	-
77825.Abbey 28m	AI	6.94	81	0.479	60	10	30	508	3	5	0
77824.Abbey 39.4m	AS	18.1	217	0.905	92	3	5	2377	11847	1148	72
77822.Abbey 54.4m	FS	17.4	166	0.546	85	5	10	2659	1853	100	34
77823.Abbey 54.4m	FS	16.3	166	0.546	80	10	10	2247	1328	100	24
77817.Hol 135.6m	AI	8.3	95	0.639	65	15	20	323	21	21	0
77826.Hol 142m	CHI	19.7	221	0.647	85	10	5	133	10170	376	118
77815.Hol 145.4m	CHI	19.5	238	0.52	89	3	8	605	7809	338	129
77821.Hol 145.6m	CHI	15.64	210	0.594	85	5	10	482	2063	244	30
77814.SM 123.6m	As	8.62	130	0.569	82	10	8	20	39	4439	0
77809.SM 138.3m	FS	6.5	171	0.538	85	5	10	192	15	113	0
77808.SM 150m	CHI	20.2	267	0.569	94	5	1	2928	12131	596	197
SM G1517	FS	21.1	227	0.633	94	5	1	7471	7471	422	104
SM G1518	CHI	17.9	146	0.495	90	5	5	407	407	79	10
SM G1520	AD	18.96	208	0.62	97	2	<1	2215	2215	265	30
SM G1521	AI	14.4	176	0.456	92	5	3	74	74	101	1

Table 2. Samples of undeformed host facies and their properties.

4.2.1. Aeolian Dune

Aeolian dune facies record grainfall-grainflow laminations of dune foresets, of fine- coarse grained, very well- sub-rounded, predominantly quartz clasts with minor amounts of feldspar. (Fig. 4.11a). The highest porosity units are aeolian dune facies, with values on average 22% and as high as 26% (Fig. 4.11a). Compositionally, all aeolian dune facies are classified as quartz arenites, with in excess of 90% quartz, <5% of feldspar and lithic grains (Fig. 4.12b). Results of permeability measurements using the handheld mini-permeameter are presented In a box and whisker plot showing the variability in permeability for each lithofacies (Fig. 4.12a). Aeolian dune facies record mean permeability of 9500md, with a large range with as low as 1000md to as high as 18000md.

4.2.2. Aeolian Sand sheet

Aeolian sand sheet facies are characterised by very well-sorted and rounded grains, that are often bi-modal in grain-size with laminations of both fine and coarse-grained clasts (Fig 4.11c). Both aeolian and fluvial sheet facies show much more variability in porosity owed to their heterolithic laminae and mixture of both aeolian and fluvial sediment sources and bi-modal grain size distributions, with average porosity values of 15% (Fig. 4.11c & e). Aeolian sand sheets classify as quartz arenites to subarkose sandstones, with >82% quartz, up to 10% feldspar and lithic grains (Fig. 4.12b). Permeability values for aeolian sheet facies are low, with a mean of 500md.

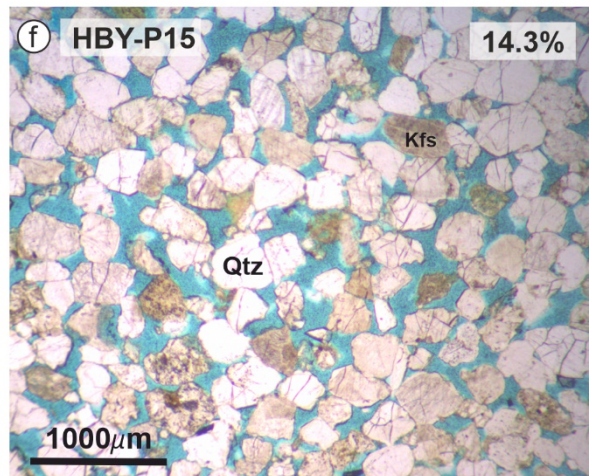
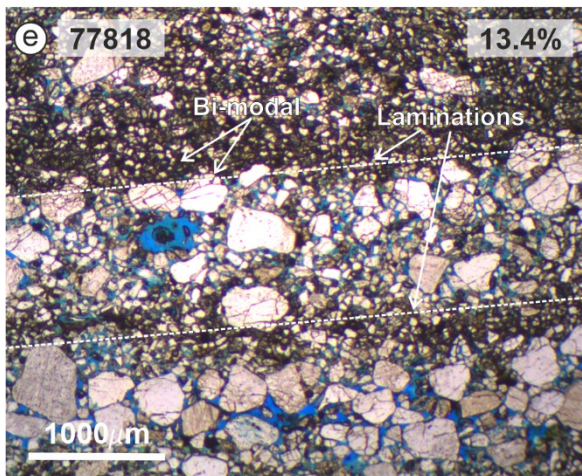
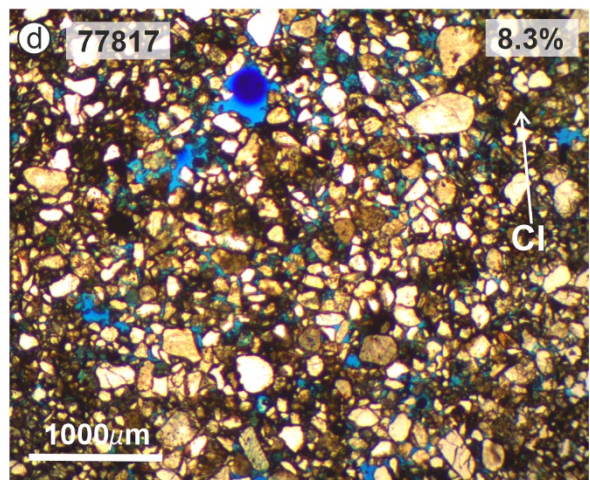
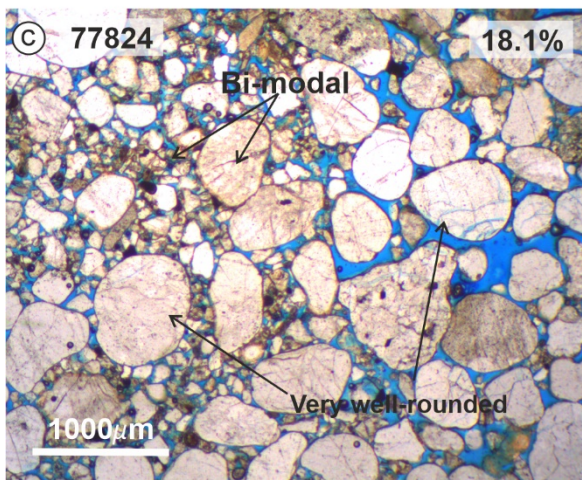
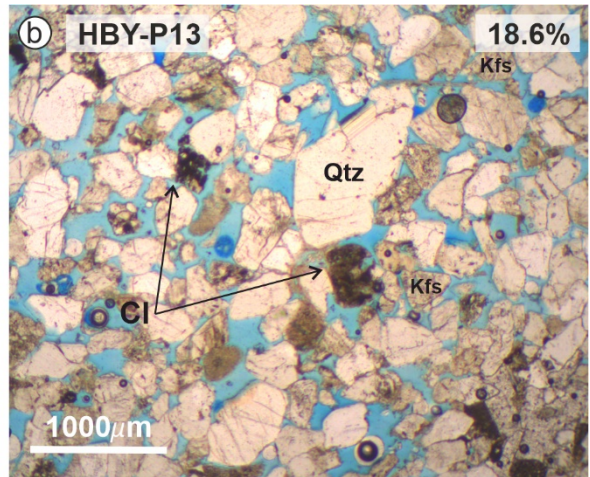
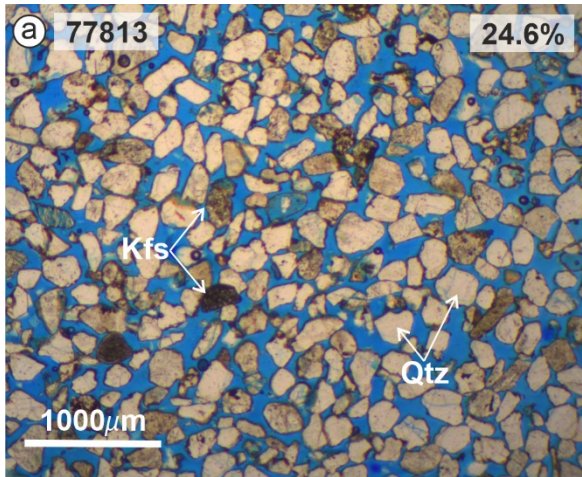


Figure 4.11. Optical photomicrographs of examples of six facies associations. Refer to logs (Fig 4.10) for sample locations. (a) Aeolian dune facies from the Saughall Massie borehole. Well-sorted, sub-rounded clasts of quartz and minor amounts of feldspar. (b) Fluvial channel facies from Helsby. Poorly-sorted, angular clasts of quartz, feldspar and minor clays. (c) Aeolian sand sheet from the Abbey Arms Wood borehole. Bi-modal grain-size distribution of very well-rounded coarse clasts and sub-rounded fine clasts. (d) Interdune/overbank facies from the Holcroft Lane borehole. Fine-grained, moderately-sorted grains in a muddy-silty matrix. (e) Fluvial sheet facies from the Holcroft Lane borehole. Bi-modal grain-size distribution with laminations of large, sub-angular grains, and fine-grained muddy clasts. (f) Fluvial bar form facies from Helsby. Moderately well-sorted, sub-angular, medium-grained quartz arenite.

4.2.3. Aeolian Interdune/Overbank

Aeolian interdune and fluvial overbank facies record very similar lithologies, characterised by mudstones, fine-grained 'dirty' sandstones bound by clays and silts (Fig. 4.11d) and finer grained rippled sandstones, with composition varying from subarkose to litharenite in those with greater mud content (Fig. 4.12b). Lower porosity hosts are generally of aeolian interdune and fluvial overbank facies, with average porosity of 9.5 %, due to fine-grained and poorly-sorted sediments. Mean permeability for both associations is approximately 800md.

4.2.4. Fluvial Sheet Flood

Fluvial sheet flood deposits are characterised by heterolithic laminations of fine-grained and coarse-grained, moderate to poorly-sorted, sub-rounded to angular sandstones (Fig. 4.11e). that range from quartz arenites, subarkose and sublitharenite composition (Fig. 4.12b). A mean porosity of 14% is recorded, and a mean permeability of 1900 md (Fig. 4.12a).

4.2.5. Fluvial Channel facies

Fluvial channel facies are characterised by medium- coarse-grained, sub-angular to angular, moderate- poorly-sorted sandstones. Channels are often identified by basal lag comprising of pebbles and clay rip up clasts. Clay grains and grain coatings are also abundant, ranging from 3-10%, and with quartz in excess of 85% and up to 10%, classify from quartz arenite to sub-litharenites (Fig 4.11b & Fig. 4.12b). Both fluvial bar and channel facies show slightly lower porosities than aeolian facies due to more immature grain textures, with average porosity values of 18% (Fig 4.6b), and mean permeability of 2100 md (Fig. 4.12a).

4.2.6. Fluvial Barforms

Fluvial bar-forms are identified by lateral accretion of bedforms, of moderately sorted, fine-medium-grained sandstones that are compositionally more mature than channel deposits

(Fig. 4.11f), ranging from quartz arenite to sub-arkose composition (Fig. 4.12b). Porosity values are high with a mean of 18%, and a high mean permeability of 11000md, with a large range of variability (Fig. 4.12a).

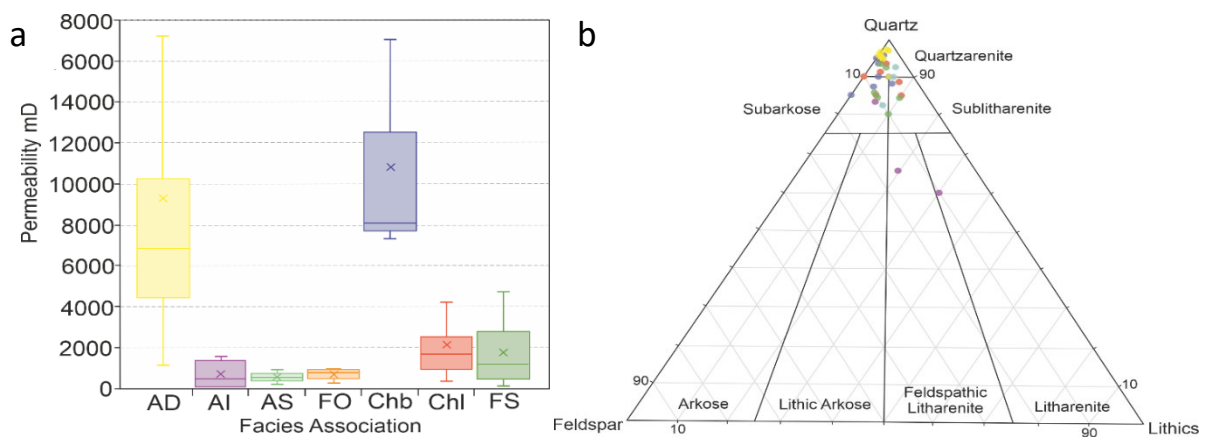


Figure 4.12. (a) Box and whisker plot of permeability by facies association. (b) Ternary diagram showing the abundance of quartz, feldspar and lithic grains for the lithofacies sampled, coloured by facies association.

Facies Association	Lithofacies description	Bed Thickness (m)
<u>AD - Aeolian Dune</u>	High porosity, Medium- coarse-grained quartz arenites. Well sorted. Rounded and frosted grain texture. Cross bedded. High density DBs	0.5 - 20 m Avg: 4 m
<u>AS - Aeolian Sand sheet/sabkha</u>	Silty fine- medium-grained sandstones. Mature, frosted rounded grains. Moderately - Poor sorted. Lack of high angle Aeolian crossbedding. Salt laminations. Parallel – irregular silty laminations.	1 - 15 m Avg: 7 m
<u>AI - Aeolian interdune</u>	Thin beds of mud-silt. Fine parallel or wavy laminations.	< 1 m Avg: 0.28 m
<u>FB - Fluvial bar</u>	Moderately-sorted, Medium- coarse-grained sandstones. Cross bedded.	2 - 20 m Avg: 4.5 m
<u>FS - Fluvial sheet flood</u>	Thin beds of Fine- coarse-grained silty sandstones. Mix of clean reworked Aeolian sediment and less mature fluvial sediment. Occasional basal lag of clay rip-up clasts. Planar, low angle and ripple laminations with wide variations in grain size.	0.5 – 4 m Avg: 2 m
<u>FC - Fluvial channel fill</u>	Moderate-high porosity, poorly-sorted, fine-coarse-grained. Often graded with pebble and clay lag. Clay intraclasts often aligned along cross bed laminations.	0.5 – 7 m Avg: 2.5 m
<u>FO – Fluvial Overbank</u>	Low porosity, Moderately-sorted. clay-siltstones. Wave and planar ripple laminations and organic material such as rootlets.	< 1 m Avg: 0.5 m

Table 3. Facies associations, lithofacies descriptions and approximate bed thickness in the Cheshire Basin.

4.3. Porosity – permeability relationship

Calculations of permeability were made using equations 1, 2 and 3 covered in section 3.3. Results show when compared to permeability data measured with the handheld mini-permeameter, there is a strong correlation between estimation of permeability using the Berg method, equation 2 and the measured results (Supplementary material fig. 1). Permeability calculated using equations 1 and 3 show very little correlation with measured results, significantly underestimating permeability. Therefore, equation 2 will be used to estimate permeability of deformation bands in future analysis. Results of porosity measurements from thin section image analysis are plotted with permeability measurements both in the field using the mini permeameter, and calculated using the Berg equation (Fig. 4.13). Both trends show a power law relationship. The trend of calculated values shows a rapid decline in permeability for porosities of <10%. Data from the Abbey Arms Wood borehole, sampled from the Wilmslow and Helsby sandstone using a similar handheld mini permeameter, is included for comparison. This data shows a similar power law trend to our measured values, with an exponent of 3.7, however one magnitude lower permeabilities.

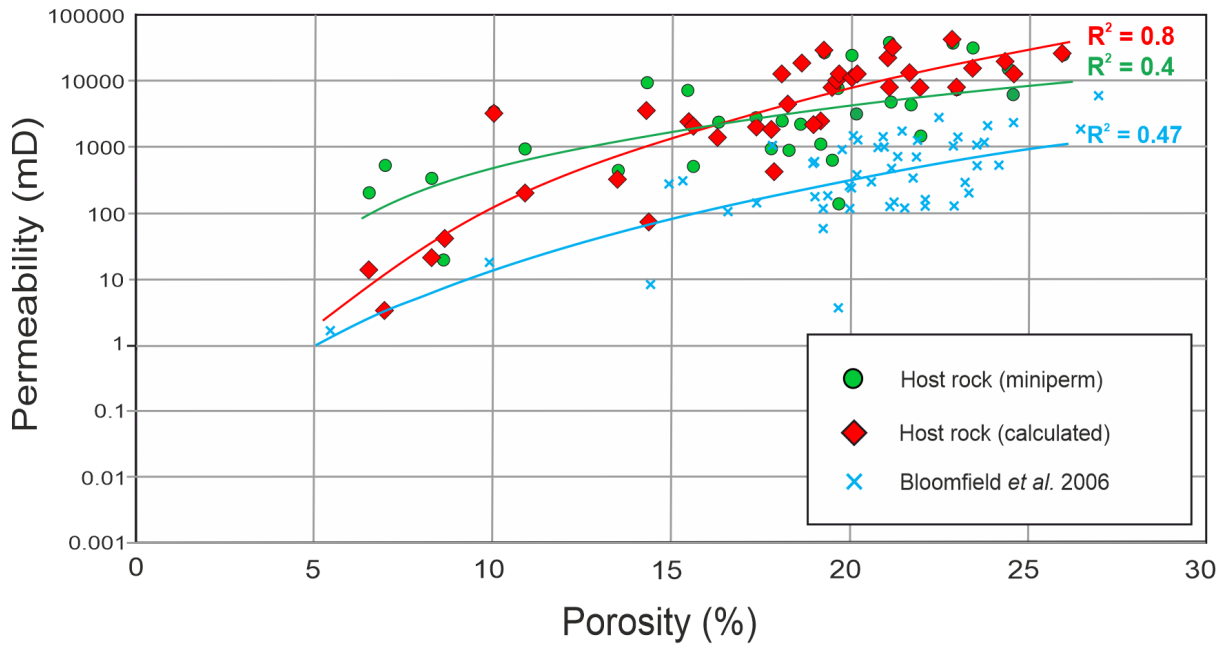


Figure 4.13. Porosity versus permeability for undeformed samples of the upper Sherwood Sandstone. Both measured permeability shown in green, and calculated permeability in red, show a power law relationship. Data from the Abbey Arms Wood borehole, obtained using mini permeameter are shown for comparison (Bloomfield et al., 2006)

4.4. Case Study 2 - Devonian Old Red Sandstone, Pease Bay, Scotland

The study location is situated in Pease Bay of SE Scotland, and lies 2.5 km west of Siccar Point, the famous site of Hutton's Unconformity, and provides up to 80m of coastal outcrop of fluvial–aeolian sandstones, siltstones and mudstones of the late-Devonian aged Old Red Sandstone (ORS) (Fig. 4.14). The ORS of Scotland was deposited from approximately 400Ma to 330Ma in the Orcadian Basin that extends offshore from the Moray Firth of Scotland to the Shetland Islands in the north and Norway in the east, the Midland Valley of Scotland, and the Central North Sea High, and is up to 4 km thick at its depocentre. The ORS is broadly divided into Lower, Middle and Upper Groups according to the dominant facies, conglomeratic, lacustrine, and aeolian-fluvial respectively (Browne et al., 2002) . The upper aeolian-fluvial sandstones prove to be large and economical reservoirs, as evident in the Clair Field, West of Shetland, the largest hydrocarbon reserve on the UKCS (Trewin, 1989; Forbes, 1993; Mark et al., 2008).

4.4.1 Stratigraphy of Pease Bay

The Upper ORS is the main focus of this study, and is exposed onshore along the periphery of the Orcadian Basin and the Midland Valley, along much of the coast of East Lothian, Scotland, from Siccar Point in the south, along the borders of the Moray Firth, to the Shetland Islands in the north. The group can be divided into three formations; the Devonian Greenheugh Sandstone and Redheugh Mudstone Formations, and part of the Carboniferous Kinnesswood Formation (Browne et al., 1999; Browne et al., 2002). Both the Devonian Greenheugh Sandstone Formation and a small part of the Carboniferous Kinnesswood Formation outcrop at Pease Bay (Fig. 4.14). The Greenheugh Sandstone Formation comprises red-brown, medium- to coarse-grained sandstones of both aeolian and fluvial origin, with subordinate

mudstones and siltstones. The Kinnesswood Sandstone Formation shows similar facies to that of the Greenheugh, and is differentiated by the occurrence of pedogenic carbonate horizons and nodules locally known as 'cornstone' (Andrews and Nabi, 1994). Strata young northwards where they are displaced in a normal sense by the ENE-trending Cove Faults that are considered part of the Southern Uplands Fault System. Historical accounts of deformation bands in the ORS use outcrop examples from Orkney and the Moray Firth, and have focused largely on their sealing or conduit capability in relation to the timing of maturity of the source rocks, where it is believed that bands pre-date hydrocarbon generation and acted as barriers to the hydrocarbon charge of stratigraphically higher reservoirs (Hippler, 1993; Parnell et al., 2004; Farrell et al., 2014). In Pease Bay, a number of outcrops display intense deformation associated with faulting, with some also displaying localised fault planes with relatively small displacements of strata of less than a couple of metres, and provide the basis of this study.

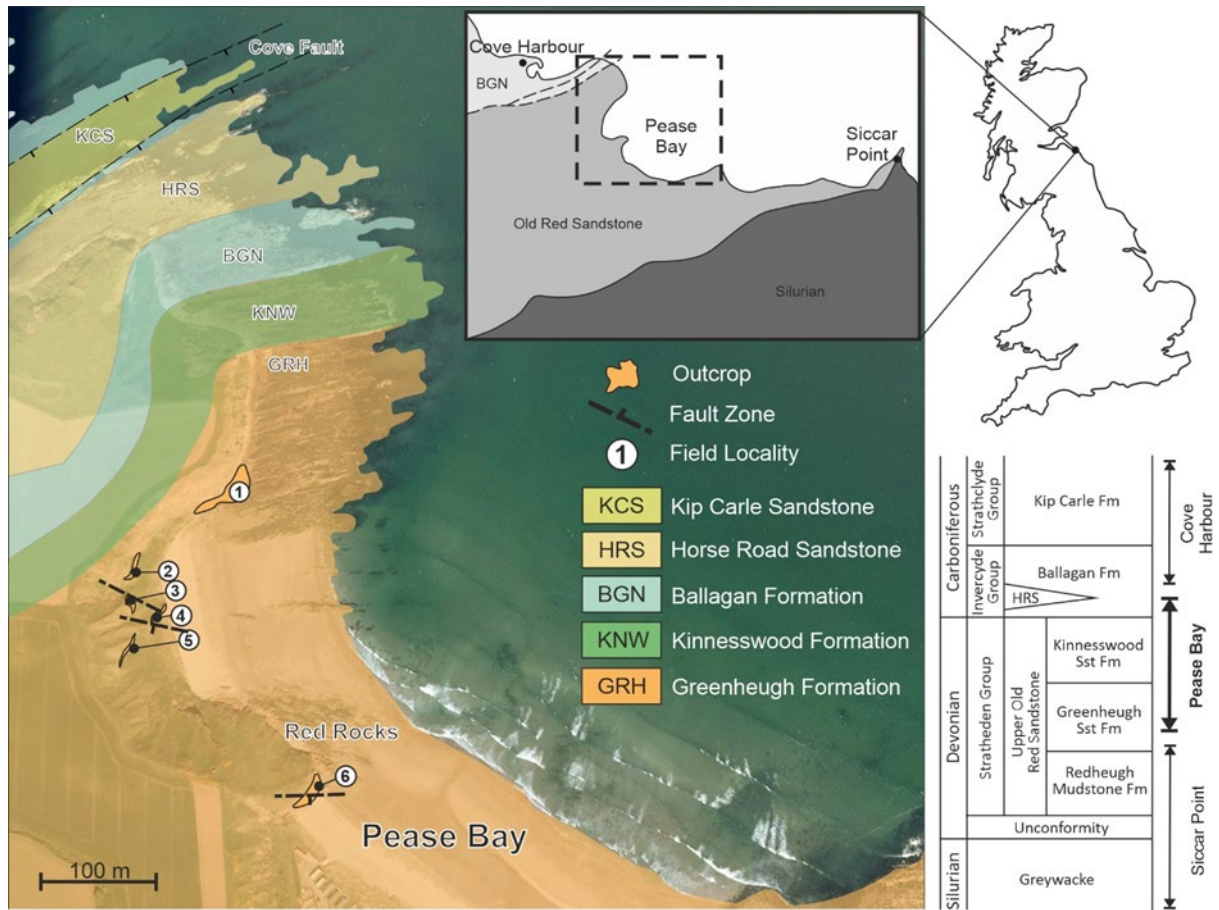


Figure 4.14. Location and geological map of the study area including mapped localities and stratigraphy of the local area.

4.4.2. Localities

Beds of the Greenheugh Sandstone Formation crop out at both ends of Pease Bay as well as at Red Rocks, in cliff sections exposed at low tide. They comprise interbedded mudstones, siltstones, and sandstones of aeolian and fluvial origin, which dip approximately 20° to the north-north-east. They are also exposed in the steep headland north of the bay in small outcrops to which access is limited. Several fault zones, with both observable and inferred faults, are identified across the bay and provide the localities on which the study is based (Fig. 4.14).

4.4.2.1 Fault Damage Zone 1 (FDZ1)

At Locality 2 (Grid Ref: 378943 671293; Fig. 4.14) a major fault is observed by an intense zone of deformation indicated by cataclastic rock textures. Bedding and other sedimentary structures such as laminae are destroyed by the intense deformation. There is evidence of diagenetic alteration with a distinct change in colour of the sediments from an oxidised red, to a bleached beige colour. A fault is not directly observed. It is inferred that faulting follows the regional trend of the extensional faulting further north at Cove Bay (Fig. 4.14) and this fault zone downthrows to the south. More distal continuation of this fault damage zone is observed at Locality 3.

4.4.2.2 Fault Damage Zone 2 (FDZ2)

Locality 3 (Grid Ref: 378940 671269; Fig. 4.14) displays intense localised deformation with a complex and dense network of deformation bands and band clusters (Fig. 4.15b). Bands show a conjugate geometry with a mean angle of intersection of 48.9°, dipping at high angles both north and south with a mean strike of 82° (Fig. 4.16a). The outcrop displays possible fault-controlled fluid flow with similar bleaching and diagenetic alteration observed at Locality 2

on one side of a cluster of deformation bands, with red oxidation preserved on the other side of the cluster. Most pre-existing sedimentary structures in this damage zone are destroyed, with only thin millimetre scale laminations showing offsets by deformation bands and minor slip surfaces.

4.4.2.3 Fault Damage Zone 3 (FDZ3)

A minor fault at Locality 4 (Grid Ref: 378960 671246; Fig. 4.14) is evidenced by a cataclastic fault core of approximately 30cm width, comprised of a dense cluster of cataclastic deformation bands with strike and dip of $087^{\circ}/54^{\circ}$ S (Fig. 4.16b). Only the footwall damage zone is exposed here, and therefore there is no marker for determining displacement. Deformation bands have a mean strike and dip of $099^{\circ}/47^{\circ}$ S (Fig. 4.15c). Logs show a similar facies trend to that of Locality 1, with texturally and mineralogically clean, medium grained, cross-bedded sandstones of aeolian origin, incised by texturally immature, coarse-grained fluvial sandstones (Fig. 4.17). Fault damage zone density transects are recorded in four units of fluvial facies association (FA3 and FA4); 1) a poorly-sorted, medium-grained, trough cross-bedded sandstone (1m thick), 2) a thin mudstone horizon (15cm thick), 3) a laminated fine-grained sandstone (30cm thick), and 4) a medium-grained cross-bedded sandstone (60cm thick) (Fig. 4.15c).

4.4.2.4 Fault Damage Zone 4 (FDZ4)

At Locality 5 (Grid Ref: 378939 671218; Fig. 4.14) ~6m thick beds of clean and texturally mature, fine- to medium-grained sandstones of aeolian dune facies association (FA1), display an extensive ~25m fault damage zone, containing deformation bands and minor slip surfaces (Fig. 4.15d), that match the structural trends of localities 3 and 4. Deformation bands have a conjugate geometry with an intersection angle of 50° , with a mean strike of 085° (Fig. 4.16c). It is unlikely this damage zone is related to the small fault observed at Locality 4 due to the

low levels of deformation there, as this would suggest an unrealistically high level of asymmetry between footwall and hangingwall damage. The damage zone is therefore inferred to be a more distal representation of the damage seen at Locality 3 in the hangingwall of the major fault zone.

4.4.2.5 Fault Damage Zone 5 (FDZ5)

At Locality 6, locally known as Red Rocks (Grid Ref: 379111 671082; Fig. 4.14), a ~30m thick cliff section exposes damage zones of minor faults (<2m displacement) within mixed sequences of mudstones and sandstones (Fig. 4.15f). This sequence displays a high degree of lithofacies variation, with well-sorted, fine-grained, trough cross-bedded sandstones of aeolian origin at its base, incised by erosional poorly-sorted, coarse-grained fluvial sandstones with pebble lags. These are followed by a relatively thick succession of laminated mudstones interbedded with fine- to medium-grained sandstones of fluvial overbank and floodplain association (Fig. 4.17). A fault damage zone is observed in a small sequence of mudstones and sandstones in the footwall of a minor fault with ~1.5m displacement and strike and dip of 096°/66° S. Deformation bands within the sandstones, and fractures within mudstones are the main damage zone elements and display a conjugate geometry to the main fault plane, with an intersecting angle of 58°, and mean strike of 087° dipping both north and south at low angles to the main fault (Fig. 4.16d). Two antithetic slip surfaces also occur within the damage zone dipping steeply to the north, showing 7cm and 18cm offsets of mudstone laminations (Fig. 4.15e). These slip surfaces occur as single fractures within the thick mudstone unit, and as deformation bands in the underlying sandstones. Fault damage zone density transects are recorded in three units; 1) a laminated mudstone (1.22m thick), 2) a fine-grained laminated sandstone (30cm thick), 3) a medium-grained, trough cross-bedded sandstone (25cm thick).

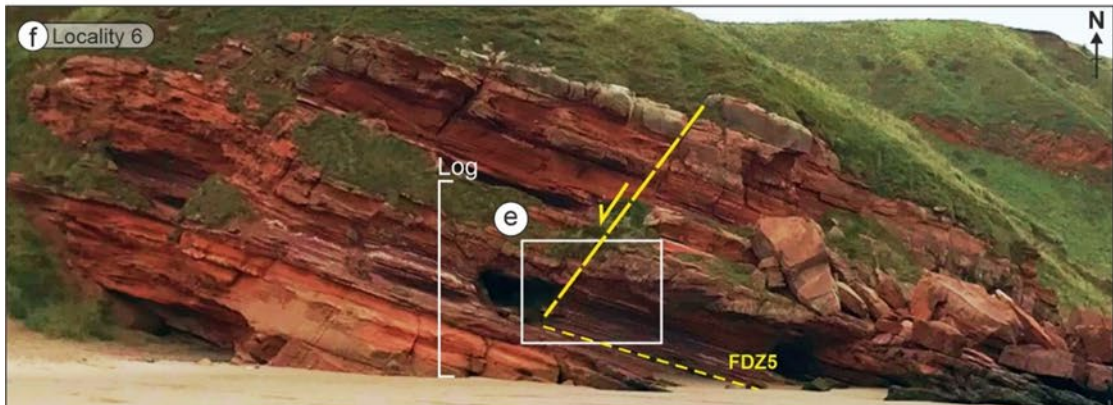
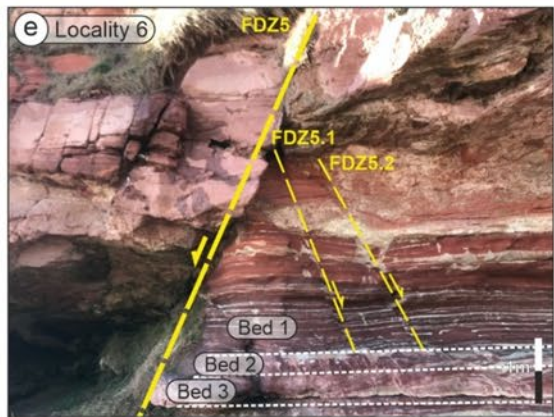
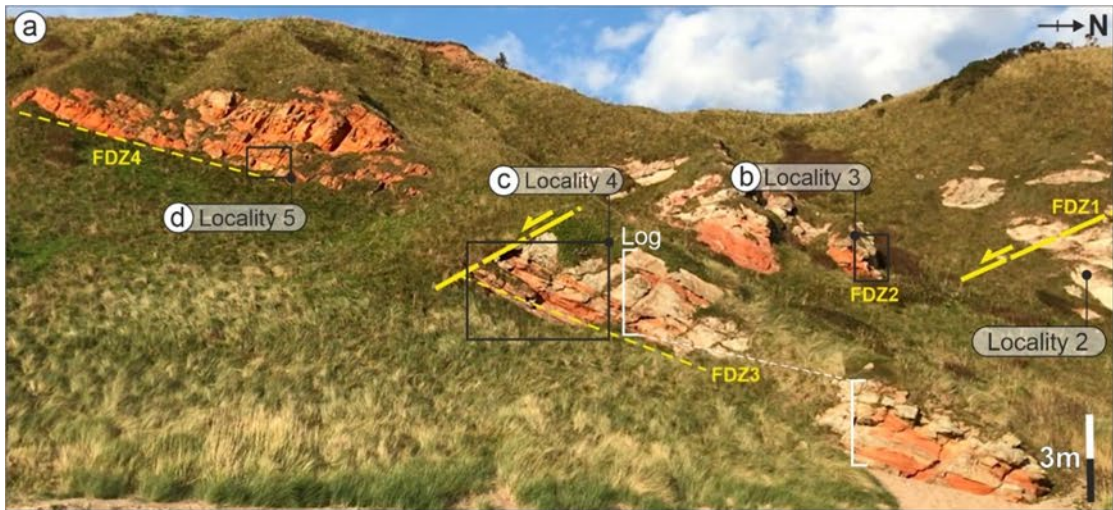


Figure 4.15. (a) Outcrops in the hillside of Pease Bay showing localities and major faults and fault damage zones. (b) Locality 3 displays a highly deformed and complex zone of deformation bands associated with an inferred fault to the north toward locality 2. (c) A fault displaces a small succession of fluvial sandstones of varying grain sizes as well as a minor mudstone horizon. Deformation band density and thickness are recorded for each of the beds. (d) Locality 5 displays a 25m damage zone of deformation bands within aeolian beds. (e) Fault zone at locality 6 in which a sequence of mudstones and small channel sandstones are displaced by a fault with approx. 1.5m throw, and a pair of antithetic faults with displacements of 7 and 18cm. Damage zone density is measured in the three beds indicated. (f) Locality 6, Red Rocks, displays faulted beds of aeolian and fluvial facies mudstones and sandstones dipping shallowly to the north-east.

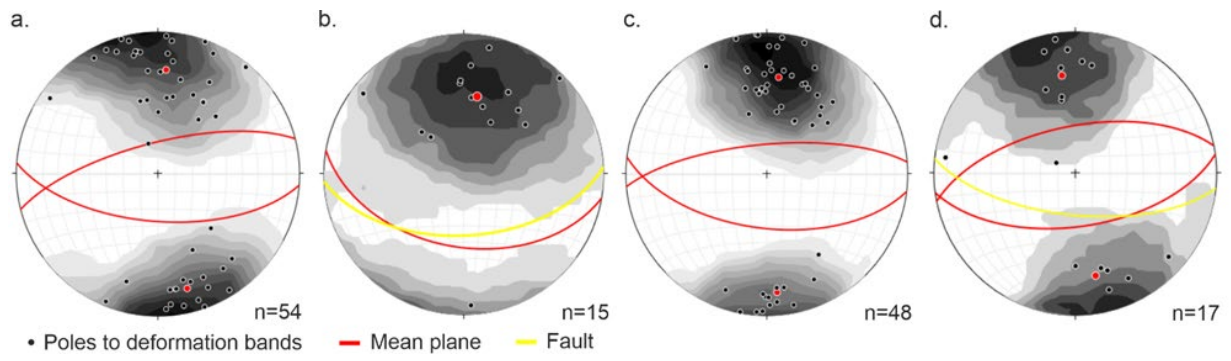


Figure 4.16. Equal area stereonet plots of deformation bands and faults for (a) Locality 3, (b) Locality 4, (c) Locality 5, and (d) Locality 6. The same structural trend is observed across the bay, with east-west trending faults and conjugate sets of deformation bands at low angle to the faults with an intersection of 45-50°.

4.4.3. Undeformed Lithofacies and Facies Associations

Sedimentary logs were taken at localities 1, 4 and 6, describing lithofacies variation through a combined total of ~28.5 m (Fig. 4.17). Logs record beds of the Greenheugh Formation, with beds of both fluvial and aeolian, sandstone, siltstone and mudstone lithofacies, that offers more lithological heterogeneity and contrast over a thinner overall thickness than the stratigraphy of the Cheshire basin, and at smaller bed scales, with bed thicknesses of the order of 0.5m – 3 m. A total of four facies associations are identified at Pease Bay, aeolian dune, aeolian interdune, fluvial channel, and fluvial overbank and floodplain deposits. A summary of these lithofacies is provided in table 4.

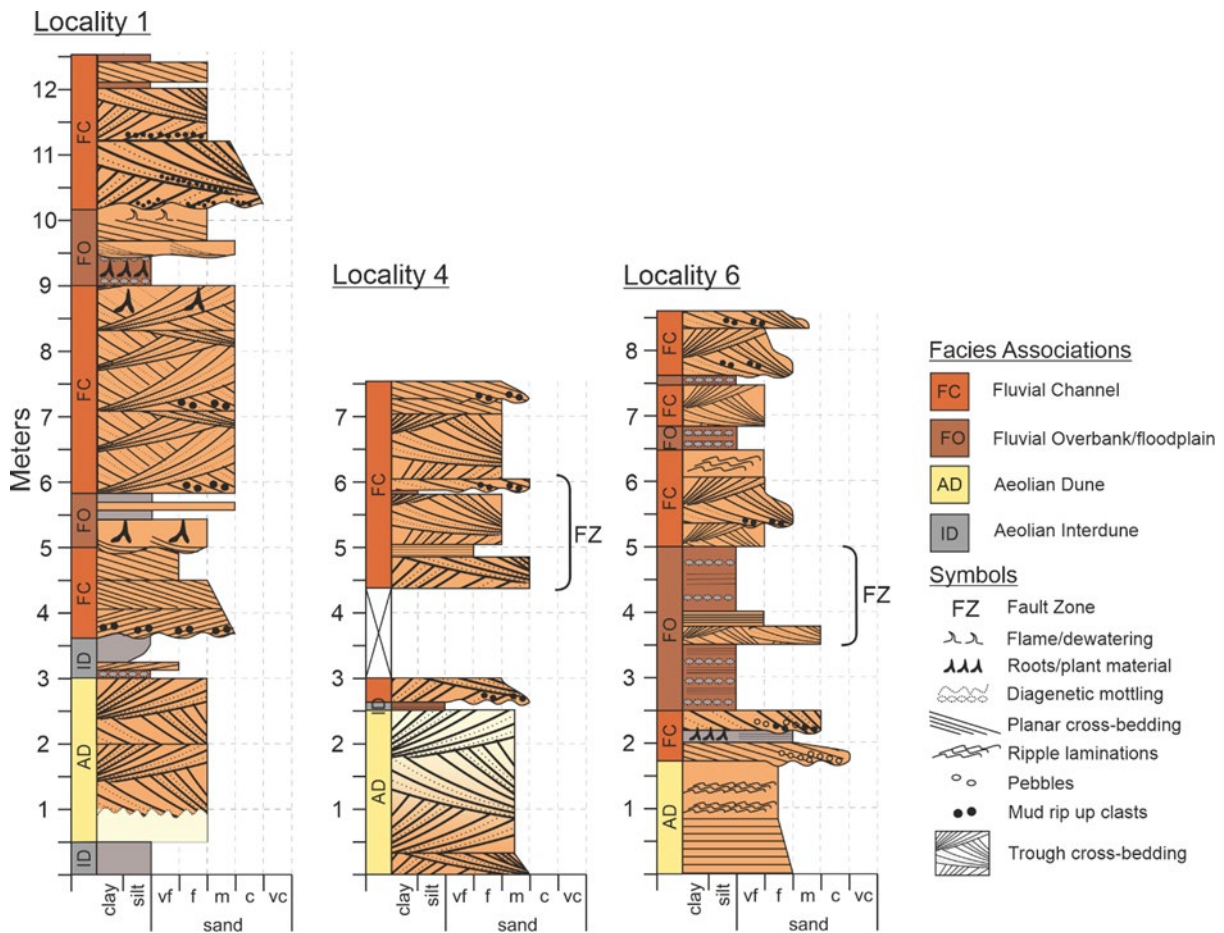


Figure 4.17. Sedimentary logs across Pease Bay recording lithofacies and facies association variation across three localities. Logs show the overall facies change within the Upper Devonian Greenheugh Formation. Recording a predominantly arid wind-blown environment to a humid fluvial environment.

	Facies Association	Lithofacies Description	Bed Thickness
1	Aeolian Dune	Yellow-orange, Fine- to medium-grained, well-sorted, trough and tabular cross-bedded sandstones.	2-3 m
2	Aeolian Interdune	Thin beds of mudstones, laminated siltstones and very fine-grained laminated sandstones, that succeed or interbed with aeolian dune facies.	0.1-0.5 m
3	Fluvial Channel	Red beds of tabular and trough cross-bedded, Fine- to coarse-grained, poorly sorted sandstones, with erosional bases containing both pebbles and mud rip-up clasts, often with entrained plant detritus.	0.5-3 m
4	Fluvial Overbank/Floodplain	Planar laminated and rippled mudstones containing rootlets and plant detritus, often interbedded with thin (<50cm) poorly sorted fine-grained sandstones containing mud and pebble clasts.	0.5-2.5 m

Table 4. Facies associations, descriptions and bed thicknesses at Pease Bay.

4.5. Conclusions

The lithofacies presented in both the Cheshire Basin and Pease Bay case studies provide sufficient facies variability for the purposes of studying the control of facies on deformation band development. Mixed aeolian-fluvial successions display complex facies interactions resulting in heterolithic sequences in terms of lithological properties, such as porosity, grain size and sorting. The Cheshire Basin localities display thick (up to 20m) sequences of predominantly sandstone lithologies with wide variations in textural and petrophysical properties. At Pease Bay, thinner beds and successions are observed (<3m), with more interbedded sequences of mudstones, siltstones and sandstones, offering additional insight into the role of bed thickness and mechanical stratigraphy. In terms of reservoir quality, aeolian dunes and fluvial barforms are the primary reservoir units, with high porosities of between 15% - 26%, and permeability of 1000md-35000md. Texturally, these units show a high degree of variation in terms of grain sorting, roundness and sphericity. Aeolian sediment is typically well rounded and spherical, whilst fluvial sands show less roundness and sphericity. Although there are distinctions between aeolian and fluvial sediment sources, many fluvial beds show reworking and mixing of sources, typical of a competing aeolian and fluvial environment (Cowan, 1993; Priddy and Clarke, 2020). Lower reservoir quality units are typically basal channel lag deposits with high clay intraclast contents, fluvial overbank mudstones and siltstones, and aeolian interdune mudstones and siltstones, with porosities of 6% - 10%, and permeabilities of less than 1000md. The Helsby and Wilmslow Sandstone Formations sampled show little mineralogical variability, which whilst a limitation of the study of lithological properties, aids in the determination of other lithological controls.

4.6. Supplementary material

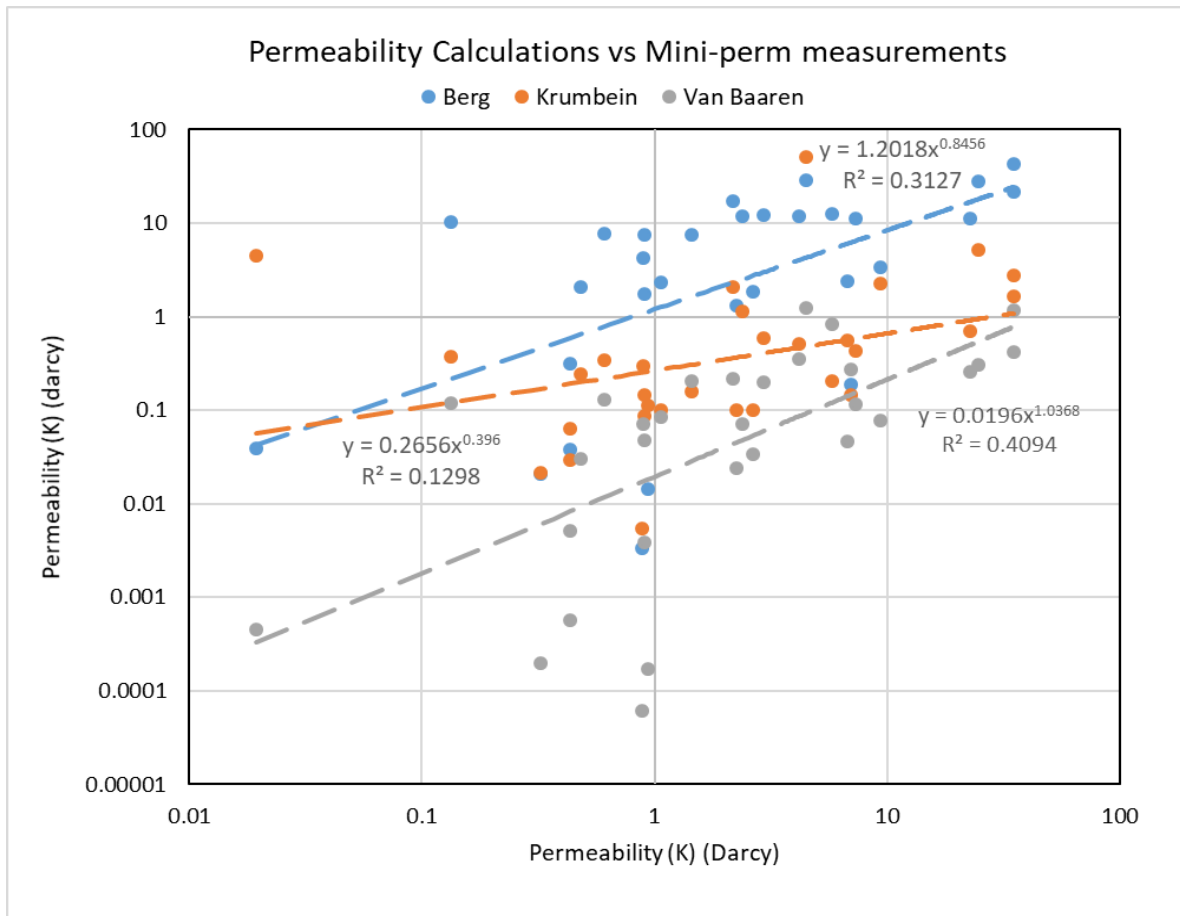


Figure 1. Three methods of permeability calculation versus measured permeability for undeformed lithofacies.

5. Microstructure and petrophysical properties of deformation bands.

As discussed in the introduction chapters, the microstructural and petrophysical properties of deformation bands are strongly controlled by the kinematics of their formation, and the mechanism/s by which they form (Fossen et al., 2007), which may be controlled by the physical properties of the undeformed host rock, such as grain size, porosity, sorting and composition (Fossen and Bale, 2007; Ballas et al., 2015; Griffiths et al., 2016; Fossen et al., 2018). In this chapter results of petrographic analysis to examine the microstructure and petrophysical properties of the bands in relation to lithofacies are presented.

5.1. Deformation band properties

Deformation bands across the localities display very different morphologies, indicating differences in their kinematics and deformation mechanisms. Cataclastic deformation bands are recorded across all of the localities. Cataclastic bands display a resistance to weathering, standing proud of the rock face, indicative of grain size reduction, reduced porosity and cementation relative to the host material (Fig. 5.1a & c). Cataclastic bands are found within a wide range of lithofacies from fine- to coarse-grained aeolian and fluvial facies. Examples of cataclastic deformation bands also show displacement of sedimentary structures such as laminations, indicating shearing, and thus may be classified as shear bands or shear enhanced compaction bands in accordance with their kinematic classification (Aydin et al., 2006)(Fig. 5.1.f).

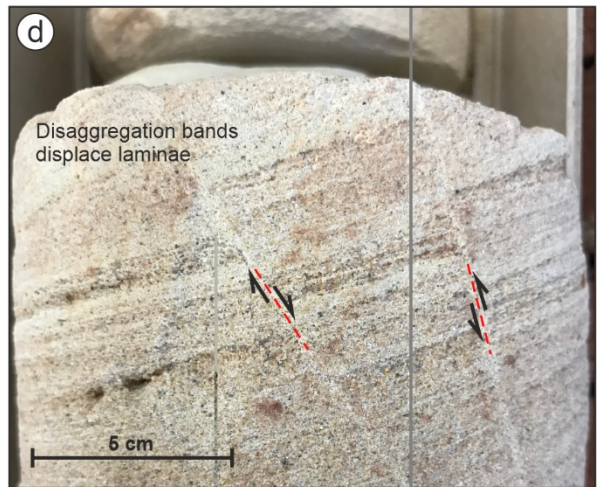
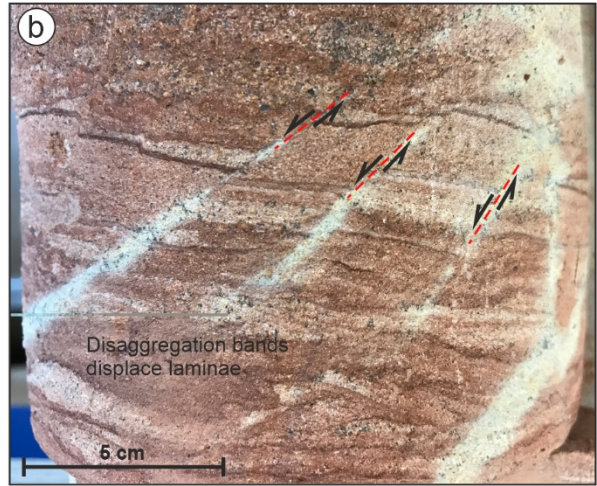


Figure 5.1. Examples of deformation bands. (a) Bands are cataclastic in the Saughall Massie borehole. (b) Disaggregation shear bands displace laminations and show evidence for fluid flow within fluvial sheet flood facies in the Holcroft Lane borehole. (c) Cataclastic bands within aeolian dune facies in Helsby Quarry. (d) Disaggregation shear bands displace laminations of fluvial sheet flood deposits in the Holcroft Lane borehole. (e) Disaggregation bands weather more than adjacent undeformed rock and show evidence for fluid flow pathways in fine-grained aeolian facies at Pease Bay. (f) Cataclastic shear deformation bands displace laminations within aeolian facies at Pease Bay.

Optical photomicrographs of cataclastic deformation bands are presented in figure 5.2, showing porosity of host and deformation band material, as well as grain sphericity, and grain fabric. Bands show well defined zones, <1mm in width, of localised compaction, grain size reduction, and porosity loss (Fig. 5.2a-c). Any pre-existing grain fabrics from sedimentary structure such as laminae, shown by a clear alignment of grains (rose diagram inset) is removed by the deformation band. Grains also undergo change in sphericity, although no clear trend is observed in a change from spherical to elongate or vice-versa. Due to fine-grained cataclastic textures, cementation of the bands, and limitations in resin impregnation, it is difficult to observe the internal textures of the bands with optical microscopy alone. Back scattered electron images of deformation bands provide a clearer image of their internal textures and porosity (Fig. 5.3). Samples show that both quartz and feldspar experience intense cataclasis, resulting in a wide grain size distribution, with finer crushed grains filling pore spaces between larger grains. Feldspar grains display a greater degree of grain size reduction, with little to no large grains. In contrast, a small number of quartz grains within deformation bands remain larger, and may remain relatively undeformed. Grain textures of cataclastic rocks may be classified by the proportion of fine-grained matrix (Sibson, 1977). In the samples of individual bands, textures range from micro-breccia (Fig. 5.3e,f), reducing porosity to 13.8%, to protocataclastic (Fig. 5.3c,d), reducing porosity to approximately 7%. A sample of fault core material from the Helsby Hill Fault shows more mature ultracataclastic textures, with very fine-grained deformed grains filling pore spaces and supporting few, relatively undeformed larger grains, resulting in a porosity of 4.7% (Fig. 5.3g,h).

Disaggregation bands are also recorded, and typically occur in finer grained lithofacies such as fine-grained dunes, interdunes, and fluvial and aeolian sand sheet facies. As the primary mechanism of deformation bands is localised grain sliding, rolling and re-organisation, with

or without a secondary component of cataclasis, disaggregation bands can present as preferentially weathered to the surrounding host rock, indicative of their kinematics of shear and/or dilation, often showing displacement of grain laminations (Fig. 5.1b & d), and evidence for acting as fluid flow pathways (Fig. 5.1e). Photomicrographs of these bands show little to no textural change, with shearing indicated by a change in grain fabric orientation (Fig. 5.2d). Estimations of porosity of lithofacies such as aeolian and fluvial sand sheets is difficult due to their heterolithic laminations of grains that represent large textural and petrophysical changes. Shearing of these laminations and re-organisation and more efficient packing of grains, as well as the entrainment of muddier and finer grained horizons within the deformation band, results in significant porosity reduction (Fig. 5.2d). Examples of dilatant disaggregation bands are difficult to sample and measure due to acting as a natural plane of weakness, however in these examples we expect porosity and therefore permeability to be increased relative to the undeformed host lithology.

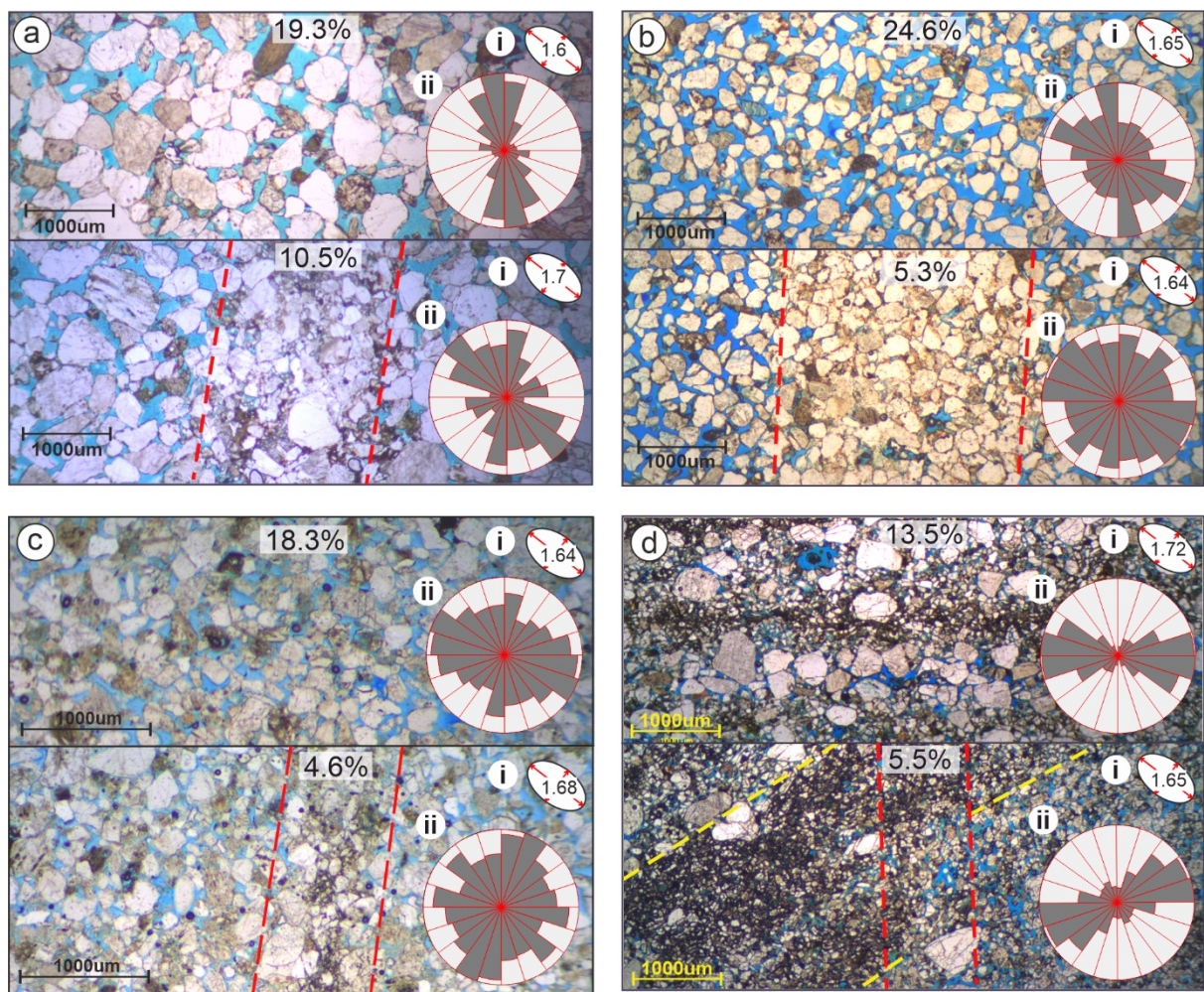


Figure 5.2. Photomicrographs of host lithologies and their deformation bands, including their respective porosity values, grain sphericity (i) and grain fabric (ii). (a) A coarse-grained fluvial channel unit from Helsby. (b) A medium-grained aeolian dune sample from the Saughall Massie borehole. (c) A fine-grained fluvial bar unit from Grinshill. (d) A fine grained, fluvial sheet flood sample from the Holcroft Lane borehole.

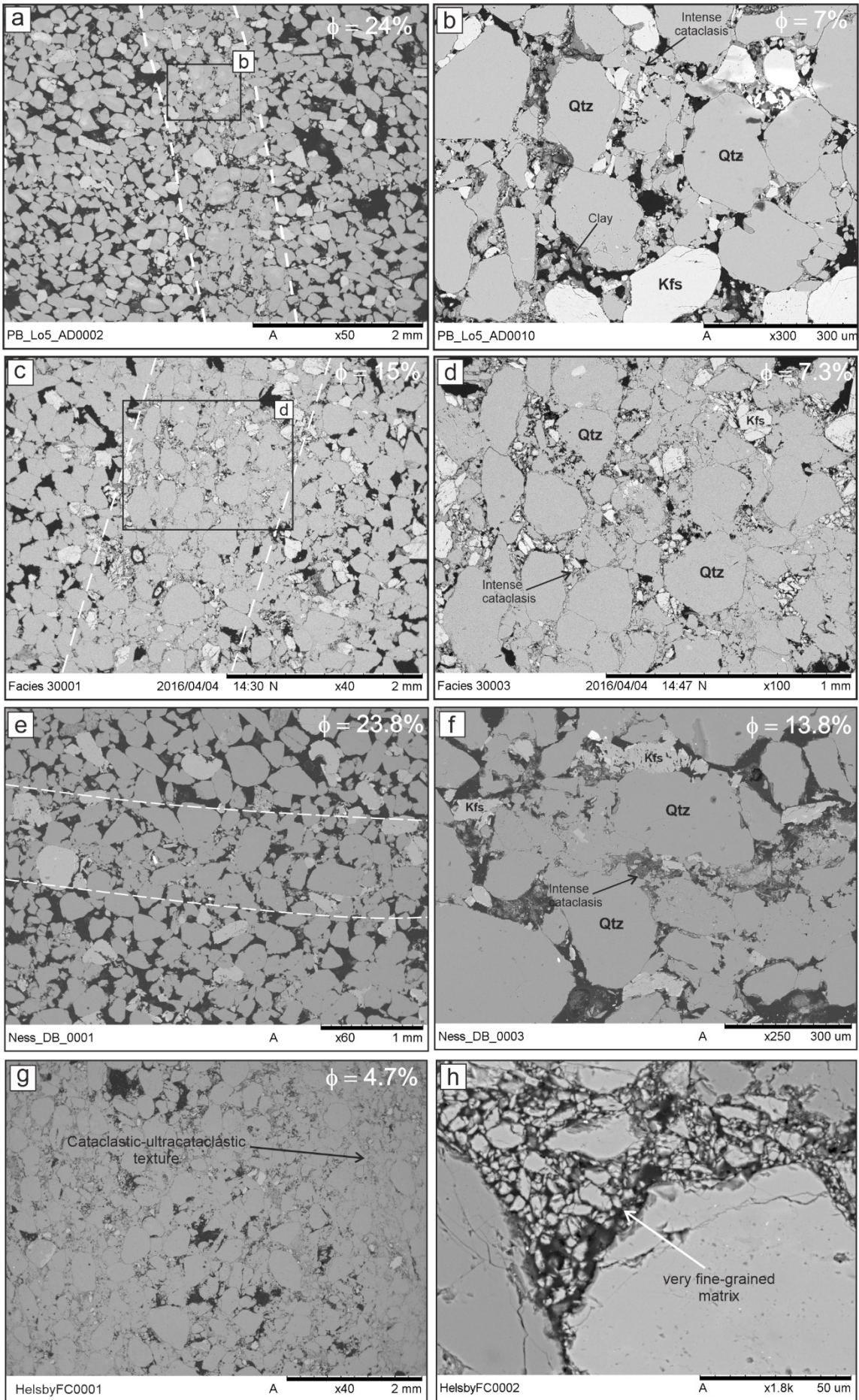


Figure 5.3. Back scattered electron (BSE) photomicrographs of the internal microstructure of deformation bands. (a) Deformation band with micro-breccia-protocataclastic texture in a fine-grained aeolian dune, Pease Bay, Scotland. (b) High magnification of image showing grain size reduction within a deformation band. (c) Protocataclastic texture within a deformation band in a coarse-grained fluvial channel, Helsby Hill, Cheshire, UK. (d) High magnification of protocataclastic texture within a deformation band. (e) Deformation band with micro-breccia texture within a fine-grained aeolian dune, Nesscliffe, Shropshire, UK. (f) High magnification image showing grain size reduction of quartz and feldspar grains. (g) Fault core sample from the Helsby Hill fault. Cataclastic-ultracataclastic texture has a low porosity of 4.7%, with large grains supported in a very fine-grained matrix. (h) High magnification of fault core ultracataclasite, very fine-grained matrix fills pore spaces.

5.2. Porosity – permeability relationships

Results of porosity measurements of both deformation bands and their undeformed lithology are plotted in a log-log plot, including data compiled from the available literature using a variety of measurement techniques including image analysis, mercury injection, and helium porosimetry (Fig. 5.4). The results here fill the lower porosity space in the data, with average porosity reductions of between 50-75%.

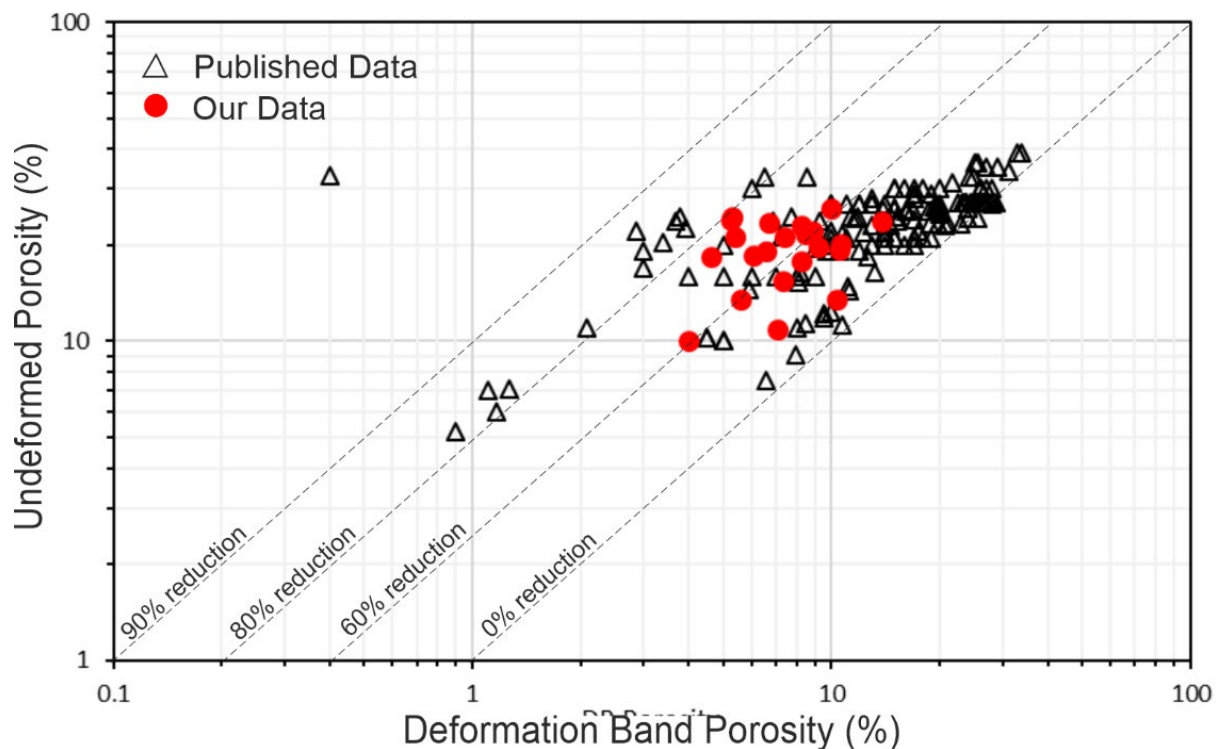


Figure 5.4. Log-log plot of host rock versus deformation band porosity. Our data shown in red against published deformation band porosity data for sandstones (Rowe and Burley, 1997; Ogilvie and Glover, 2001; Shipton and Cowie, 2001; Shipton et al., 2002; Torabi and Fossen, 2009; Farrell et al., 2014; Ballas et al., 2015; de Lima Rodrigues et al., 2015; Wilkins et al., 2019)

Porosity-permeability relationships for undeformed lithofacies, using both measured values with the mini-perm permeameter, and calculated values using equations 2, and deformed lithofacies using calculated values, are plotted in figure 5.5. Results of both calculated and measured values of undeformed host rocks show a power-law trend, with exponents (D) of 3 and 6 respectively. Calculating band permeability using the same equation reveals a similar power-law trend that occupies the lower poro-perm region with an exponent $D = 6$. Data from Torabi et al. (2013) which include image based porosity and permeability measurements of both aeolian and fluvial facies sandstones, are shown for a comparison, where power-law trends for host rock ($D = 8$) and deformation bands ($D = 6$) are observed. For a given porosity, measured values of host rock permeability are slightly higher than those of deformation bands, although the opposite is true of calculated host permeability. This is the opposite of the calculated permeabilities presented by Torabi et al. (2013) which finds permeability higher in host rock for a given porosity. This is likely due to the host rock data in this study including finer-grained, lower porosity sand and siltstones that do not host deformation bands. Removal of these data points shows that our deformation bands are lower porosity than any host rock values. Whereas the compared data shows deformation bands with porosity as high as 20%.

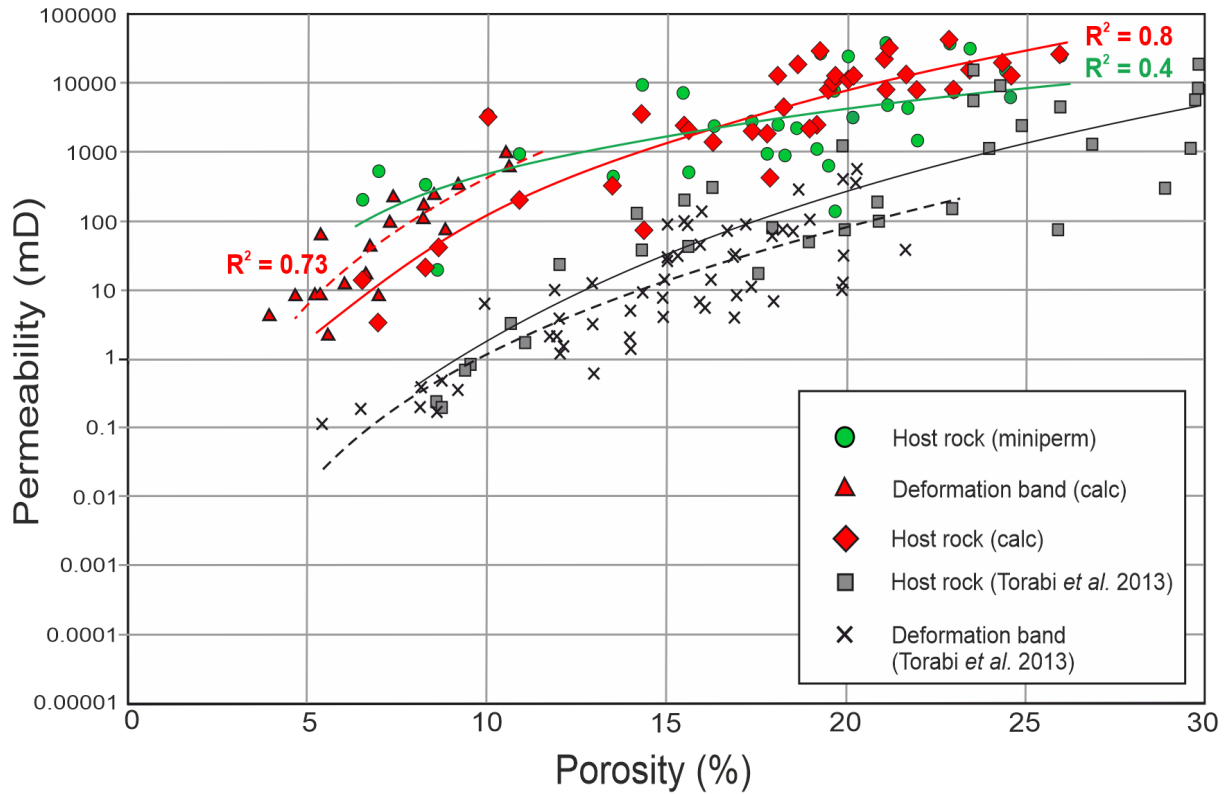


Figure 5.5. Porosity permeability relationships for undeformed lithofacies and deformation bands measured with both permeameter (green) and calculated using Berg's method for permeability estimation (red). Shown for comparison is a data set also obtained from image analysis from Torabi et al. (2013).

5.3. Grain size distribution analysis

Optical and back scattered electron (BSE) images of deformation bands show that their grain size is reduced relative to their undeformed hosts, due to processes of cataclasis such as transgranular fracturing and grain chipping. This results in a wider grain size distribution, or poorer sorting. Results of point counting grain size of undeformed and deformed samples are plotted in a line graph (Fig. 5.6) and show significant grain size reduction and increase in size distribution, and/or change in the profile of distributions, which commonly show a normal distribution in undeformed sample, to a log-normal distribution with positive skew in deformation bands.

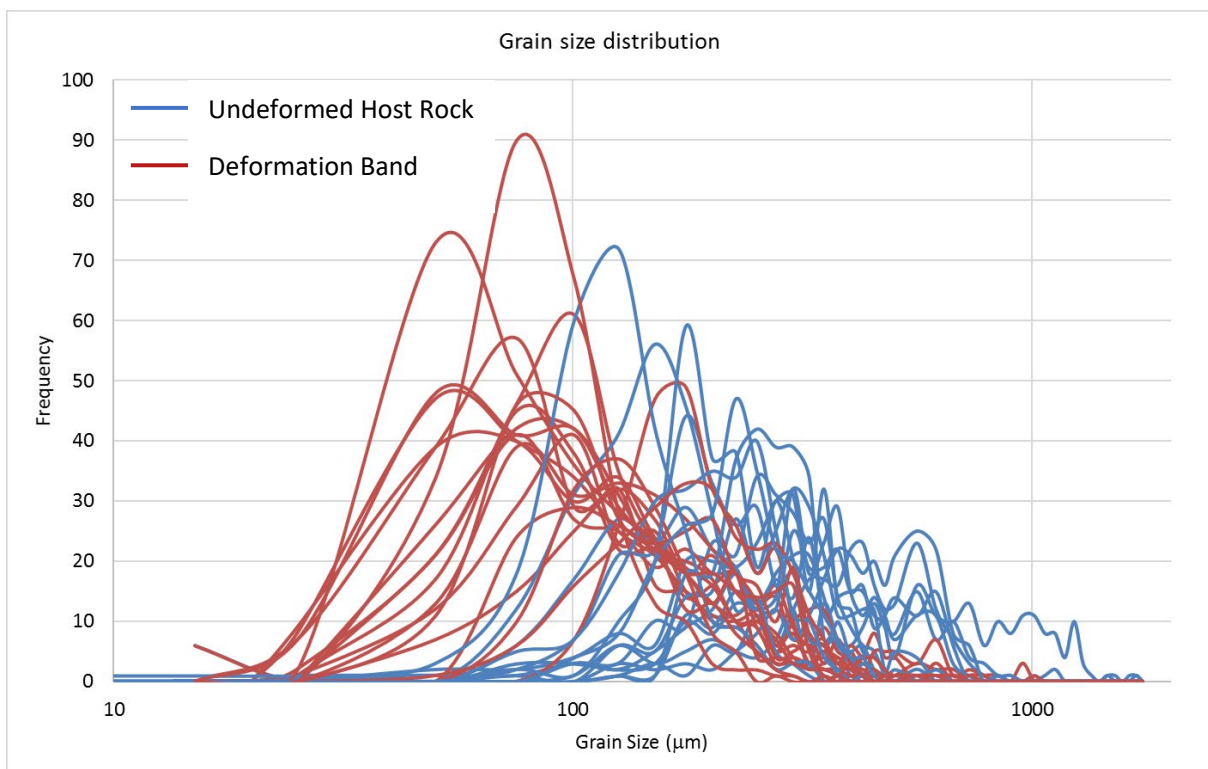


Figure 5.6. Graph showing the grain size distribution of undeformed host rock and deformation bands. Data shows the results of cataclasis in which grains fracture and grain size is reduced. Both host rock and deformation bands show a high degree of variability.

Both grain size and sorting are major controls on the permeability of sands and sandstones (Beard and Weyl, 1973; Cade et al., 1994; Nelson, 1994), and may be an important property of deformation bands to quantify, and relate deformation band sorting to the sorting of the host material. The sorting of sediments and sedimentary rocks is typically quoted as dimensionless coefficients and Phi units derived from statistical measures of grain size (Friedman, 1962). For fault rocks and cataclastic gouge in particular, sorting of grains may instead be described by a fractal distribution. Mathematically this means that particle frequency and size have a power-law relationship, and is independent of scale. The fractal distribution is then described by the fractal dimension D , the power-law exponent of the grain size – frequency relationship. An example of how grain size distribution, and the fractal range changes with increasing strain is shown in figure 5.7. It has been shown that in both naturally and experimentally produced fault rocks that a fractal grain size distribution develops as a result of cataclastic processes (Marone et al., 1990; Blenkinsop, 1991). It was first proposed that the process of producing a fractal grain size distribution via cataclasis is a result of grain comminution, whereby tensile fracturing of grains is independent of individual grain strength and size, but instead is dependent on having similar size neighbouring grains. It is hypothesised that this process of grain fracturing would produce a grain size distribution such that there are no neighbouring grains of similar size, resulting in a maximum theoretical fractal dimension of $D = 2.58$ (Sammis et al., 1987). However, natural examples of cataclastic fault rocks have been observed with fractal dimensions of up to $D = 3$, caused by high strain fault zones, where particles of the similar dimensions that were initially isolated by comminution, would subsequently come into contact and fracture (Sammis and King, 2007). Very little has been done to characterise deformation bands in terms of their fractal distribution, aside from a study of deformation bands within poorly lithified sandstones

where the fractal dimensions were used to infer deformation mechanism (Rawling and Goodwin, 2003). Fractal distributions may therefore offer insight into the deformation mechanism of fault rocks, or may also offer insight into the petrophysical properties of deformation bands. The grain size distributions for both host rock and deformation bands are plotted in log-log space of grain size against number of grains. A line of best fit is applied to the deformation band data where it deviates from the host rock curve, and the fractal dimension and fractal range at which a power-law is observed is recorded (Fig. 5.7).

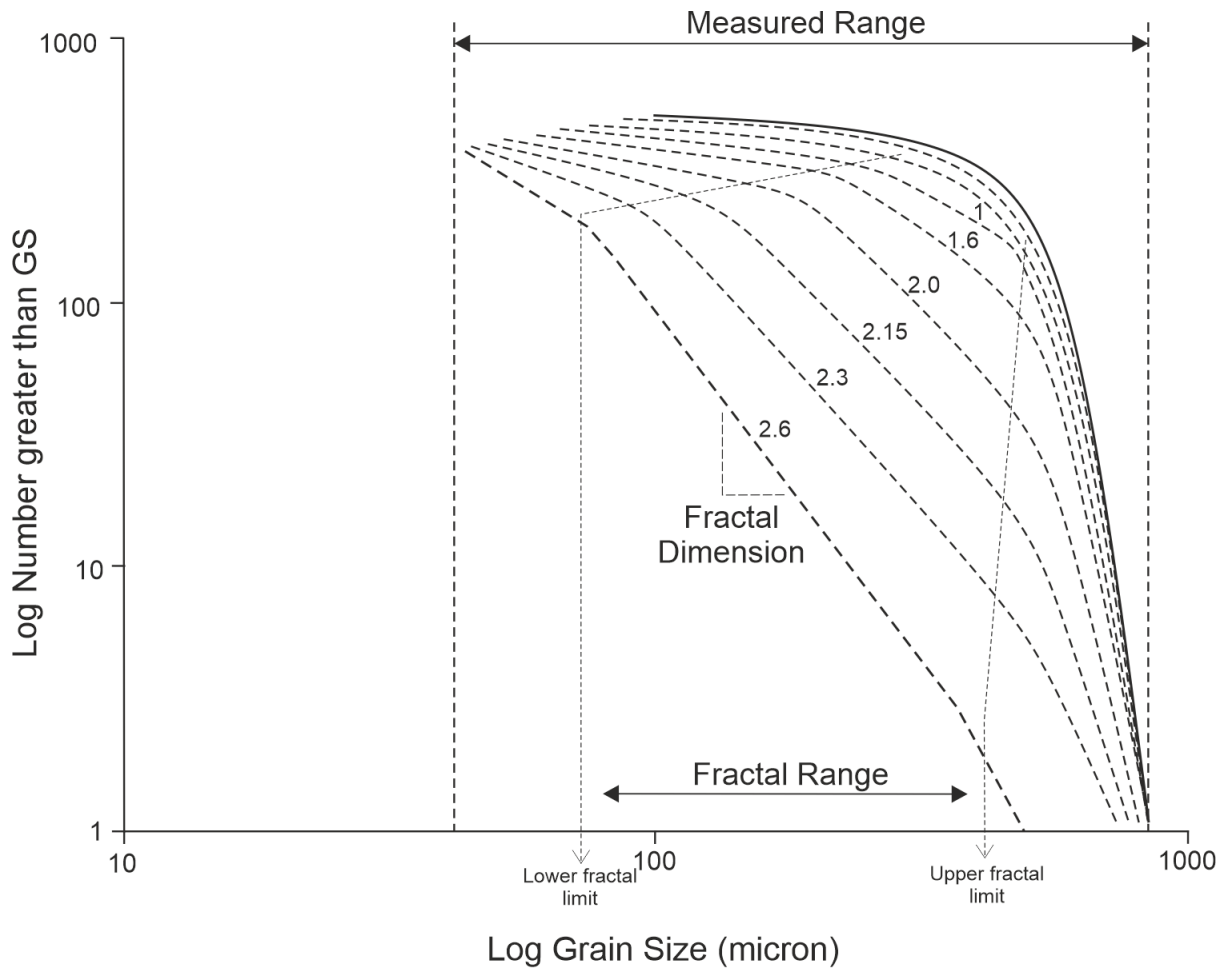


Figure 5.7. Grain size distribution represented on a log-log plot of grain size against number of grains. A power-law relationship is indicative of a fractal distribution where the exponent D is the fractal dimension. It is proposed that D will develop with increasing cataclasis as well as increasing fractal range. Figure adapted from Blenkinsop (1991) & Zhong et al. (2018)

Plots are shown in figure 5.8 and include the fractal dimension and correlation coefficient (R^2). A range of fractal dimensions from 1.95 up to 2.84 are observed. Such a range in values suggest varying deformation mechanisms and amounts of cataclasis and grain size reduction. It is worth noting that a fractal distribution was not observed for disaggregation bands such as those presented in figures 5.1 & 5.2. Grain size distribution profiles for these bands show a logarithmic relationship instead of a power-law relationship as these bands do not exhibit cataclasis as the primary deformation mechanism.

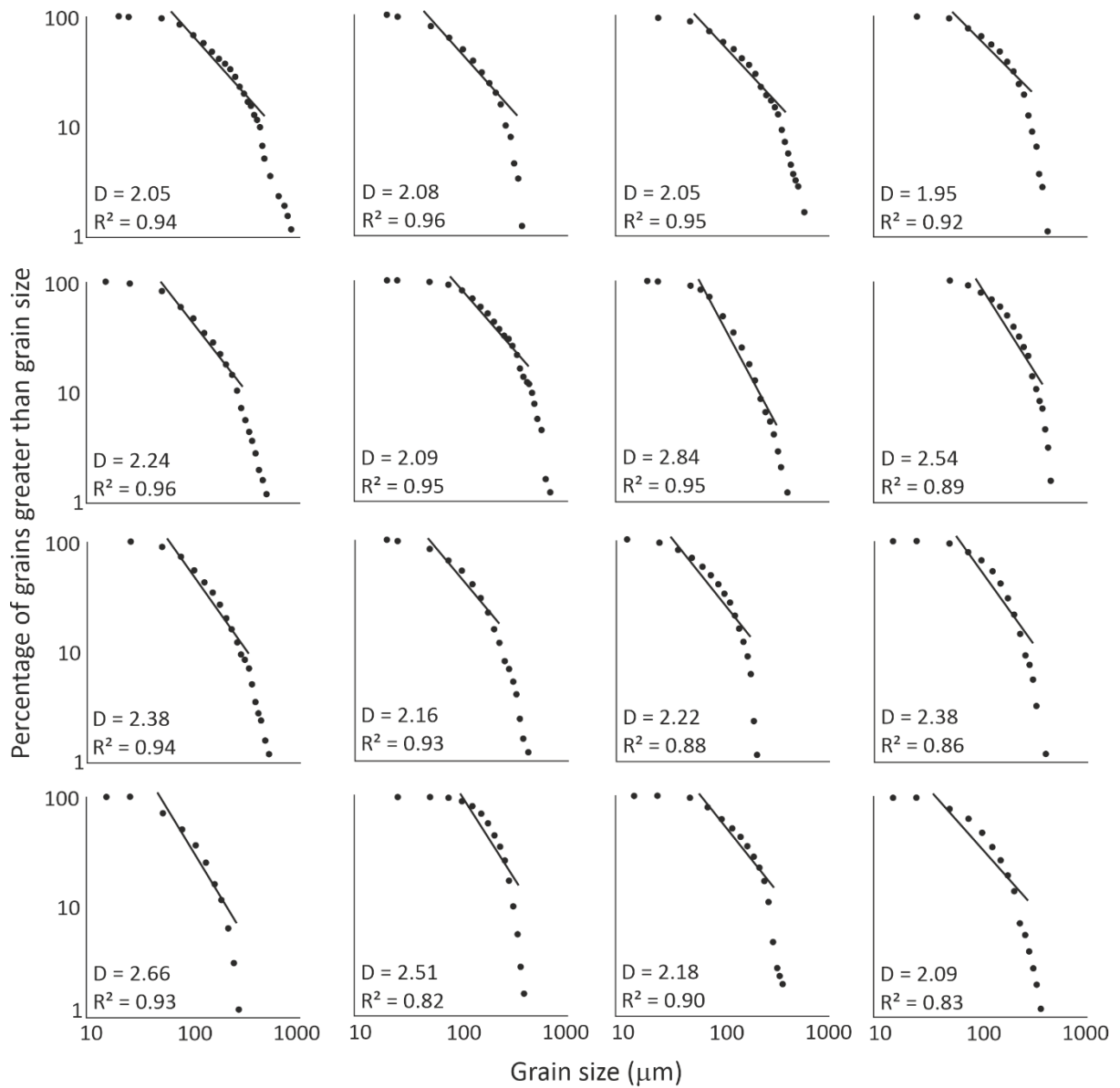


Figure 5.8. Log-log plots of grain size distribution for deformation bands, used to record the fractal dimension and fractal range.

Sample	Facies	Host Porosity	DB porosity	Host grain size (µm)	DB grain size (µm)	Sorting (Phi)	DB Sorting (Phi)	Fractal Dimension (D)	Fractal Range	Host Permeability	Host Perm (Berg) (mD)	Band Perm (Berg) (mD)	Qtz	Kfs	Lithics
HBV-P14-FC	Chl	21.2	5.39	636	200	0.918	1.089	2.05	351	4487	29000	63	90	10	Trace
HBV-P16-FC	CHb	15.5	7.3	266	123	0.53	1.118	2.08	175	6720	2370	96	94	5	1
HBV-P17-FC	CHI	19.3	10.5	375	168	0.686	1.065	2.05	251	24525	27738	927	89	8	3
HBV-P18-FF	FF	21.7	8.5	274	158	0.443	0.974	1.95	201	4148	11765	213	92.9	6.1	1
TH-AI	AI	10	4	170	-	0.5	-	-	-	3197	3197		83	11	7
TH-AD	AD	26	10	537	-	0.4	-	-	-	24194	24194		96	4	trace
GR-P1-AD	AD	19.2	6.59	189	84	0.391	0.964	2.22	139	1069	2358	17	97	3	0
GR-P2-AD	AD	23	8.2	206	150	0.408	0.854	2.38	226	6949	7611	106	97	3	0
GR-P3-FF	FF	10.9	7	188	124	0.465	0.473	-	-	906	188	8	85	10	5
GR-P3-FB2	CHb	17.8	8.25	174	124	0.43	1.079	2.16	150	906	1772	160	90	7	3
GR-P4-FB	CHb	18.3	4.63	210	144	0.559	0.965	2.38	251	891	4201	8	85	15	trace
HBV-P6-AD	AD	21.1	7.37	348	220	0.534	0.946	2.09	276	35039	21514	214	96	3	1
HBV-P11-FB	CHb	20.08	10.6	291	191	0.487	0.81	2.54	276	22837	11224	603	95	5	0
HBV-P12-FB	CHb	19.7	9.2	218	124	0.701	1.089	2.24	201	7309	11340	330	96	3	1
HBV-P13-FC	CHI	18.65	6.05	350	121	0.609	0.832	2.84	251	2169	17022	12	92	5	3
Holcroft 109.bmp	FS	13.49	5.58	130	89	0.541	0.614	-	-	433	318	2	80	10	10
Holcroft 109.bmp	FS	13.49	10.3	130	89	0.541	0.614	-	-	433	318	38			
Holcroft 144.1.bmp	CHb	22	8.85	202	94	0.481	0.86	2.66	150	1452	7435	73	88	5	7
Saughall 127.3.bmp	AD	24.6	5.3	258	198	0.326	0.613	2.58	201	5775	12474	8	96	3	<1
Saughall G1519	AD	23.44	6.72	230	151	0.474	0.863	2.18	226	30990	14512	42	95	3	2
Saughall G1519.2	AD	24.4	5.25	230	111	0.474	0.971	2.09	200	13842	17809	9	97	2	1
Nescliffe 001	AD	23.8	13.8	-	-	-	-	-	-	-	-	-	97	3	0
Pease Bay_1	AD	23.8	8.67	-	-	-	-	-	-	-	-	-	-	-	-
Pease Bay_2	AD	23.8	15.5	-	-	-	-	-	-	-	-	-	-	-	-

Table 5. Deformation band samples and their properties.

5.4. Discussion

Textural, microstructural and petrophysical properties of deformation bands are summarised in table 5. We observe both cataclastic and disaggregation bands across the localities of the Cheshire Basin study and Pease Bay, both evident in their morphology in outcrop, and in their microstructural texture. The type of deformation band formed is inherently linked to the lithological properties of the sandstones. Disaggregation bands are hosted within finer grained and low porosity facies of aeolian and fluvial origin, typically interdune, aeolian and fluvial sheet flood deposits, which exhibit thin beds, and often lamination scale heterogeneity of grain size, sorting and mineralogy (Fig. 5.1b & d). Microstructural observations of disaggregation bands show that porosity is reduced primarily through compaction and repacking of grains via shearing, rotation and sliding, as shown by grain fabric changes between host and DB material (Fig. 5.2d). Cataclasis and grain size reduction is a minor component of these bands, as such, grain size distribution shows little change. Any textural change is attributed to lamination scale heterogeneity of the host rock, and entrainment of these laminae into the shear zones of the deformation band (Fig. 5.2d). Despite the lack of grain size reduction, these bands often show significant reductions in permeability. The permeability reduction of deformation bands is shown on a log-log plot of host permeability versus band permeability, with a catalogue of published data also included for comparison (Ballas et al., 2015) (Fig. 5.9). Deformation bands are coloured according to their depositional facies, aeolian and fluvial, and interdune and overbank facies are grouped separately. We plot both host rock permeability values obtained with the probe permeameter (solid symbols), and permeability values calculated from the Berg equation (2) (open symbols). Permeability reduction for aeolian interdune and fluvial overbank facies, which typically, although not

exclusively, exhibit disaggregation bands, show a permeability reduction of approx. 1.5 orders of magnitude.

Cataclastic bands occur within coarser grained and higher porosity lithologies of both aeolian and fluvial origin, and show cataclastic and proto-cataclastic textures at their core, with grain size and porosity reduction relative to their host material, resulting in high reductions in permeability. Deformation bands in aeolian facies show a slightly higher permeability reduction with an average of 1.8 orders of magnitude, compared to 1.47 orders of magnitude for fluvial facies (Fig. 5.9). It is useful to be able to predict deformation band properties for different depositional facies, however our results show that properties of both aeolian and

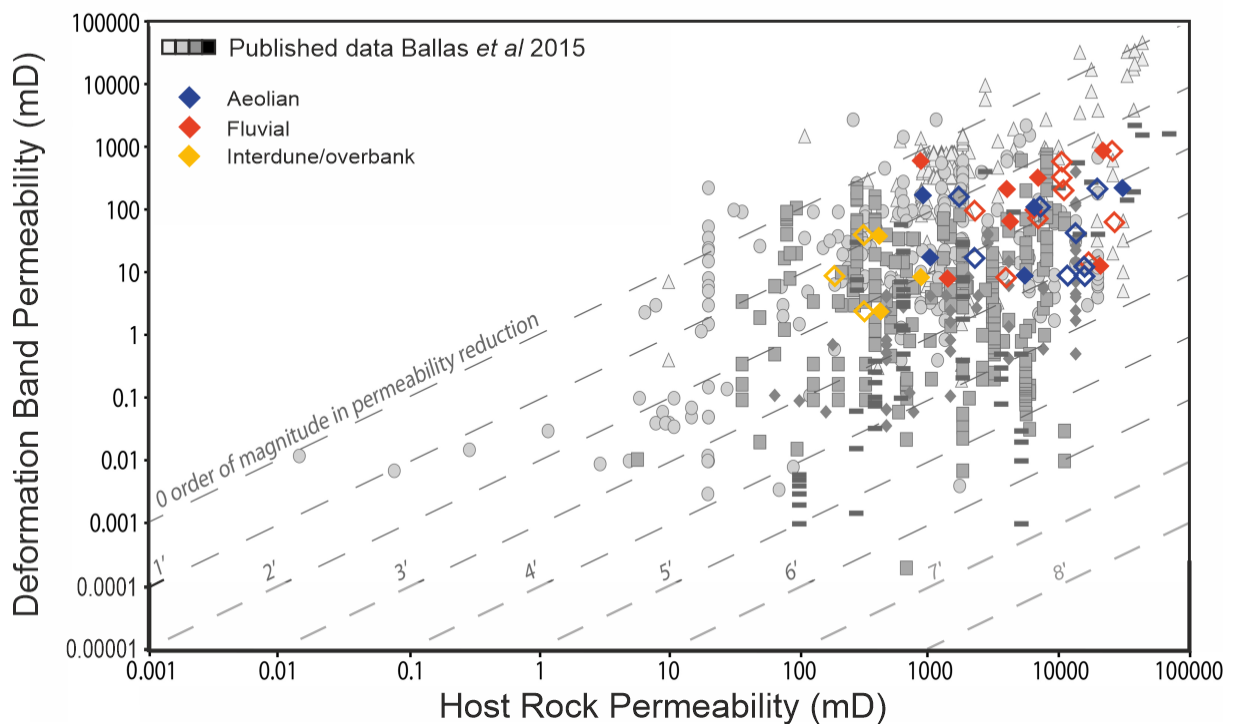


Figure 5.9. Log-log plot of deformation band permeability versus host rock permeability for our deformation bands. Solid symbols represent measured host permeability. Open symbols represent calculated host permeability. Included is a large published data set of different cataclastic structures; individual bands, slipped bands, band clusters and fault core, from Ballas et al. (2015) and references therein.

fluvial hosted deformation bands are remarkably similar. This is due to similarities of lithological properties of the host rock, particularly within mixed aeolian-fluvial systems in which aeolian sediments are reworked and deposited in fluvial systems in the absence of a strong secondary sediment source. This is apparent when observing samples in thin section, where both fluvial and aeolian lithologies are very similar in terms of porosity, grain size, mineralogy and sorting. Therefore, cross plots of lithological properties and deformation band permeability, and porosity and grain size reduction are shown in figure 5.10. Strong relationships between grain size and porosity with grain size reduction and porosity reduction are observed (Fig. 5.10g & h), which reflects the strong control of porosity and grain size on the mechanical failure of sandstones. These parameters, irrespective of grain sorting, are the dominant control on cataclasis, and it may also be inferred the dominant control on permeability, since porosity and grain size strongly control permeability. The effects of grain sorting on deformation band properties remains poorly understood, although some reports of greater permeability reduction within well-sorted versus poorly-sorted sands suggest some minor influence (Ballas et al., 2015). There is a subtle trend in permeability with host rock sorting (Fig. 5.10b), which also supports slightly higher permeability reduction observed in aeolian facies. Well-sorted sandstones favour Hertzian, intragranular fracturing and grain comminution (Sammis et al., 1987; Cheung et al., 2012), therefore it may be possible to observe this within the grain size distribution. Plots of grain size distribution in log-log space reveal varied fractal dimensions (D) that represent different grain textures that are inherently linked to micromechanical processes. Both lower and higher values of D than that predicted by the constrained comminution model are observed, which predicts $D = 2.58$, suggesting other processes such as grain chipping and flaking (Marone et al., 1990), and high strain shearing respectively (Sammis and King, 2007). Higher fractal dimensions are observed within

better sorted sandstones, supporting the constrained comminution model within well-sorted sandstones, and less so in poorly-sorted sandstones (Fig. 5.10c), although it is difficult to make comparisons without comparative levels of strain. Classification of deformation bands in terms of their fractal dimension, whilst conventionally used as an indicator of deformation mechanism, should theoretically provide insight into the textural evolution, and therefore petrophysical properties of the bands. However, we observe only a weak positive relationship between fractal dimension and the permeability of deformation bands (Fig. 5.10a) that suggests the fractal dimension only partly describes the permeability of the bands. As we only observe a fractal relationship for part of the total grain size distribution, the fractal dimension only partly captures the textural properties of the bands. This suggests the fractal range may also play an important part in determining the permeability, since permeability is so strongly controlled by grain size (Nelson, 1994), but also that the whole GSD should be accounted for in order to relate texture and permeability. Variations in micromechanical processes are governed not only by the lithological properties of the sandstones, but also in relation to the state of stress at failure (Fig. 2.7). In a later chapter we examine the relationship between fractal grain size distributions and stress.

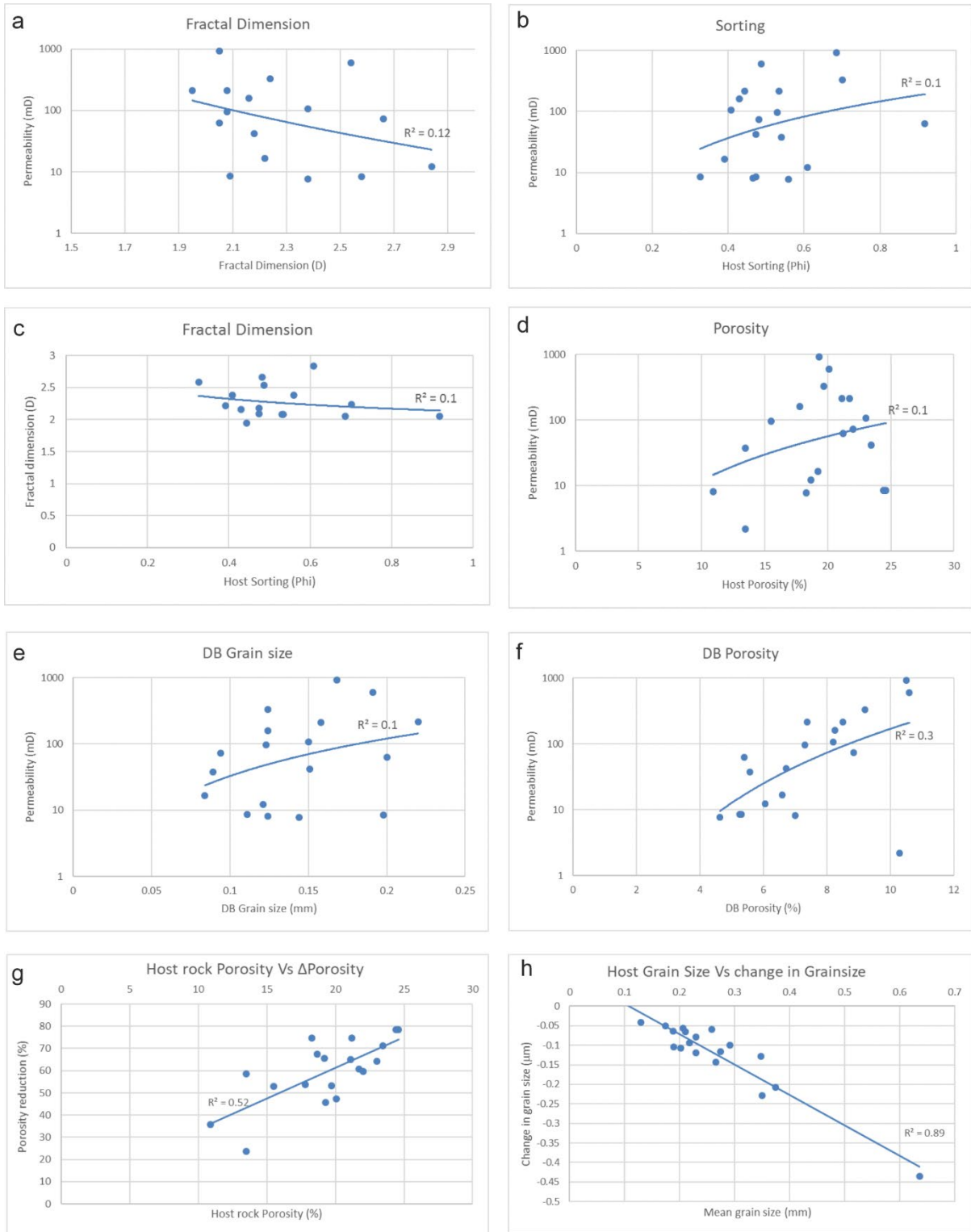


Figure 5.10. Cross plots of lithological properties of host sandstones and deformation bands.

5.5. Conclusions

Results of petrographic analysis of deformation bands reveal a variety of different types of deformation bands in terms of deformation mechanism. Porosity and grain size are the primary controls on the type of deformation band formed, particularly whether formed by disaggregation or cataclasis, and in the case of cataclastic deformation bands, are also the primary controls on porosity and grain size reduction as coarser grained, higher porosity hosts exhibit greater cataclasis and the development of fractal grain size distributions. Grain sorting is shown to be a secondary control on grain size reduction and porosity loss, and therefore permeability. For this reason, deformation bands in aeolian facies, which are typically better sorted, show slightly higher permeability reductions than deformation bands in fluvial facies sandstones, which are typically poorer sorted.

A wide range of grain size reduction and textural modification is observed, which is represented in terms of fractal relationships of grain size and frequency. The fractal dimension reflects the micromechanical mechanisms of cataclasis. A fractal dimension of $D = 2.58$ is predicted by the constrained comminution model of cataclasis (Sammis et al., 1987). It is found that constrained comminution is a more dominant mechanism of cataclasis within well-sorted sandstones, which yield higher fractal dimensions. No correlation between fractal dimension and permeability reduction is observed, and therefore, fractal dimension cannot be used to wholly describe the textural and subsequent petrophysical modification of deformation bands. It also remains to be seen whether the fractal distribution of cataclastic deformation bands can be linked to stress.

6. Deformation Band Fault Damage zones

This chapter investigates damage zone architecture within sequences of mixed aeolian-fluvial facies sandstones in two principal case studies; the first a regional study within the Cheshire Basin of North West England, focusing on the upper-most formations of the Triassic Sherwood Sandstone Group, which exhibit aeolian-fluvial sandstone lithofacies heterogeneity on scales of 1-20m. The second, a localised study within the Upper Devonian – Lower Carboniferous Old Red Sandstone Supergroup of the United Kingdom, observed at Pease Bay, Scotland, which displays facies heterogeneity in interbedded sandstones, siltstones and mudstones, at scales of less than 3m. Using areal-window damage zone sampling, the control of both lithology and bed thickness on deformation band intensity and width, are examined in order to improve the understanding of band formation and fault damage zone architecture in mixed aeolian-fluvial successions.

6.1. Introduction

The impact of deformation bands on any reservoir is ultimately determined by the effective permeability contrast of the bands to that of the surrounding undeformed host rock, the total number of deformation bands in the system between an injector and producer, their cumulative width (Manzocchi et al., 1999; Fossen and Bale, 2007) and their connectivity (Rotevatn et al., 2013). Therefore, it is important to understand the type, geometry and spatial distribution of these structures in a variety of lithologies in proximity to faults.

The width of a fault damage zone only partially controls its fluid flow properties and an understanding of the intensity and distribution of deformation bands within that zone is crucial in determining both the faulting mechanics and the fluid flow properties. Band frequency within fault damage zones has been shown to decay logarithmically with distance

from the fault, with the variance attributed to band clustering and initiation of isolated slip zones away from the principal slip surface (Schueller et al., 2013). There exists a great deal of variability in deformation band attributes, including width, damage intensity, band type, and subsequent petrophysical modification that is strongly controlled by lithology and factors such as grain size, shape, sorting, as well as composition and the abundance of clay minerals (Fisher and Knipe, 2001; Schultz et al., 2010; Exner and Tschegg, 2012). Relationships between band density and bed thickness have also been observed, with density reduced in beds less than 3m thick, but with no trends observed with bed thicknesses greater than this (Johansen and Fossen, 2008). These trends have been observed in studies of aeolian successions such as in the Jurassic rocks of the Midwest United States, where band densities and damage zone widths are much higher in the mineralogically mature, thicker, coarser and higher porosity aeolian dune units (Shipton and Cowie, 2001; Fossen et al., 2011a; Fossen and Rotevatn, 2012). These successions, however, display either very little facies variability. There remains the question of whether the same trends are observed in different facies, or those with more facies and bed thickness variability, such as in mixed aeolian-fluvial reservoirs (Meadows and Beach, 1993; Priddy and Clarke, 2020). Inherent lithological variables influence the mechanical properties of the sandstones, which may be reflected in the spatial distribution and morphology of the bands, in addition to the microstructure and petrophysical properties. Fault damage zone attributes were recorded for fourteen faults within different lithologies at both Pease Bay and across the Cheshire Basin localities. Results of fault zone measurements, including damage intensity, band width, fault displacement if known, and damage zone width are shown in table 6, together with lithological properties such as grain size, porosity, sorting, and bed thickness.

Fault ID	Thickness (cm)	Porosity (%)	Grain size (µm)	Sorting (Phi)	Inner DZ Intensity	Outer DZ Intensity.	Mean Band width (mm)	Lens width (mm)	Displacement (m)	DZ 1/2 width (m)	DZ width (m)
Thurst.F1	600	26	537	0.4	13.25	2.75	2.1	5.4	0.19	2	4
Thurst.F2	600	26	537	0.4	7.75	2.5	2.1	5.4	0.64	3.1	6.2
Gr.Corbet	600	19.2	189	0.391	18	5	0.5	4.2	0.1	1	2
Gr.Hill	400	18.3	210	0.559	9	6	2.4	7.6	0.3	1.8	3.6
HbyHill.FW	150	21.2	636	0.918	1.6	0.38	3.5	12	7	17	34
HbyHill.HW	200	20	291	0.487	8	0.7	4	16.8	7	10	20
PB.FDZ3.1	100	-	-	-	6.1	-	3	6.65	1	4	8
PB.FDZ3.2	15	-	-	-	-	-	-	-	1	4	8
PB.FDZ3.3	50	-	-	-	2.1	-	2.3	4	1	4	8
PB.FDZ3.4	60	-	-	-	3.5	-	4.5	11.75	1	4	8
PB.FDZ4	600	23.9	220	-	6.2	1.7	-	-	-	17	34
PB.FDZ5.1	25	-	-	-	17	-	1.7	4.9	1.5	5.2	10.4
PB.FDZ5.2	30	-	-	-	5	-	0.6	-	1.5	5	10
PB.FDZ5.3	122	-	-	-	3.3	-	-	-	1.5	5	10

Table 6. Results of fault damage zone measurements and lithological properties.

6.2. Fault Damage Zone Intensity

6.2.1. Cheshire Basin

Results of fault damage zone intensity measurements for four faults at Helsby and Grinshill are shown in figure 6.1. Intensity is plotted both as linear bar plots and cumulative intensity, for which the linear best fit provides a measure of average intensity of the fault zone, as well as defining different zones of intensity which may be used to infer the damage zone width, based on a drop in intensity to what may be considered background levels of deformation (Choi et al., 2016; Torabi et al., 2019).

In the footwall of the Helsby Fault, deformation band intensity was recorded within a coarse-grained and poorly sorted fluvial channel bed with a porosity of 21%, using 50cm quadrats, and therefore intensity per 0.25m^2 . Band intensity within the footwall is approximately 1.6m of bands per 0.25m^2 , decaying to 0.38m approximately 17m from the fault, which we record as the damage zone half width. Beyond this, intensity is low and constant, and deformation bands become less frequent, with a 1-4 m spacing (Fig. 6.1a). In the hanging wall, intensity was recorded in a medium-grained, moderately sorted fluvial bar unit with a similar porosity of 20%. Band intensity is much higher at 8m per 0.25m^2 (Fig. 6.1b). A gap in outcrop is observed until 10m from the fault before deformation bands are recorded with a low intensity of 0.7m, similar to the footwall. We record this 10m as an over-estimate of damage zone half width in the absence of directly observing a change in band intensity. A small displacement fault with approximately 2cm offset is observed at 16.5m from the main fault, recording a spike in band intensity, but the 0.7m trend is resumed for 25.5m, where there is no more available outcrop.

At Grinshill, two fault damage zones were sampled, the first in the hanging wall of the NW-SE trending Corbet Wood Fault with very minor displacement (<10cm) within a 6m thick, fine-grained and well-sorted aeolian dune succession with a porosity of 19%. The second in the hanging wall of the NNE-SSW trending Grinshill Hill Fault with displacement of approximately 30cm, within a thick succession of medium-grained, moderately-sorted fluvial bar and channel succession with porosity of 18%. In the fine-grained aeolian damage zone, band intensity shows a high inner zone with an average of 18m bands per 0.25m², decaying to approximately 5m approximately 1 metre from the fault plane. The change in band intensity may record the transition from a high intensity Inner damage zone, to a lower intensity outer damage zone of the fault, as is observed in many fault damage zones (Johansen and Fossen, 2008; Schueller et al., 2013; Choi et al., 2016; Torabi et al., 2019). Band intensity is only recorded for 2m of available outcrop, and so we use this as an absolute minimum for damage zone half width for the purposes of plotting displacement-width trends. In the fluvial succession, deformation band intensity is lower, despite an increase in displacement of approximately 30cm, with an inner zone recording an average of 9m of deformation bands per 0.25m², reducing to 6m in an outer zone approximately 1.8m from the fault plane, and is observed for a total of 4.8m of observable outcrop, which we use for an absolute minimum measure of damage zone half width.

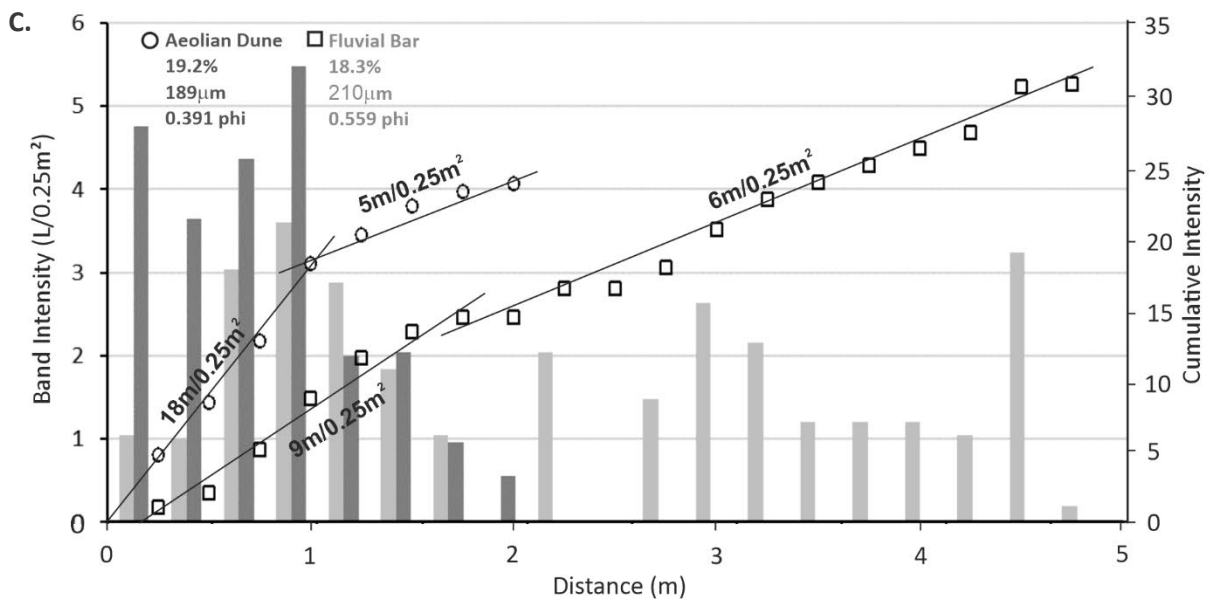
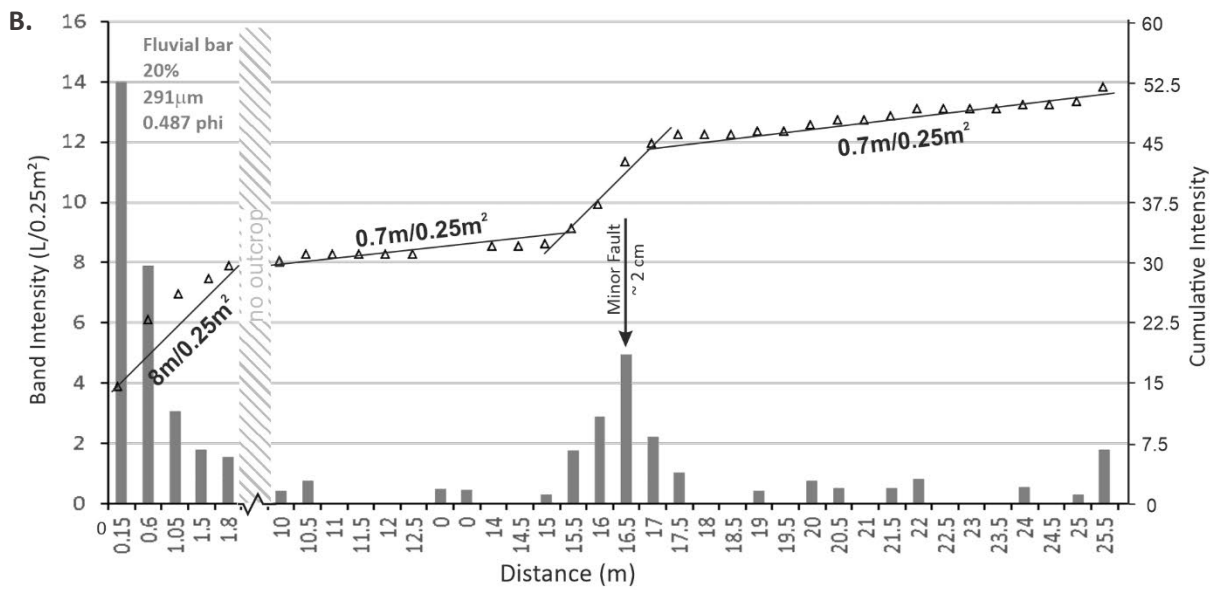
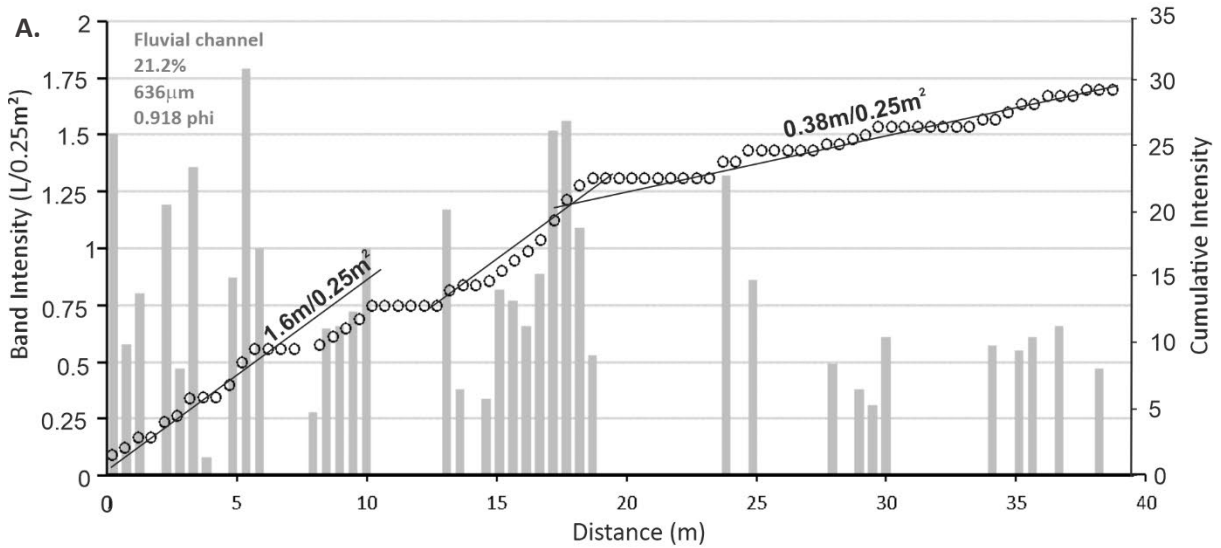


Figure 6.1. Linear and cumulative plots of deformation band intensity for a series of fault damage zones within different lithologies. Lithological properties are included in each plot. (a) Footwall of the Helsby Hill Fault within a medium-grained fluvial sandstone. (b) Hanging wall of the Helsby Hill Fault within a medium-grained fluvial sandstone. (c) Hanging wall of the Grinshill Hill Fault within a fine-grained fluvial sandstone, and Corbet Wood Fault within a fine-grained aeolian dune sandstone at Grinshill.

Deformation band frequency, sometimes referred to as one-dimensional density (P10) (Fig. 3.5) is recorded in 30cm intervals within a ~6m thick succession of coarse-grained, very well-sorted aeolian dune facies at Telegraph Road in Thurstaston, with 2 fault planes of approximately 19 and 64 cm displacement in close proximity (<3m) to one another, and provides a high density damage zone within texturally very mature sandstones (Griffiths et al., 2016). The cumulative frequency of deformation bands reveals two clear sub-zones within the damage zones of these faults. An inner zone of 31 and 53 bands per metre, reducing to an average of 10 and 11 bands per meter in the outer zone, 2-3 m from the fault planes which extends for total observable distance of 6 m. To compare linear 1-dimensional measurements of band intensity to areal 2-dimensional measurements, assumptions of the length, geometry and orientation of the bands must be made, making any interpretation of P21 from P10 measurements an inaccurate and underrepresentation of the outcrop (Fig. 3.5). None the less, for the purposes of comparison to other outcrops, the Thurstaston data may be compared to other localities. 53 bands per meter equates to 26.5 for the same sample area of the other localities. Assuming full length, straight geometry, and perpendicular geometry within a 0.5x0.5m area, this gives a 2-dimensional intensity estimate of approximately

13.25m/0.25m² in the Inner damage zone, and 2.75m/0.25m² for the outer damage zone for fault 1, and 7.75m and 2.5m for fault 2. Allowing some comparison to other fault damage zones.

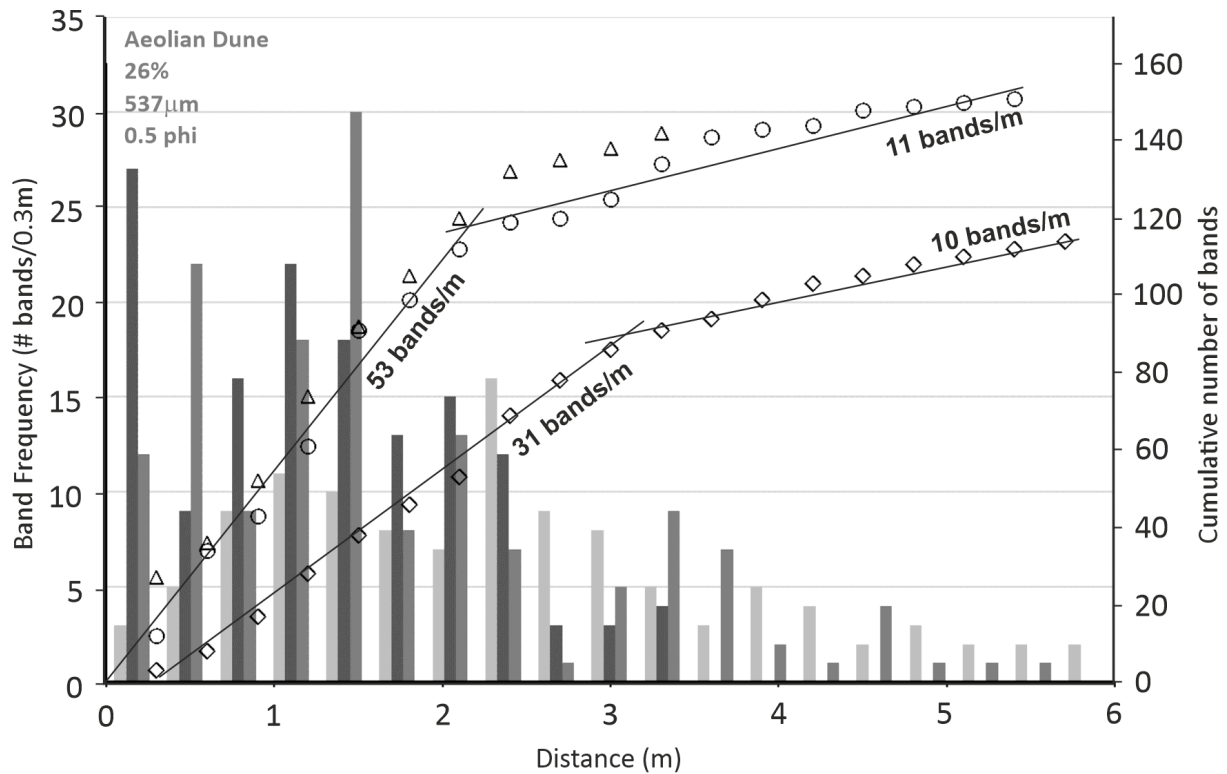


Figure 6.2. Deformation band density for fault damage zones at Telegraph road, Thurstaston. Data from Griffiths et al. (2016). Both damage zones occur in coarse-grained quartz arenites, aeolian in origin, adjacent to faults with displacements of approx. 19 and 64 cm.

6.2.2. Pease Bay

At Pease Bay, deformation band intensity was also measured for 7 different lithologies of 3 different faults (Fig. 6.3). Fault damage zone 4 (FDZ4), within a fine- to medium-grained, well-sorted sandstone of aeolian dune facies association with a porosity of 23.9%, records an average band intensity of $6.2\text{m}/0.25\text{m}^2$, which extends for a distance of 17m, including an area of no available outcrop, after which band intensity decreases to 1.7m per unit area, extending for 26m, with the exception of a number of minor faults with bedding offsets indicating displacements of less than 20cm, resulting in localised spikes in band intensity of 12m per unit area. As the fault plane for this damage zone is not directly observed, we interpret the change in band intensity as a minimum estimate of damage zone half width.

Fault damage zone 3 (FDZ3) contains four lithologies of fluvial channel facies association. Band intensity in the thickest unit of the poorly-sorted, medium-grained sandstone shows a spatial relationship and intensity decline with distance from the fault. A spike in band intensity in the uppermost bed is recorded at 1.5 metres, corresponding to deformation band occurrence in the underlying fine- and medium-grained sandstones. Deformation bands or fractures are not observed in the thin (15cm) mudstone (Fig. 4.15c). Plots of cumulative intensity show the highest average intensity of $6\text{m}/0.25\text{m}^2$ in Bed 1, a poorly-sorted medium-grained sandstone, whilst the underlying finer-grained and thinner Beds 3 and 4 show lower intensities of 3.5 and 2.1m bands respectively (Fig.6.3).

Three lithologies of fluvial overbank and floodplain facies association are recorded in fault damage zone 5 (FDZ5), adjacent to a fault with displacement of 1.5m. In comparison to FDZ3, a sandstone dominated sequence with subordinate mudstone, this fault zone displays a succession dominated by mudstones with subordinate sandstones (Fig. 4.15e). The thickest

and finest grained unit, a 1.22m thick laminated mudstone, contains antithetic faults to the main fault with small displacements (7-18cm) and has an average fracture density of 3.3 metres of fractures per 0.25m². The antithetic faults observed in the mudstone occur as deformation bands within the underlying sandstone beds, and often result in a spike in band intensity due to deformation band clustering. Unlike deformation bands, fractures show no increase in density where minor faults are present, indicative of their strain weakening behaviour (Marone et al., 1990). The second unit, a 30cm thick, fine-grained laminated sandstone, shows an average intensity of 5m/0.25m². The third unit, the thinnest at 25cm, is a medium-grained, cross-bedded sandstone and records an average intensity of 17m/0.25m², with significant band clustering at the site of the overlying antithetic faults (Fig. 6.3).

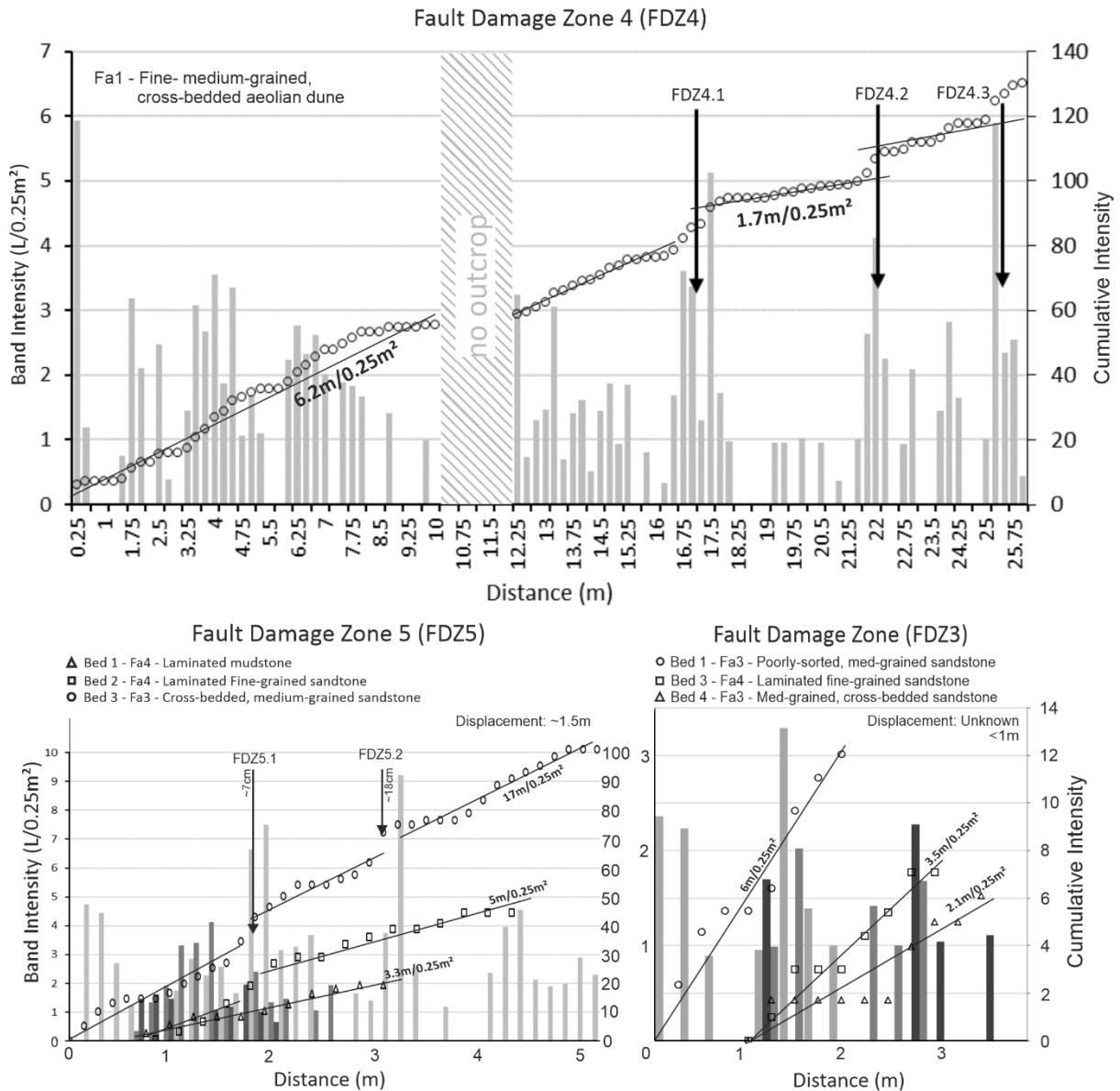


Figure 6.3. Intensity and cumulative Intensity plots of deformation bands within different lithofacies in three fault zones, FDZ3, FDZ4 and FDZ5. Bands decay logarithmically with distance in FDZ4 up until a series of minor faults induce spikes in frequency. The cumulative data plot shows damage zone intensity of $6.2m/0.25m^2$, until 17m where a decrease to $1.7m/0.25m^2$ is observed. FDZ5 and FDZ3 show band intensity within three distinct lithologies, with minor faults corresponding to peaks in intensity. Cumulative intensity shows variation in average band intensity (trend lines) between lithofacies.

6.3. Deformation Band Width

Width measurements of individual deformation bands in sandstones were taken for each damage zone transect, and are plotted as histograms (Fig. 6.4 & 6.5). There is a high degree of variability in overall band widths from 0.2 mm up to 30 mm within individual sandstone units, indicating width variation along their lengths, and between different sedimentary units, demonstrating the effects of lithology on band widths. The development of deformation band lenses is well documented (Awdal et al., 2014) and appear as very localised increases in band width. These can be observed as outliers in the histogram data. These lenses are classified as being twice the median width of all width measurements. We then record the mean for deformation bands below this width threshold, and the mean for deformation band lenses above this threshold width. In mudstones and siltstones, the deformation structure type differs, having fractures of effectively zero measurable width, and are therefore not included.

6.3.1. Pease Bay

Deformation bands in FDZ3 display a wide range of width variation in three of the four beds in which damage zone transects were recorded (Fig. 6.4). Bed 1, a medium-grained sandstone, shows a log-normal distribution of widths, with the peak of the distribution corresponding to a median width of approx. 2.65mm. A mean band width of 2.4mm, and lenses of 6.65mm. Bed 3 at Locality 4, a fine-grained sandstone, shows a similar width distribution over a much finer range, having a median width of 1.95mm, mean band width of 1.94mm and lenses of 4.05mm. Bed 4, a medium- coarse-grained, poorly-sorted sandstone, shows the most width variation, with a median of 5.25mm, mean band width of 4.58mm, showing a greater potential for fault lenses and width variation, with 20% of bands greater than 10mm, with a mean width of 11.75.

Deformation band width was measured for two of three units in FDZ5, both sandstones, and records much thinner band widths than those within FDZ3. Bed 2, a fine-grained sandstone, records a median and mean width of 1.5mm and 1.71mm respectively, with lenses of 4.9mm. Bed 3, a medium-grained fluvial sandstone, records a very narrow distribution. with a mean and median width of 0.6mm with very little width variation and no record of lenses.

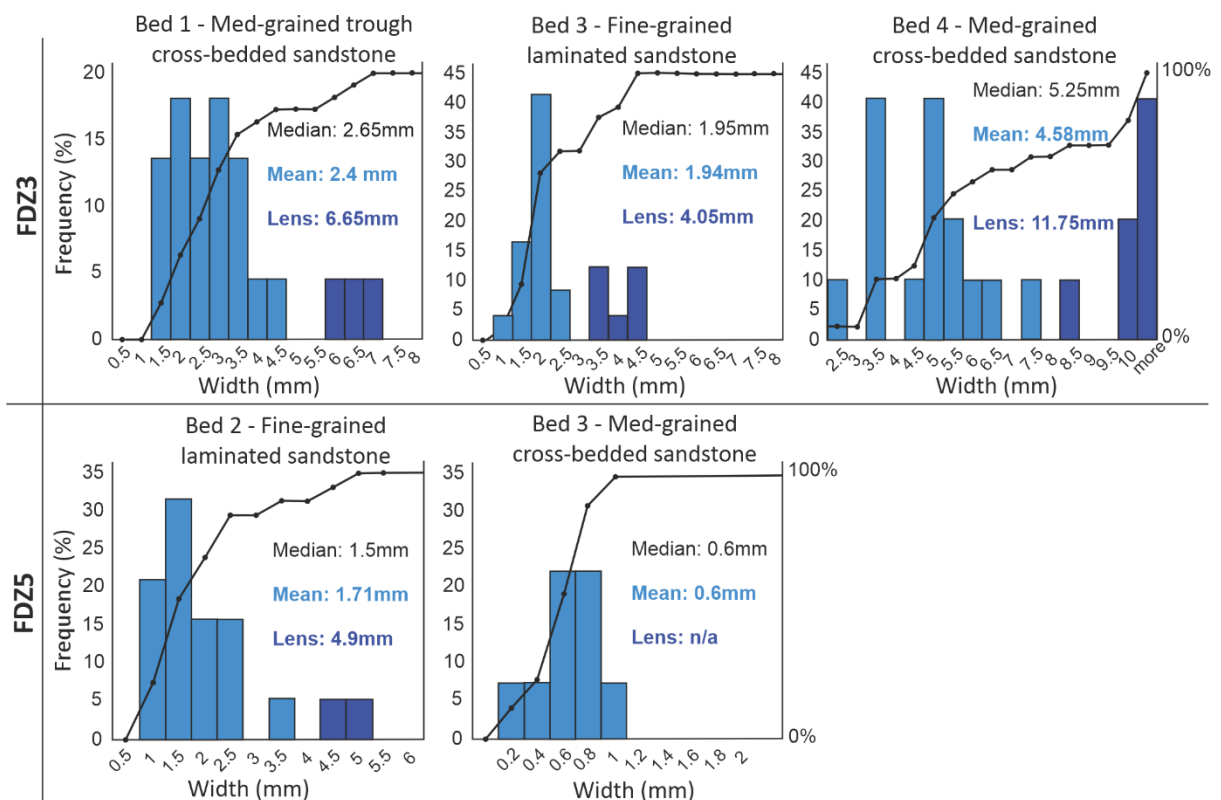


Figure 6.4. Histograms of deformation band width for fault zones at Pease Bay.

6.3.2. Cheshire Basin

The widths of individual deformation bands were recorded within the corresponding units of each fault damage zone transect across the Cheshire Basin localities. Only single deformation bands were measured in the field, choosing to omit deformation band clusters, which are amalgamations of individual deformation bands, so as to not skew any interpretations of the data. Deformation band width varies greatly across the localities and within individual sedimentary units, with widths between 0.3mm and up to 81mm. We classify deformation band lenses in the same manner as for Pease Bay. Deformation band width is presented in histograms for a number of different lithofacies (Fig. 6.5). Average deformation band width varies between the different units from 0.5mm to 4.1mm, whilst deformation band lenses vary between 4mm and 17mm. Fluvial lithofacies from Helsby and Grinshill display the thickest deformation bands (3.1-4mm) and lenses (12-17mm), and the most thickness variation (Fig. 6.5a-c,h). Aeolian lithofacies of Nesscliffe, Thurstaston and Grinshill display the thinnest deformation bands (0.5-2mm) and lenses (4-6.5mm) with the least thickness variation (Fig. 6.5d-g).

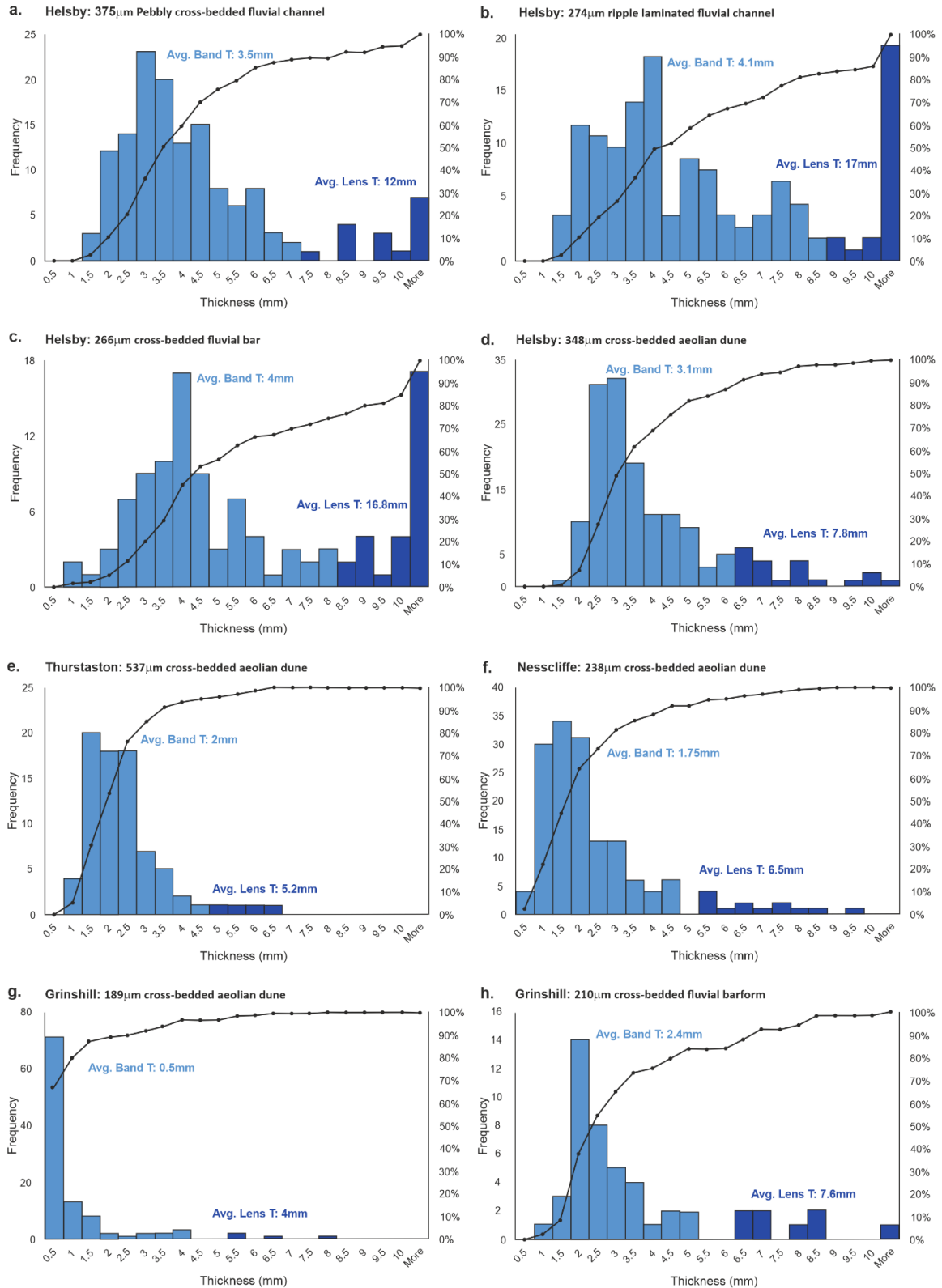


Figure 6.5. Histograms of deformation band width for a variety of lithologies within fault damage zones of the Cheshire Basin case study.

6.4. Discussion

6.4.1. Deformation band geometry

Anderson's theory of faulting predicts a normal faulting angle of 60° in accordance with Coulomb failure criterion (Anderson, 1905). Faults across the localities of this study are all recorded or observed as being normal with minor components of strike-slip displacement, and show moderate to high angles of dip between $59-79^\circ$ with a mean of 69.5° . Small components of strike-slip displacement may account for steeper than Andersonian fault dip values. Deformation bands across the localities of this study show a conjugate geometry, with sets of bands dipping at similar angles to the principal fault plane with which they are associated. Because Anderson's theory predicts a fault angle of 60° , or 30° to the maximum principal stress, a dihedral angle between conjugate dipping sets of faults of 60° is predicted ($2 \times \theta \sigma_1$). However, the formation of angles of deformation bands is not accurately predicted by this criterion due to lack of consideration of volume changes (Schultz, 2019). Results by Klimczak and Schultz (2013) show that the angle of conjugate deformation bands to the maximum principal stress decreases with increasing amounts of dilation, or in terms of deformation band type, from compaction bands, shear-enhanced compaction bands, compactional shear bands, shear bands, to finally dilatational shear bands, and predicts dihedral angles as low as 20° . Dihedral angles of between $20-60^\circ$ for the mean plane of opposing dipping sets of deformation bands are recorded here. A summary of fault and deformation band geometry is shown in figure 6.6. Variations in the dihedral angle of deformation bands and the dip of major faults across the localities may reflect subtle differences in band type. For example, Nesscliffe records very steep dip angles of $\sim 80^\circ$ with small dihedral angle of $\sim 20^\circ$, which may reflect deformation bands with a greater component

of shear and less compaction, than other localities with lower dip angles and therefore higher dihedral angles, such as Pease Bay or Helsby Quarry with fault dip and dihedral angles of $\sim 60^\circ$. Such changes in deformation band type may therefore be recognised in microstructural analysis, supporting this relationship between conjugate deformation band angle and deformation mechanism. Indeed, it is observed in petrographic analysis that the deformation bands at Nesscliffe show less texturally mature micro-breccia textures (Fig. 5.3e), whereas those at Helsby, with shallower dip and larger dihedral angles display proto-cataclastic to cataclastic textures. The latter of which record greater reductions in permeability. The angle of faulting and deformation band formation may then be used to infer petrophysical modifications in the reservoir.

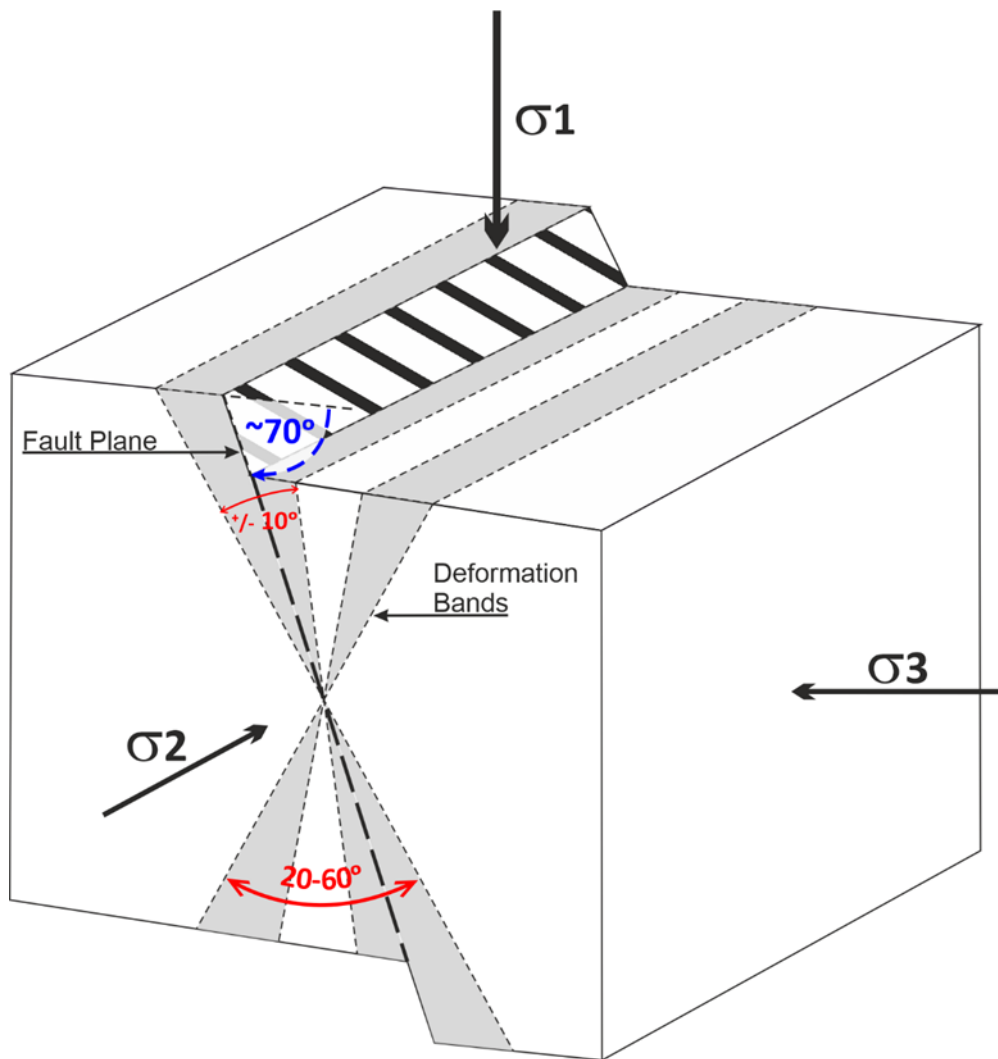


Figure 6.6. Summary diagram showing faulting and deformation band geometry across the localities of the study.

6.4.2. Displacement versus damage zone width scaling

Previous studies have defined damage zone width using cumulative band frequency plots by marking the point at which intensity changes to what might be considered 'background levels' of deformation (Choi et al., 2016; Torabi et al., 2019). In some cases, the damage zone width can be defined by this change in gradient to background levels of deformation, where logarithmic decay with distance is no longer observed, or where band spacing becomes increased. A change in band intensity to low levels of $<2\text{m}/0.25\text{m}^2$ for a number of transects is observed (Fig. 6.1 & 6.3). However, in many cases this change in deformation band intensity is not observed and consequently, the damage zone width cannot be estimated with much accuracy. However, linear trends of cumulative number of bands, with confidence of 83-99 % over the complete transect distance give a robust estimate of band intensity for the distance recorded, and therefore, this distance is used as a minimum damage zone width in order to see how damage zone width and displacement trends develop. As many of the damage zone transects measure only one side of the damage zone of the fault, or half-width, with the exception of the Helsby Hill fault for which both hangingwall and footwall are recorded (Fig. 6.1), damage zone width estimates are multiplied by 2 in order to compare data with published examples of total damage zone width (Choi et al., 2016). These results are summarised in table 6. Plotting these estimations of damage zone width and displacement shows a high degree of scatter in log-log space of up to two orders of magnitude, however, they show an overall power-law distribution with an exponent of 0.68. The data from this thesis show a similar power-law trend in displacement-width with an exponent of 0.58, even despite best estimates of both damage zone width and displacement (Fig. 6.7). A positive correlation between deformation band intensity and displacement is not observed, suggesting that damage zone intensity may be more strongly controlled by lithological factors,

and supporting the use and comparison of cumulative number of bands between faults of varying displacements, as indicated in models of fault damage zone growth (Schueller et al., 2013) (Fig. 3.6).

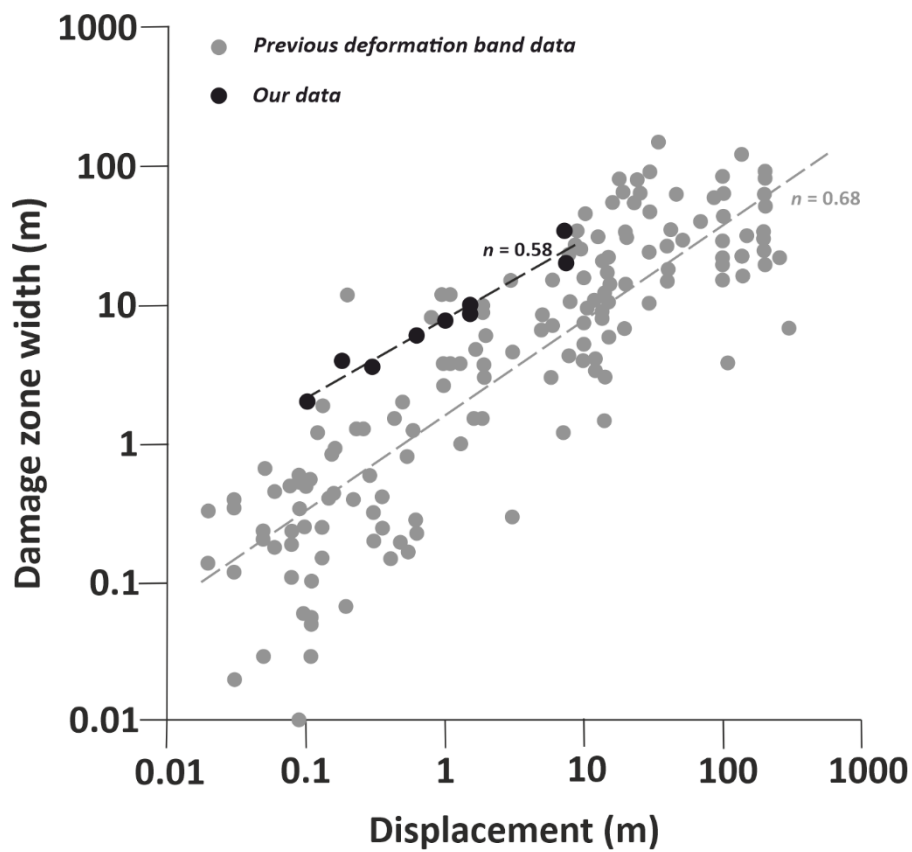


Figure 6.7. Log-log plots of deformation band damage zone width versus displacement. Previous data compiled by Choi et al. (2016) and references therein.

6.4.3. Lithological Control on Deformation Band Attributes

A total of fourteen deformation band damage zones are recorded adjacent to major faults of varying displacements, in a range of different lithofacies of both aeolian and fluvial origin, in which the intensity of deformation bands and their width are recorded. These band attributes show a great deal of variation in fault zones with variations in lithofacies and therefore in porosity, grain size and sorting. Deformation band intensity is plotted for both inner and outer fault damage zones where observed, as well as deformation band and lens width, against lithological properties such as grain size, sorting, and the thickness of the beds or successions (Fig. 6.8). Although quantitative measures of lithological properties were not obtained for Pease Bay, little to no correlation of band intensity with grain size or porosity on a qualitative level is observed, that has been recorded in other studies (Schultz et al., 2010). For damage zones across the Cheshire Basin, no correlation with porosity is observed, although porosity values of host sandstones have a relatively narrow range of 18-26%, which is considered high for band formation, and may not offer the variance to observe any influence of porosity on the intensity of deformation bands. A negative trend between grain size and band intensity of both the inner and outer zones is observed, with low to moderate correlations of 0.34 and 0.45 respectively (Fig. 6.8a). This result is conflicting with current understandings of both band formation and the mechanical properties of sandstones, which are governed so strongly by grain size and porosity (Sammis and Ashby, 1986; Wong, 1990; Zhang et al., 1990; Wong and Baud, 1999). These results suggest that, at least for these examples, band intensity maybe controlled by other factors such as sorting, or bed thickness, which introduces the concept of mechanical stratigraphy playing an important role in strain distribution in mixed lithology successions. Plots of deformation band intensity for both inner and outer damage zones against grain sorting, shows negative trends, with a particularly strong trend for the inner-

most damage zone, with moderate correlation coefficient of $R^2 = 0.62$ (Fig. 6.8c & e), showing that band intensity decreases in poorly sorted sandstones, typically of fluvial association. This observation agrees with current understanding of band formation, where poorer sorting is found to inhibit band localization (Cheung et al., 2012). It is also worth considering that the coarser lithologies of this study are typically of fluvial association, which demonstrate wider grain size distributions and poorer sorting than aeolian facies. Slightly higher band intensities in aeolian lithofacies than in fluvial lithofacies are observed, which may then explain the negative trend observed with grain size.

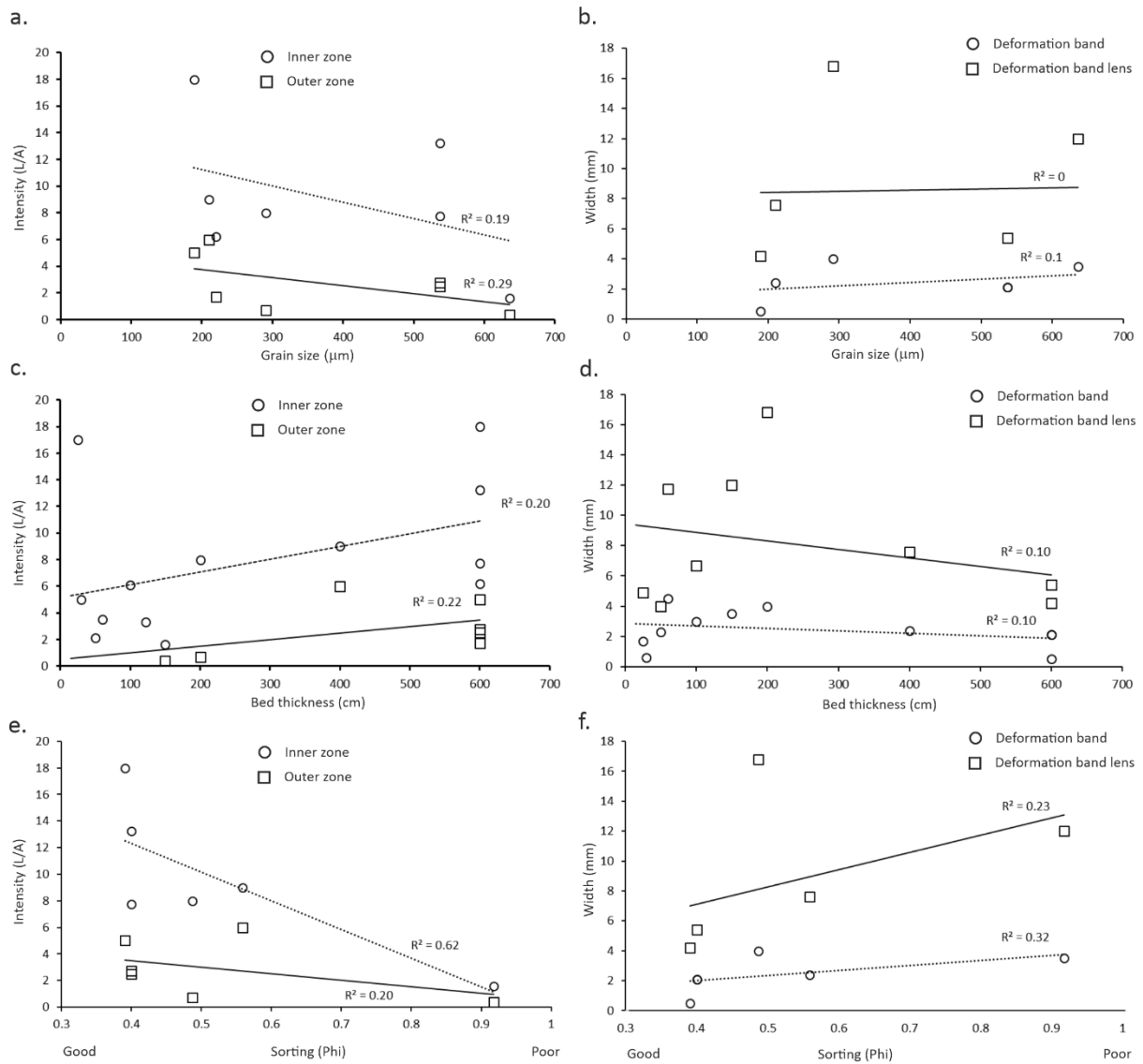


Figure 6.8. Cross-plots of deformation band attributes with lithological properties. (a) Inner and outer damage zone intensity against grain size. (b) Deformation band and lens width against grain size. (c) Inner and outer damage zone intensity against bed thickness. (d) Deformation band and lens width against bed thickness. (e) Inner and outer damage zone intensity against sorting. (f) Deformation band and lens width against sorting.

When considering fluid flow through a deformation band damage zone, we must consider their cumulative thickness, and therefore understand their mean deformation band thickness in combination with their spatial distribution. A wide range of band widths between different lithofacies are observed across the fault damage zones of the study. In such lithologically variable successions as the Devonian Old Red Sandstone and Triassic Sherwood Sandstone, which exhibit both very favourable and unfavourable lithologies for band formation in terms of their grain sorting, deformation band morphology is likely to be highly variable, with changes in lithological variables influencing along-strike variations in deformation band width. Rotevatn et al. (2013) discussed the role of natural along-strike width variation in the form of lenses, on cross-band fluid flow using fluid flow simulations, concluding that variation in deformation band width has little impact on the overall fluid propagation front, which takes a path of least resistance, and therefore the mean width of deformation bands is a more important factor on effective permeability than along strike width variation. A positive correlation between band width and grain size is logical for cataclastic deformation bands, which deform via grain-to-grain fracturing (Sammis et al., 1987), thus a larger grain size results in a wider zone of cataclasis proportional to the size of the grains. Comparing band width data, there appears more variation and inconsistencies in both the band and lens widths between different lithologies than can be attributed to grain size control alone, with no correlations between band or lens width with grain size (Fig. 6.8b). Whilst at some localities there is a trend in increasing band width with the grain size of the host sandstone (Pease Bay, FDZ3. Fig. 6.4), at others the coarser sandstone has the narrowest bands with the least width variation of all of those measured (Thurstaston, Fig. 6.5e). Width variation may therefore be controlled by variables other than grain size, such as sorting. A weak positive correlation between deformation band width and grain sorting is found. That is, band width increases

with poorer levels of sorting and wider grain size distributions (Fig. 6.8f). Sorting appears then to partly control both the intensity and width of deformation bands. In well-sorted sandstones, typically aeolian, the potential for deformation band formation remains high, showing that they deform via the nucleation of additional bands as opposed to increasing the width of existing bands. This may be due to the ease with which localisation occurs within such sandstones, or perhaps strain hardening is more easily achieved, resulting in strain accommodation through new band nucleation. The opposite may be true of poorly-sorted sandstones, which have been shown to inhibit strain localisation (Cheung et al., 2012), and do not nucleate bands or strain harden as easily (Crawford et al., 2004). This predisposition may then result in lower band intensity, and accommodation of strain through increased width as opposed to nucleation of new bands. To support this theory, band width is plotted by facies association; well-sorted aeolian facies, and poorly-sorted fluvial facies. Two main distributions are shown by the data (Fig. 6.9); a normal distribution in the fluvial lithofacies, which are generally more poorly-sorted, showing a high degree of width variation with a mean deformation band width of 3.3mm and a lens width of 12mm. Aeolian lithofacies show a log-normal distribution with much less width variation, with a 40% narrower mean band width of 2mm, and nearly 50% narrower lens width of 6.6mm.

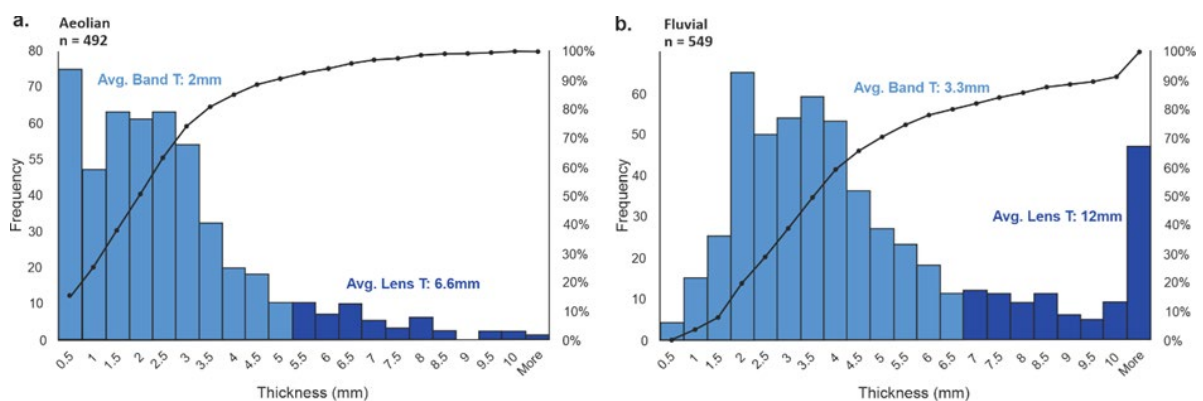


Figure 6.9. Deformation band width data by facies association

6.4.4. Role of Bed Thickness

The relationship between bed thickness and the development of stress induced structures is well documented for jointing in fractured reservoirs, particularly in shales and carbonates, showing that fracture frequency decreases as bed thickness increases. The question of whether deformation bands exhibit a similar bed thickness control is an important one, especially for understanding deformation band formation in reservoirs which exhibit a high degree of lithology and bed thickness variation. The same relationship as for jointing cannot be assumed for deformation bands in sandstones as they do not form under tension, and the stresses required for band formation are extremely varied (Wong, 1990; Wong et al., 1997; Mair et al., 2002). A limited number of studies report a wider damage zone width with increasing bed thickness (Heynekamp et al., 1999), and that the opposite spacing trend is observed: deformation band frequency increases with bed thickness. Johansen and Fossen (2008) report a bi-linear correlation between bed thickness and deformation band density, with a linear correlation at thicknesses <3m, and no dependence at thicknesses greater than this up to 25m. Modelled fault damage zone growth models suggest average band density thresholds of approximately 15 bands per metre independent of fault displacement (Schueller et al., 2013). However, this is contrary to the high band densities in and around fault cores and slip surfaces in thick aeolian sandstones sequences of Utah, USA, which has been shown to increase to values of ~100 bands (Johansen and Fossen, 2008). This may indicate greater potential for band formation and clustering within thicker successions. Weak positive trends of deformation band intensity of both the inner and outer fault damage zones with bed thickness are found, with low correlation coefficients of $R^2=0.2$ and $R^2=0.22$ respectively (Fig. 6.8c). There is large scatter in the data and very little correlation with bed thickness and deformation band width (Fig. 6.8d) although a minor negative trend is observed. It is difficult

to ascertain if any relationship between bed thickness and intensity is entirely causal or due to natural thickness variations of different depositional facies that have higher potential for band formation. For example, finer grained facies such as interdune small-scale dunes and small fluvial deposits are typically much thinner than coarser grained facies of larger scale aeolian dunes or fluvial channel systems, which exhibit greater potential for deformation band formation. Any relationship does pose an important question of the role of mechanical stratigraphy, which encompasses the control of mechanical properties and thicknesses of units on fault properties when lithological description alone cannot explain them (Ferrill et al., 2017). The ratio of competent (sandstone) to incompetent beds (mudstone) is an important factor in strain distribution, leading to more variable fault zone widths and fault zone damage intensity. In successions with high ratios of incompetent-competent beds, fault nucleation begins in thin competent sandstone beds, and may explain the high deformation band densities observed in the thin sandstone of FDZ5 at Pease Bay (Fig. 6.3) (Schöpfer et al., 2006). More work on the effects of mechanical stratigraphy on deformation band formation is required.

6.4.5. Implications for Fluid Flow

The impact of deformation structures on the petrophysical properties of a hydrocarbon, geothermal or carbon capture reservoir depends on the type of damage zone structure produced, which itself is a function of the textural and petrophysical properties of the host rock and the stresses under which they form. Experimental studies on the failure of porous rocks have shown that the strength of a rock increases with decreasing porosity and grain size (Zhang et al., 1990; Wong and Baud, 1999; Schultz et al., 2010). This relationship has been observed in fault damage zones in outcrop, where the damage zone width, the type of deformation structure, and the frequency varies with porosity and grain size (Schultz and

Siddharthan, 2005). However, our findings show that porosity and grain size are not the dominant factors controlling damage zone width and the intensity of deformation bands (Chapter 6.2), but are a major control on the type of deformation band formed, and the petrophysical properties of the bands. Variation in deformation structure amongst different lithologies is observed across the localities at Pease Bay with fractures and dilatational deformation bands forming in mudstones and siltstones, and cataclastic deformation bands within coarser grained facies. Often it is observed that deformation band structures vary along their length, changing from fractures within a mudstone into cataclastic deformation bands as they pass into underlying sandstone (Fig. 4.15e). This has huge implications for the petrophysical properties of these successions since fracture development acts to create permeable pathways in an otherwise impermeable rock, whereas cataclastic deformation bands generally create lower permeability baffles in an otherwise permeable rock (Ballas et al., 2015). Evidence for fluid flow along fractures in the mudstones and siltstones is seen by a colour change along their length and into the walls of the fractures, indicating diagenetic modification due to the presence of fluids. The same diagenetic alteration is observed in the deformation bands of fine-grained sandstones indicating that they have also been conduits for fluid flow (Fig. 6.10a). This indicates different kinematics and deformation mechanisms compared to the more common cataclastic compaction bands observed in the coarser sandstones of aeolian dune and fluvial channel associations, which typically show diagenetic evidence of fluid baffling by cataclastic deformation band clusters (Fig. 6.10b). Variations in deformation structures can be graphically represented using the Q-P-r diagram, which plots the yield envelope of a rock of any given porosity and grain size (z axis) in stress space (x and y axis) (Fig. 6.10c). The yield envelope defines the point of rock failure in terms of differential and effective mean stress, for which the failure mechanism varies. The peaks of the yield

envelopes, can be joined by a line dividing the yield envelopes broadly into two regions, a dilating regime, which is regarded as porosity enhancing, in which dilatational deformation bands or shear fractures may be formed, and the compacting regime (light grey, Fig. 6.10c), which is porosity reducing, in which shear enhanced compaction bands and pure compaction bands may be formed. For a single stress path, two different rocks such as those presented in figure 6.10a & b, may fail in different regions of their yield envelopes resulting in very different damage structures.

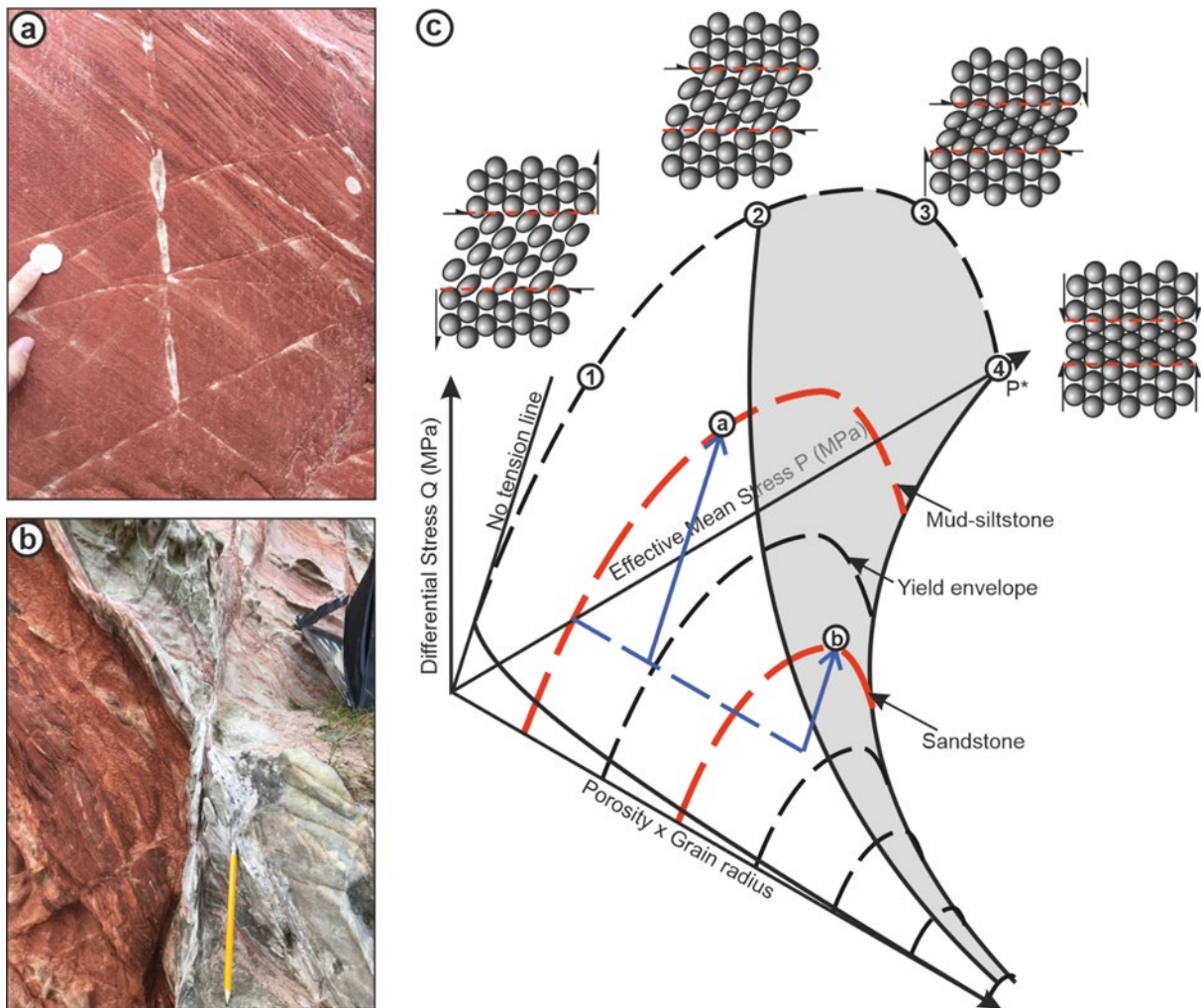


Figure 6.10. (a) An example of a deformation band providing a conduit to fluid flow due to porosity increase due to dilation. (b) An example of a deformation band acting as a fluid flow barrier due to porosity loss due to compaction. (c) Q-P-r diagram showing how the strength of porous rocks scales with grain size and porosity. Q is differential stress, P is effective mean stress, and r is porosity x grain radius. The peaks of yield envelopes join to separate two regions of deformation: dilation and porosity increase (1), and compaction and porosity loss (3). This illustrates how a single stress path (blue arrows) can lead to different types of rock failure and deformation structure.

Such variation in fault structures and their internal fluid flow properties must be considered in reservoirs with complex lithofacies variation and interactions to completely understand their effect on reservoir scale fluid flow behaviour. Since deformation band formation is related to two major controls on permeability, the grain size and porosity, they can control the bulk reservoir properties. It has been suggested that deformation bands may homogenise reservoirs and act to improve sweep by forming only in, and baffling, those units with good reservoir quality, such that the effective permeability is reduced to levels of the lesser permeable units (Fossen et al., 2011a; Fossen et al., 2018). It is also suggested that sorting is a major control on strain localisation (Cheung et al., 2012), inhibiting deformation band formation in fluvial facies, which typically comprise texturally and mineralogically immature sediments. On this basis it may be assumed that in a mixed aeolian-fluvial reservoir, the texturally mature aeolian units are more affected by deformation band formation, whilst the fluvial units remain little affected. Consequently, the aeolian units would become homogenised with the fluvial units in terms of permeability. However, the results here show the contrary, that deformation band formation is very prominent in both aeolian *and* fluvial lithofacies. If fluvial units are equally affected by permeability reducing deformation bands, either in terms of band density, or in terms of cumulative thickness as these results show, then heterogeneity of the reservoir may be maintained, although, if permeability enhancing deformation bands and fractures are present, the connectivity of different reservoir units could be improved. Permeability reduction due to cataclastic deformation bands is on average between 3 to 5 orders of magnitude, with the amount of cataclasis and grain size reduction being the major control.

6.5. Conclusions

The effects of deformation bands on the bulk fluid flow properties of a mixed aeolian-fluvial reservoir requires understanding of the spatial distribution, geometry, and the types of structures and their effects on relative permeability. Areal based measurements of fault damage zones more accurately capture subtleties in intensity between different sedimentary units, whilst also capturing differences in band geometry. This allows variations in fault zone attributes to be captured at scales where heterogeneity may exist, allowing for better understanding of processes and controls, leading to more accurate damage zone models and ultimately prediction of such features in the subsurface.

Deformation bands form in a conjugate geometry to the principal stress direction, with faults and deformation bands forming at angles of between 60-80 degrees. We show that the angle of faulting and dihedral angle of deformation bands, which is controlled by stress, influences the deformation mechanism and therefore the texture and petrophysical properties of the bands. Stress therefore plays an important role in the type of deformation band formed and the petrophysical properties of the bands.

Through detailed measurements of band Intensity, band width, bed thickness, and structure type within two major case studies of heterogenous fluvial and aeolian siliciclastic successions, it is concluded that sandstone facies variation can exert controls on many aspects of fault damage zones including the type of deformation band structure formed, the intensity of deformation bands, and their width. The Intensity of deformation bands within fault damage zones shows weak correlations with grain size and porosity of the host sandstone, and cannot wholly explain their occurrence or morphology. Grain sorting is identified as a primary control on deformation band intensity and their width. Poorly sorted sandstones typically display lower intensity deformation bands, but consistently develop thicker

deformation bands with greater thickness variations. Although this trend with sorting and not grain size may be attributed to coarser sandstones in this study being of a poorer level of sorting. Bed thickness is found to be a significant control on deformation band development. Whilst there is an overall positive correlation with band density at thicknesses below 10m, particularly shown in the Cheshire Basin case study, outcrops at Pease Bay show the opposite trend, with deformation band density highest in thin, isolated sandstone beds, indicating that mechanical stratigraphy may play an important role in the nucleation and density of deformation bands, particularly with high ratios of incompetent-competent lithologies at small bed scales <1.5m. Deformation band width shows a negative correlation with band density, indicating that some sandstones deform via the nucleation of additional bands as opposed to increasing the width of existing bands. This is attributed to other textural controls that govern both localisation and strain hardening behaviour, such as grain sorting. Fluvial lithofacies consistently display thicker deformation bands than aeolian lithofacies, whilst also showing greater band width variation and the development of deformation band lenses. This has major implications for the modelling of fault damage zones and the prediction of deformation bands in the subsurface, as fluvial lithofacies are typically regarded as non-favourable for their formation. The results show that such units can develop deformation bands in mixed-successions, and their lower deformation band intensities may be outweighed by increased thickness and thickness variations, an important consideration for fluid flow models.

7. Insights from experimental rock mechanics

7.1. Introduction

In previous chapters it has been found that grain sorting is a very important factor in the formation of, and properties of deformation bands in mixed aeolian-fluvial reservoirs. Current understanding of the role of sorting on the deformation of sandstones is drawn from field studies and laboratory experiments in which sorting is poorly constrained, and other variables such as porosity, grain size and mineralogy are poorly controlled and accounted for. In this chapter, results of triaxial deformation experiments on unconsolidated quartz sand aggregates are presented. Unconsolidated materials offer the unique opportunity to precisely control and study lithological variables. In this work, porosity, grain size and mineralogy are fixed, while sorting is systematically varied. The role of sorting on the elastic and inelastic deformation, and the micromechanics of deformation with increasing stress, accompanied by fractal grain size analysis, with an aim to link grain textures to deformation mechanisms and fluid flow properties.

As siliciclastic sediments are deposited and buried in a sedimentary basin they undergo a range of diagenetic processes, turning unconsolidated sands into consolidated sandstones over thousands to millions of years. These processes include diagenetic chemical reactions, grain cementation and compaction of pore-space, all of which change the physical properties of the deposited materials. Compaction is the primary mechanism of porosity loss in sediments and occurs in response to increased stresses acting on the basin as a result of progressive burial or from compressive tectonic forces. In the initial stages of burial, compaction primarily occurs via mechanical processes such as grain rearrangement, grain crushing and localized faulting, with chemical compaction mechanisms such as dissolution of

mineral phases being more prevalent at greater depths (Worden and Burley, 2003). Compaction and porosity reduction strongly impact fluid flow and reduce permeability in sedimentary basins, which has important implications for reservoir production, as well as for potential injection sites for CO₂ storage projects. Thus, in order to fully understand the evolution of sedimentary basins, it is important to determine how sediments with different petrographic and physical properties respond to deformation and compaction.

There have been extensive experimental investigations into the inelastic deformation behaviour and micromechanics of porous sandstones e.g. (Wong et al., 1997; Cuss et al., 2003; Baud et al., 2006; Bedford et al., 2019), as well as many other types of porous rock including limestone (Baud et al., 2000; Vajdova et al., 2004; Cilona et al., 2014), volcanoclastics (Zhu et al., 2011; Heap et al., 2015a; Eggertsson et al., 2020) and rocks where porosity has formed via metamorphic devolatilization reactions (Rutter et al., 2009; Bedford et al., 2018). These studies have shown that inelastic deformation can be broadly divided into two macroscopic categories, brittle dilatant failure via fracturing and faulting at low effective pressures, and ductile compaction via cataclastic flow at higher effective pressures (Wong, 1990; Zhang et al., 1990; Wong et al., 1997; Mair et al., 2002; Charalampidou et al., 2011). The deformation may be further classified based on grain scale micromechanics, for which cataclasis, the process of grain size reduction via brittle fracturing and comminution, is the dominant mechanism by which porous sandstone compacts (Wong and Baud, 2012). Cataclasis may occur as a pervasive deformation mechanism, in which the entire rock deforms via bulk cataclastic flow accompanied by dilation or compaction, or it may localise, either as discrete or diffuse compaction bands. The process of cataclasis results in textural modification of the host material through grain size reduction. This textural change directly impacts the porosity

and permeability of the material and in the case of localised cataclasis, can lower permeability by up to five orders of magnitude (Fossen and Bale, 2007). In a fluid bearing reservoir, this has huge implications for the economic production of these fluids. It is therefore essential to understand the mechanism and textural evolution of cataclasis with stress in order to understand the petrophysical modifications. The failure and onset of cataclasis in porous sandstone is primarily influenced by the textural and petrophysical properties, in particular porosity and grain size, which are found to have a positive relationship with the inelastic grain crushing pressure (P^*) (Dunn et al., 1973; Zhang et al., 1990; Wong and Baud, 1999; Cuss et al., 2003; Rutter and Glover, 2012). Laboratory investigations have allowed the testing of sandstones with different properties over a range of stress conditions, providing insights into the lithological controls on deformation behaviour. However, due to the highly variable nature of natural sandstones it is difficult to systematically investigate the role of individual lithological properties on rock behaviour, producing uncertainty in our understanding of basin-scale evolution. The testing of unconsolidated sands, or artificially made sandstones enables the precise control of lithological variables whilst systematically varying those of interest. Experiments on unconsolidated materials also provides information on the deformation behaviour of sediments in the upper parts of a basin before any significant lithification or cementation has occurred.

7.1.1. Deformation of unconsolidated sands

A number of previous experimental deformation studies on unconsolidated materials have been performed to understand their evolution during simulated burial, including quantification of elastic and inelastic deformation during subcritical compaction (Karner et al., 2003), examining the effects of stress path on failure and permeability reduction (Nguyen

et al., 2014), and investigating the role of time-dependant compaction (Chester et al., 2004; Brzesowsky et al., 2014). Using unconsolidated materials in experimental studies allows for detailed investigations of the textural controls on micromechanics, with previous work on sands of different provenance highlighting that textural properties such as grain size and grain angularity affect the mechanical response and the yielding behaviour of unconsolidated sands (Crawford et al., 2004). The effects of porosity, grain size, and initial packing density (i.e. degree of consolidation prior to deformation) have also been examined by manipulating the starting material, where it is found that packing density effects the stiffness of the material and the shape of the stress-strain curve, with the onset of failure being controlled by porosity and grain size (Skurtveit et al., 2013; Skurtveit et al., 2014), similar to observations on consolidated sandstone (e.g. Zhang et al., 1990). However, the effect of grain sorting or grain size distribution (GSD) on the mechanical response and deformation of unconsolidated sands is not well understood. For example previous experimental work has suggested that localised cataclasis is inhibited in sandstones with poor grain sorting (Cheung et al., 2012), whereas field observations of deformation bands occurring in a variety of natural sandstones with a range of grain size distributions suggest that this is not always the case (Fossen and Bale (2007). It has also been shown previously that grain sorting has minimal effect on the stress-strain behaviour of unconsolidated sands, although the process of cataclasis is more prevalent in well-sorted sands due to enhanced grain comminution (Hangx and Brantut, 2019). However, there is still a sparsity of data on the role of cataclasis in the deformation of unconsolidated sands over a wide range of effective pressures and grain size distributions, and how the microphysical properties of the sand evolve with continued deformation.

Although little is known about the evolution of grain size distribution during the mechanical deformation of unconsolidated sands, it has been shown that in both naturally and

experimentally produced fault rocks that a fractal grain size distribution (i.e. one that is independent of scale, or self-similar) develops as a result of cataclasis (Marone et al., 1990; Blenkinsop, 1991). As cataclasis is the operative micromechanical process during failure of unconsolidated sands it would be expected that similar fractal distributions will develop to those observed in fault rocks. Fractal distributions have been reported in low permeability deformation bands within poorly consolidated sediments, although they exhibit a fractal dimensions of $D = 2.1$, suggesting that grain comminution may not be the sole deformation mechanism in their formation (Rawling and Goodwin, 2003). It is therefore important to understand the deformation mechanisms and the grain textures produced within unconsolidated sands with increasing stress, to understand the deformation history of sedimentary basins, fault rocks and their petrophysical evolution.

In this study the effects of grain sorting on the micromechanics and process of cataclasis are investigated, and the evolution of grain size and the development of fractal grain size distributions, by performing a suite of triaxial deformation experiments on unconsolidated quartz sands, in which we vary sorting whilst holding the mean grain size, porosity, and composition constant. Microstructural observations are made using scanning electron microscopy to identify the changing deformation mechanisms under different stress conditions, as well as investigate the role of grain size distribution on textural and permeability evolution in unconsolidated sands.

7.2. Methods

7.2.1. Sample material and preparation

The material used for the experiments is sourced from Pleistocene glacial deposits of the Chelford Sand Formation. The formation provides one of the UK's primary sources of 'frac

sand', a proppant for hydraulic fracturing of unconventional hydrocarbon reservoirs (Sammis and Ashby, 1986; Mitchell, 2015). Its suitability as a proppant, despite its glacial secondary origin, is owed to being primarily sourced from Permo-Triassic sandstones of predominantly aeolian origin, and as such, is very mineralogically mature, with 98.4% silica, and high textural maturity, with well-rounded, spherical grains (Fig. 7.1). Two sources of the sand were collected and used in the interest of obtaining a wide range of sizes, the first from the Dingle Bank Quarry near Chelford, and the second from the Arclid quarry in Congleton, known as the Congleton Sand, part of the Chelford Formation. As supplied, the Chelford Sand is unimodal, well-sorted, and coarse-grained with a mean grain size of 491 μm (Fig. 7.1a, b). The Congleton sand is supplied as unimodal, moderately well-sorted, and medium grained with a mean grain size of 308 μm (Fig. 7.1a, b). Despite differences in origin, both sands are texturally and mineralogically indistinguishable.

The sand was sieved into 100-micron bins, from 100 to 800 μm using sieve trays, and agitated using a shaking plate. Once sieved, samples were placed in to a Beckman Coulter LS13 320 Laser Particle Size Analyser (LPSA) to obtain grain size data for each bin. Grain size from LPSA analysis is given by both particle number (the number of particles of X size as % of total analysed) and by particle mass (as a % of total analysed mass). Data from LPSA was then processed using Gradistat, a program plug-in for Microsoft Excel, to obtain grain size distribution statistics such as mean, mode, sorting, skewness, kurtosis and a range of percentiles (Blott and Pye, 2001). An example of statistical output from Gradistat is shown in figure 7.2.

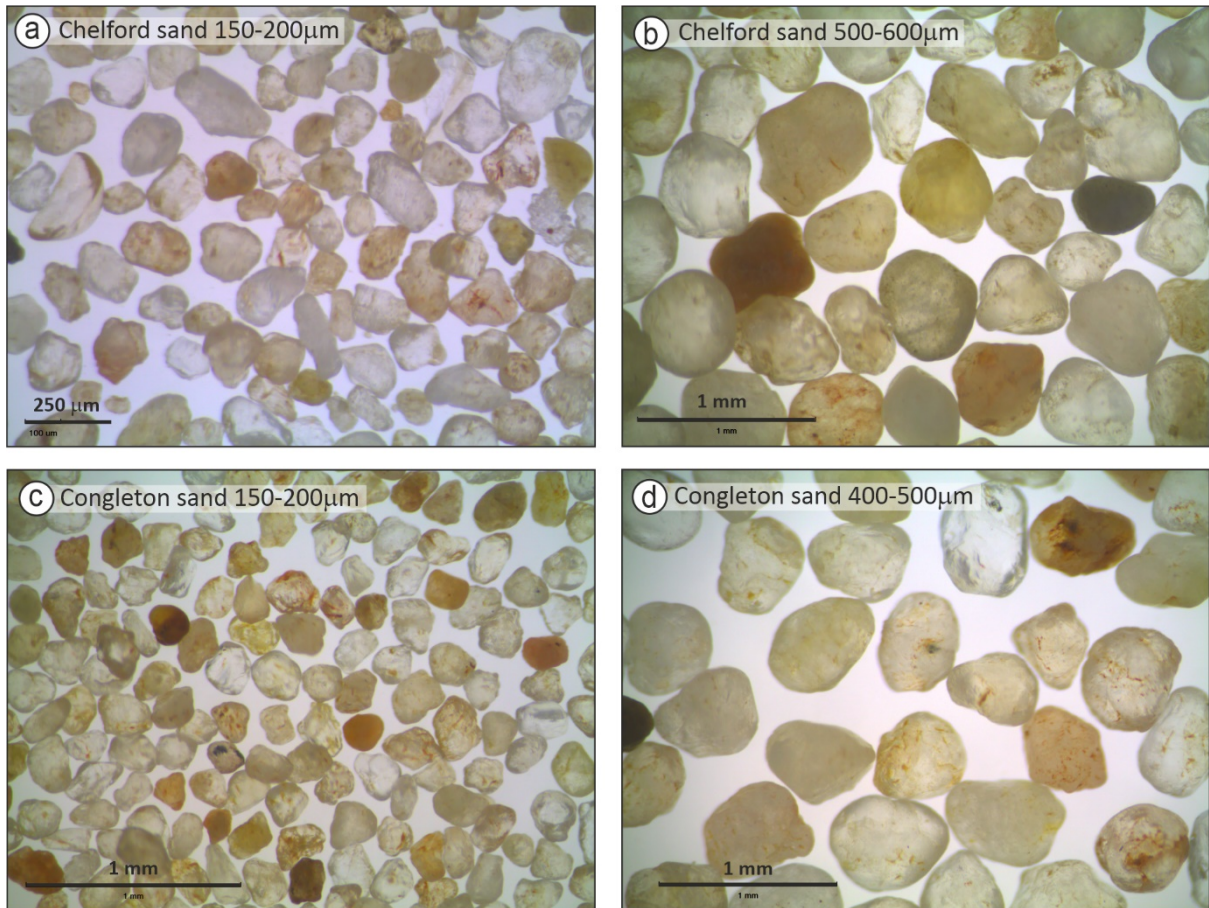


Figure 7.1. Photomicrographs of sand material used in experiments. (a) Fine grains (150-200µm) from the Chelford Sand Formation. (b) Coarse grains (500-600µm) of the Chelford Sand Formation. (c) Fine grains (150-200µm) of the Congleton Sand. (d) Coarse grains (400-500µm) of the Congleton sand.

SAMPLE STATISTICS

SAMPLE IDENTITY: **Exp S4**

ANALYST & DATE: KC, 17/06/19

SAMPLE TYPE: Unimodal, Moderately Well Sorted TEXTURAL GROUP: Sand

SEDIMENT NAME: Moderately Well Sorted Medium Sand

	μm	ϕ	GRAIN SIZE DISTRIBUTION	
MODE 1:	356.5	1.489	GRAVEL: 0.0%	COARSE SAND: 24.7%
MODE 2:			SAND: 100.0%	MEDIUM SAND: 55.6%
MODE 3:			MUD: 0.0%	FINE SAND: 19.6%
D ₁₀ :	210.7	0.603		V FINE SAND: 0.0%
MEDIAN or D ₅₀ :	368.0	1.442	V COARSE GRAVEL: 0.0%	V COARSE SILT: 0.0%
D ₉₀ :	658.3	2.246	COARSE GRAVEL: 0.0%	COARSE SILT: 0.0%
(D ₉₀ / D ₁₀):	3.124	3.724	MEDIUM GRAVEL: 0.0%	MEDIUM SILT: 0.0%
(D ₉₀ - D ₁₀):	447.6	1.643	FINE GRAVEL: 0.0%	FINE SILT: 0.0%
(D ₇₅ / D ₂₅):	1.842	1.879	V FINE GRAVEL: 0.0%	V FINE SILT: 0.0%
(D ₇₅ - D ₂₅):	228.2	0.881	V COARSE SAND: 0.1%	CLAY: 0.0%

	METHOD OF MOMENTS			FOLK & WARD METHOD		Description
	Arithmetic	Geometric	Logarithmic	Geometric	Logarithmic	
	μm	μm	ϕ	μm	ϕ	
MEAN (\bar{x}):	403.9	369.7	1.435	369.3	1.437	Medium Sand
SORTING (σ):	172.4	1.519	0.603	1.546	0.629	Moderately Well Sorted
SKEWNESS (Sk):	0.900	0.058	-0.058	0.019	-0.019	Symmetrical
KURTOSIS (K):	3.348	2.334	2.334	0.934	0.934	Mesokurtic

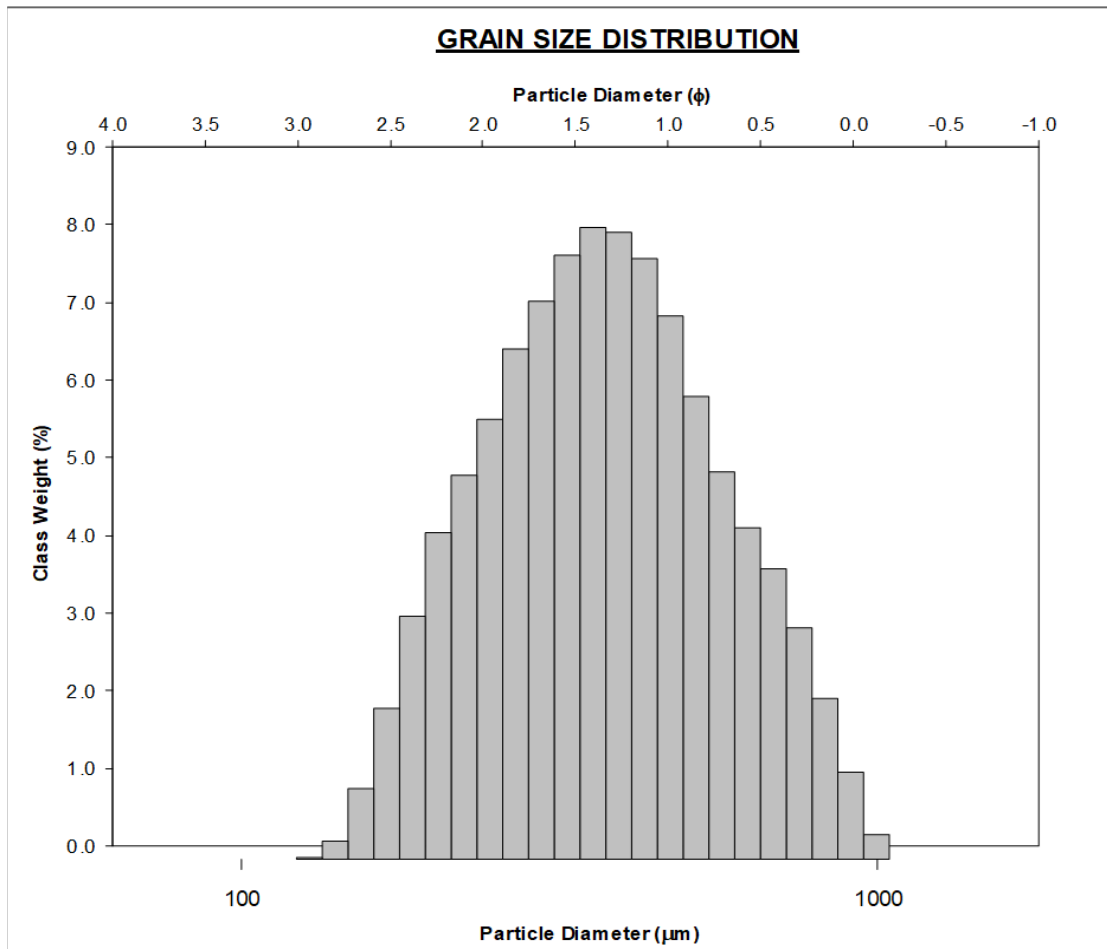


Figure 7.2. Example sample statistics output from Gradistat analysis of grain size data obtained using LPSA.

Four different grain size samples, 128, 200, 390 and 700 μm , of very well-sorted sand were chosen for initial hydrostatic testing in order to understand material behaviour, to test estimations of strength, also known as the grain crushing pressure (P^*), and refine experimental technique before conducting triaxial experiments on samples of varied sorting. Grain size distribution profiles of these four different grain size bins are shown in figure 7.3, and demonstrate very well-sorted distributions produced from sieving.

A medium-grained, $\sim 350\mu\text{m}$ by number (395 μm by grain volume) sample was chosen as the reference 'very well-sorted' sample to test grain sorting, as this proved to be a grain size easy enough to inelastically deform at a variety of pressures. Sieving of the sand into 100-micron bins also revealed subtle variations in textural maturity amongst different bins, with finer grains being more well-rounded and spherical than coarser grains, owed to greater transport distances upon deposition. This grain size was therefore chosen to minimise any potential effects of grain shape or angularity variation.

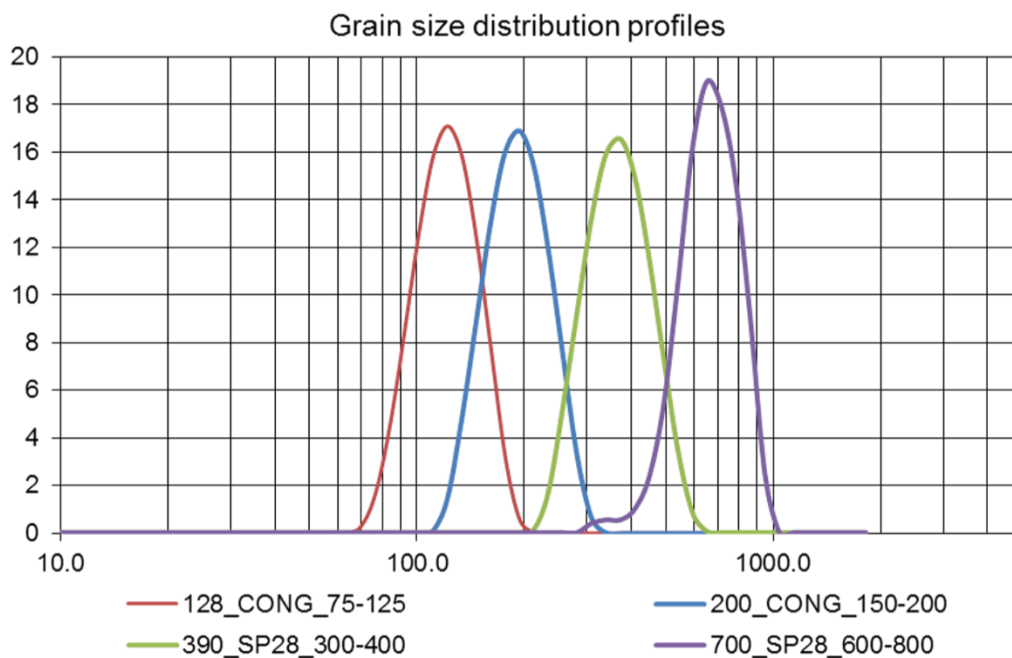


Figure 7.3. Grain size distribution profiles of four samples used in hydrostatic loading experiments.

Samples of different grain size distributions were prepared prior to the deformation experiments by mixing together sands from the different sieved bins to achieve a desired level of sorting whilst maintaining a mean grain size of $\sim 350\mu\text{m} \pm 5$ (Fig. 7.4). The Folk and Ward (1957) classification of sorting is used, given in phi units with very well-sorted to poorly-sorted ranging from 0 to 1, calculated using the following formula:

$$\phi = \frac{\phi_{84} - \phi_{16}}{4} + \frac{\phi_{95} - \phi_5}{6.6} \quad (11)$$

Where ϕ_{84} , ϕ_{16} , ϕ_{95} and ϕ_5 are the phi grain size values at their respective percentiles. This is considered a good representation of sorting as it accounts for 90% of the total grain size distribution. Four samples were produced; a very well-sorted (VWS) sample with a sorting of 0.286, well-sorted (WS) with a sorting of 0.379, moderately well-sorted (MWS) with a sorting of 0.523, and a moderately-sorted (MS) sample with a sorting of 0.633, and are summarised in table 7.

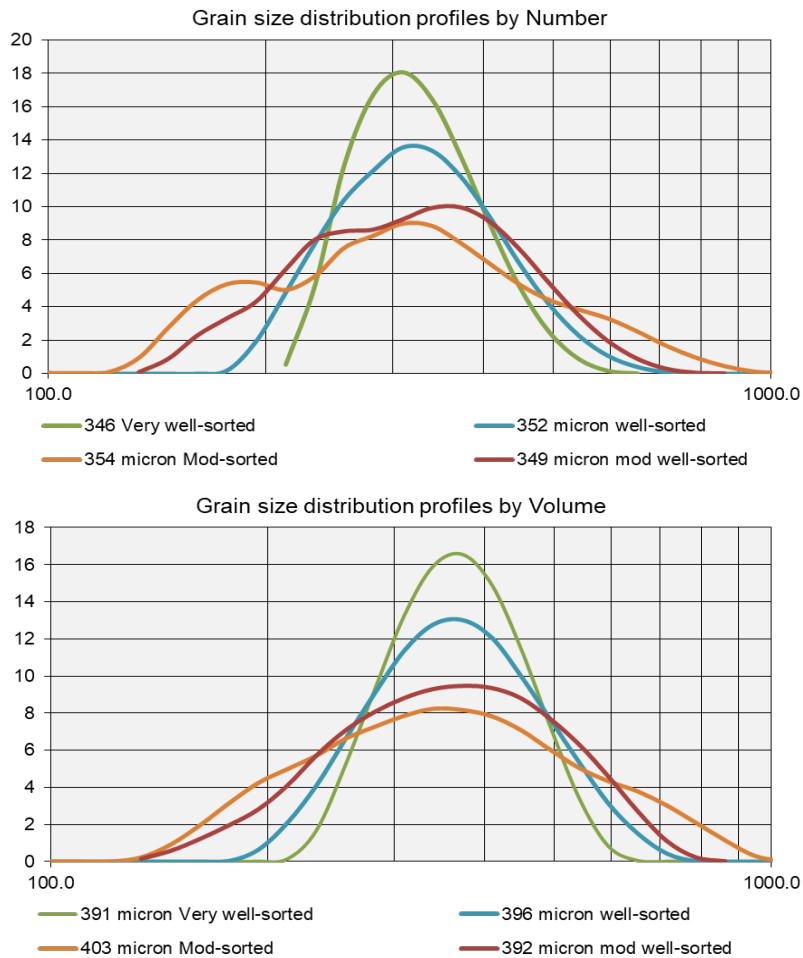


Figure 7.4. Grain size distribution profiles for samples prepared for hydrostatic and triaxial testing. (a) Grain size distribution by number of grains. (b) Grain size distribution by volume of grains.

	Mean grain size (micron)	P10 Grain size (micron)	P90 Grain size (micron)	Sorting (Phi)	Porosity (%)*
Very well-sorted	346	265	443	0.286	35.5
Well-sorted	352	242	480	0.379	35
Moderately well-sorted	344	192	500	0.523	34.5
Moderately -sorted	354	182	578	0.633	34

Table 7. Textural properties of four sand samples for testing. * Porosity estimated prior to isotropic loading, calculated from sample dimensions and a sample density for quartz of 2.66 g/cm³.

Samples are prepared for triaxial testing by pouring approximately 22g of pre-mixed sand into a 20mm diameter, 0.15mm wall thickness, annealed copper jacket, capped at each end by a ~10mm length spacer of Penrith sandstone to contain the unconsolidated sample (Fig. 7.5). Copper jackets were used to provide rigidity to the unconsolidated samples, which helps to preserve the sample microstructure upon removal of confining pressure at the end of the experiment. Jackets were annealed to ensure malleability during the deformation experiments, and to minimise brittle failure of the jacket. For annealing, jackets were placed in a Carbolite CWF13/13 furnace at 800°C for 30 minutes, followed by cleaning in 30% nitric acid to remove oxidation. As a precaution, a PVC jacket with a 3mm wall thickness was placed over the copper jacket, to prevent contamination of pore fluid with the confining medium in case the thin-walled copper jacket were to rupture during deformation. Penrith Sandstone was used for the spacers due to its strength, P^* of at least 140 MPa (Cuss et al., 2003), that far exceeds the expected strength of our unconsolidated sand sample, and its high porosity (26%) and permeability that allow for accurate control of the pore fluid pressure through the sample. Additional porous stainless-steel spacers, with a permeability of 131mD, are also placed between the sandstone spacers and the sample assembly, to both protect the surface of the assembly, and ensure even distribution of pore fluid across the sample. Once assembled, samples were pressed using a hand pumped hydraulic press until visible bulging of the jackets, to ensure compaction of the sand. Overall sample dimensions are approximately 64mm x 20mm including all spacers, with the quartz sand sample approximately 40x20mm (Fig. 7.5). Porosity of the sand sample was estimated from the sample dimensions and the volume of quartz based on sample mass and a density of pure quartz of 2.66 g/ cm³.

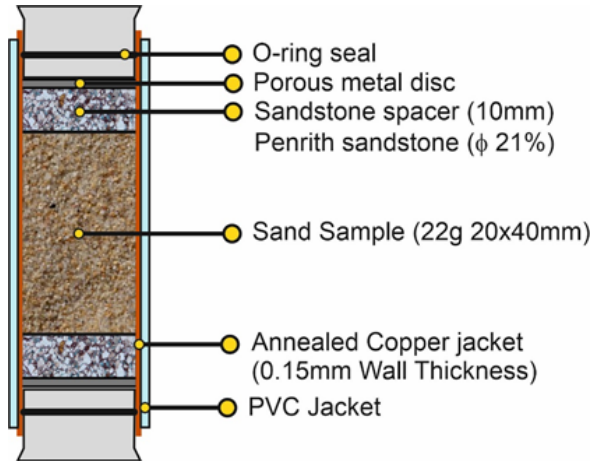


Figure 7.5. Sample configuration for triaxial experiments.

7.2.2. Experimental Procedure

All tests were performed with silicone oil as confining fluid, and de-ionized water for pore fluid, with pore pressure held constant at 10MPa for all tests in this study.

In an effort to normalise the starting material porosity, and mitigate against the effects of packing density on the mechanical response of the samples (Skurtveit et al., 2013; Skurtveit et al., 2014), all tests performed included both a pre-consolidation and over-consolidation sequence prior to deformation experiments, similar to that employed by Crawford et al. (2008). Samples were pre-consolidated dry (no pore fluid) to 20MPa, followed by introduction of pore fluid into the sample until a pressure of 10MPa was maintained, and held constant throughout the experiments. Samples were then over-consolidated to +5MPa greater than the target starting pressure, until pore fluid volume was maintained, and then unloaded to the starting effective mean pressure.

2.2.1 Hydrostatic monotonic loading

Firstly, hydrostatic loading experiments were performed on each of the samples to establish the grain crushing pressure (P^*), a point in stress-strain space typically used to define and separate the onset of permanent inelastic deformation in the form of grain crushing, from elastic deformation. Samples were monotonically loaded, from an initial effective pressure of approximately 3MPa, in increments of between 3-5MPa, as pore volume was monitored with each pressure step to determine the amount of compaction. Subsequent increases in confining pressure were only taken once pore volume had stabilised (Fig. 7.6a). This loading procedure was continued until a maximum effective pressure of 100MPa was achieved, before unloading in a series of 10MPa steps, again observing for pore volume to stabilise before each unload, to observe for permanent deformation. To calculate how much of

compaction was occurring in just the unconsolidated sand sample, a hydrostatic loading experiment was also performed on a core plug of Penrith Sandstone (Fig. S1) so that the amount of elastic compaction within the sandstone spacers could be quantified and subtracted from the overall bulk compaction of the unconsolidated samples recorded by the pore volumometer.

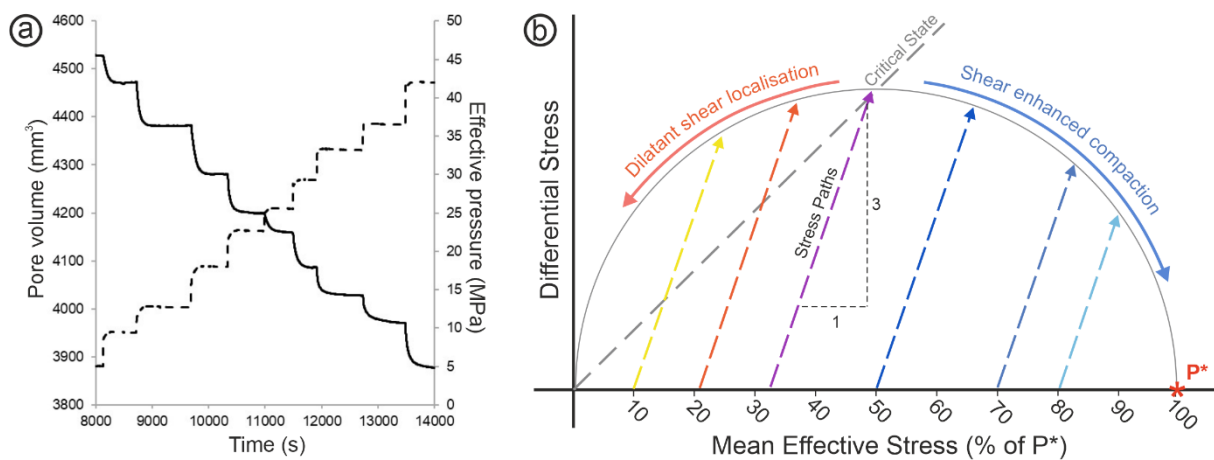


Figure 7.6. (a) The hydrostatic loading method used for all experiments. Confining pressure is increased in small increments of 3-5MPa once pore volume has equalised with each increment. (b) A Q-P diagram showing the triaxial experimental strategy. P^* defines the point of failure during hydrostatic compaction experiments. Further triaxial tests are performed at effective stress conditions as a percentage of this value, in order to explore deformation at different points around the yield envelope, and make fair comparisons between samples with slight variations in strength.

2.2.2 Hydrostatic stress cycling

Although P^* is often used to define the onset of permanent inelastic deformation, it has been shown for both unconsolidated sands (Karner et al., 2003) and consolidated sandstones (Pijnenburg et al., 2019) that significant amounts of inelastic deformation can occur during hydrostatic loading at effective pressures below P^* . Therefore, hydrostatic stress cycling tests were also performed to quantify the amount of inelastic deformation during hydrostatic loading prior to reaching P^* . For this, samples were hydrostatically loaded from an initial effective pressure of 5MPa up to an effective pressure of 15MPa, and then unloaded back to 5MPa. Samples were then re-loaded and unloaded for a total of five cycles, increasing the effective pressure by 10MPa with each cycle until P^* was reached. The amount of inelastic strain is calculated from the difference in pore volume between the start and end of each loading cycle once the effective pressure has returned to 5MPa.

2.2.3 Triaxial loading

Triaxial experiments were performed on two of the four grain size distributions, the very well-sorted (VWS) and the moderately well-sorted (MWS) sands, which represent two endmember grain size distributions produced in this study. The effective pressures at which triaxial loading was initiated was determined from the P^* values obtained during the hydrostatic experiments. On a yield curve plotted in Q-P space, where Q is the differential stress ($\sigma_1 - \sigma_3$) and P is the effective mean stress ($((\sigma_1 + \sigma_2 + \sigma_3) / 3 - \text{pore-fluid pressure})$), P^* is the point where the curve intersects the effective mean stress axis (Fig. 7.6b). Once P^* is established for a given grain size distribution, a suite of samples can be triaxially loaded from different starting effective mean stresses to explore deformation at various points in q-p space. Here, VWS and MWS samples were triaxially deformed at effective mean stresses at

approximately 10, 15, 20, 26, 32, 50, 70 and 80% of their respective P^* values, so that equivalent regions of q - p space were being explored. Once the starting effective pressure was reached, samples were axially loaded at a rate of $1\mu\text{m/s}$ until yielding was reached and then further loaded to achieve a post-yield axial strain of 5%.

7.2.3. Microstructural analysis

Once the sample is removed from the deformation apparatus at the end of the experiment, it is vacuum impregnated, while still inside the copper jacket to preserve the microstructure, with a low viscosity epoxy resin, before being cut and thin sectioned along its long axis (parallel to σ_1). The thin section is then polished and carbon coated ready for microstructural analyses. Microstructural observations are made from optical microscope and back scattered electron (BSE) images obtained using a Hitachi TM3000 scanning electron microscope (SEM). Porosity of the deformed samples was determined from image analysis of the BSE images using ImageJ and the jPORv1.1 plug-in (Grove and Jerram, 2011), to corroborate with the pore volume data from the experiments.

7.2.4. Grain size distribution analysis

Grain size analysis on deformed samples is performed using Petrog petrographic software, as covered in detail in chapter 4. Grain size statistics such as mean and median grain size, percentiles, sorting, skewness and kurtosis are obtained from point counting, measuring the long and short axis of grains whilst scanning the thin section. A total of 250 grains were counted per sample from 2D thin sections.

7.3. Results

7.3.1. Hydrostatic loading experiments

7.3.1.1. Testing grain size variation.

Results of hydrostatic compaction tests on four different grain sizes (128, 200, 390, 700 μm by volume) are shown in figure 7.7a. All samples show an initial non-linear compaction up to approximately 10 MPa, followed by a quasi-linear behaviour representing elastic deformation. In two of the four samples the onset of inelastic compaction is marked by an inflection from this linear trend, denoted as P^* . Unloading of samples shows significant permanent deformation of between 8-17% porosity reduction. The 700 μm and 390 μm samples show P^* values of approximately 20 and 60 MPa respectively. The finer samples, 128 μm and 200 μm do not indicate inelastic deformation from the stress-strain curves alone. SEM photomicrographs of thin sectioned samples are used to verify the onset of inelastic deformation, indicated by grain fracturing (Fig. 7.8). Grain fracturing is observed to occur in 200 μm , 390 μm and 700 μm samples. For the 200 μm sample this indicates P^* was reached below the maximum effective pressure achieved of ~ 110 MPa. P^* values correspond very well with theoretical predictions calculated from the porosity and grain size relationship proposed by Zhang et al. (1990):

$$\log P^* = - 1.5 \log (\phi r). \quad (12)$$

This relationship gives a predicted P^* value of 23, 56, 146 and 285 MPa for the samples tested, and confirms P^* was unlikely reached in the finer grained sand. Results are plotted in figure 7.7b alongside data from previous studies for both unconsolidated sand (Zhang et al., 1990; Wong et al., 1997; Karner et al., 2003; Crawford et al., 2008; Skurtveit et al., 2014), and consolidated sandstones (Wong et al., 1997; Cuss et al., 2003; Tembe et al., 2008; Rutter and

Glover, 2012), showing that the data are in good agreement with the theoretical relationship proposed by Zhang et al., (1990). With a P^* value of approximately 60 MPa, the medium-grained 390 μm (350 μm by number) sample used for the tests of varied grain sorting, as triaxial tests will fall comfortably within the safety limits of the apparatus.

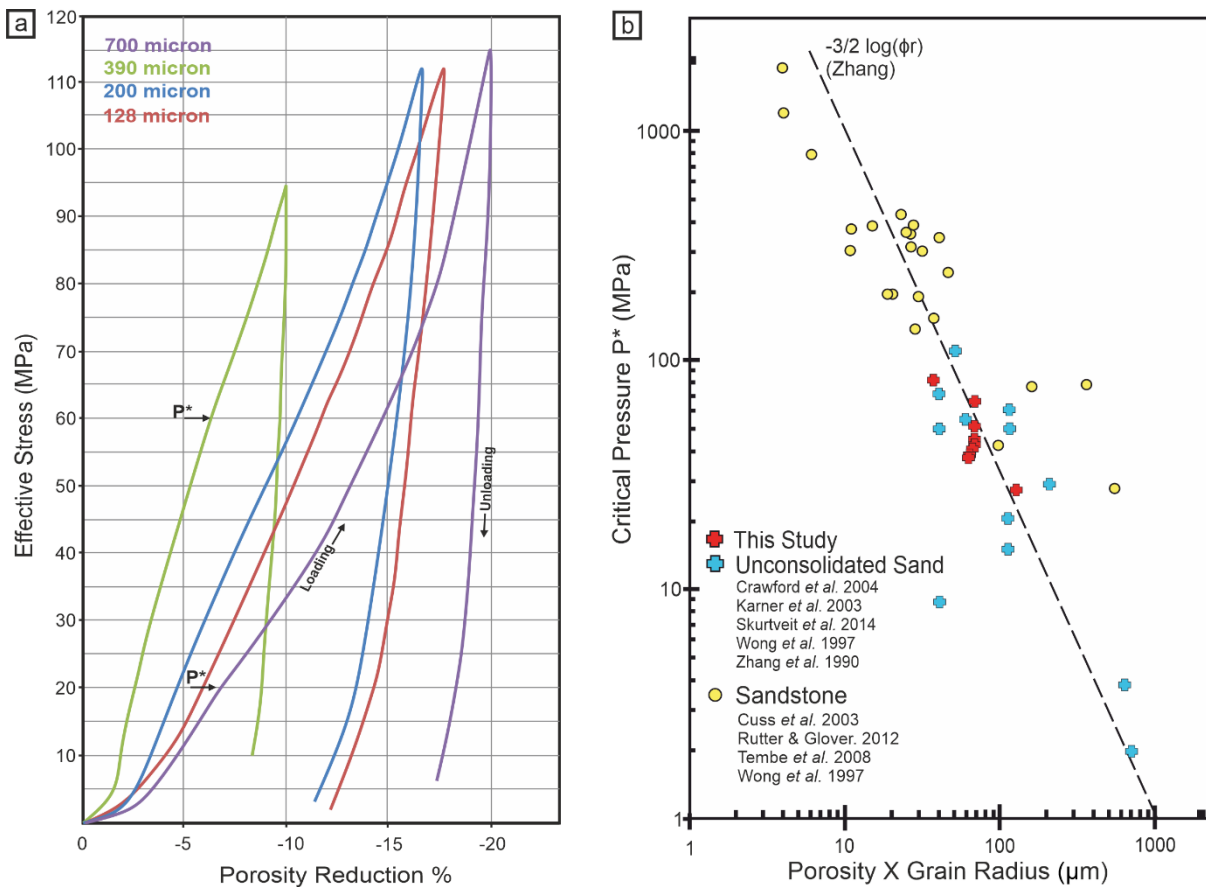


Figure 7.7. (a) Results of hydrostatic loading experiments on samples of different grain size. Samples show an initial non-linear loading, followed by a quasi-linear elastic phase of deformation. In two of the four samples (700 μm and 390 μm) an inflection marks the onset of permanent deformation, P^* , followed by a region of non-linear compaction. All samples show considerable unrecoverable deformation upon unloading. (b) P^* values from hydrostatic tests are plotted on a log P^* vs log (porosity x grain radius), as well as a compilation of results from the literature of both sandstone and unconsolidated materials, references shown in key.

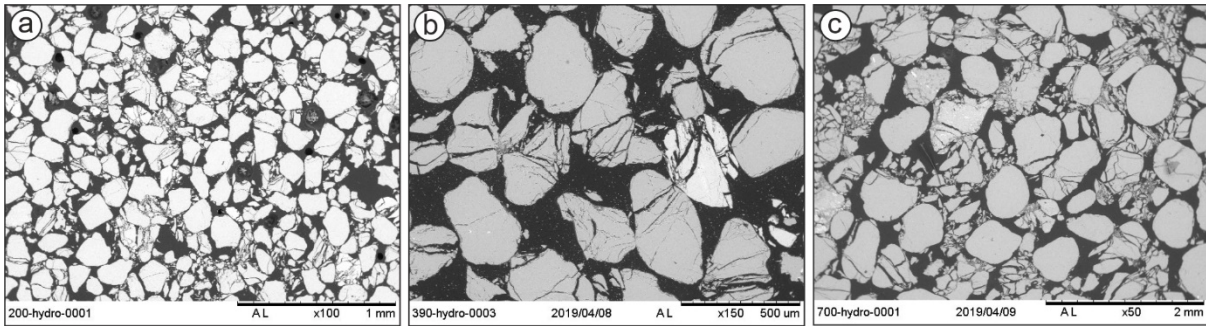


Figure 7.8. SEM photomicrographs of 200µm (a), 390µm (b), and 700µm (c) samples deformed hydrostatically showing grain crushing and surpassing of the critical pressure P^* .

7.3.1.2. Testing grain sorting variation

Hydrostatic monotonic loading experiments were performed on four different grain size distributions of 350µm sand to establish their grain crushing pressure (P^*). The hydrostatic loading curves are shown in figure 7.9a. Some samples, particularly the well-sorted sand, show a slight decrease in stiffness at approximately 2% porosity loss, beyond this all samples show quasi-linear elastic loading until approximately -6%, where a slight inflection from linear loading occurs, which is identified as P^* (marked by arrows in Fig. 7.9a). Beyond this point the samples show increasing non-linearity in their loading behaviour, as the rate of porosity reduction decreases with increasing stress. All samples show significant permanent deformation upon unloading, with porosity reduction of 9-10.5%. The P^* values for the different sands range from 48 – 65MPa, which is in close agreement with the predicted value of ~56 MPa (Fig. 7.7b). Results show that P^* decreases as grain sorting gets worse, corresponding also to an increase in overall compaction and inelastic porosity loss.

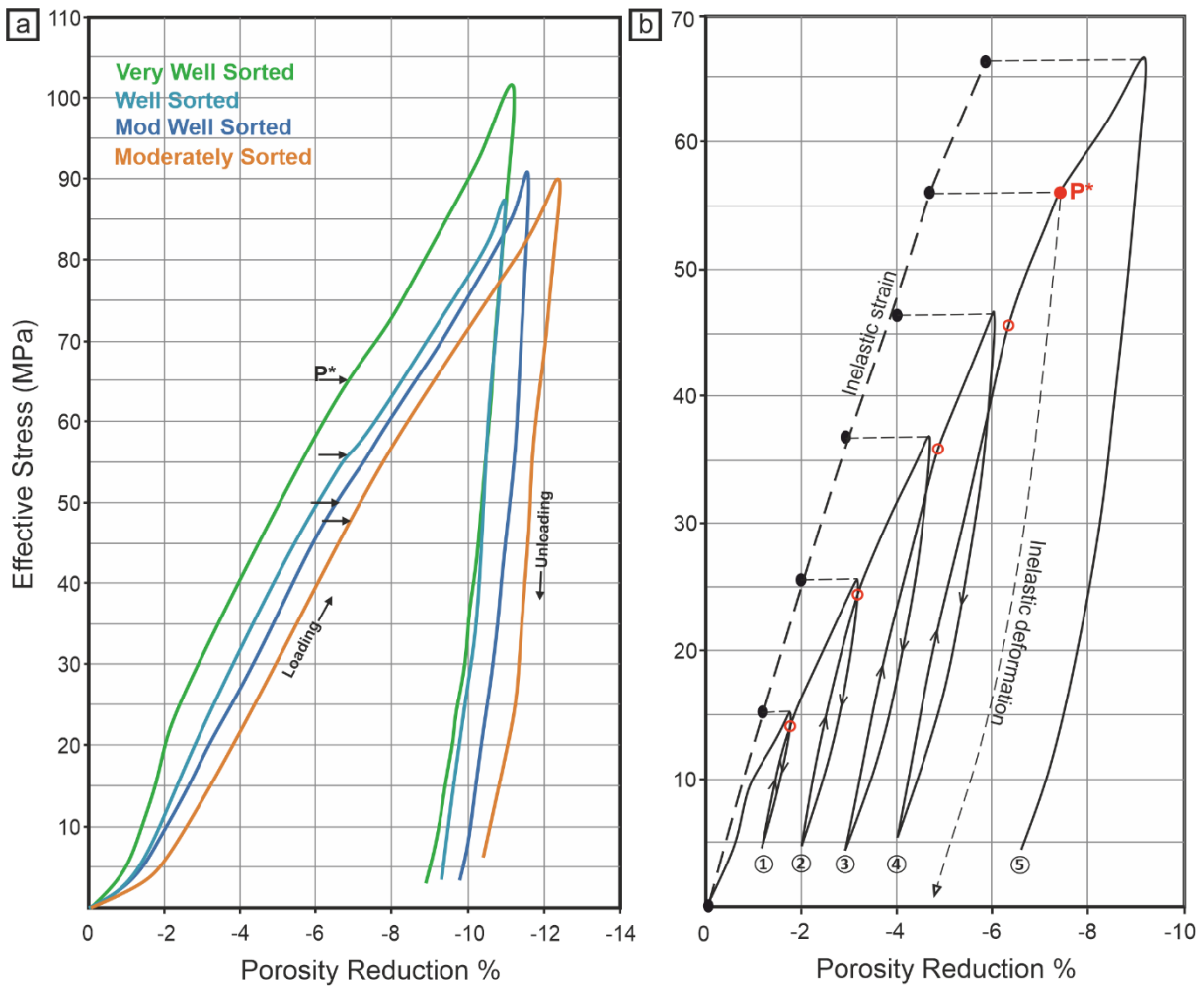


Figure 7.9. (a) Results of hydrostatic compaction tests on $350\mu\text{m}$ sand with four levels of grain sorting. (b) Results of hydrostatic stress cycling experiments on a sample of VWS sand. Unloading curves of each cycle show accumulation of inelastic strain. Inelastic strain is plotted against the maximum stress of each cycle, and accounts for approximately 65% of total strain.

As the inflection in the hydrostatic loading curve is very subtle there is some uncertainty in the identification of P^* from the mechanical data alone. To confirm that the samples had indeed reached P^* photomicrographs of samples loaded to various effective pressures were analysed. Figure 7.10 shows three samples of moderately well-sorted (MWS) sand deformed to 19, 37 and 75MPa. No evidence for grain crushing is observed for samples taken up to 37MPa, with all grains remaining intact (Figs. 7.10a and b). In contrast, the sample deformed to 75MPa shows pervasive intragranular fracturing, particularly in the finer grains (Fig. 7.10c). This, alongside the agreement with theoretical predictions provides confirmation of P^* and the onset of grain crushing that we identified from the hydrostatic loading curves (Fig. 7.9a). Hydrostatic stress cycling tests were also performed on a sample of VWS sand to determine how much inelastic deformation occurs at effective pressures below P^* , in this case <55MPa, in what is typically considered to be the elastic regime (Fig. 7.9b). The results show a significant amount of inelastic deformation and porosity loss is accumulated in this regime, with the sample retaining approximately 65% of the maximum porosity loss after each unloading cycle (Fig. 7.9b). Further evidence for inelastic deformation can be seen in the apparent yielding of the sample as it is reloaded after each cycle (open red circles), after which it resumes a loading curve similar to the monotonic hydrostat with a reduction in stiffness. The bulk modulus can be calculated from the loading data. The bulk modulus is calculated to be approximately 0.3GPa. However, the bulk modulus is calculated to increase from 0.65 to 0.9GPa with cycling and increasing effective pressure, further suggesting that inelastic deformation is occurring and is responsible for the apparent stiffening of the material. Inelastic strain is plotted separately adjacent to the total strain cycles for comparison.

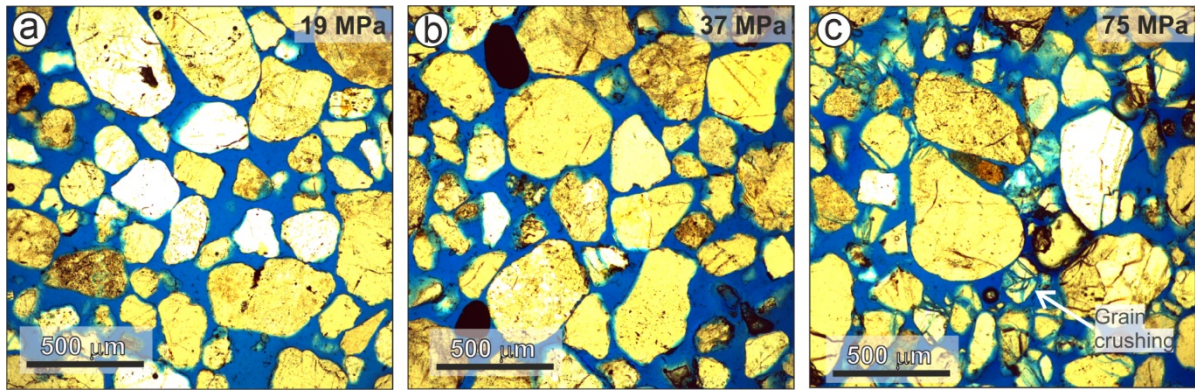


Figure 7.10. Photomicrographs of a 344 μ m moderately well-sorted sand. Deformed hydrostatically and removed at 19 (a), 37 (b) and 75MPa (c) to confirm the onset of grain crushing (P^). Samples taken to 19 and 37MPa display no grain deformation. Sample taken to 75MPa confirms the occurrence of P^* , marked by pervasive grain fracturing.*

7.3.2. Triaxial loading experiments

Samples of both very well-sorted (VWS) and moderately well-sorted (MWS) sands were triaxially deformed in a series of experiments with increasing effective pressure, at conditions approximately 10,16,22,26,32,50,70 and 80% of their P^* value. Results of triaxial tests are plotted as porosity change vs mean effective stress (Fig. 7.11a & 7.12a), and differential stress vs axial strain (Fig. 7.11b & 7.12b), for the VWS and MWS sands respectively.

The yield of the samples in the triaxial experiments can be identified from the pore volume data where the porosity reduction with increasing effective mean stress deviates from the trend of the hydrostat (solid circles on Figs. 7.11a & 7.12a). The data show that at low effective pressures (<15% of P^*), samples experience initial 'elastic' volume reduction followed by post-yield dilation (C'). At intermediate effective pressures (15-20% of P^*), samples show post yield initial compaction and porosity reduction of ~1% at 3% strain, followed by constant volume deformation, indicating critical state failure characterised by shearing (Rutter and Glover, 2012). At higher effective stresses (>20% of P^*), samples experience significant post-yield porosity reduction, representing the onset of shear enhanced compaction (C^*).

346 micron Very well-sorted triaxial tests

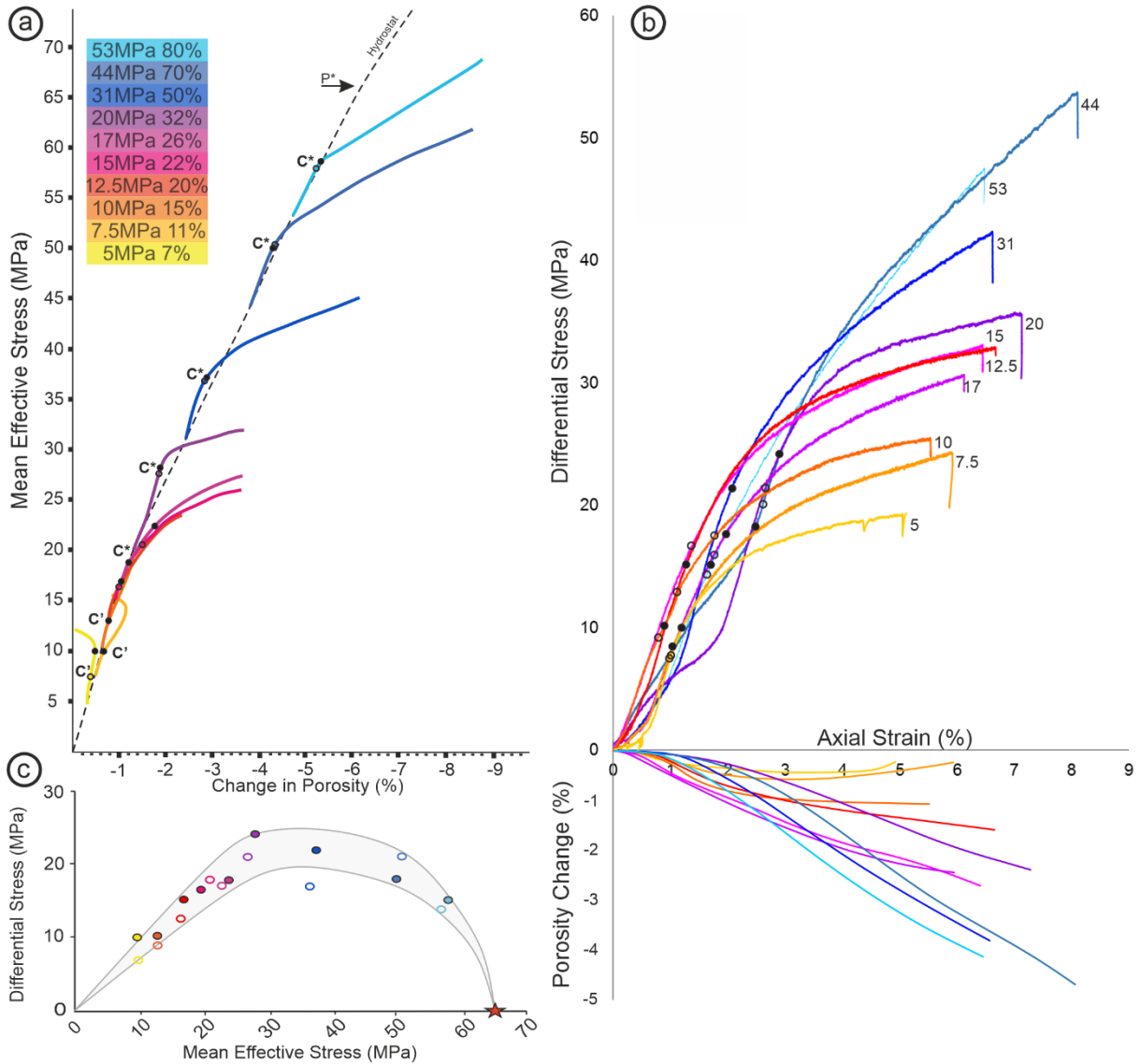


Figure 7.11. Results of triaxial experiments for very well-sorted sand. Yield (C'/C^*) is determined from two methods; deviation of porosity change from the hydrostat with mean effective stress (a), indicated by solid symbols, and differential stress vs axial strain curves where the data becomes non-linear(b), indicated by open symbols. The conditions at which samples were axially loaded are indicated next to data curves. (c) Yield points are plotted in differential stress (Q) versus mean effective stress (P) space, and form a broadly elliptical yield envelope.

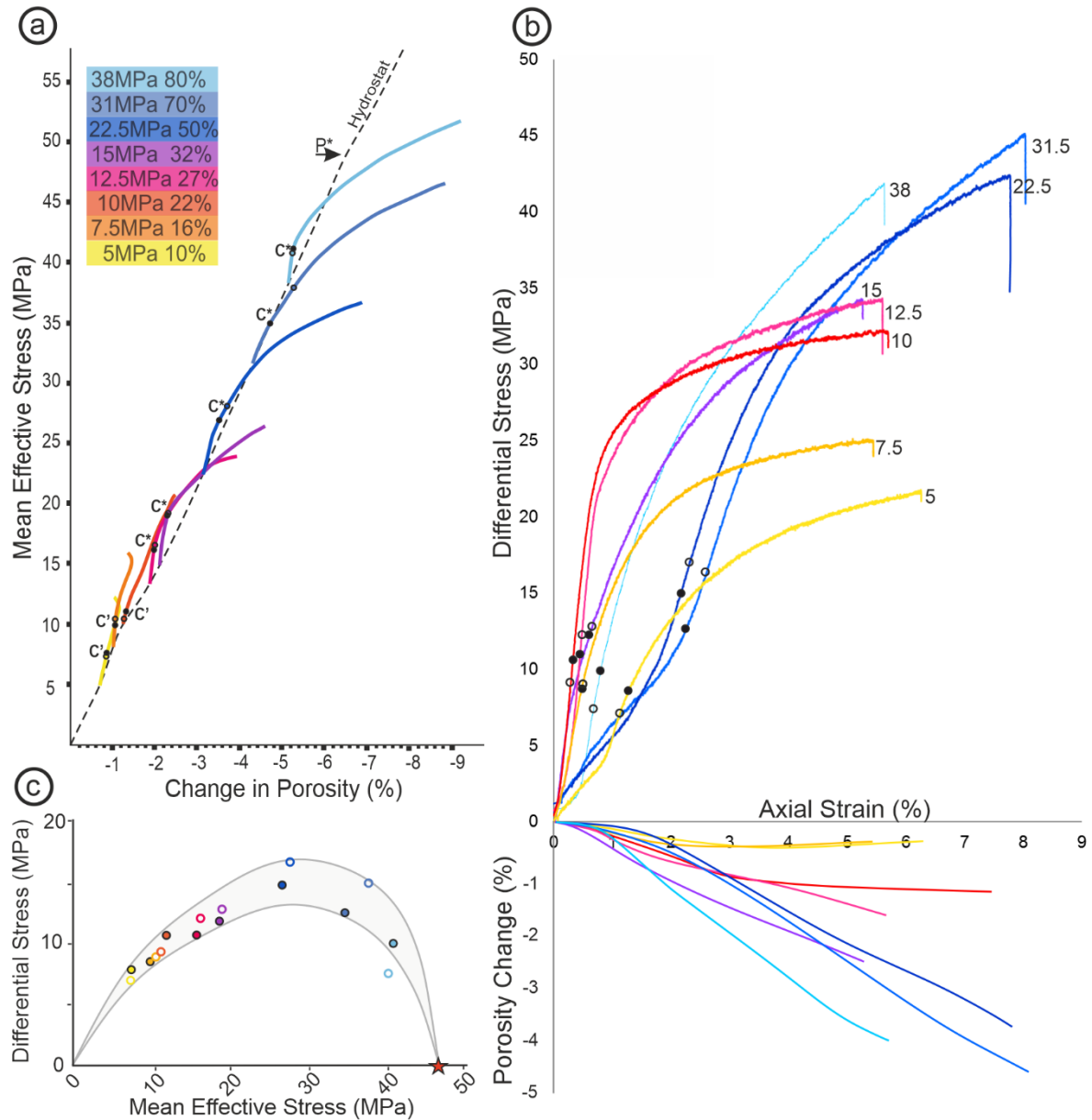


Figure 7.12. Results of triaxial experiments for moderately well-sorted sand. Yield (C'/C^*) is determined from two methods; deviation of porosity change from the hydrostat with mean effective stress (a), indicated by solid symbols, and differential stress vs axial strain curves where data becomes non-linear (b), indicated by open symbols. (c) Yield points are plotted in differential stress (Q) versus mean effective stress (P) space, and form a broadly elliptical yield envelope.

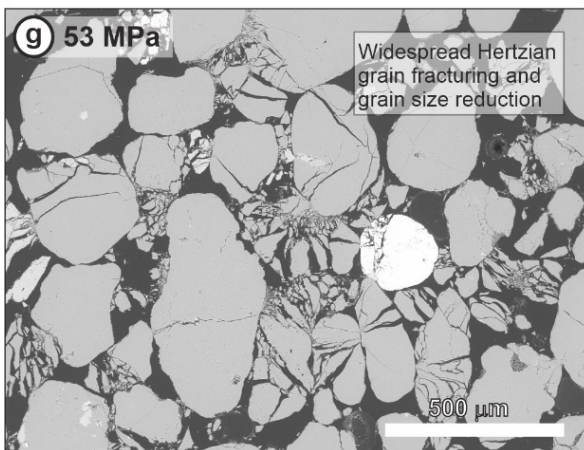
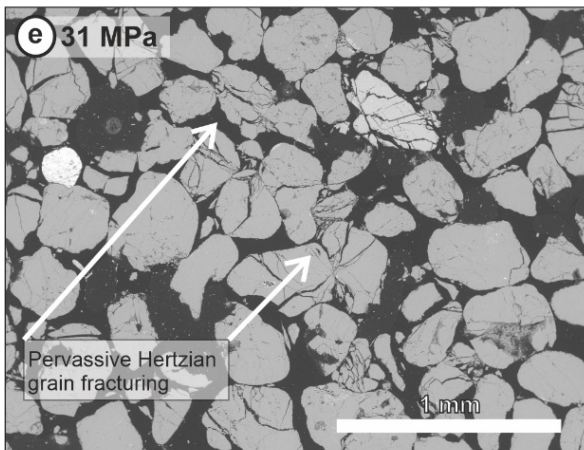
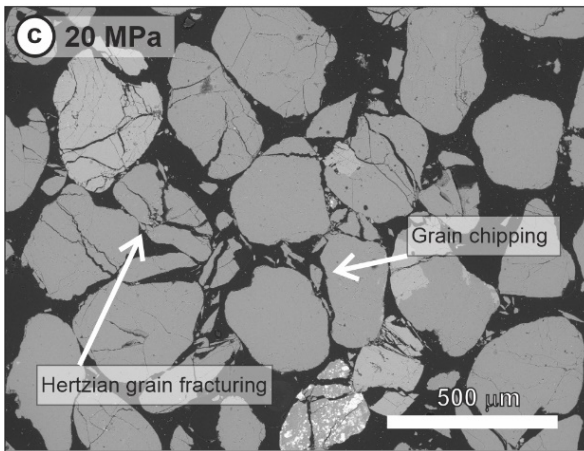
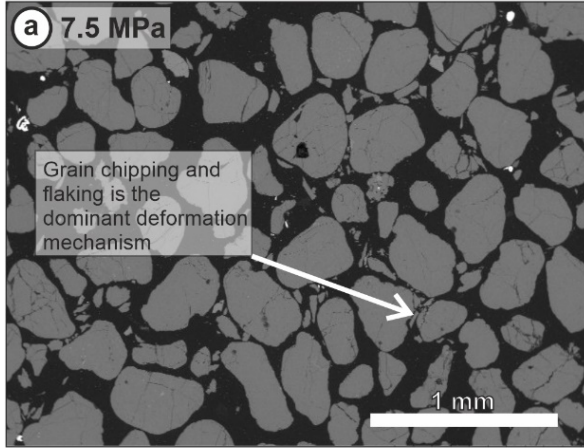
For triaxial data yield can also be determined from a deviation from quasi-linear loading on a plot of axial strain versus differential stress (see for example Bedford et al. (2018); (2019)). However, for our unconsolidated sands it is difficult to determine yield in this way as the samples do not display a well-defined elastic quasi-linear trend (Figs. 7.11b & 7.12b). Instead, the samples display an initially weak linear loading followed by a prolonged non-linear regime as they undergo yielding. Yield is marked as the deviation from this weak linear trend, shown by open circles, and also included are the equivalent yield points determined from the pore volume data (Figs. 7.11a and 7.12a) for comparison (solid circles). Yield points determined via both methods are plotted in Q-P space to define the yield curves for the different sands (Figs. 7.11c & 7.12c). In both the VWS and MWS sands the yield points map out a broadly elliptical yield envelope using both methods, with slight variance in differential stress. In both the VWS and MWS samples, points map out an approximately linear trend at low effective stresses up to ~ 30 MPa, representing brittle failure. The brittle-ductile transition is marked by the peak of the yield curve, occurring between approximately 26MPa and 32MPa. At pressures greater than this, deformation is characterised ductile shear-enhanced compaction, with an elliptical yield envelope with a steep limb observed up to the maximum effective stresses up to P^* .

7.3.3. Microstructural and grain size analysis

Photomicrographs from thin sections of triaxially deformed samples are shown in figure 7.13. Samples of VWS and MWS sand deformed at low effective pressures of 7.5MPa ($<15\%$ of P^*) (Fig. 7.13a, b) show minimal amounts of cataclasis, which is expected as these samples experienced predominantly dilatant deformation (Figs. 7.11a and 7.12a). The primary micro-mechanism is grain disaggregation and rearrangement with minor amounts of grain chipping and flaking as grains slide and rotate against one another, resulting in minor grain size reduction for both sands of approximately 12%. At intermediate effective pressures of 15-

20MPa (~32% of P^*) (Fig. 7.13c, d), the amount of cataclasis increases, with grain chipping as the primary deformation mechanism, accompanied by minor amounts of Hertzian fracturing at grain point contacts. In the VWS sample (Fig. 7.13c), Hertzian fractures are better developed between adjacent grains of similar size in accordance with the constrained comminution model of Sammis et al. (1987), whereas the MWS sample (Fig. 7.13d) shows less well developed Hertzian fracturing, with it being restricted to the smaller grain fractions in the sample. At high effective pressures, in excess of 50% of P^* where samples experience a significant amount of compaction, Hertzian grain fracturing becomes the primary deformation mechanism (Fig. 7.13e-h). In the VWS sand, at 31MPa (50% of P^*), Hertzian fracturing is pervasive and well developed (Fig. 7.13e), resulting in a large degree of grain size reduction. At the highest effective stresses of 53MPa (80% of P^*), grain size is reduced dramatically, with only large outliers remaining intact (Fig. 7.13g). In the poorer sorted MWS sample deformed at 50% of P^* (22.5MPa) (Fig. 13f), Hertzian fracturing is the primary deformation mechanism but is less pervasive than the VWS sample, with fracturing only occurring amongst a small amount of connected finer grains, leaving many coarser outliers intact. At the highest pressures of 38MPa (80% of P^*) (Fig. 7.13h), more intense cataclasis is observed amongst these finer grain fractions, again leaving larger grains intact. The earlier onset and more pervasive Hertzian fracturing within the VWS sample results in greater overall mean grain size reduction compared to the MWS sample at comparable conditions (Table 8).

VWS



MWS

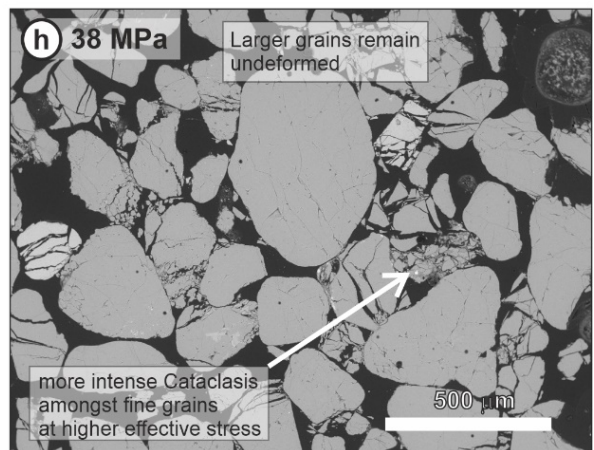
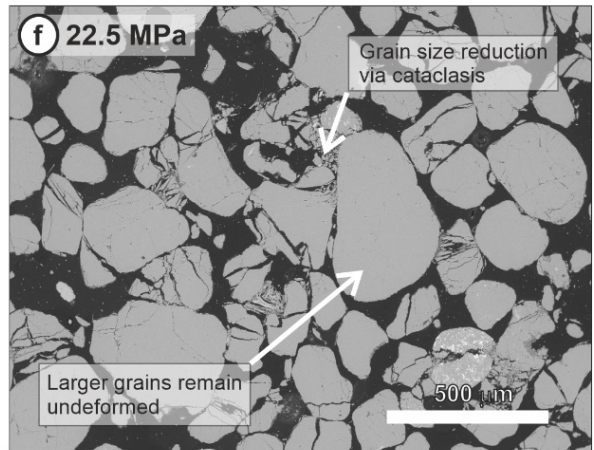
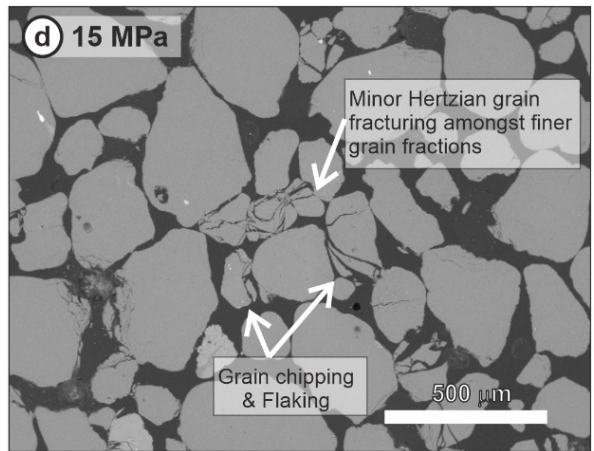
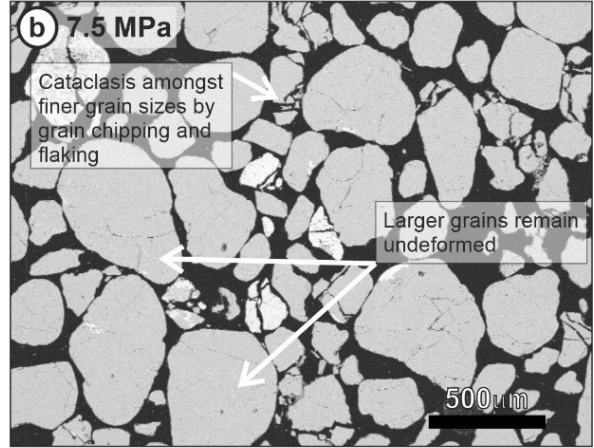


Figure 7.13. Back Scattered Electron (BSE) photomicrographs of triaxially deformed very well-sorted sands (a, c, e, g), and moderately well-sorted sands (b, d, f, h) deformed at approximately 10, 32, 50 and 80% of P^ respectively. Samples are shown side by side for comparison, with the confining conditions at which each sample was deformed indicated. Samples show a transition in deformation mechanism from grain chipping (a, b), to chipping accompanied by Hertzian grain fracturing between grains of similar size at intermediate pressures (c, d). At higher pressures, Hertzian grain fracturing becomes the primary deformation mechanism, resulting in pervasive hertzian fracture networks and cataclasis in VWS sample (e, g), to more isolated pockets of cataclasis within MWS samples, which display lots of undeformed coarse outliers (f, h).*

Sample ID	Effective stress (MPa)	Yield'	Yield'	Yield*	Yield*	Peak stress @ 5% Strain		Grain size (micron)	porosity (%)	Sorting (Phi)	Fractal Dimension (D)	R2	Fractal range (micron)	Permeability mD
		(P) (MPa)	(Q) (MPa)	(P) (MPa)	(Q) (MPa)	P	Q							
VWS	Undeformed	-	-	-	-	-	-	346	36	0.305	-	-	-	15252
VWS 7%	5	10	10	7.5	7.5	11.4	19.3	328	35	0.393	-	-	-	10149
VWS 11%	7.5	10	8	10	7	15.6	24.2	303	34	0.656	1.53	0.93	101-309	3122
VWS 15%	10	13	10	13	9	18.5	25.5	300	33.5	0.698	1.64	0.9	101-309	1509
VWS 20%	12.5	17	15	16.5	12.5	22.4	29.7	250	32.7	0.785	1.75	0.94	83-309	1012
VWS 23%	15	19	16	20.8	17.5	27	36	247	31.5	0.802	1.71	0.92	83-339	870
VWS 26%	17	23	18	22	16	27.2	30.6	274	31.1	0.742	1.75	0.9	92-339	988
VWS 32%	20	28	24	27	21	31.9	35.6	250	30	0.824	1.89	0.91	83-339	672
VWS 50%	31	37	21.5	36.6	17	45	42.3	241	28.9	0.771	1.94	0.91	83-339	540
VWS 70%	44	50	18	50.6	20	61.8	53.7	226	27	0.857	1.95	0.94	76-339	271
VWS 80%	53	58	15	57	14	68.8	47.5	212	26.9	0.94	2.19	0.96	63-373	151
Hydrostatic	100	66	-	-	-	-	-	259	27	0.719	1.97	0.89	92-339	592
MWS	Undeformed	-	-	-	-	-	-	344	34	0.522	-	-	-	6257
MWS 10%	5	7.6	8	7	7	12.2	21.6	290	33	0.5	-	-	-	4162
MWS 16%	7.5	10	8.5	10.5	9	15.8	24.8	300	32.8	0.692	1.62	0.89	101-256	2384
MWS 22%	10	11	10.5	10.5	9	20.7	31.6	276	31.6	0.702	1.75	0.89	101-309	1149
MWS 27%	12.5	16	10.6	16.5	12	23.9	34.3	261	30.2	0.712	2	0.92	92-339	993
MWS 32%	15	19	12	19.3	13	26.4	34	261	29.5	0.663	2.2	0.89	101-339	988
MWS 50%	22.5	27	15	28	17	36.6	42.2	248	27.3	0.698	2.2	0.82	92-339	551
MWS 70%	31.5	35	12.5	38	16	46.5	45	231	25.4	0.862	2	0.86	69-373	209
MWS 80%	38	41	10	40.5	7.5	51.9	41.3	227	24.9	0.858	2.05	0.91	69-373	188
Hydrostatic	100	47	-	-	-	-	-	256	25	0.905	1.9	0.96	83-373	192

Table 8. Summary table of results. Mechanical, textural and petrophysical data for triaxially deformed samples. ' Yield determined from deviation of porosity from the hydrostat with mean effective stress. * Yield determined from differential stress vs axial strain curves.

The evolution of micro-mechanisms with increasing effective stress can be seen in the grain size distribution (GSD) data when plotted on a logarithmic plot of grain size (GS) versus number of grains greater than size GS. Naturally occurring cataclases show a fractal distribution indicated by a power-law relationship between number and size given by:

$$N(S) \sim S^{-D} \quad (13)$$

With the exponent D as the fractal dimension (Turcotte, 1986) (Fig. 14a). The fractal dimension is recorded for all deformed samples over a fractal range where a power-law trend is observed with a correlation coefficient of 90% and greater, and is used, in conjunction with BSE images, to quantify cataclasis with increasing effective stress. This provides quantitative indication of GSD evolution, where the fractal dimension and fractal range are recorded (summarised in Table 8). Due to the inaccuracies of measuring three-dimensional grain size distribution from a two-dimensional method such as thin sections, a correction of the fractal

dimension to a three dimensional value is required simply by adding one to the two-dimensional value (Sammis et al., 1987). All values of fractal dimension given in this study are three-dimensional.

The VWS sample shows a large and progressive evolution in grain size distribution with increasing stress. The transition from disaggregation and grain chipping to predominantly Hertzian cataclasis results in the development of a fractal grain size distribution which evolves rapidly with increasing effective stress (Fig. 7.14c- d). The poorer sorted MWS sample shows less dramatic GSD evolution with less overall reduction in mean grain size with increasing effective stress. This also supports microstructural observations of less pervasive and developed Hertzian cataclasis. Despite greater overall grain size reduction within the well sorted sample, both samples evolve to a D of 2.2 at the highest effective mean stress. However, the MWS sample, a fractal grain size distribution of 2.2 is achieved at a lower relative effective pressure (% of P^*) than the VWS sample, albeit with a correlation coefficient less than our 90% limit. At low effective pressures (<23% of P^*), where disaggregation and grain flaking dominate, the fractal dimensions between the VWS and MWS samples are largely similar, both evolving to a fractal dimension of 1.75. However, beyond these effective stresses, the MWS sample shows a rapid development of a fractal distribution to a dimension of >2 at ~30% of P^* , where shearing and grain chipping is the dominant deformation mechanism, whilst the VWS sample only reaches a fractal value of 2 at higher effective stresses of 70% of P^* , rising to 2.2 at 80% of P^* , where Hertzian grain fracturing dominates. Differences in the correlation coefficient and fractal range between both samples are also observed, that is the grain size range at which a fractal distribution is observed. The VWS sand evolves a wider and finer fractal range than the MWS sand at similar conditions, with consistently higher correlation coefficients.

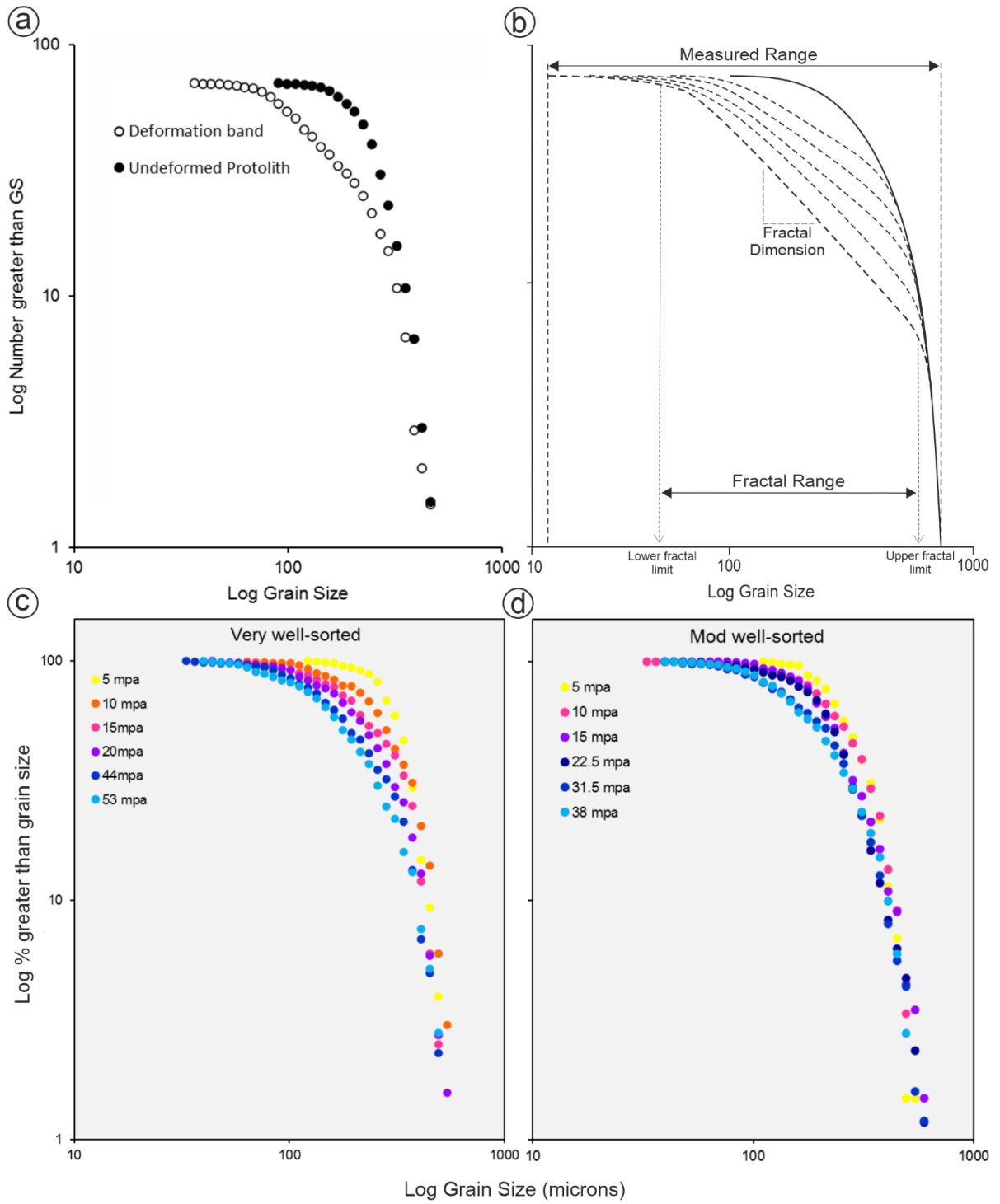


Figure 7.14. (a) Particle size distribution for a naturally deformed cataclastic deformation band and undeformed host. (b) Fault rocks can be described as fractal when a power-law relation when plotted in a log-log plot of grain size (GS) versus number of particles greater than size GS, where the exponent D is the fractal dimension. The fractal dimension, and the fractal range increases with increasing grain comminution to a fractal dimension of up to 2.58 (Sammis et al., 1987). Grain size distribution (GSD) plots for triaxially deformed samples of both very well sorted (c) and moderately well-sorted (d) quartz sands. GSD is observed for a linear trend deviating from the undeformed GSD curve, indicating a fractal, or power law distribution. The gradient of the linear trend corresponds to a fractal dimension D . GSD curves show a progressive shift and steepening to the left with increasing effective pressure. Data colours correspond to different effective confining pressures as in figures 7.11 & 7.12.

7.4. Discussion

7.4.1. Inelastic deformation during hydrostatic compaction of unconsolidated sands.

The results from hydrostatic loading experiments on loose sands shows deformation behaviour that shares both similarities and differences with consolidated sandstones. During hydrostatic compaction of sandstones, loading is typically characterised by an initial quasi-linear loading behaviour, which is thought to represent elastic deformation of the sample, followed by some deviation from this linear trend that marks the transition to inelastic deformation, where a non-linear hardening compaction trend follows (Zhang et al., 1990; Wong and David, 1992; Wong and Baud, 2012). However, the monotonically loaded unconsolidated sands, the identification of yield is difficult to determine from hydrostatic loading data alone, as the samples show a very minor inflection from quasi-linear loading (Fig. 7.7a & 7.9a). Photomicrographs are used to confirm the onset of grain crushing, which show pervasive intragranular fracturing of grains beyond the interpreted P^* pressures from the mechanical data (Fig. 7.8 & 7.10). These P^* values are also in very close agreement with the theoretical grain crushing pressure given by the numerical relationship with porosity and grain size (Fig. 7.7b) (Zhang et al., 1990). In other studies on unconsolidated materials where a similar absence of an obvious inflection in the loading data has been observed, the onset of inelastic deformation has been determined by the point of maximum curvature (Nguyen et al., 2014), or confirmed by monitoring acoustic emissions which record a peak at P^* (Lockner, 1993; Brzesowsky et al., 2014; Hangx and Brantut, 2019).

The results of previous investigations and the new mechanical data presented here suggest that the elastoplastic behaviour that is observed in many sandstones, where there is a clear transition between elastic and inelastic behaviour with increasing pressure, may not

necessarily be applicable to unconsolidated sands. This is confirmed in the hydrostatic stress cycling experiments which show increasing amounts of permanent deformation with each cycle (Fig. 7.9b), revealing approximately 65% of the total strain is inelastic during the initial loading phase (i.e. at pressures below the onset of grain crushing, P^*), which is typically thought to represent the 'elastic' regime. Recent work has shown similar behaviour can also be observed for some consolidated sandstones (Pijnenburg et al., 2019), where between 30-50% of total strain during initial loading is inelastic. Pijnenburg et al. (2019) show that deformation occurs in three stages as pressure is increased; (i) an initial closure of pre-existing cracks and fractures, (ii) intergranular fracturing and cement breakage, and (iii) a final stage dominated by intragranular Hertzian fracturing. As the samples are not consolidated or supported by intergranular cements, it is reasonable to assume that stage (ii) will not occur in these experiments. Instead, inelastic strain at pressures below P^* is accommodated by grain sliding and rearrangement. This process achieves a more geometric packing arrangement, reducing porosity until packing of the grains reaches a critical limit, where stage (iii) initiates and the sample deforms via intragranular fracturing. Successive cycling results in a stiffer stress-strain response with re-loading curves recording a higher bulk modulus of 0.6-0.7GPa (compared to 0.3GPa during monotonic loading), rising with increasing effective stress, a common observation in the deformation of sandstones as porosity decreases and grain-contact surface-area increases at higher normal stresses (Zhang and Bentley, 1999; Wang et al., 2020). Once re-loading reaches the maximum stress level of the previous cycle, samples exhibit yielding behaviour where the sample resumes 'normal' hydrostatic compaction, accommodated by both elastic and inelastic strains simultaneously. Karner et al. (2003) found similar behaviour during experiments on a fine-grained St Peter's quartz sand, albeit with lower inelastic strains of ~22%, owed to the samples being pre-consolidated prior

to loading. Packing density plays an important role in controlling the micromechanical deformation mechanism and the degree of cataclasis in unconsolidated granular materials (Skurtveit et al., 2013). Together with the results here, this highlights the importance of consolidation on loading behaviour of unconsolidated sands, and the micromechanics of deformation prior to P^* , emphasizing that care should be taken when interpreting inelastic yield in unconsolidated materials.

Since porosity values are strongly dependant on packing arrangements and therefore affected by grain sorting (Worden and Burley, 2003), there may be a critical porosity value at which unconsolidated sands may behave entirely elastic during loading, that varies with sorting. There is a theoretical minimum porosity value of 26% for tightly compact spherical grains with a tetrahedral arrangement (Beard and Weyl, 1973). However, this is likely to be a higher porosity in sands with grains that are not perfectly spherical and with a degree of angularity. Our samples undergo $\sim 4.5\%$ inelastic porosity reduction from an initial 36% before P^* is reached, suggesting a critical porosity of approximately 31.5%, where samples may behave entirely elastically during isotropic loading up to brittle failure. Our results show no influence of grain sorting on the degree of compaction and inelastic porosity loss, with both VWS and MWS exhibiting $\sim 65\%$ inelastic strains, although this may become more apparent with more sorting contrast, in which we would expect inelastic porosity loss to increase, and the critical porosity lowered with poorer sorting.

7.4.2. The role of grain sorting on micromechanics and post-yield deformation

The unconsolidated sands tested in this study are characterised by a broadly elliptical shaped yield envelope when plotted in Q-P space (Figs. 7.11c and 7.12c), in agreement with previous investigations on unconsolidated sands (Crawford et al., 2004; Nguyen et al., 2014) and

porous sandstones (Baud et al., 2006; Bedford et al., 2019; Cuss et al., 2003; Wong et al., 1997), as well as the Cam-Clay model which much of the understanding on yielding of granular materials is based on (Schofield and Wroth, 1968; Wood, 1990). Beyond yield, in what is typically considered to be the inelastic regime, grain sorting exerts a significant control on the micromechanics of deformation, which evolve with increasing effective mean stress. Three micromechanical mechanisms are identified from photomicrographs of samples triaxially deformed at different effective mean stresses (Fig. 7.15); (i) grain sliding and rearrangement at low effective stress, (ii) grain chipping at moderate effective stresses, and (iii) intragranular grain fracturing at high mean effective stresses, consistent with previous observations on the mechanisms of deformation of unconsolidated quartz sands (Karner et al., 2005; Skurtveit et al., 2013; Hangx and Brantut, 2019). Although three different mechanisms are identified, they do not occur exclusively, rather they are likely to occur simultaneously, with the dominant mechanism being controlled by the effective mean stress, as schematically shown in Figure 7.15. Very well-sorted sands show a more rapid transition from rearrangement and grain chipping to predominantly intragranular fracturing than poorly-sorted sand. This can be attributed to the greater ease with which well-sorted sediments compact to form a structurally supportive packing arrangement, as demonstrated by the constrained comminution model of Sammis et al. (1987), where grain-to-grain fracturing is favoured when neighbouring grains are of similar size. In a very well-sorted aggregate, this results in simultaneous intragranular fracture of grains, with limited outliers remaining undeformed. In poorly-sorted sands, constrained comminution is itself constrained by limited neighbouring grains of similar size, resulting in less intragranular fracturing and grain size reduction.

Microstructural observations of deformation mechanisms are also supported in their grain size distribution evolution and fractal analysis. Whilst both sands evolve to a very similar fractal distribution with a dimension of $D = 2.2$, there are differences in how the fractal distributions develop with increasing stress and cataclasis, that is reflective of the dominant deformation mechanisms. In accordance with the constrained comminution model (Sammis et al., 1987), intragranular fracturing predicts a fractal dimension of $D = 2.58$ for mature fault gouge subject to high strain. Although our samples do not achieve this critical value, the VWS sample shows a progression in D with increasing stress that suggests potential to develop further with increasing strain beyond the 5% achieved in our experiments. In contrast, the

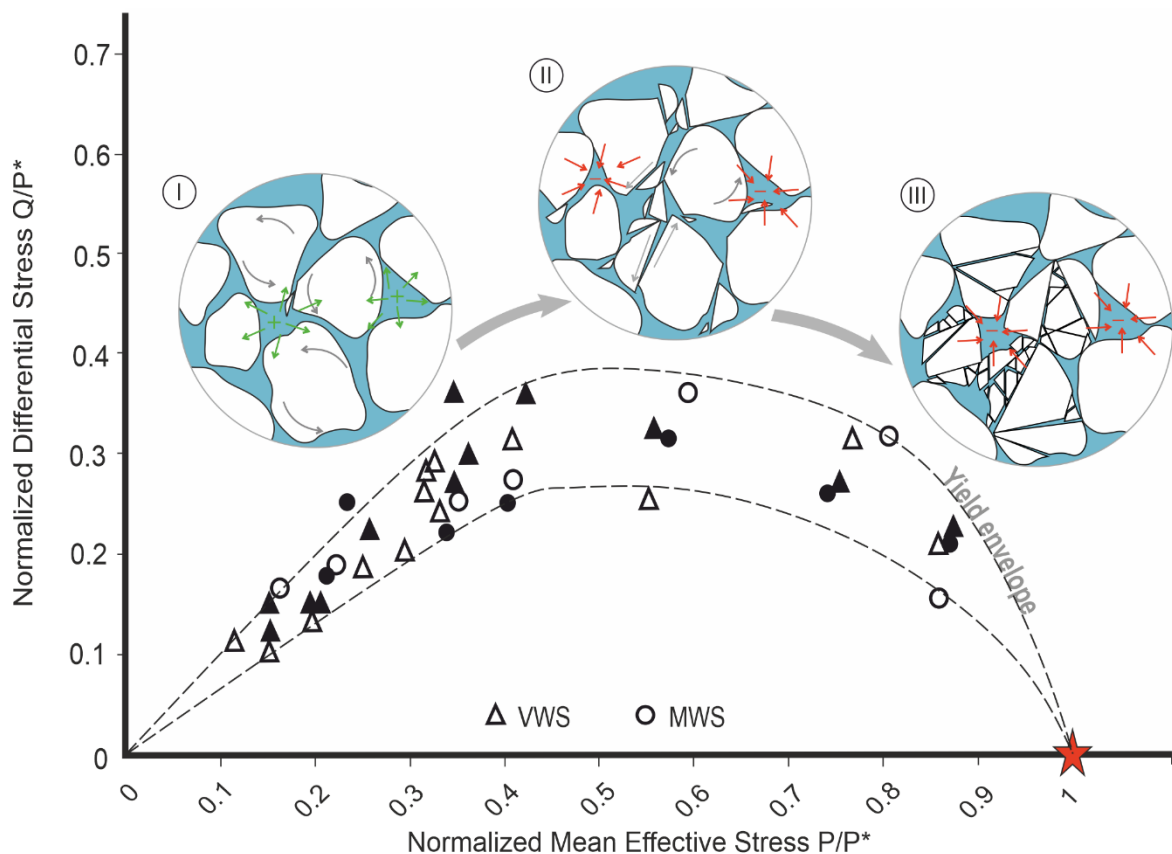


Figure 7.15. Experimental results plotted in Q - P space normalized to P^* . Results plot an elliptical yield envelope. Micromechanics of deformation show a broad continuum with dominant mechanism increasing with stress. (I) Grain sliding and rearrangement. (II) Grain chipping. (III) Intragranular grain fracturing.

MWS in which grain chipping appears to be the more dominant mechanism, with minor intragranular fracturing, develops a fractal dimension $D = 2.2$ at moderate levels of stress (30-50% P^*), and does not develop further with increasing effective stress, suggesting a possible fractal limit achieved by the process of grain chipping and limited Hertzian fracture. The data suggest that grain sorting exerts a significant control on the micromechanics of deformation and subsequent evolution in both grain textures and petrophysical properties, highlighting that the maturity of sediment and its burial history can play an important role in the mechanical and petrophysical development of the basin.

7.4.3. Implications for Sedimentary Basins

A suite of experiments has been presented investigating the elastic and inelastic compaction of unconsolidated sands, and the micromechanical processes that govern deformation, which offers important insight into the burial of sediments during basin formation. The mechanical behaviour of unconsolidated and poorly consolidated sediments is sensitive to the degree of compaction and grain packing, which is modified significantly from initial deposition, where porosity values may be as high as 40%, to burial at depth, where porosities may be as low as 26% (Beard and Weyl, 1973). Understanding the evolution of compaction is essential in trying to unravel the burial history of both unconsolidated and consolidated sediments in the subsurface, and highlights the importance of when and where cementation takes place in order to preserve porosity and permeability. Large inelastic strains are recorded during compaction, which has implications for geomechanical and geotechnical applications in predicting material behaviour. Pijnenburg et al. (2019) demonstrates the importance of understanding elastic and inelastic strains during pressure changes in a reservoir associated with fluid production and pressure depletion, where in-situ pressure changes were best represented by an incorporated elastic + inelastic geomechanical model.

Compositional and textural properties of sands strongly control the compaction of sands during burial, and therefore their porosity and permeability evolution (Worden and Burley, 2003). The evolution of micromechanical processes with increasing effective stress has been demonstrated, allowing for prediction of how grain textures evolve, and ultimately impact permeability. Sorting is identified as a major control on the micromechanical behaviour, with greater cataclasis and grain size reduction within better sorted sands. Estimates of permeability based on the textural properties of the sands combined with porosity values are made using the Berg (1970) method, allowing calculation of relative permeability change. Results show up to two orders permeability reduction, with greater permeability reduction in well-sorted versus poorly-sorted sand, due to greater overall grain size reduction (Fig. 7.16). Fractal dimension alone is not a basis for permeability prediction, as despite very similar values, the VWS samples display greater overall grain size reduction. This is reflected in the fractal range, the range of grain sizes at which a fractal distribution is observed, for which the VWS sand is finer. Previous attempts to represent permeability in Q-P space show that permeability in the elastic regime is predominantly controlled by mean effective stress, and in the post yield inelastic regime, is more influenced by differential stress and controlled by the stress path (Faulkner and Armitage, 2013; Nguyen et al., 2014). Plotting the permeability of our samples at their peak stress at 5% axial strain in Q-P space creates a picture of how permeability evolves with stress in the inelastic regime, although a complete picture of permeability in the post yield regime requires further experiments at different levels of strain (Fig. 7.17). It is extremely valuable to understand how permeability evolves with stress perturbations, for example associated with the production of fluids from subsurface reservoirs. Of particular interest is the formation and fluid flow impact of localised deformation bands in the subsurface, and although not identified in these samples, the results

have implications for strain localisation and development of these bands in both sandstones and sands. Hangx and Brantut (2019) investigated localisation in unconsolidated sands and concluded that it may be inhibited in due to the ease with which grains can slide and rearrange, even after brittle failure had occurred. However, accounts of deformation bands occurring in both unconsolidated and poorly consolidated sandstones suggests the possibility of such structures, with further experimentation required (Cashman and Cashman, 2000; De Rosa et al., 2018; Wilkins et al., 2019). The microstructural observations in poorly-sorted sands, where intragranular fracturing and comminution is less prominent in favour of grain chipping, illustrates why deformation bands have been very difficult to produce in experiments on poorly-sorted sandstones (Cheung et al., 2012), and also supports findings presented in chapter 5, with poorly sorted deformation bands showing less overall cataclasis and permeability reduction.

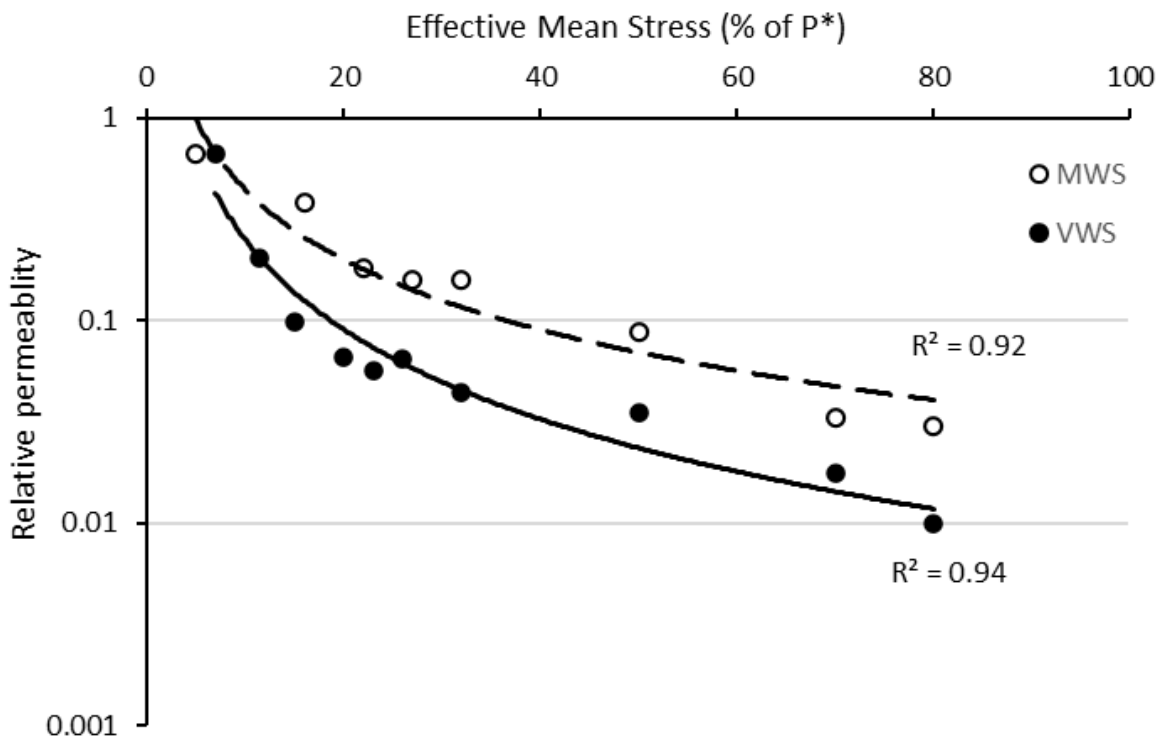


Figure 7.16. Relative permeability reduction as a function of effective mean stress.

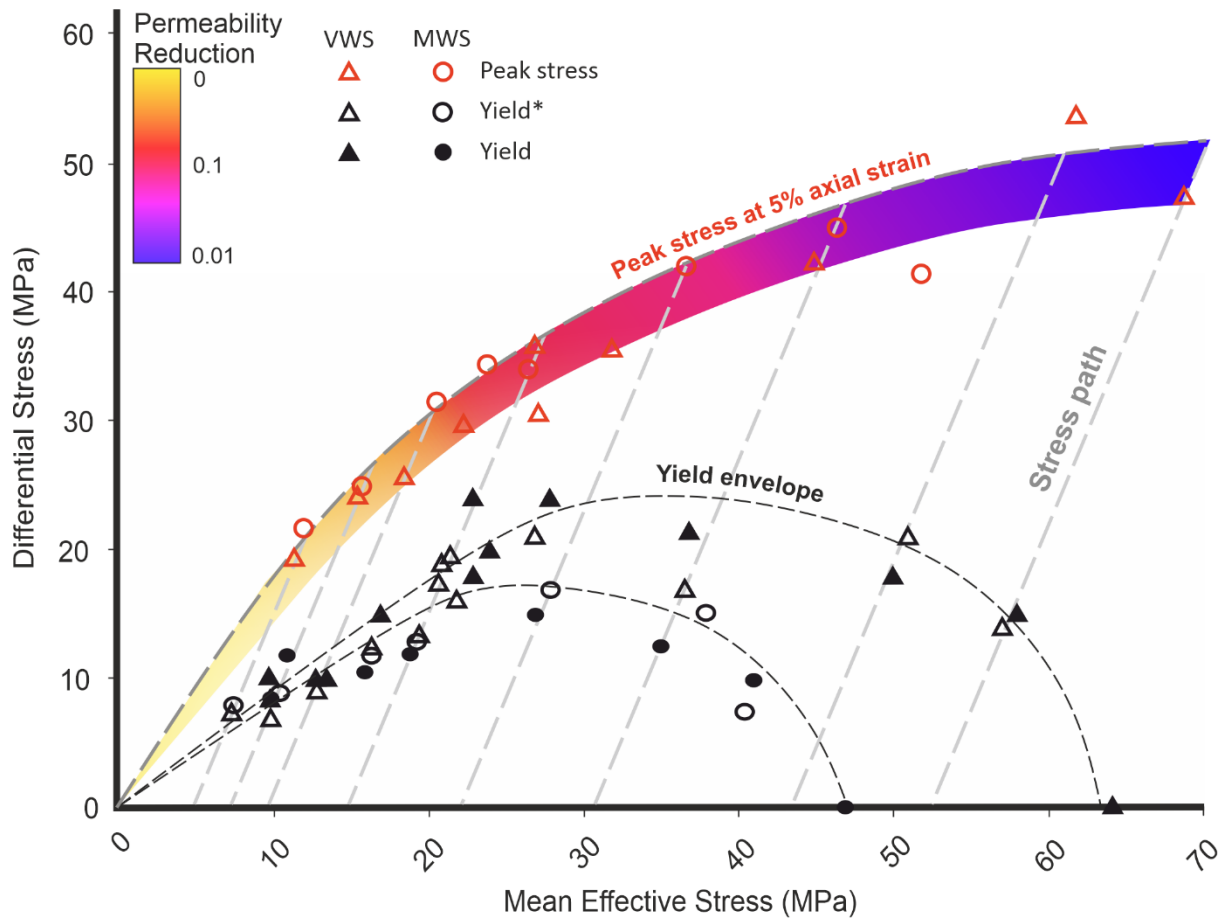


Figure 7.17. Experimental results of yield plotted in Q-P space form elliptical envelopes. Solid symbols represent values obtained from deviation from the hydrostat. Open symbols represent values obtained from differential stress-strain curves. Permeability reduction of samples calculated from textural properties can be plotted in the post yield region up to the peak stress values attained during triaxial loading (red symbols).

7.5 Conclusions

In this study the effects of grain sorting on the micromechanics of deformation during hydrostatic and triaxial loading of unconsolidated quartz sand were investigated in order to understand the evolution of sediments during deformation, and its effects on porosity and permeability.

- The mechanical behaviour of unconsolidated quartz sands is sensitive to the degree of compaction and grain packing. The transition from quasi-linear elastic behaviour to inelastic strain hardening behaviour is poorly defined due to inelastic strains accommodated by grain sliding and reorganisation during 'elastic' loading which account for approximately 65% of total strain. Removal of this deformation during stress cycling results in a stiffer elastic response.
- Under triaxial deformation, three micromechanical processes are identified with increasing effective pressure.
 - (i) At low effective pressures, grain disaggregation and rearrangement accompanied by minor grain chipping are the primary mechanisms.
 - (ii) With increasing effective pressure, deformation transitions to grain chipping with compaction.
 - (iii) At high effective pressures, constrained comminution Hertzian grain fracturing becomes the primary deformation mechanism.
- Grain sorting is identified as a major textural control on the micromechanics of deformation. In relatively poorly sorted samples, the onset of Hertzian intragranular fracturing occurs at much higher effective mean stresses relative to P^* , instead

favouring non-brittle mechanisms such as sliding and rearrangement, as well as grain chipping.

- At comparative conditions, very well-sorted samples display more pervasive Hertzian fracturing than more poorly sorted sands, due to the connectivity of similar sized grains in accordance with Sammis et al. (1987) constrained comminution model, resulting in greater mean grain size reduction and textural modification.
- Micromechanics of deformation is reflected in the development of fractal grain size distribution with stress. VWS sands progressively develop a fractal distribution with increasing effective stress from $D = 1.5$ to a maximum of 2.2. MWS sands develop a fractal dimension of 2.2 at relatively low effective stresses where grain chipping is the dominant mechanism, but cease to develop any further with increasing stress.
- There is greater permeability reduction as a result of increased cataclasis in very well-sorted sands, due to earlier onset Hertzian fracturing, resulting in greater grain size reduction, and textural evolution to a fractal distribution akin to that of low permeability fault core material.
- Microstructural and petrophysical results are in direct agreement with observations made on deformation bands in the field (chapters 5 & 6). Where it is observed that poor grain sorting reduces the amount of grain size and porosity reduction such that better sorted aeolian facies show greater permeability reductions than poorly sorted fluvial facies.

8. Summary and Conclusions

An integrated approach, utilising both naturally occurring examples of deformation bands analysed at a variety of scales, in combination with laboratory-controlled deformation of sands and sandstones offers unique opportunities to control lithological properties and test theories and observations made in the field. Links between inherent properties of sandstones, to the micromechanical processes with stress, to the properties of deformation bands and other fault rocks are made.

The properties of lithofacies and the presence of deformation bands across the localities of two case studies was presented. Both case studies of mixed aeolian-fluvial sandstones in the Triassic Sherwood Sandstone Group, and the Devonian Old Red Sandstone display a wide variation of lithofacies of varying reservoir quality that are affected by deformation bands within the damage zones of faults. Aeolian dunes and fluvial channels and bar-forms are the dominant reservoir units in terms of their porosity and permeability, whilst also displaying a wide degree of variation of lithological properties such as grain size, porosity and sorting that is reflected in the occurrence and properties of deformation bands. Lower reservoir quality mudstones, siltstones, and fine-grained sandstones are of aeolian interdune, fluvial overbank, aeolian sheet and fluvial sheet flood facies.

There are predominantly two types of deformation bands formed, which are controlled by the properties of the sandstone. Disaggregation bands are favoured in finer grained, and poorly sorted facies that display heterolithic laminations, and are typically of fluvial sheetflood and aeolian sheet and interdune facies. They are characterised by shearing and offset laminations, with minimal to no cataclasis due to minimal compaction, and in some cases dilation. Of those sampled, they display porosity reduction due to grain reorganisation

and packing. Cataclastic deformation bands form in coarser, more porous and texturally more uniform facies, such as aeolian dune, interdune, fluvial channel, fluvial bar-form, and are characterised by grain size and porosity reduction associated with compaction and shearing.

Porosity and grain size are found to be the primary controls on cataclasis, characterised by grain size reduction and porosity reduction. Bands in high porosity and coarser grained sandstones show greater amounts of cataclasis. Permeability reduction of cataclastic deformation bands is on the order of 1 – 3 orders of magnitude. Grain sorting is identified as a secondary control on cataclasis of cataclastic deformation bands, and as such, permeability reduction within well-sorted aeolian facies is slightly greater than in poorly-sorted fluvial facies sandstones. This is reflected in grain size distributions of deformation bands revealed by fractal analysis. Cataclastic deformation bands, like larger scale fault gouges, develop fractal grain size distributions that reflect the deformation micromechanics. Deformation bands develop similar fractal dimensions to high strain fault gouges over part of their total distribution, defined as the fractal range. The fractal dimensions of deformation bands, and therefore the micromechanical processes are controlled strongly by the initial sorting of the sandstone. Well-sorted sandstones develop higher fractal distributions (D) than poorly-sorted sandstones, indicating grain size independent cataclasis via constrained comminution and Hertzian intragranular fracturing (Frank and Lawn, 1967; Sammis et al., 1987). Poorer sorted sandstones develop slightly lower values of D , indicating cataclasis may be grain size dependant, and may occur via different mechanisms that may include grain chipping.

Macroscale observations of deformation bands are presented in chapter 6, where two-dimensional measurements of band intensity are made within fault damage zones of different lithologies, as well as measures of deformation band width and geometry. The geometry of

deformation bands is conjugate to the principal stress (σ_1) with dihedral angles of between 20° and 60° , and with faults dipping at angles of $70^\circ \pm 10^\circ$.

Damage zone intensity measures using a two-dimensional window sampling method provide measures of intensity with less error due to sampling bias and censoring, and in fault damage zones within heterogeneous successions, offer a more precise measure for comparison between different sedimentary units. Whilst the type of deformation band formed, and porosity reduction and cataclasis of deformation bands is controlled by porosity and/or grain size, damage zone intensity does not show a clear positive correlation. Grain sorting shows a strong correlation with deformation band intensity, indicating that well-sorted sandstones yield higher intensity. Although there is a negative trend between grain size and intensity, this is attributed to the coarser grained lithofacies being poorer sorted sandstones of fluvial facies association. It is therefore necessary to consider trends of lithological properties with one another. Sorting is also found to be the primary control on deformation band width, with poorly-sorted sandstones exhibiting consistently thicker deformation bands with greater thickness variations in the development of deformation band lenses. Whilst counter-intuitive, deformation band width shows little to no dependence on grain size, despite coarser sandstones being typically poorly sorted fluvial facies, with some of the narrowest band width ranges occurring in coarse-grained, well-sorted sandstones. The role of bed thickness on the formation of deformation bands remains unclear, with two opposing trends from the Cheshire Basin study and Pease Bay study. The former largely consists of sandstone dominated sequences with very minor mudstone and siltstone horizons, whilst the latter comprises much thicker and abundant mudstones and siltstone beds, which raises the question of whether mechanical stratigraphy plays a role in the distribution of strain in the

form of deformation bands in successions with greater contrasts of competent-incompetent beds.

Grain sorting was a constant variable in the field study and a consistent factor controlling many aspects of deformation band properties. Triaxial deformation experiments aimed at understanding the role of grain sorting on the deformation of sandstones and the formation of deformation bands were performed under controlled conditions. Deformation experiments reaffirm grain size and porosity controls on the deformation of sandstones, particularly their strength which scales positively. Grain sorting is found to potentially increase the amount of inelastic deformation during 'elastic' loading, with implications for the burial and compaction of sediments. Microstructural observations using back scattered electron microscopy, and fractal grain size analysis relate and show the influence of grain sorting and stress on the micromechanics of deformation. Micromechanical processes transition from grain disaggregation at low effective pressures (<30% of P^*), to grain chipping and flaking at intermediate pressures (30-60% of P^*), and grain comminution and Hertzian fracturing at higher effective pressures (>60% of P^*). This is reflected in grain size fractal distributions, with greater fractal dimensions at higher effective stresses. This is also in agreement with field observations of fault geometry, in which the dihedral angle of conjugate deformation bands is linked to stress and also controls the deformation mechanisms of deformation band formation.

Grain sorting acts to inhibit grain comminution and Hertzian fracturing, resulting in less overall cataclasis and grain size reduction, supporting conclusions in chapter 5 and observations made on natural deformation bands. Calculations of permeability show that permeability reduction is greater in well-sorted sands than in poorly sorted sands, again

reaffirming observations made of naturally occurring deformation bands in well and poorly-sorted sandstones.

In combining the findings of chapters 5, 6 & 7, it can be concluded that in order to predict the occurrence of deformation bands within a mixed aeolian-fluvial reservoir, porosity and grain size should be a primary initial consideration, but the sorting of sandstones should be a strong secondary consideration. In aeolian successions it has been proposed that the increase of deformation bands within aeolian dune facies of the highest reservoir quality, would homogenise the reservoir by reducing those units to the properties of the lesser reservoir quality units (Fossen and Bale, 2007; Fossen et al., 2007). Results of this thesis suggest that the same cannot be said of mixed aeolian-fluvial successions. Despite an increase in band intensity within aeolian sandstones versus fluvial sandstones, resulting in permeability reductions of up to 3 orders of magnitude, it is demonstrated that deformation bands hosted in fluvial sandstones can be of sufficient intensity, and are consistently wider, and with more width variation. The decrease in intensity and slightly less permeability reduction may therefore be outweighed by an increase in cumulative width of the bands. If this were the case, the inherent permeability heterogeneity of an aeolian-fluvial reservoir could be maintained.

References

- Ambrose, K., Hough, E., Smith, N., Warrington, G., 2014. Lithostratigraphy of the Sherwood Sandstone Group of England, Wales and south-west Scotland. Geology and Regional Geophysics Directorate Research Report RR/14/01.
- Anderson, E.M., 1905. The dynamics of faulting. Transactions of the Edinburgh Geological Society 8, 387-402.
- Andrews, J.E., Nabi, G., 1994. Lithostratigraphy of the Dinantian Inverclyde and Strathclyde Groups, Cockburnspath Outlier, East Lothian–North Berwickshire. Scottish Journal of Geology 30, 105-119.
- Antonellini, M.A., Aydin, A., Pollard, D.D., 1994. Microstructure of deformation bands in porous sandstones at Arches National Park, Utah. Journal of structural geology 16, 941-959.
- Armitage, P., Worden, R., Faulkner, D., Aplin, A., Butcher, A., Espie, A., 2013. Mercia Mudstone Formation caprock to carbon capture and storage sites: petrology and petrophysical characteristics. 170, 119-132.
- Audley-Charles, M.G., 1970. Stratigraphical correlation of the Triassic rocks of the British Isles. Quarterly Journal of the Geological Society 126, 19-46.
- Awdal, A., Healy, D., Alsop, G.I., 2014. Geometrical analysis of deformation band lozenges and their scaling relationships to fault lenses. Journal of Structural Geology 66, 11-23.
- Aydin, A., 1978. Small faults formed as deformation bands in sandstone. Pure and Applied Geophysics 116, 913-930.
- Aydin, A., Borja, R.I., Eichhubl, P., 2006. Geological and mathematical framework for failure modes in granular rock. Journal of Structural Geology 28, 83-98.
- Aydin, A., Johnson, A.M., 1978. Development of faults as zones of deformation bands and as slip surfaces in sandstone, Rock Friction and Earthquake Prediction. Springer, pp. 931-942.
- Aydin, A., Johnson, A.M., 1983. Analysis of faulting in porous sandstones. Journal of Structural Geology 5, 19-31.
- Baaren, J.v., 1978. Quick-look permeability estimates using sidewall samples and porosity logs, Koninklijke/Shell Exploratie en Productie Lab. Publ.
- Ballas, G., Fossen, H., Soliva, R., 2015. Factors controlling permeability of cataclastic deformation bands and faults in porous sandstone reservoirs. Journal of Structural Geology 76, 1-21.

- Ballas, G., Soliva, R., Benedicto, A., Sizun, J.-P., 2014. Control of tectonic setting and large-scale faults on the basin-scale distribution of deformation bands in porous sandstone (Provence, France). *Marine and Petroleum Geology* 55, 142-159.
- Ballas, G., Soliva, R., Sizun, J.-P., Fossen, H., Benedicto, A., Skurtveit, E., 2013. Shear-enhanced compaction bands formed at shallow burial conditions; implications for fluid flow (Provence, France). *Journal of Structural Geology* 47, 3-15.
- Baud, P., Schubnel, A., Wong, T.f., 2000. Dilatancy, compaction, and failure mode in Solnhofen limestone. *Journal of Geophysical Research: Solid Earth* 105, 19289-19303.
- Baud, P., Vajdova, V., Wong, T.f., 2006. Shear-enhanced compaction and strain localization: Inelastic deformation and constitutive modeling of four porous sandstones. *Journal of Geophysical Research: Solid Earth* Vol 111.
- Beach, A., Brown, J.L., Welbon, A.I., McCallum, J.E., Brockbank, P., Knott, S., 1997. Characteristics of fault zones in sandstones from NW England: application to fault transmissibility. Geological Society, London, Special Publications 124, 315-324.
- Beach, A., Welbon, A.I., Brockbank, P.J., McCallum, J.E., 1999. Reservoir damage around faults; outcrop examples from the Suez Rift. *Petroleum Geoscience* 5, 109-116.
- Beard, D., Weyl, P., 1973. Influence of texture on porosity and permeability of unconsolidated sand. *AAPG Bulletin* 57, 349-369.
- Bedford, J.D., Faulkner, D.R., Leclère, H., Wheeler, J., 2018. High-resolution mapping of yield curve shape and evolution for porous rock: The effect of inelastic compaction on porous bassanite. *Journal of Geophysical Research: Solid Earth* 123, 1217-1234.
- Bedford, J.D., Faulkner, D.R., Wheeler, J., Leclère, H., 2019. High-resolution mapping of yield curve shape and evolution for high-porosity sandstone. *Journal of Geophysical Research: Solid Earth* 124, 5450-5468.
- Beke, B., Fodor, L., Millar, L., Petrik, A., 2019. Deformation band formation as a function of progressive burial: Depth calibration and mechanism change in the Pannonian Basin (Hungary). *Marine and Petroleum Geology* 105, 1-16.
- Berg, R.R., 1970. Method for determining permeability from reservoir rock properties.
- Bésuelle, P., Desrues, J., Raynaud, S., 2000. Experimental characterisation of the localisation phenomenon inside a Vosges sandstone in a triaxial cell. *International Journal of Rock Mechanics and Mining Sciences* 37, 1223-1237.

Blenkinsop, T.G., 1991. Cataclasis and processes of particle size reduction. *Pure and Applied Geophysics* 136, 59-86.

Bloomfield, J., Moreau, M., Newell, A., 2006. Characterization of permeability distributions in six lithofacies from the Helsby and Wilmslow sandstone formations of the Cheshire Basin, UK. Geological Society, London, Special Publications 263, 83-101.

Blott, S.J., Pye, K., 2001. GRADISTAT: a grain size distribution and statistics package for the analysis of unconsolidated sediments. *Earth Surface Processes and Landforms* 26, 1237-1248.

Braathen, A., Tveranger, J., Fossen, H., Skar, T., Cardozo, N., Semshaug, S., Bastesen, E., Sverdrup, E., 2009. Fault facies and its application to sandstone reservoirs. *AAPG bulletin* 93, 891-917.

Brandenburg, J., Alpak, F.O., Solum, J.G., Naruk, S.J., 2012. A kinematic trishear model to predict deformation bands in a fault-propagation fold, East Kaibab monocline, Utah. *AAPG bulletin* 96, 109-132.

Brown, C., Cassidy, N., Egan, S., Griffiths, D., 2019a. Evaluating the Response of Geothermal Reservoirs in the Cheshire Basin: A Parameter Sensitivity Analysis, *AAPG Annual Convention and Exhibition*.

Brown, C., Cassidy, N., Egan, S., Griffiths, D., 2019b. Modelling low-enthalpy deep geothermal reservoirs in the Cheshire Basin, UK as a future renewable energy source, *Geophysical Research Abstracts*.

Browne, M., Dean, M., Hall, I.H., McAdam, A., Monro, S., Chisholm, J., 1999. A lithostratigraphical framework for the Carboniferous rocks of the Midland Valley of Scotland. Version 2.

Browne, M., Smith, R., Aitken, A.M., 2002. Stratigraphical framework for the Devonian (Old Red Sandstone) rocks of Scotland south of a line from Fort William to Aberdeen. *British Geological Survey*.

Brzesowsky, R., Spiers, C., Peach, C., Hangx, S., 2014. Time-independent compaction behavior of quartz sands. *Journal of Geophysical Research: Solid Earth* 119, 936-956.

Cade, C., Evans, I., Bryant, S.L., 1994. Analysis of permeability controls: a new approach. *Clay Minerals* 29, 491-501.

Caine, J.S., Evans, J.P., Forster, C.B., 1996. Fault zone architecture and permeability structure. *Geology* 24, 1025-1028.

- Cashman, S., Cashman, K., 2000. Cataclasis and deformation-band formation in unconsolidated marine terrace sand, Humboldt County, California. *Geology* 28, 111-114.
- Chadwick, R., 1997. Fault analysis of the Cheshire Basin, NW England. Geological Society, London, Special Publications 124, 297-313.
- Charalampidou, E.-M., Hall, S.A., Stanchits, S., Lewis, H., Viggiani, G., 2011. Characterization of shear and compaction bands in a porous sandstone deformed under triaxial compression. *Tectonophysics* 503, 8-17.
- Chester, J.S., Lenz, S.C., Chester, F.M., Lang, R., 2004. Mechanisms of compaction of quartz sand at diagenetic conditions. *Earth and Planetary Science Letters* 220, 435-451.
- Cheung, C.S., Baud, P., Wong, T.f., 2012. Effect of grain size distribution on the development of compaction localization in porous sandstone. *Geophysical Research Letters* 39.
- Childs, C., Manzocchi, T., Walsh, J.J., Bonson, C.G., Nicol, A., Schöpfer, M.P., 2009. A geometric model of fault zone and fault rock thickness variations. *Journal of Structural Geology* 31, 117-127.
- Childs, C., Watterson, J., Walsh, J., 1995. Fault overlap zones within developing normal fault systems. *Journal of the Geological Society* 152, 535-549.
- Choi, J.-H., Edwards, P., Ko, K., Kim, Y.-S., 2016. Definition and classification of fault damage zones: A review and a new methodological approach. *Earth-Science Reviews* 152, 70-87.
- Cilona, A., Baud, P., Tondi, E., Agosta, F., Vinciguerra, S., Rustichelli, A., Spiers, C.J., 2012. Deformation bands in porous carbonate grainstones: Field and laboratory observations. *Journal of Structural Geology* 45, 137-157.
- Cilona, A., Faulkner, D.R., Tondi, E., Agosta, F., Mancini, L., Rustichelli, A., Baud, P., Vinciguerra, S., 2014. The effects of rock heterogeneity on compaction localization in porous carbonates. *Journal of Structural Geology* 67, 75-93.
- Cowan, G., 1993. Identification and significance of aeolian deposits within the dominantly fluvial Sherwood Sandstone Group of the East Irish Sea Basin UK. Geological Society, London, Special Publications 73, 231-245.
- Crawford, B., Faulkner, D., Rutter, E., 2008. Strength, porosity, and permeability development during hydrostatic and shear loading of synthetic quartz-clay fault gouge. *Journal of Geophysical Research: Solid Earth* (1978–2012) 113.

Crawford, B., Gooch, M., Webb, D., 2004. Textural controls on constitutive behavior in unconsolidated sands: Micromechanics and cap plasticity, Gulf Rocks 2004, the 6th North America Rock Mechanics Symposium (NARMS). American Rock Mechanics Association.

Cuss, R., Rutter, E., Holloway, R., 2003. The application of critical state soil mechanics to the mechanical behaviour of porous sandstones. *International Journal of Rock Mechanics and Mining Sciences* 40, 847-862.

De Joussineau, G., Aydin, A., 2007. The evolution of the damage zone with fault growth in sandstone and its multiscale characteristics. *Journal of Geophysical Research: Solid Earth* 112.

de Lima Rodrigues, M.C.N., Trzaskos, B., Lopes, A.P., 2015. Influence of deformation bands on sandstone porosity: A case study using three-dimensional microtomography. *Journal of Structural Geology* 72, 96-110.

De Rosa, S.S., Shipton, Z.K., Lunn, R.J., Kremer, Y., Murray, T., 2018. Along-strike fault core thickness variations of a fault in poorly lithified sediments, Miri (Malaysia). *Journal of Structural Geology* 116, 189-206.

Deng, S., Aydin, A., 2012. Distribution of compaction bands in 3D in an aeolian sandstone: The role of cross-bed orientation. *Tectonophysics* 574, 204-218.

Dershowitz, W.S., Herda, H.H., 1992. Interpretation of fracture spacing and intensity, The 33th us symposium on rock mechanics (USRMS). American Rock Mechanics Association.

Du Bernard, X., Eichhubl, P., Aydin, A., 2002a. Dilation bands: A new form of localized failure in granular media. *Geophysical Research Letters* 29, 29-21-29-24.

Du Bernard, X., Labaume, P., Darcel, C., Davy, P., Bour, O., 2002b. Cataclastic slip band distribution in normal fault damage zones, Nubian sandstones, Suez rift. *Journal of Geophysical Research: Solid Earth* 107, ETG 6-1-ETG 6-12.

Dunn, D.E., LaFountain, L.J., Jackson, R.E., 1973. Porosity dependence and mechanism of brittle fracture in sandstones. *Journal of Geophysical Research* 78, 2403-2417.

Eggertsson, G.H., Kendrick, J.E., Weaver, J., Wallace, P.A., Utley, J.E., Bedford, J.D., Allen, M.J., Markússon, S.H., Worden, R.H., Faulkner, D.R., 2020. Compaction of hyaloclastite from the active geothermal system at Krafla volcano, Iceland. *Geofluids* 2020.

Eichhubl, P., Hooker, J.N., Laubach, S.E., 2010. Pure and shear-enhanced compaction bands in Aztec Sandstone. *Journal of Structural Geology* 32, 1873-1886.

Engelder, J.T., 1974. Cataclasis and the generation of fault gouge. *Geological Society of America Bulletin* 85, 1515-1522.

Evans, D., Rees, J., Holloway, S., 1993. The Permian to Jurassic stratigraphy and structural evolution of the central Cheshire Basin. *Journal of the Geological Society* 150, 857-870.

Exner, U., Kaiser, J., Gier, S., 2013. Deformation bands evolving from dilation to cementation bands in a hydrocarbon reservoir (Vienna Basin, Austria). *Marine and Petroleum Geology* 43, 504-515.

Exner, U., Tschegg, C., 2012. Preferential cataclastic grain size reduction of feldspar in deformation bands in poorly consolidated arkosic sands. *Journal of Structural Geology* 43, 63-72.

Farrell, N., Healy, D., Taylor, C., 2014. Anisotropy of permeability in faulted porous sandstones. *Journal of Structural Geology* 63, 50-67.

Faulkner, D., Armitage, P., 2013. The effect of tectonic environment on permeability development around faults and in the brittle crust. *Earth and Planetary Science Letters* 375, 71-77.

Faulkner, D., Jackson, C., Lunn, R., Schlische, R., Shipton, Z., Wibberley, C., Withjack, M., 2010. A review of recent developments concerning the structure, mechanics and fluid flow properties of fault zones. *Journal of Structural Geology* 32, 1557-1575.

Faulkner, D., Mitchell, T., Jensen, E., Cembrano, J., 2011. Scaling of fault damage zones with displacement and the implications for fault growth processes. *Journal of Geophysical Research: Solid Earth* 116.

Ferrill, D.A., Morris, A.P., McGinnis, R.N., Smart, K.J., Wigginton, S.S., Hill, N.J., 2017. Mechanical stratigraphy and normal faulting. *Journal of Structural Geology* 94, 275-302.

Filomena, C., Hornung, J., Stollhofen, H., 2014. Assessing accuracy of gas-driven permeability measurements: a comparative study of diverse Hassler-cell and probe permeameter devices. *Solid Earth* 5, 1-11.

Fisher, Q., Knipe, R., 2001. The permeability of faults within siliciclastic petroleum reservoirs of the North Sea and Norwegian Continental Shelf. *Marine and Petroleum Geology* 18, 1063-1081.

Folk, R.L., Ward, W.C., 1957. Brazos River bar: a study in the significance of grain size parameters. *Journal of Sedimentary Research* 27.

Forbes, D., 1993. Reservoir characterization and potential of the old red sandstone around the inner moray firth, NE Scotland. Durham University.

Fossen, H., Bale, A., 2007. Deformation bands and their influence on fluid flow. AAPG bulletin 91, 1685-1700.

Fossen, H., Hesthammer, J., 1998. Deformation bands and their significance in porous sandstone reservoirs. First Break 16, 21-25.

Fossen, H., Hesthammer, J., 2000. Possible absence of small faults in the Gullfaks Field, northern North Sea: implications for downscaling of faults in some porous sandstones. Journal of Structural Geology 22, 851-863.

Fossen, H., Rotevatn, A., 2012. Characterization of deformation bands associated with normal and reverse stress states in the Navajo Sandstone, Utah: Discussion. AAPG bulletin 96, 869-876.

Fossen, H., Schultz, R.A., Shipton, Z.K., Mair, K., 2007. Deformation bands in sandstone: a review. Journal of the Geological Society 164, 755-769.

Fossen, H., Schultz, R.A., Torabi, A., 2011a. Conditions and implications for compaction band formation in the Navajo Sandstone, Utah. Journal of Structural Geology 33, 1477-1490.

Fossen, H., Schultz, R.A., Torabi, A., 2011b. Conditions and implications for compaction band formation in the Navajo Sandstone, Utah. Journal of Structural Geology 33, 1477-1490.

Fossen, H., Soliva, R., Ballas, G., Trzaskos, B., Cavalcante, C., Schultz, R.A., 2018. A review of deformation bands in reservoir sandstones: geometries, mechanisms and distribution. Geological Society, London, Special Publications 459, 9-33.

Frank, F.C., Lawn, B.R., 1967. On the theory of Hertzian fracture. Proceedings of the Royal Society of London. Series A. Mathematical and Physical Sciences 299, 291-306.

Friedman, G.M., 1962. On sorting, sorting coefficients, and the lognormality of the grain-size distribution of sandstones. The Journal of Geology 70, 737-753.

Friedman, M., Logan, J., 1973. Lüders' bands in experimentally deformed sandstone and limestone. Geological Society of America Bulletin 84, 1465-1476.

Griffiths, J., Faulkner, D.R., Edwards, A.P., Worden, R.H., 2016. Deformation band development as a function of intrinsic host-rock properties in Triassic Sherwood Sandstone. Geological Society, London, Special Publications 435, SP435. 411.

Griffiths, K., Shand, P., Ingram, J., 2003. The Permo-Triassic sandstones of Manchester and east Cheshire. Baseline Report Series 8.

Grove, C., Jerram, D.A., 2011. jPOR: An ImageJ macro to quantify total optical porosity from blue-stained thin sections. *Computers & Geosciences* 37, 1850-1859.

Hangx, S.J., Brantut, N., 2019. Micromechanics of High-Pressure Compaction in Granular Quartz Aggregates. *Journal of Geophysical Research: Solid Earth* 124, 6560-6580.

Hausegger, S., Kurz, W., Rabitsch, R., Kiechl, E., Brosch, F.-J., 2010. Analysis of the internal structure of a carbonate damage zone: Implications for the mechanisms of fault breccia formation and fluid flow. *Journal of Structural Geology* 32, 1349-1362.

Heap, M., Farquharson, J., Baud, P., Lavallée, Y., Reuschlé, T., 2015a. Fracture and compaction of andesite in a volcanic edifice. *Bulletin of volcanology* 77, 55.

Heap, M.J., Brantut, N., Baud, P., Meredith, P.G., 2015b. Time-dependent compaction band formation in sandstone. *Journal of Geophysical Research: Solid Earth* 120, 4808-4830.

Hesthammer, J., Bjorkum, P.A., Watts, L., 2002. The effect of temperature on sealing capacity of faults in sandstone reservoirs: Examples from the Gullfaks and Gullfaks Sor fields, North Sea. *AAPG bulletin* 86.

Hesthammer, J., Johansen, T., Watts, L., 2000. Spatial relationships within fault damage zones in sandstone. *Marine and Petroleum Geology* 17, 873-893.

Heynekamp, M.R., Goodwin, L.B., Mozley, P.S., Haneberg, W.C., 1999. Controls on fault-zone architecture in poorly lithified sediments, Rio Grande Rift, New Mexico: Implications for fault-zone permeability and fluid flow. Washington DC American Geophysical Union Geophysical Monograph Series 113, 27-49.

Hippler, S., 1993. Deformation microstructures and diagenesis in sandstone adjacent to an extensional fault: implications for the flow and entrapment of hydrocarbons. *AAPG bulletin* 77, 625-637.

Hirst, C.M., Gluyas, J.G., Adams, C.A., Mathias, S.A., Bains, S., Styles, P., 2015. UK Low Enthalpy Geothermal Resources: the Cheshire Basin, Proceedings World Geothermal Congress Melbourne, Australia.

Hirth, G., Tullis, J., 1989. The effects of pressure and porosity on the micromechanics of the brittle-ductile transition in quartzite. *Journal of Geophysical Research: Solid Earth* (1978–2012) 94, 17825-17838.

Hull, E., 1869. The Triassic and Permian rocks of the Midland counties of England. HM Stationery Office, Longmans, Green, and Company.

Jamison, W.R., Stearns, D.W., 1982. Tectonic deformation of Wingate Sandstone, Colorado National Monument. AAPG Bulletin 66, 2584-2608.

Johansen, T.E.S., Fossen, H., 2008. Internal geometry of fault damage zones in interbedded siliciclastic sediments. Geological Society, London, Special Publications 299, 35-56.

Johansen, T.E.S., Fossen, H., Kluge, R., 2005. The impact of syn-faulting porosity reduction on damage zone architecture in porous sandstone: an outcrop example from the Moab Fault, Utah. Journal of Structural Geology 27, 1469-1485.

Johri, M., Dunham, E.M., Zoback, M.D., Fang, Z., 2014. Predicting fault damage zones by modeling dynamic rupture propagation and comparison with field observations. Journal of Geophysical Research: Solid Earth 119, 1251-1272.

Kaproth, B.M., Cashman, S.M., Marone, C., 2010. Deformation band formation and strength evolution in unlithified sand: the role of grain breakage. Journal of Geophysical Research: Solid Earth 115.

Karner, S.L., Chester, F.M., Kronenberg, A.K., Chester, J.S., 2003. Subcritical compaction and yielding of granular quartz sand. Tectonophysics 377, 357-381.

Karner, S.L., Chester, J.S., Chester, F.M., Kronenberg, A.K., Hajash, A., 2005. Laboratory deformation of granular quartz sand: Implications for the burial of clastic rocks. AAPG Bulletin 89, 603-625.

Kim, Y.-S., Peacock, D.C., Sanderson, D.J., 2004. Fault damage zones. Journal of structural geology 26, 503-517.

Klimczak, C., Schultz, R.A., 2013. Shear-enhanced compaction in dilating granular materials. International Journal of Rock Mechanics and Mining Sciences 64, 139-147.

Knott, S., 1994. Fault zone thickness versus displacement in the Permo-Triassic sandstones of NW England. Journal of the Geological Society 151, 17-25.

Knott, S.D., Beach, A., Brockbank, P.J., Brown, J.L., McCallum, J.E., Welbon, A.I., 1996. Spatial and mechanical controls on normal fault populations. Journal of Structural Geology 18, 359-372.

Krumbein, W., Monk, G., 1943. Permeability as a function of the size parameters of unconsolidated sand. Transactions of the AIME 151, 153-163.

Kyrkjebø, R., Gabrielsen, R., Faleide, J., 2004. Unconformities related to the Jurassic–Cretaceous synrift–post-rift transition of the northern North Sea. *Journal of the Geological Society* 161, 1-17.

Labbaume, P., Moretti, I., 2001. Diagenesis-dependence of cataclastic thrust fault zone sealing in sandstones. Example from the Bolivian Sub-Andean Zone. *Journal of Structural Geology* 23, 1659-1675.

Laubach, S., Eichhubl, P., Hargrove, P., Ellis, M., Hooker, J., 2014. Fault core and damage zone fracture attributes vary along strike owing to interaction of fracture growth, quartz accumulation, and differing sandstone composition. *Journal of Structural Geology* 68, 207-226.

Lee, K.L., Farhoomand, I., 1967. Compressibility and crushing of granular soil in anisotropic triaxial compression. *Canadian Geotechnical Journal* 4, 68-86.

Leveille, G.P., Knipe, R., More, C., Ellis, D., Dudley, G., Jones, G., Fisher, Q.J., Allinson, G., 1997. Compartmentalization of Rotliegendes gas reservoirs by sealing faults, Jupiter Fields area, southern North Sea. Geological Society, London, Special Publications 123, 87-104.

Lockner, D., 1993. The role of acoustic emission in the study of rock fracture, *International Journal of Rock Mechanics and Mining Sciences & Geomechanics Abstracts*. Elsevier, pp. 883-899.

Lucas, S.E., Moore, J.C., 1986. Cataclastic deformation in accretionary wedges: Deep Sea Drilling Project Leg 66, southern Mexico, and on-land examples from Barbados and Kodiak Islands. *Geological Society of America Memoirs* 166, 89-104.

Mair, K., Elphick, S., Main, I., 2002. Influence of confining pressure on the mechanical and structural evolution of laboratory deformation bands. *Geophysical Research Letters* 29, 49-41-49-44.

Manzocchi, T., Walsh, J., Nell, P., Yielding, G., 1999. Fault transmissibility multipliers for flow simulation models. *Petroleum Geoscience* 5, 53-63.

Mark, D.F., Green, P.F., Parnell, J., Kelley, S.P., Lee, M.R., Sherlock, S.C., 2008. Late Palaeozoic hydrocarbon migration through the Clair field, West of Shetland, UK Atlantic margin. *Geochimica et Cosmochimica Acta* 72, 2510-2533.

Marone, C., Raleigh, C.B., Scholz, C., 1990. Frictional behavior and constitutive modeling of simulated fault gouge. *Journal of Geophysical Research: Solid Earth* 95, 7007-7025.

Mauldon, M., 1998. Estimating mean fracture trace length and density from observations in convex windows. *Rock Mechanics and Rock Engineering* 31, 201-216.

Mauldon, M., Dunne, W., Rohrbaugh Jr, M., 2001. Circular scanlines and circular windows: new tools for characterizing the geometry of fracture traces. *Journal of Structural Geology* 23, 247-258.

McKie, T., Williams, B., 2009. Triassic palaeogeography and fluvial dispersal across the northwest European Basins. *Geological Journal* 44, 711-741.

Meadows, N., 2006. The correlation and sequence architecture of the Ormskirk sandstone formation in the Triassic Sherwood sandstone group of the East Irish Sea Basin, NW England. *Geological Journal* 41, 93-122.

Meadows, N.S., Beach, A., 1993. Structural and climatic controls on facies distribution in a mixed fluvial and aeolian reservoir: the Triassic Sherwood Sandstone in the Irish Sea. Geological Society, London, Special Publications 73, 247-264.

Medici, G., West, L.J., Mountney, N.P., Welch, M., 2019. Permeability of rock discontinuities and faults in the Triassic Sherwood Sandstone Group (UK): insights for management of fluvio-aeolian aquifers worldwide. *Hydrogeology Journal* 27, 2835-2855.

Mikkelsen, P., Floodpage, J., 1997. The hydrocarbon potential of the Cheshire Basin. Geological Society, London, Special Publications 124, 161-183.

Mitchell, C., 2015. UK Frac Sand Resources.

Mitchell, T., Faulkner, D., 2009. The nature and origin of off-fault damage surrounding strike-slip fault zones with a wide range of displacements: a field study from the Atacama fault system, northern Chile. *Journal of Structural Geology* 31, 802-816.

Mitchell, T., Faulkner, D., 2012. Towards quantifying the matrix permeability of fault damage zones in low porosity rocks. *Earth and Planetary Science Letters* 339, 24-31.

Moore, D.E., Lockner, D.A., 2004. Crystallographic controls on the frictional behavior of dry and water-saturated sheet structure minerals. *Journal of Geophysical Research: Solid Earth* (1978–2012) 109.

Morgan, J.K., Boettcher, M.S., 1999. Numerical simulations of granular shear zones using the distinct element method: 1. Shear zone kinematics and the micromechanics of localization. *Journal of Geophysical Research: Solid Earth* 104, 2703-2719.

Mountney, N.P., Thompson, D.B., 2002. Stratigraphic evolution and preservation of aeolian dune and damp/wet interdune strata: an example from the Triassic Helsby Sandstone Formation, Cheshire Basin, UK. *Sedimentology* 49, 805-833.

Nelson, P.H., 1994. Permeability-porosity relationships in sedimentary rocks. *The log analyst* 35.

Nguyen, V., Gland, N., Dautriat, J., David, C., Wassermann, J., Guelard, J., 2014. Compaction, permeability evolution and stress path effects in unconsolidated sand and weakly consolidated sandstone. *International Journal of Rock Mechanics and Mining Sciences* 67, 226-239.

Ogilvie, S., Glover, P., 2001. High resolution petrophysical measurements of deformation bands in sandstones. *Physics and Chemistry of the Earth, Part A: Solid Earth Geodesy* 26, 27-32.

Parnell, J., Watt, G.R., Middleton, D., Kelly, J., Baron, M., 2004. Deformation band control on hydrocarbon migration. *Journal of Sedimentary Research* 74, 552-560.

Pijnenburg, R., Verberne, B., Hangx, S., Spiers, C., 2019. Inelastic deformation of the Slochteren sandstone: Stress-strain relations and implications for induced seismicity in the Groningen gas field. *Journal of Geophysical Research: Solid Earth* 124, 5254-5282.

Pittman, E.D., 1981. Effect of fault-related granulation on porosity and permeability of quartz sandstones, Simpson Group (Ordovician), Oklahoma. *AAPG Bulletin* 65, 2381-2387.

Priddy, C.L., Clarke, S.M., 2020. The sedimentology of an ephemeral fluvial–aeolian succession. *Sedimentology* 67.

Rawling, G.C., Goodwin, L.B., 2003. Cataclasis and particulate flow in faulted, poorly lithified sediments. *Journal of Structural Geology* 25, 317-331.

Rotevatn, A., Sandve, T.H., Keilegavlen, E., Kolyukhin, D., Fossen, H., 2013. Deformation bands and their impact on fluid flow in sandstone reservoirs: the role of natural thickness variations. *Geofluids* 13, 359-371.

Rotevatn, A., Torabi, A., Fossen, H., Braathen, A., 2008. Slipped deformation bands: a new type of cataclastic deformation bands in Western Sinai, Suez rift, Egypt. *Journal of Structural Geology* 30, 1317-1331.

Rowe, J., Burley, S.D., 1997. Faulting and porosity modification in the Sherwood Sandstone at Alderley Edge, northeastern Cheshire: an exhumed example of fault-related diagenesis. Geological Society, London, Special Publications 124, 325-352.

Ruffell, A., 2003. Permian and Triassic red beds and the Penarth Group of Great Britain by MJ Benton, E. Cook and P. Turner, Geological Conservation Review Series, No. 24, Joint Nature Conservation Committee, Peterborough, 2002. No. of pages: 337. ISBN 1 86107 493 X (hardback). Wiley Online Library.

Rutter, E., Glover, C., 2012. The deformation of porous sandstones; are Byerlee friction and the critical state line equivalent? *Journal of Structural Geology* 44, 129-140.

Rutter, E., Llana-Fúnez, S., Brodie, K., 2009. Dehydration and deformation of intact cylinders of serpentinite. *Journal of Structural Geology* 31, 29-43.

Saillet, E., Wibberley, C.A., 2010. Evolution of cataclastic faulting in high-porosity sandstone, Bassin du Sud-Est, Provence, France. *Journal of Structural Geology* 32, 1590-1608.

Sammis, C., Ashby, M., 1986. The failure of brittle porous solids under compressive stress states. *Acta Metallurgica* 34, 511-526.

Sammis, C., King, G., Biegel, R., 1987. The kinematics of gouge deformation. *Pure and Applied Geophysics* 125, 777-812.

Sammis, C.G., King, G.C.J.G.R.L., 2007. Mechanical origin of power law scaling in fault zone rock. 34.

Sanderson, D.J., Nixon, C.W., 2015. The use of topology in fracture network characterization. *Journal of Structural Geology* 72, 55-66.

Savage, H.M., Brodsky, E.E., 2011. Collateral damage: Evolution with displacement of fracture distribution and secondary fault strands in fault damage zones. *Journal of Geophysical Research: Solid Earth* 116.

Schofield, A., Wroth, P., 1968. *Critical state soil mechanics*. McGraw-hill.

Schöpfer, M.P., Childs, C., Walsh, J.J., 2006. Localisation of normal faults in multilayer sequences. *Journal of Structural Geology* 28, 816-833.

Schueller, S., Braathen, A., Fossen, H., Tveranger, J., 2013. Spatial distribution of deformation bands in damage zones of extensional faults in porous sandstones: Statistical analysis of field data. *Journal of Structural Geology* 52, 148-162.

Schultz, R., Siddharthan, R., 2005. A general framework for the occurrence and faulting of deformation bands in porous granular rocks. *Tectonophysics* 411, 1-18.

Schultz, R.A., 2019. *Geologic Fracture Mechanics*. Cambridge University Press.

Schultz, R.A., Okubo, C.H., Fossen, H., 2010. Porosity and grain size controls on compaction band formation in Jurassic Navajo Sandstone. *Geophysical Research Letters* 37.

Scruggs, V., Tullis, T., 1998. Correlation between velocity dependence of friction and strain localization in large displacement experiments on feldspar, muscovite and biotite gouge. *Tectonophysics* 295, 15-40.

Shipton, Z., Cowie, P., 2001. Damage zone and slip-surface evolution over μm to km scales in high-porosity Navajo sandstone, Utah. *Journal of Structural Geology* 23, 1825-1844.

Shipton, Z., Evans, J., Thompson, L., 2005. The geometry and thickness of deformation-band fault core and its influence on sealing characteristics of deformation-band fault zones.

Shipton, Z.K., Cowie, P.A., 2003. A conceptual model for the origin of fault damage zone structures in high-porosity sandstone. *Journal of Structural Geology* 25, 333-344.

Shipton, Z.K., Evans, J.P., Robeson, K.R., Forster, C.B., Snelgrove, S., 2002. Structural heterogeneity and permeability in faulted eolian sandstone: Implications for subsurface modeling of faults. *AAPG bulletin* 86, 863-883.

Shipton, Z.K., Soden, A.M., Kirkpatrick, J.D., Bright, A.M., Lunn, R.J., 2006. How thick is a fault? Fault displacement-thickness scaling revisited. *Earthquakes: Radiated energy and the physics of faulting*, 193-198.

Sibson, R., 1977. Fault rocks and fault mechanisms. *Journal of the Geological Society* 133, 191-213.

Skurtveit, E., Ballas, G., Fossen, H., Torabi, A., Soliva, R., Peyret, M., 2014. Sand textural control on shear-enhanced compaction bands in poorly-lithified sandstone.

Skurtveit, E., Torabi, A., Gabrielsen, R.H., Zoback, M.D., 2013. Experimental investigation of deformation mechanisms during shear-enhanced compaction in poorly lithified sandstone and sand. *Journal of Geophysical Research: Solid Earth* 118, 4083-4100.

Soliva, R., Schultz, R.A., Ballas, G., Taboada, A., Wibberley, C., Sallet, E., Benedicto, A., 2013. A model of strain localization in porous sandstone as a function of tectonic setting, burial and material properties; new insight from Provence (southern France). *Journal of Structural Geology* 49, 50-63.

Solum, J.G., Brandenburg, J., Naruk, S.J., Kostenko, O.V., Wilkins, S.J., Schultz, R.A., 2010. Characterization of deformation bands associated with normal and reverse stress states in the Navajo Sandstone, Utah. *AAPG bulletin* 94, 1453-1475.

Sternlof, K.R., Karimi-Fard, M., Pollard, D., Durlofsky, L., 2006. Flow and transport effects of compaction bands in sandstone at scales relevant to aquifer and reservoir management. *Water Resources Research* 42.

Tembe, S., Baud, P., Wong, T.f., 2008. Stress conditions for the propagation of discrete compaction bands in porous sandstone. *Journal of Geophysical Research: Solid Earth* 113.

Thompson, D.B., 1970. The stratigraphy of the so-called Keuper Sandstone Formation (Scythian–? Anisian) in the Permo–Triassic Cheshire Basin. *Quarterly Journal of the Geological Society* 126, 151-181.

Torabi, A., Ellingsen, T., Johannessen, M., Alaei, B., Rotevatn, A., Chiarella, D., 2019. Fault zone architecture and its scaling laws: where does the damage zone start and stop? *Geological Society, London, Special Publications* 496, SP496-2018-2151.

Torabi, A., Fossen, H., 2009. Spatial variation of microstructure and petrophysical properties along deformation bands in reservoir sandstones. *AAPG bulletin* 93, 919-938.

Torabi, A., Fossen, H., Braathen, A., 2013. Insight into petrophysical properties of deformed sandstone reservoirs. *AAPG bulletin* 97, 619-637.

Trewin, N., 1989. The petroleum potential of the Old Red Sandstone of northern Scotland. *Scottish Journal of Geology* 25, 201-225.

Turcotte, D., 1986. Fractals and fragmentation. *Journal of Geophysical Research: Solid Earth* 91, 1921-1926.

Twiss, R.J., Moores, E.M., 1992. *Structural geology*. Macmillan.

Ujiie, K., Maltman, A.J., Sánchez-Gómez, M., 2004. Origin of deformation bands in argillaceous sediments at the toe of the Nankai accretionary prism, southwest Japan. *Journal of structural geology* 26, 221-231.

Vajdova, V., Baud, P., Wong, T.f., 2004. Compaction, dilatancy, and failure in porous carbonate rocks. *Journal of Geophysical Research: Solid Earth* 109.

Wakefield, O.J., Hough, E., Peatfield, A.W., 2015. Architectural analysis of a Triassic fluvial system: the Sherwood Sandstone of the East Midlands Shelf, UK. *Sedimentary Geology* 327, 1-13.

Walderhaug, O., 1994. Temperatures of quartz cementation in Jurassic sandstones from the Norwegian continental shelf--evidence from fluid inclusions. *Journal of Sedimentary Research* 64.

Wang, L., Rybacki, E., Bonnelye, A., Bohnhoff, M., Dresen, G., 2020. Experimental investigation on static and dynamic bulk moduli of dry and fluid-saturated porous sandstones. *Rock Mechanics and Rock Engineering*, 1-20.

Waters, C., Davies, S., 2006. Carboniferous: extensional basins, advancing deltas and coal swamps. In: *The geology of England and Wales*/edited by PJ Brenchley and PF Rawson. London: Geological Society of London 2006, 173-223.

Watkins, H., Bond, C.E., Healy, D., Butler, R.W., 2015. Appraisal of fracture sampling methods and a new workflow to characterise heterogeneous fracture networks at outcrop. *Journal of Structural Geology* 72, 67-82.

Wibberley, C.A., Petit, J.-P., Rives, T., 1999. Mechanics of high displacement gradient faulting prior to lithification. *Journal of Structural Geology* 21, 251-257.

Wilkins, S.J., Davies, R.K., Naruk, S.J., 2019. Subsurface observations of deformation bands and their impact on hydrocarbon production within the Holstein Field, Gulf of Mexico, USA. Geological Society, London, Special Publications 496, SP496-2018-2139.

Williams, G., Eaton, G., 1993. Stratigraphic and structural analysis of the Late Palaeozoic–Mesozoic of NE Wales and Liverpool Bay: Implications for hydrocarbon prospectivity. *Journal of the Geological Society* 150, 489-499.

Wilson, J.E., Goodwin, L.B., Lewis, C.J., 2003. Deformation bands in nonwelded ignimbrites: Petrophysical controls on fault-zone deformation and evidence of preferential fluid flow. *Geology* 31, 837-840.

Wong, T.-F., 1990. Mechanical compaction and the brittle—ductile transition in porous sandstones. Geological Society, London, Special Publications 54, 111-122.

Wong, T.-f., Baud, P., 2012. The brittle-ductile transition in porous rock: A review. *Journal of Structural Geology* 44, 25-53.

Wong, T., Baud, P., 1999. Mechanical compaction of porous sandstone. *Oil & Gas Science and Technology* 54, 715-727.

Wong, T., David, C., 1992. Grain crushing and pore collapse as controlling mechanisms for the brittle-ductile transition. *EOS Trans. Am. geophys. Un.* 73, 515.

Wong, T.f., David, C., Zhu, W., 1997. The transition from brittle faulting to cataclastic flow in porous sandstones: Mechanical deformation. *Journal of Geophysical Research: Solid Earth* (1978–2012) 102, 3009-3025.

Wood, D.M., 1990. *Soil behaviour and critical state soil mechanics*. Cambridge university press.

Worden, R.H., Burley, S.D., 2003. Sandstone diagenesis: the evolution of sand to stone. *Sandstone diagenesis: Recent and ancient*, 3-44.

Yale, D., Nieto, J.A., Austin, S., 1995. The effect of cementation on the static and dynamic mechanical properties of the Rotliegendes sandstone, The 35th U.S. Symposium on Rock Mechanics (USRMS), Reno, Nevada, pp. 169-175.

Zeeb, C., Gomez-Rivas, E., Bons, P.D., Blum, P., 2013. Evaluation of sampling methods for fracture network characterization using outcrops. AAPG bulletin 97, 1545-1566.

Zhang, J., Wong, T.F., Davis, D.M., 1990. Micromechanics of pressure-induced grain crushing in porous rocks. *Journal of Geophysical Research: Solid Earth* (1978–2012) 95, 341-352.

Zhang, J.J., Bentley, L.R., 1999. Change of bulk and shear moduli of dry sandstone with effective pressure and temperature. *CREWES Res Rep* 11, 01-16.

Zhong, W., Yue, F., Ciancio, A., 2018. Fractal behavior of particle size distribution in the rare earth tailings crushing process under high stress condition. *Applied Sciences* 8, 1058.

Zhu, W., Baud, P., Vinciguerra, S., Wong, T.f., 2011. Micromechanics of brittle faulting and cataclastic flow in Alban Hills tuff. *Journal of Geophysical Research: Solid Earth* 116.

Zoback, M.D., 1975. High pressure deformation and fluid flow in sandstone, granite, and granular materials. Stanford University.

Zuluaga, L.F., Fossen, H., Rotevatn, A., 2014. Progressive evolution of deformation band populations during Laramide fault-propagation folding: Navajo Sandstone, San Rafael monocline, Utah, USA. *Journal of Structural Geology* 68, 66-81.

Appendix

Appendix A. Petrog results of field samples.

Appendix B. Mini-permeameter measurements.

Appendix C. Triaxial test data.

Appendix D. Petrog results of triaxial samples.

Appendix E. Correction of hydrostat due to volume change of sandstone spacers.